

Atomic and Molecular Aspects of Astronomical Spectra

Taha Sochi

A dissertation submitted to the
Department of Physics & Astronomy
University College London
in fulfilment of the requirements for the degree of
Doctor of Philosophy

September 2012

Declaration

The work presented in this thesis is the result of my own effort, except where otherwise stated. All sources are acknowledged by explicit reference.

Taha Sochi

Abstract

In the first section of this thesis, we present the atomic part of our investigation. A C^{2+} atomic target was prepared and used to generate theoretical data required in the investigation of recombination lines that arise from collisions between electrons and ions in thin plasma found in planetary nebulae and other astrophysical objects. The **R**-matrix method of electron scattering theory was used to describe the C^{2+} plus electron system. Theoretical data concerning bound and autoionizing states were generated in the intermediate-coupling approximation by **R**-matrix and Autostructure codes and compared to experimental data. The comparison revealed very good agreement. These theoretical data were then used to generate dielectronic recombination data for C^+ which include transition lines, oscillator strengths, radiative transition probabilities, as well as emissivity and dielectronic recombination coefficients. The data were cast in the form of a line list, called SS1, containing 6187 optically-allowed transitions which include many C II lines observed in astronomical spectra. The data were validated by comparison to C^+ recombination data obtained from a number of sources in the literature. This line list was used to analyze the spectra from a number of astronomical objects, mainly planetary nebulae, and identify their electron temperature where the observational data were obtained from the literature. The electron temperature investigation was also extended to include free electron energy analysis which uses observational and theoretical data of FF and FB transitions to investigate the long-standing problem of discrepancy between the results of recombination and forbidden lines analysis and its possible connection to the electron distribution (Maxwellian or non-Maxwellian). In the course of this investigation two elaborate methods, one

for finding and analyzing resonances (**K**-matrix method) and the other for analyzing and identifying electron temperature from astronomical spectra (least squares minimization), were employed. A computer program for atomic transition analysis was also developed and used as the main tool for obtaining the line list and analyzing the observational spectra.

In the second section of the thesis we present the results of our molecular investigation; the generation of a comprehensive, calculated line list of frequencies and transition probabilities for the singly deuterated isotopologue of H_3^+ , H_2D^+ . The line list, which is the most comprehensive one of its kind in existence, contains over 22 million rotational-vibrational transitions occurring between more than 33 thousand energy levels and covers frequencies up to 18500 cm^{-1} . All energy levels with rotational quantum number, J , up to 20 are considered, making the line list useful for temperatures up to at least 3000 K. About 15% of these levels are fully assigned with approximate rotational and vibrational quantum numbers. The list is calculated using a previously proposed, highly accurate, *ab initio* model implemented in a high-accuracy computer code based on a two-stage discrete variable representation (DVR) approach. Various consistency checks were carried out to test and validate the results. All these checks confirmed the accuracy of the list. A temperature-dependent partition function, valid over a more extended temperature range than those previously published, and cooling function are presented. Temperature-dependent synthetic spectra for the temperatures $T = 100, 500, 1000$ and 2000 K in the frequency range $0\text{-}10000\text{ cm}^{-1}$ were also generated and presented graphically.

Acknowledgements and Statements

I would like to thank my supervisors Professor Peter Storey and Professor Jonathan Tennyson for their kindness, guidance and advice. It is a great privilege and gratifying experience to work with them over several years and learn from their deep knowledge and vast expertise in atomic, molecular and astro physics.

I also would like to thank the external examiner Professor Nigel Badnell from the University of Strathclyde, and the internal examiner Dr Sergey Yurchenko from the University College London for their constructive remarks and corrections and valuable recommendations for possible future work.

Apart from RMATRIX-I and Autostructure atomic codes and DVR3D molecular code which were used as the main computing tools, I also used RESMESH and another piece of code from Pete to calculate f -values from photoionization cross sections. The rest of tools and techniques belong to me. Anyway, I assume full responsibility for any error or failure.

The emphasis in this thesis is on the practical aspects of my work in an attempt to provide a full and credible account of how this investigation was conducted and how the conclusions were reached. Bare minimum of theory will be given when necessary for motivation and background as the theory is readily available in the literature and mainly belongs to other contributors.

Finally, I should acknowledge the encouragement and motivation which I received from family and friends while doing this PhD with special tribute to my wife.

The following articles are based on results and activities related directly to the research presented in this thesis:

- Taha Sochi. Emissivity: A program for atomic transition calculations. *Communications in Computational Physics*, 7(5):1118-1130, 2010.
- Taha Sochi; Jonathan Tennyson. A computed line list for the H_2D^+ molecular ion. *Monthly Notices of the Royal Astronomical Society*, 405(4):2345-2350, 2010.
- Taha Sochi; Peter J. Storey. Dielectronic Recombination Lines of C^+ . *Atomic Data and Nuclear Data Tables* (Accepted), 2012.
- Peter J. Storey; Taha Sochi. Electron Temperature of Planetary Nebulae from C II Recombination Lines. Submitted, 2012.

Contents

Declaration	1
Abstract	2
Acknowledgements and Statements	4
Contents	6
List of Figures	10
List of Tables	13
Nomenclature	18
Part I: Atomic Physics	24
1 Introduction	25
1.1 Recombination Processes	25
1.1.1 Radiative Recombination	26
1.1.2 Dielectronic Recombination	27
1.2 Literature Review	29
1.2.1 Theory of Recombination Lines	29
1.2.2 Recombination Lines of Carbon	33
1.3 Recombination versus Forbidden Lines Analysis	38
2 Physics of Scattering and Recombination	41
2.0.1 Close Coupling Approximation	42
2.0.2 R-matrix Method	45
2.0.2.1 Inner and Outer Regions	47
2.0.2.2 Matching of Solutions	48
2.0.2.3 Bound States	48
2.0.2.4 Resonances	48
2.0.2.5 Oscillator Strengths	49
2.0.2.6 Photoionization Cross Sections	50
2.0.2.7 Relativistic Effects	50

2.0.3	RMATRIX-I Code	51
3	Dielectronic Recombination Lines of C II	55
3.1	Theoretical Background	56
3.2	Autoionizing and Bound States Calculations	62
3.2.1	Methods for Investigating Resonances	63
3.2.1.1	QB Method	64
3.2.1.2	Time-Delay Method	66
3.2.1.3	K-Matrix Method	67
3.2.2	Preparing Target	68
3.2.3	Developing and Implementing K -matrix Method	69
3.2.4	Calculations	72
3.3	<i>f</i> -Values Calculations	75
3.3.1	<i>f</i> -Values for Free-Free Transitions	76
3.3.2	<i>f</i> -Values for Free-Bound Transitions	77
3.3.3	<i>f</i> -Values for Bound-Bound Transitions	82
3.4	Recombination and Emissivity Calculations	82
3.4.1	Practical Aspects	83
3.5	Comparison to Previous Work	84
4	Electron Temperature of Astronomical Objects	89
4.1	Method	91
4.1.1	Least Squares Minimization	95
4.2	Astronomical Objects	98
4.2.1	NGC 7009	99
4.2.2	NGC 5315	105
4.2.3	NGC 7027	109
4.2.3.1	Baluteau <i>et al</i>	109
4.2.3.2	Zhang <i>et al</i>	110
4.2.4	IC 418	115
4.2.5	NGC 2867	120
4.2.6	DQ Herculis 1934	123
4.2.7	CPD - 56°8032	126
4.2.8	He 2-113	129
4.3	Electron Distribution	132
4.4	Epilogue	136

Part II: Molecular Physics	140
5 Computed Line List for H₂D⁺	141
5.1 Introduction	141
5.1.1 Literature Review	144
5.1.2 Line Lists	146
5.2 Method	147
5.3 Validation and Primary Results	154
5.3.1 Comparison to Experimental and Theoretical Data	154
5.3.2 Partition Function	155
5.3.3 Cooling Function	158
5.3.4 Synthetic Spectra	161
6 Conclusions and Future Work	164
6.1 Conclusions	164
6.2 Recommendations for Future Work	167
Bibliography	169
A Using Lifetime Matrix to Investigate Single-Channel Resonances	190
B Error Analysis	195
B.1 Observed Error	196
B.2 Fixed Percentage Error	197
B.3 Poisson Error	197
C Emissivity Program Documentation	199
C.1 Theoretical background	200
C.2 Input and Output Files	202
C.2.1 ‘Input’ Data File	202
C.2.2 ‘ResEmis’ Input Data File	209
C.2.3 ‘ELEVEmis’ Input Data File	210
C.2.4 ‘Transitions’ Output Data File	211
C.3 Tests	211
D Input Data for R-matrix and Autostructure	213
D.1 R-matrix Input Data	213
D.1.1 STG1	213
D.1.2 STG2	214

D.1.3	STGJK	215
D.1.4	STG3	216
D.1.5	STGF	216
D.1.6	STGB	217
D.1.7	STGBF	217
D.1.8	STGBB	217
D.1.9	STGQB	217
D.2	Autostructure Input Data	218
D.2.1	Polarizability	218
D.2.2	Transition Probabilities	218
D.2.3	f -values	218
E	Tables	220
	Bound States	222
	Resonances	227
	FB f -values	229
	Sample of SS1	233
F	Input Data for DVR3D Code	233
F.1	Input Files for Stage DVR3DRJZ	233
F.2	Input Files for Stage ROTLEV3	234
F.3	Input Files for Stage DIPOLE	235
F.4	Input Files for Stage SPECTRA	235
F.5	Input Files for Spectra-BT2	235

List of Figures

2.1	Flow chart of the RMATRIX-I suite.	53
3.1	Schematic diagram of the low-lying autoionizing quartet and doublet states and their interaction in intermediate coupling scheme.	73
3.2	Examples of photoionization cross sections in mega barn (y -axis) of the indicated bound states near to the designated autoionizing states versus photon energy in Rydberg (x -axis).	80
4.1	Two prominent planetary nebulae, NGC 7027 and Cat's eye	99
4.2	The ratio of theoretical emissivity to observational flux as a function of temperature for the selected C II lines of NGC 7009 spectra of Fang and Liu [1].	100
4.3	Temperature dependence of χ^2 for NGC 7009 with the inclusion of line $\lambda 4267$. The temperature at χ_{min}^2 and the confidence interval are shown.	102
4.4	Temperature dependence of χ^2 for NGC 7009 with the exclusion of line $\lambda 4267$. The temperature at χ_{min}^2 and the confidence interval are shown.	102
4.5	Ratio of normalized observed flux to normalized theoretical emissivity (NFER) versus temperature on log-linear scales for the planetary nebula NGC 5315.	105
4.6	Temperature dependence of χ^2 for NGC 5315 with the inclusion of line $\lambda 4267$. The temperature at χ_{min}^2 and the confidence interval are shown.	107
4.7	Temperature dependence of χ^2 for NGC 5315 with the exclusion of line $\lambda 4267$. The temperature at χ_{min}^2 and the confidence interval are shown.	107
4.8	Temperature dependence of χ^2 for NGC 7027 of Baluteau <i>et al</i> [2]. The temperature at χ_{min}^2 and the confidence interval are shown. . .	111

4.9	Temperature dependence of χ^2 for NGC 7027 of Zhang <i>et al</i> [3] with the inclusion of line $\lambda 4267$. The temperature at χ_{min}^2 and the confidence interval are shown.	113
4.10	Temperature dependence of χ^2 for NGC 7027 of Zhang <i>et al</i> [3] with the exclusion of line $\lambda 4267$. The temperature at χ_{min}^2 and the confidence interval are shown.	113
4.11	The ratio of theoretical emissivity to observational flux as a function of temperature for the selected C II lines of IC 418 spectra of Sharpee <i>et al</i> [4].	115
4.12	Temperature dependence of χ^2 for IC 418 with the inclusion of line $\lambda 4267$. The temperature at χ_{min}^2 and the confidence interval are shown.	117
4.13	Temperature dependence of χ^2 for IC 418 with the exclusion of line $\lambda 4267$. The temperature at χ_{min}^2 and the confidence interval are shown.	118
4.14	Temperature dependence of χ^2 for NGC 2867-1. The temperature at χ_{min}^2 and the confidence interval are shown.	121
4.15	Temperature dependence of χ^2 for NGC 2867-2. The temperature at χ_{min}^2 and the confidence interval are shown.	122
4.16	Temperature dependence of χ^2 for DQ Herculis 1934. The temperature at χ_{min}^2 and the confidence interval are shown.	124
4.17	Temperature dependence of χ^2 for CPD - 56°8032. The temperature at χ_{min}^2 and the confidence interval are shown.	127
4.18	Temperature dependence of χ^2 for He 2-113. The temperature at χ_{min}^2 and the confidence interval are shown.	131
4.19	Electron distribution plot for NGC 7009 data of Fang and Liu [1], alongside Maxwell-Boltzmann, κ ($= 5.0$) and Druyvesteyn (with $x = 2.0$) distributions for $T = 5700$ K. The y -axis is in arbitrary units.	137
4.20	Electron distribution plot for NGC 7027 data of Zhang <i>et al</i> [3], alongside Maxwell-Boltzmann, κ ($= 5.0$) and Druyvesteyn (with $x = 2.0$) distributions for $T = 12300$ K. The y -axis is in arbitrary units.	138
4.21	Electron distribution plot for IC 418 data of Sharpee <i>et al</i> [4], alongside Maxwell-Boltzmann, κ ($= 5.0$) and Druyvesteyn (with $x = 2.0$) distributions for $T = 8200$ K. The y -axis is in arbitrary units.	138

4.22	Electron distribution plot for CPD - 56°8032 data of De Marco <i>et al</i> [5], alongside Maxwell-Boltzmann, κ (= 5.0) and Druyvesteyn (with $x = 2.0$) distributions for $T = 17300$ K. The y -axis is in arbitrary units.	139
4.23	Electron distribution plot for He 2-113 data of De Marco <i>et al</i> [5], alongside Maxwell-Boltzmann, κ (= 5.0) and Druyvesteyn (with $x = 2.0$) distributions for $T = 16200$ K. The y -axis is in arbitrary units.	139
5.1	Jacobi scattering coordinate system.	150
5.2	The H_2D^+ partition functions of ST1 (upper curve) and Sidhu <i>et al</i> [6] (lower curve).	160
5.3	A graph of per molecule emission of H_2D^+ (upper curve) and H_3^+ (lower curve) as a function of temperature on a log-log scale. The H_2D^+ curve is obtained from ST1 while the H_3^+ curve is obtained from a digitized image from Neale <i>et al</i> [7].	162
5.4	A graph of integrated absorption coefficient in cm.molecule^{-1} (on y axis) as a function of wave number in cm^{-1} (on x axis) within the range $0 - 10000 \text{ cm}^{-1}$ for $T = 100, 500, 1000$ and 2000 K.	163

List of Tables

3.1	The seven orbitals used to construct the C^{2+} target and their Slater Type Orbital parameters. The bar marks the pseudo orbitals. . . .	70
3.2	Orbital scaling parameters (λ 's) for Autostructure input. The rows stand for the principal quantum number n , while the columns stand for the orbital angular momentum quantum number l	77
3.3	Autoionization probabilities in s^{-1} of four resonance states as obtained in the current work (SS) compared to those obtained by De Marco <i>et al</i> [5] (DSB).	86
3.4	A sample of radiative transition probabilities in s^{-1} as obtained from this work compared to corresponding values found in the literature. The prime indicates an excited $1s^2 2s 2p(^3P^o)$ core. The $1s^2$ core is suppressed from all configurations.	87
3.5	Effective dielectronic recombination rate coefficients in $cm^3.s^{-1}$ of a number of transitions for the given 10-based logarithmic temperatures. The first row for each transition corresponds to Badnell [8], while the second row is obtained from the current work. The superscripts denotes powers of 10. The prime indicates an excited $1s^2 2s 2p(^3P^o)$ core. The $1s^2$ core is suppressed from all configurations.	88
4.1	The observational C II transition lines of Fang and Liu [1] that were used in the least squares minimization procedure to find the electron temperature of the line emitting region in the planetary nebula NGC 7009. The given flux is the normalized to the H_β flux.	101
4.2	The electron temperature in Kelvin of NGC 7009 from different atoms, ions and transitions as obtained from the cited literature, where BJ stands for Balmer Jump and PJ for Paschen Jump. CW refers to the current work. For reference [9] we followed the apparent labeling of the authors although the temperatures may have been derived from CEL lines.	104

4.3	The observational C II transition lines of Peimbert <i>et al</i> [10] that were used in the least squares minimization procedure to find the electron temperature of the line emitting region in the planetary nebula NGC 5315. The given flux is the normalized to the H_{β} flux.	106
4.4	The electron temperature in Kelvin of NGC 5315 from different atoms, ions and transitions as obtained from the cited literature, where BJ stands for Balmer Jump. CW refers to the current work.	108
4.5	The observational C II transition lines of Baluteau <i>et al</i> [2] that were used in the least squares minimization procedure to find the electron temperature of the line emitting region in the planetary nebula NGC 7027. The given flux is the normalized to the H_{β} flux.	110
4.6	The electron temperature in Kelvin for NGC 7027 derived from different atoms, ions and transitions as obtained from the cited literature, where BJ stands for Balmer Jump and PJ for Paschen Jump. CW refers to the current work where the first value was obtained from Baluteau <i>et al</i> data while the other two are obtained from Zhang <i>et al</i> data.	112
4.7	The observational C II transition lines of Zhang <i>et al</i> [3] that were used in the least squares minimization procedure to find the electron temperature of the line emitting region in the planetary nebula NGC 7027. The given flux is the normalized to the H_{β} flux.	114
4.8	The observational C II transition lines of Sharpee <i>et al</i> [4] that were used in the least squares minimization procedure to find the electron temperature of the line emitting region in the planetary nebula IC 418. The given flux is the normalized to the H_{β} flux.	116
4.9	The electron temperature in Kelvin of IC 418 from different atoms, ions and transitions as obtained from the cited literature, where BD stands for Balmer Discontinuity and RF for Radio Frequency. CW refers to the current work.	119
4.10	The observational C II transition lines of García-Rojas <i>et al</i> [11] that were used in the least squares minimization procedure to find the electron temperature of the line emitting region in the planetary nebula NGC 2867. The given flux is the normalized to the H_{β} flux. The first I value belongs to knot 1 and the second to knot 2. . . .	120

4.11	The electron temperature in Kelvin of NGC 2867 from different species and transitions as obtained from the cited literature, where BD stands for Balmer Decrement and K1 and K2 for knot 1 and knot 2. CW refers to the current work where the first value is related to knot 1 and the second to knot 2.	122
4.12	The observational C II transition lines of Ferland <i>et al</i> [12] that were used in the least squares minimization procedure to find the electron temperature of the line emitting region in DQ Herculis 1934. The given flux is the normalized to the H_{β} flux.	125
4.13	The electron temperature in Kelvin of DQ Herculis 1934 from different species and transitions as obtained from the cited literature, where BC stands for Balmer Continuum. CW refers to the current work.	125
4.14	The observational C II transition lines of De Marco <i>et al</i> [5] that were used in the least squares minimization procedure to find the electron temperature of the line emitting region in the planetary nebula CPD - 56°8032. The given flux is the absolute value in units of $\text{erg.s}^{-1}.\text{cm}^{-2}$	127
4.15	The electron temperature in Kelvin of the stellar wind of the CPD - 56°8032 Wolf-Rayet star from different species and transitions as obtained from the cited literature. CW refers to the current work. Also Davey [13] seems to support the value of 12800 K derived by Barlow and Storey [14].	128
4.16	The observational C II transition lines of De Marco <i>et al</i> [5] that were used in the least squares minimization procedure to find the electron temperature of the line emitting region in the planetary nebula He 2-113. The given flux is the absolute value in units of $\text{erg.s}^{-1}.\text{cm}^{-2}$	129
4.17	The electron temperature in Kelvin of the stellar wind of the He 2-113 Wolf-Rayet star as obtained from the cited literature. CW refers to the current work.	130
4.18	The 64 autoionizing states of C^{+} used in the current study with their energy in Ryd, departure coefficient, and autoionization probability in s^{-1} . The $1s^2$ core is suppressed from all configurations.	134

5.1	Sample of the ST1 levels file. The columns from left to right are for: index of level in file, J , symmetry, index of level in block, frequency in cm^{-1} , v_1 , v_2 , v_3 , J , K_a , K_c . We used -2 to mark unassigned quantum numbers.	153
5.2	Sample of the ST1 transitions file. The first two columns are for the indices of the two levels in the levels file, while the third column is for the A coefficients in s^{-1}	154
5.3	The main experimental data sources used to validate the ST1 list. Columns 2 and 3 give the number of data points and the frequency range of the experimental data respectively, while the last four columns represent the minimum, maximum, average, and standard deviation of discrepancies (i.e. observed minus calculated) in cm^{-1} between the ST1 and the experimental data sets.	156
5.4	Comparison between measured (Asvany <i>et al</i> [15]) and calculated (ST1) frequencies and relative Einstein B coefficients for a number of transition lines of H_2D^+ . These coefficients are normalized to the last line in the table. The absolute B coefficients, as obtained from the A coefficients of ST1 list using Equation 5.2, are also shown in column 5 as multiples of 10^{14} and in units of m.kg^{-1}	156
5.5	Asvany [15] data for the second overtone and combination transitions of H_2D^+ compared to the corresponding data as calculated from the ST1 list.	157
5.6	Asvany [15] data for the transitions of the (1,0,0) band of H_2D^+ detected with an optical parametric oscillator systems compared to the corresponding data as calculated from the ST1 list.	157
5.7	The partition function of H_2D^+ for a number of temperatures as obtained from Sidhu <i>et al</i> [6] and ST1 line lists.	159
E.1	The available experimental data from NIST for the bound states of C^+ below the $\text{C}^{2+} \text{ } ^1\text{S}_0^e$ threshold alongside the theoretical results from R -matrix calculations.	222
E.2	The available experimental data from NIST for the resonance states of C^+ above the $\text{C}^{2+} \text{ } ^1\text{S}_0^e$ threshold alongside the theoretical results as obtained by K -matrix and QB methods.	227

E.3	Free-bound f -values for bound symmetry $J^\pi = 1/2^o$ obtained by integrating photoionization cross sections from R -matrix calculations. The superscript denotes the power of 10 by which the number is to be multiplied.	229
E.4	Free-bound f -values for bound symmetry $J^\pi = 3/2^o$ obtained by integrating photoionization cross sections from R -matrix calculations. The superscript denotes the power of 10 by which the number is to be multiplied.	230
E.5	Free-bound f -values for bound symmetry $J^\pi = 5/2^o$ obtained by integrating photoionization cross sections from R -matrix calculations. The superscript denotes the power of 10 by which the number is to be multiplied.	231
E.6	Sample of the SS1 line list where several lines have been observed astronomically. The first column is for experimental/theoretical energy identification for the upper and lower states respectively where 1 refers to experimental while 0 refers to theoretical. The other columns are for the atomic designation of the upper and lower states respectively, followed by the air wavelength in angstrom and effective dielectronic recombination rate coefficients in $\text{cm}^3.\text{s}^{-1}$ for the given logarithmic temperatures. The superscript denotes the power of 10 by which the number is to be multiplied. The $1s^2$ core is suppressed from all configurations.	232

Nomenclature and Notation

α	indicial parameter in spherical oscillator
α	fine structure constant ($= e^2/(\hbar c 4\pi\epsilon_o) \simeq 7.2973525376 \times 10^{-3}$)
Γ^a	autoionization transition probability (s^{-1})
Γ^r	radiative transition probability (s^{-1})
Γ_{ul}^r	radiative transition probability from upper state u to lower state l (s^{-1})
δ	eigenphase sum
$\bar{\delta}$	eigenphase background
δ'	eigenphase gradient of \mathbf{K} -matrix with respect to energy (J^{-1})
Δ_E	full width at half maximum for energy distribution (J)
Δ_r	width of resonance (J)
ΔE	energy difference (J)
ϵ	energy of resonance (J)
ϵ_i	energy of colliding electron (J)
ϵ_o	permittivity of vacuum ($\simeq 8.854187817 \times 10^{-12} \text{F.m}^{-1}$)
ϵ	emissivity of transition line ($\text{J.s}^{-1}.\text{m}^{-3}$)
ϵ^{nt}	normalized theoretical emissivity
ϵ_{ul}	emissivity of transition line from state u to state l ($\text{J.s}^{-1}.\text{m}^{-3}$)
ζ	effective charge (C)
η	number of degrees of freedom
θ	function of colliding electron
ϑ	Coulomb function
κ	characteristic parameter of κ distribution
λ	wavelength (m)
λ_{lab}	laboratory wavelength (m)
λ_v	vacuum wavelength (m)
Λ	eigenvalue
μ	reduced mass (kg)
ν	frequency (s^{-1})
ξ_i	exponent in Slater Type Orbital formulation

π	parity
ϱ_e	recombination coefficient for capture process ($\text{m}^3.\text{s}^{-1}$)
ϱ_f	effective recombination coefficient ($\text{m}^3.\text{s}^{-1}$)
σ	photoionization cross section (m^2)
τ	lifetime of state (s)
τ_o	atomic time unit ($= \hbar/E_h \simeq 2.418884326505 \times 10^{-17}\text{s}$)
ϕ	vector coupled function
Φ	function of bound-state type in close coupling expansion
χ^2	goodness-of-fit index
χ	spin and angle functions of colliding electron
ψ	function of N -electron target
Ψ	wavefunction of Schrödinger equation
ω_e	fundamental frequency in Morse and spherical oscillators (s^{-1})
a_0	Bohr radius ($\simeq 5.2917720859 \times 10^{-11}\text{m}$)
\mathbb{A}	anti-symmetrization operator
\mathcal{A}	inner region radius in R -matrix formulation (m)
A	Einstein A coefficient (s^{-1})
\AA	angstrom
b	departure coefficient
b_u	departure coefficient of state u
B	Einstein B coefficient ($\text{m}.\text{kg}^{-1}$)
B	matrix in QB method
c	speed of light in vacuum ($299792458 \text{ m}.\text{s}^{-1}$)
c	coefficient in close coupling expansion
C_i	coefficient in Slater Type Orbital formulation
C_p	contribution to polarizability
D	dipole operator
D_e	dissociation energy in Morse oscillator (J)
e	elementary charge ($\simeq 1.602176487 \times 10^{-19}\text{C}$)
e^-	electron
E	energy (J)
E_h	Hartree energy ($\simeq 4.35974394 \times 10^{-18}\text{J}$)

E_i	energy point in K -matrix method (J)
E_0	position of K -matrix pole on energy mesh (J)
E_p	photon energy (J)
E_r	energy position of resonance (J)
E_x	characteristic energy of Druyvesteyn distribution
E_κ	characteristic energy of κ distribution
f	oscillator strength
f_{ul}	oscillator strength of transition from state u to state l
F	radial function
F	energy flux ($\text{J.s}^{-1}.\text{m}^{-2}$)
\mathbf{F}	vector of radial functions
g	parameter in K -matrix method (J)
g	statistical weight in coupling schemes ($= 2J + 1$ for IC)
g	nuclear spin degeneracy factor
h	Planck's constant ($\simeq 6.6260693 \times 10^{-34}$ J.s)
\hbar	reduced Planck's constant ($= h/2\pi \simeq 1.0545717 \times 10^{-34}$ J.s)
H	Hamiltonian of the whole system
H_{bp}	Breit-Pauli Hamiltonian
H_{nr}	non-relativistic Hamiltonian
H_{rc}	relativistic correction Hamiltonian
i	imaginary unit ($\sqrt{-1}$)
I	de-reddened flux ($\text{J.s}^{-1}.\text{m}^{-2}$)
\mathbf{I}	identity matrix
I^{no}	normalized observational flux
J	total angular momentum quantum number
J	rotational quantum number
k	Boltzmann's constant ($\simeq 1.3806505 \times 10^{-23}$ J.K $^{-1}$)
k	the projection of J along the body-fixed z -axis
\mathbf{K}	reactance matrix in R -matrix theory
K	single-element K -matrix
K_i	scalar value of single-element K -matrix at energy E_i
K_o	background contribution to K -matrix
l	orbital angular momentum quantum number

L	total orbital angular momentum quantum number
m	mass (kg)
m_e	mass of electron ($\simeq 9.10938215 \times 10^{-31}$ kg)
\mathbf{M}	lifetime matrix
M	single-element \mathbf{M} -matrix
M_{max}	maximum value of single-element \mathbf{M} -matrix
n	principal quantum number
n_f	effective quantum number
N	number density (m^{-3})
N_e	number density of electrons (m^{-3})
N_i	number density of ions (m^{-3})
N^S	Saha population (m^{-3})
O	number of observations
P	number of fitting parameters
\mathcal{P}	partition function
$P_{nl}(r)$	radial function in Slater Type Orbital formulation
P_i	power of r in Slater Type Orbital formulation
\mathbf{Q}	matrix in \mathbf{QB} method
\mathbf{R}	resonance matrix in \mathbf{R} -matrix theory
r	radius (m)
\mathbf{r}	radius vector
r_1	diatomic distance in triatomic coordinate system (m)
r_2	distance of third atom from the diatom center of mass (m)
r_e	equilibrium distance in Morse oscillator (m)
\mathbf{S}	scattering matrix in \mathbf{R} -matrix theory
S	single-element \mathbf{S} -matrix
S	total spin angular momentum quantum number
\mathcal{S}	line strength (J^{-1})
t	time (s)
T	temperature (K)
T_e	electron temperature (K)
v	vibrational quantum number
$V_{ii'}$	multipole potentials ($\text{J}\cdot\text{C}^{-1}$)

w	statistical weight in least squares procedure
x	characteristic parameter of Druyvesteyn distribution
W	cooling function (J.s^{-1})
X_{n+}	ion of effective positive charge n
$X_{(n-1)+}^*$	excited bound state of ion with effective positive charge $n - 1$
$X_{(n-1)+}^{**}$	doubly-excited state with effective positive charge $n - 1$
y^c	calculated value
y^o	observed value
z	residual charge
Z	atomic number
∇	del operator
∇^2	Laplacian operator

Abbreviations

$[\cdot]^*$	complex conjugate of matrix
'	upper
"	lower
au	atomic unit
BB	Bound-Bound
BJ	Balmer Jump
C	Coulomb
CCD	Charge-Coupled Device
CEL	Collisionally-Excited Lines
DR	Dielectronic Recombination
DVR	Discrete Variable Representation
eV	electron-Volt
F	Faraday
FB	Free-Bound
FF	Free-Free
FWHM	Full Width at Half Maximum
$(\cdot)_f$	final
GHz	Gigahertz
IC	Intermediate Coupling
IUE	International Ultraviolet Explorer

$(\cdot)_i$	initial
J	Joule
K	Kelvin
kg	kilogram
kpc	kiloparsec ($\simeq 3.1 \times 10^{19}$ meters)
$(\cdot)_l$	lower
$(\cdot)^L$	length form
m	meter
$(\cdot)_{max}$	maximum
$(\cdot)_{min}$	minimum
NIST	National Institute of Standards and Technology
ORL	Optical Recombination Lines
PJ	Paschen Jump
PN(e)	Planetary Nebula(e)
RR	Radiative Recombination
Ryd	Rydberg
s	second
STO	Slater Type Orbital
THz	Terahertz
u	atomic mass unit
$(\cdot)_u$	upper
$(\cdot)_{ul}$	upper to lower
$(\cdot)^V$	velocity form
\forall	for all

Note: units, when relevant, are given in the SI system. Vectors and matrices are marked with boldface. Some symbols may rely on the context for unambiguous identification. The physical constants are obtained from the National Institute of Standards and Technology (NIST) [16].

Part I

Atomic Physics:

Dielectronic Recombination Lines of C II and Their Application in Temperature Diagnosis of Astronomical Objects

Chapter 1

Introduction

Many atomic processes can contribute to the production of carbon spectral lines. These processes include radiative and collisional excitation, and radiative and dielectronic recombination. The current study is concerned with some of the carbon lines produced by dielectronic recombination and subsequent radiative cascades. In the following we outline the recombination processes of primary interest to our investigation.

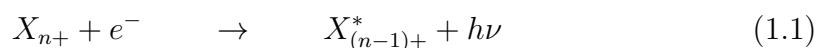
1.1 Recombination Processes

The low-density plasma of nebulae heated by energetic photons from their progenitors provides an ideal environment for many physical processes. These include radiative recombination, dielectronic recombination, three body recombination and charge transfer. Recombination is believed to play a vital role in the physical processes that occur in nebulae, and hence a deep understanding of its role is required for analyzing nebular spectroscopy and modeling nebular evolution. The principal electron-ion recombination processes which are responsible for the emission of recombination lines are Radiative Recombination (RR) and Dielectronic Recombination (DR).

ination (DR). Recombination of an electron and ion may take place through a background continuum known as radiative recombination, or through a resonant recombination process involving doubly-excited states known as dielectronic recombination. The latter can lead either to autoionization, which is a radiationless transition to a lower state with the ejection of a free electron, or to stabilization by radiative decay of the core to a lower bound state, possibly the ground state, with a bound electron. The RR and DR processes are closely linked and the difference between them may therefore be described as artificial; quantum mechanically they are indistinguishable. Recombination is mainly due to dielectronic processes which are especially important at high temperatures when the autoionizing levels are energetically accessible to the free electrons [17–19]. In the following sections we give a brief account of these two important recombination processes.

1.1.1 Radiative Recombination

Radiative recombination (RR) is the time inverse of direct photoionization where a single electron is captured by an ion to a true bound state with the subsequent emission of photons. Symbolically, the RR process is given by

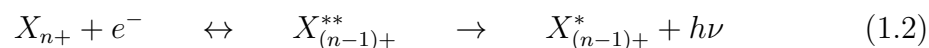


where X_{n+} is an ion of effective positive charge n , e^{-} is an electron, $X_{(n-1)+}^{*}$ is an excited bound state of the recombined ion with effective positive charge $(n-1)$, h is the Planck's constant and ν is the frequency of radiation. The rate for RR rises as the free electron temperature falls and hence it tends to be the dominant recombination process at low temperatures. It is particularly significant in the cold ionized plasmas found, for instance, in some supernova remnants. Radiative recombination is also the only route to recombination for single electron systems,

such as H and He⁺, because dielectronic recombination does not work on these systems [17–21].

1.1.2 Dielectronic Recombination

Dielectronic recombination (DR) is a two step process that involves the capture of a colliding continuum electron by an ion to form a doubly excited state. Symbolically, DR can be described by the relation



where $X_{(n-1)+}^{**}$ is a doubly-excited autoionizing state with effective positive charge $(n-1)$. This can be followed either by autoionization to the continuum with probability Γ^a , or by stabilization through a radiative decay of the captured electron or an electron in the parent to a true bound state of the excited core ion with probability Γ^r . The latter, which is the dielectronic recombination process, is responsible for the production of many recombination lines. Depending on the autoionizing state, the probabilities of these competing processes can go in either direction, that is $\Gamma^a > \Gamma^r$ or $\Gamma^a < \Gamma^r$. These excited autoionizing systems underly resonances in the photoionization cross sections. The resonance states are normally unstable and hence they decay primarily by autoionization rather than radiative decay. The resonance phenomenon is a highly important feature in atomic and molecular collisions as it plays a vital role in electron scattering with atoms, ions and molecules. The Auger effect is one of the early examples of the resonance effects that have been discovered and extensively investigated [20, 21].

Dielectronic recombination dominates at high temperatures as it requires sufficiently energetic electrons to excite the target, though it is still highly significant at low temperatures by recombination through low-lying resonances near the ion-

ization threshold, where at these temperatures the free electrons can enter only these states. As the temperature rises, higher autoionizing levels can be reached and the process becomes more complicated by the involvement of many autoionizing states. As the energy of the resulting system in dielectronic recombination is greater than the binding energy of the whole system, the state normally autoionizes spontaneously and hence it is usually described as an autoionizing state. Because the dielectronic recombination and autoionization occur rapidly, the population of the autoionizing state can be held at its local thermodynamic equilibrium level relative to the ion-free electron system [22].

DR is a fundamental atomic process that has many manifestations in astrophysics and fusion plasmas; these include planetary nebulae and laboratory laser-induced plasmas. More specifically, the recombination lines produced by this process can be used to determine elemental abundances and electron temperatures in planetary nebulae and to diagnose plasma conditions in laboratory. The process is also important for evaluating the energy balance and degree of ionization in hot and cold plasmas as it contributes to the determination of state population and ionization balance at various ranges of temperature and electronic number density. DR can occur through numerous transitional autoionizing states; possibly the whole Rydberg series [19, 23].

We may distinguish three types of dielectronic recombination mechanism with relevance at different temperatures

1. High-temperature dielectronic recombination which occurs through Rydberg series of autoionizing states, and in which the radiative stabilization is via a decay within the ion core.
2. Low-temperature dielectronic recombination which operates via a few near-threshold resonances with radiative stabilization usually through decay of the

outer, captured electron. These resonances are usually within a few thousand wave numbers of threshold, so this process operates at thousands to tens of thousands of degrees Kelvin.

3. Fine structure dielectronic recombination which is due to Rydberg series resonances converging on the fine structure levels of the ground term of the recombining ion, and is necessarily stabilized by outer electron decays. This process can operate at very low temperatures, down to tens or hundreds of Kelvin.

In the current work we are concerned only with low-temperature dielectronic recombination and the resulting spectral lines.

1.2 Literature Review

In this section we present a short literature review to highlight some important developments in the theory of recombination lines, followed by a brief account on the previous work on the carbon lines in the spectra of planetary nebulae and similar astronomical objects.

1.2.1 Theory of Recombination Lines

Recombination of electrons and ions during scattering processes, which commonly occurs in many gaseous and plasmic environments, is a fundamental atomic process that has a strong impact on many physical systems. Recombination lines produced by such a process can be used as a diagnostic tool to determine elemental abundances and electron temperatures in planetary nebulae. In the laboratory, these lines can be used to probe the conditions of laser induced plasmas and provide

information that is essential for plasma modeling and fusion conditions. Therefore, there is a huge amount of literature on all aspects of this important phenomenon. In this section we present a non-comprehensive overview on some developments in the theory of recombination lines. As dielectronic recombination is the principal recombination process in most systems of interest to us and is the only one that we considered in our recombination calculations, this overview will be dedicated to this process.

Dielectronic recombination was investigated by Massey and Bates [24, 25] in connection with the Earth's atmosphere using intuitive non-rigorous arguments focusing on recombination in plasma at rather low electron temperatures with consideration of low-lying resonances just above the ionization threshold. Burgess [26] investigated dielectronic recombination in the solar corona and highlighted the importance of this process at high temperatures in low-density hot plasma making it a possible dominant recombination process at coronal temperature. Goldberg [27] pointed out to the significance of dielectronic recombination at low temperatures in the context of analyzing the intensity of transition lines in the spectrum of planetary nebulae.

The general theory of electron-ion scattering was developed by Seaton [28] in a study to analyze resonance structures on the basis of quantum defect theory using the \mathbf{R} -matrix formulation. In another study, Davies and Seaton [29] investigated optical radiation in the continuum caused by recombination of an electron with a positive ion using a radiation damping approach for bound states transitions, and hence generalized this theory to the case of an optical continuum. Their techniques are capable of solving the problem of overlapping resonances found in dielectronic recombination. The results obtained from this investigation contributed to the subsequent development of quantum mechanical treatment of DR.

Presnyakov and Urnov [30] examined the problem of positive ion excitation by

electron collision, which leads to resonance structures in the cross sections, using Green functions to describe the Coulomb field. Their investigation concluded that the dielectronic recombination processes can lead to significant alteration in the rate coefficients of collisionally-excited ions. Beigman and Chichkov [31] examined dielectronic recombination through the forbidden levels and found that this process essentially increases the rate of total recombination at low temperatures. They also observed that dielectronic recombination is significant for low-temperature highly-ionized thin plasma. The importance of dielectronic recombination in general at low temperatures, typical of planetary nebulae, for the low-lying autoionizing states was also established by Storey [32] and Nussbaumer and Storey (e.g. [33]).

Using quantum defect theory of Seaton [28] and radiation damping treatment of Davies and Seaton [29], Bell and Seaton [34] developed a theory for dielectronic recombination process to accommodate resonance overlapping and the interaction with the radiation field. In a subsequent study, Harmin [35] extended this theory to incorporate the effect of electric fields in the scattering matrix where the Rydberg series of autoionizing states have been analyzed within a unified Stark quantum-defect treatment.

In a succession of papers, mainly focused on the second-row elements of the periodic table, Nussbaumer and Storey (e.g. [36]) developed the theory of dielectronic recombination rate coefficient calculations which is widely used nowadays in the computational work and simulation of recombination processes. Their approach is based on the use of experimental data for autoionizing energy levels with the possibility of using theoretical data obtained from atomic scattering and structure codes, such as RMATRX-I and Autostructure, to fill the gaps in the experimental data. The current work follows this approach in computing dielectronic recombination rate coefficients of C^+ .

Badnell [37] developed a fast accurate method for computing the total dielec-

tronic recombination rate coefficients for He-like ions using his previously-developed [38] frozen-core approximation, and applied this method to the highly charged ion Fe^{24+} . He also made other contributions to the theory and application of dielectronic recombination which include calculating dielectronic recombination rate coefficients for several ions (e.g. [8, 39, 40]), assembly of a comprehensive dielectronic recombination database [19], and the development and maintenance of the Autostructure code and its theoretical foundations [41]. Autostructure was used by many researchers to compute theoretical data related to dielectronic recombination as well as other types of atomic structure and scattering processes. This includes the current study where Autostructure was used, alongside the \mathbf{R} -matrix code, to generate theoretical dielectronic recombination data for the SS1 line list.

Using the isolated resonance approximation and the distorted wave theory, LaGattuta *et al* [42] proposed a theoretical approach for calculating the effect of static electric fields on the target cross section in dielectronic recombination processes. In another theoretical study based on a multichannel quantum defect theory of the Stark effect, dielectronic recombination under the effect of electric fields was examined by Sakimoto [43] with the derivation of simple formulae for computing the cross sections in DR to account for the effect of externally-imposed electric fields. Nahar and Pradhan [44, 45] presented a unified recombination *ab initio* treatment which incorporates both radiative and dielectronic processes within the close coupling approximation of electron-ion scattering to enable the calculation of a single, total recombination rate coefficient that may be employed for a variety of astrophysical applications.

1.2.2 Recombination Lines of Carbon

There is an extensive literature on the applications of recombination lines theory. However, in this section we only highlight some studies on the recombination lines of carbon relevant to the applications of PNe and similar astronomical objects with special interest in the C II lines.

Leibowitz [46] investigated the energy level population of ions in planetary nebulae with particular emphasis on the contribution of radiative excitation. The results were then applied to the intensity ratios of C IV lines in several planetary nebulae under various excitation conditions. In another study [47], he investigated the polarization of C IV emission lines in the spectra of planetary nebulae. Investigating the structure of the Orion Nebula and the surrounding neutral medium, Balick *et al* [48] mapped the recombination line C 85 α of carbon using high spatial resolution all over the nebula to determine the ionized carbon distribution and its relationship to the H II region.

Nussbaumer and Storey [49] examined a number of recombination lines of carbon in the context of studying the effect of the solar radiation field on the ionization balance for the purpose of analyzing the transition region in the solar chromosphere-corona. In a subsequent study [50] they computed the effective dielectronic recombination coefficients for selected lines of ions of carbon and other elements. The effective recombination coefficients were then fitted, as a function of temperature, to a suitable empirical formula in a temperature range found in planetary nebulae and similar astrophysical objects. Boughton [51] investigated several carbon recombination lines observed in the direction of Orion Nebula to construct two-cloud models which can replicate the observed intensities of the carbon lines and the velocities of the emitting regions.

In a series of papers, Harrington *et al* [52] discussed the recombination processes

in the context of investigating the carbon abundance in the low-excitation planetary nebula IC 418 using ultraviolet spectral observations. In another study, Harrington *et al* [9] investigated some recombination lines of carbon using in their analysis results obtained earlier by Storey. In another paper of the same series, Clavel *et al* [53] analyzed the C II $\lambda 1335$ Å dielectronic recombination multiplet observed in the spectra of the planetary nebula IC 418.

Clegg *et al* [54] investigated a bright nebular region in the low-excitation planetary nebula NGC 40 using optical and IUE spectra for the purpose of probing the physical conditions and determining elemental abundances. This investigation led to the identification and determination of relative intensity of several C II recombination lines in NGC 40 and IC 418. Hayes and Nussbaumer [55] examined the effect of dielectronic recombination process on the emissivity of the C II $\lambda 1335$ Å multiplet observed in various astronomical objects including planetary nebulae, and compared this to the effect of collisional excitation.

Investigating the abundance of carbon in planetary nebulae, Kholtygin [56] calculated the intensities of recombination lines of C²⁺ ion and used the observed intensities of several lines belonging to a number of carbon ions to determine their abundances, as well as the total abundance of carbon, in 46 planetary nebulae. In a later study [57] he used the calculated and observed intensities of carbon recombination and intercombination lines to find the effect of small temperature and density fluctuations on the intensities in the spectra of planetary nebulae. Bogdanovich *et al* [58] calculated the relative intensities of a number of C II recombination lines, and used the observed intensities of these lines to determine the abundances of C²⁺ ion in 12 nebulae.

Badnell [8] used the Autostructure code within an intermediate coupling scheme to compute configuration mixing effective dielectronic recombination rate coefficients for the recombined C⁺ ion at temperatures $T = 10^3 - 6.3 \times 10^4$ K applicable

to planetary nebulae, and the results were tabulated for the quartet-quartet lines and some doublet-doublet lines. He also compared the total rate coefficients for dielectronic recombination and radiative recombination where the former have been obtained within an LS as well as an intermediate coupling schemes. Péquignot *et al* [17] computed effective and total radiative recombination coefficients for selected optical and ultraviolet transitions of ions of carbon and other elements that produce most recombination lines observed in nebulae. The results were fitted to a four-parameter empirical expression which is valid over a wide range of electron temperature and at low electron number density.

In their investigation of the carbon abundance in planetary nebulae and the long-standing problem of discrepancy between recombination and forbidden lines results, Rola and Stasińska [59] examined the C II $\lambda 4267$ Å recombination multiplet and analyzed the observational data obtained from various sources for many planetary nebulae. Baluteau *et al* [2] examined several recombination lines of carbon in the course of studying the far-red spectrum of the bright and spectrum-rich NGC 7027 planetary nebula. Davey *et al* [60] presented effective recombination coefficients for C II lines originating from transitions between doublet states in LS -coupling scheme using **R**-matrix code. Their results span a wide temperature range between 500-20000 K with an electron number density of 10^4 cm⁻³ relevant to planetary nebulae.

Investigating the chemical abundances of planetary nebulae, Liu *et al* [61] examined several optical recombination lines of carbon observed in a number of planetary nebulae. Peng *et al* [62] investigated theoretically the C II recombination line $\lambda 8794$ Å, which is important for determining carbon abundance in planetary nebulae, using the **R**-matrix method. In a similar study [23] they investigated dielectronic recombination processes of C²⁺ ion in planetary nebulae where several C II recombination lines were examined in the course of this study. Zhang *et al*

[3] thoroughly examined the rich spectra of the planetary nebula NGC 7027. The extensive line list presented in this study comprises over 1100 transition lines from many atoms and ions of various elements and includes many recombination lines of carbon and its ions.

Extensive observational studies, similar to that of Zhang *et al*, are those of Liu *et al* [63] on the M 1-42 and M 2-36 planetary nebulae, Sharpee *et al* [4, 64] related to the planetary nebula IC 418, Peimbert *et al* [10] on NGC 5315, and Fang and Liu [1] on the bright planetary nebula NGC 7009. There are many other studies which are not as extensive as the previous ones but contain some observational spectral data from planetary nebulae and similar objects that include carbon recombination lines in general and C II in particular. Examples of these studies are: Flower [65], Barker [66], Aller and Keyes [67], Petitjean *et al* [68], Liu *et al* [61, 69–71], Esteban *et al* [72–76], De Marco *et al* [5], Garnett and Dinerstein [77], Bernard-Salas *et al* [78–81], Peimbert [82], Wesson *et al* [83–86], Tsamis *et al* [87–90], Ruiz *et al* [91], García-Rojas *et al* [11, 92–95], Ercolano *et al* [96], Stasińska *et al* [97], Robertson-Tessi and Garnett [98], Wang and Liu [99], Sharpee *et al* [100], and Williams *et al* [101]. Some of these studies are used as sources of observational data in our investigation, as will be examined later on in this thesis.

This review highlights the diversity of the work that has been done on the C II recombination lines although this topic has not been comprehensively investigated as there are many gaps to be filled. From the perspective of atomic physics, the most comprehensive of these studies and most relevant to the current investigation are those of Badnell [8] who calculated configuration mixing effective dielectronic recombination coefficients for the recombined C⁺ ion at temperatures $T = 10^3 - 6.3 \times 10^4$ K applicable to planetary nebulae, and Davey *et al* [60] who computed effective recombination coefficients for C II transitions between doublet states for the temperature range 500-20000 K with an electron density of 10^4 cm^{-3} relevant

to planetary nebulae. Badnell performed calculations in both LS and intermediate coupling schemes and over a wide temperature range, using the Autostructure code [41, 102, 103] which treats the autoionizing states as bound and the interaction with the continuum states by a perturbative approach. On the other hand, Davey *et al* performed their calculations using the **R**-matrix code [104] which utilizes a more comprehensive recombination theory based on a unified treatment of bound and continuum states but worked in the LS -coupling scheme and hence their results were limited to doublet states.

The aim of the current study is to build on these investigations and elaborate on them by using the **R**-matrix code with an intermediate coupling scheme. However, our investigation will be limited to the dielectronic recombination concentrating our attention on the low-lying autoionizing states. On the observational perspective, most of the previous studies have focused on a few recombination lines employing the traditional method of using intensity ratio to analyze the physical conditions, especially electron temperature and number density, of the line-emitting regions. The current study tries to broaden some of these aspects first by using any reliable data, and second by adopting a more comprehensive method of analysis, namely the least squares optimization, which is a collective method that can involve several transitions simultaneously to analyze the physical conditions. However, we do not use first-hand observational data and therefore we rely on data reported in the refereed literature. Moreover, we will focus our attention on electron temperature diagnosis of the line-emitting regions.

1.3 Recombination versus Forbidden Lines Analysis

In this section we briefly discuss the long-standing dilemma in the physics of nebulae demonstrated by the discrepancy between recombination and forbidden lines results and the implication of this on our investigation. Resolving this puzzle is extremely important not only for understanding the nebular conditions but also for identifying possible flaws in the underlying physical models. The collisionally-excited lines (CEL), also generally known in this context as forbidden lines, are produced by collision between energetic electrons and atoms and ions with a subsequent excitation and decay, while the optical recombination lines (ORL) are produced when electrons combine with ions by one of the aforementioned recombination mechanisms. These lines are detected either in emission or absorption modes. Both CELs and ORLs can in principle provide information about the physical and chemical conditions of the emitting and absorbing regions such as temperature, number density, pressure, elemental abundance, chemical composition and so on. Until recently, the main means used in the planetary nebula investigation is the CELs. One reason is the relative ease of observing and analyzing these lines as they are more abundant and intense than the ORLs. However, the ORLs are also used in the elemental abundance determination studies by using their relative intensities to the hydrogen lines [22, 88, 89, 105].

Although the forbidden lines are much stronger than the recombination lines, they are highly dependent on temperature and density structure and hence can lead to large systematic errors when used for instance in ionic abundance estimation. On the other hand, the faint recombination lines can be easily contaminated by radiation from other excitation processes such as fluorescence. Despite all these differences, there is a common feature between the results obtained from these lines;

that is for all the atomic species investigated so far (mainly from the second row of the periodic table such as C, N, O and Ne) the forbidden lines in planetary nebulae normally produce lower ionic abundances than the corresponding values obtained from the recombination lines. The ratio of the ORLs to the CELs abundances is case dependent and can vary by a factor of 30 or even more. This has cast doubt on the validity of the previously accepted CELs analysis results. The systematic nature of this problem rules out the possibility of recombination line contamination by resonance fluorescence or the inaccuracies in recombination coefficients as possible reasons as may have been suggested. This problem may be correlated to the dichotomy between the temperature obtained from the Balmer jump of H I recombination lines and that from the collisionally-excited forbidden lines where the latter is systematically higher than the former [57, 106, 107]. In fact, obtaining higher electron temperatures from forbidden lines than those deduced from recombination lines is a general trend in nebular studies.

Several explanations have been proposed to justify these discrepancies individually or collectively, though no one seems to be satisfactory or universally accepted. One explanation is the sensitivity of the collisionally-excited lines to temperature and structure fluctuations (e.g. exponential temperature dependency of the emissivity of these lines) which amplifies the errors that are intrinsically associated with these parameters. However, this reason alone cannot explain why the forbidden lines always produce lower abundance values. Another explanation is that the large temperature and density fluctuations within the nebular structure result in systematic underestimation of the heavy element abundances from the forbidden lines. The existence of knots depleted of hydrogen with high heavy element contents within the nebular gas has been proposed as a possible reason for these fluctuations and subsequent implications. The temperature inside these knots of high metallicity, and hence high opacity to stellar ultraviolet emissions and large

cooling rates, is expected to be too low for efficient production of forbidden lines though it is still sufficiently high for the emission of recombination lines. Consequently, the recombination and collisional lines originate in different regions of the nebular gas with different elemental abundances and different temperatures. However, the existence and composition of these knots and their effect on the selectivity of emission lines is unsettled issue and a matter of debate. Moreover, in some cases the discrepancy between the collisional and recombination abundances is too large to explain by temperature fluctuation alone although it may be partially responsible [61, 69, 87, 108].

In a recent paper by Nicholls *et al* [109] it is claimed that this long-standing problem in planetary nebulae and H II regions could arise from the departure of the electron energy distribution from the presumed Maxwell-Boltzmann equilibrium condition, and hence it can be solved by assuming a κ -distribution for the electron energy following a method used in the solar data analysis. One possible criticism to this approach is that the large discrepancy obtained in some cases may not be explicable by this adjustment to the electron distribution. Electron distribution will be the subject of a fairly thorough investigation in section 4.3 where we used lines originating from resonance states (that is FF and FB transitions) to obtain a direct sampling of the electron energy distribution based on the observational de-reddened flux with theoretically-obtained parameters such as the departure coefficients of the involved autoionizing states and the radiative probabilities of these transitions.

Amid the uncertainties highlighted by the CELs versus ORLs puzzle, it is extremely important to do more research especially on the recombination lines theory to have a breakthrough in this long-standing problem. We hope that our research on carbon recombination lines will be a valuable contribution in this direction.

Chapter 2

Physics of Scattering and Recombination

In this chapter we give a brief theoretical background about the physics of scattering and recombination which forms the basis for our computational model. Our scattering quantum system comprises an N -electron atomic or ionic target plus a colliding electron where the particles are assumed to interact through electromagnetic forces only. The quest then is to solve the following time independent Schrödinger equation with suitable boundary conditions

$$H\Psi = E\Psi \quad (2.1)$$

where H is the Hamiltonian of the whole system (nucleus plus $N + 1$ electrons), Ψ is the quantum wavefunction, and E is the total energy of the system. In the case of light atoms and ions, the relativistic effects can be ignored and hence H in atomic units is given by

$$H = \sum_{n=1}^{N+1} \left(-\frac{1}{2} \nabla_n^2 - \frac{Z}{r_n} + \sum_{m>n}^{N+1} \frac{1}{r_{nm}} \right) \quad (2.2)$$

In this equation, ∇^2 is the Laplacian operator, Z is the nuclear atomic number, r_n is the distance between the nucleus and the n^{th} electron, and $r_{nm} = |r_n - r_m|$ is the distance between the n^{th} and m^{th} electrons. The assumption here is that the nucleus is a massive motionless point charge compared to the surrounding electrons. The first term of Equation 2.2 represents the total kinetic energy of the electrons, the second term is the total potential energy due to the attractive Coulomb forces between the nucleus and each electron, and the last one is the total potential energy due to the Coulomb repulsive forces between each pair of electrons. The first two are called the one-electron terms while the third is called the two-electron term [104].

There are several ways for solving this system, one of which is to employ the close coupling technique which provides a powerful framework for performing scattering computations involving collisions between an electron and an N -electron target. The method can be used to analyze such quantum systems and obtain valuable information such as wavefunctions, energy of states, photoionization cross sections, oscillator strengths, and so on. In the following we outline this method and its realization based on the **R**-matrix theory.

2.0.1 Close Coupling Approximation

In the close coupling approach, the wavefunction is expanded in the following form

$$\Psi = \mathbb{A} \sum_i \psi_i \theta_i \quad (2.3)$$

where \mathbb{A} is an anti-symmetrization operator accounting for the exchange effects between the colliding electron and target electrons, ψ_i are functions representing

the target, and θ_i are functions of the free electron given by

$$\theta_i = \chi_i \frac{1}{r} F_i \quad (2.4)$$

In the last equation, χ_i are the spin and angle functions and F_i are the radial functions of the scattered electron. The target functions are usually computed by employing the configuration interaction theory with the use of identical set of radial functions. The radial functions can be either spectroscopic physical orbitals of the kind employed in a central field approach, or pseudo orbitals used to represent electron correlation effects and improve accuracy. On introducing functions ϕ_i , which are vector-coupled products of ψ_i and χ_i , and imposing an orthogonality condition, the close coupling expansion of Equation 2.3 becomes

$$\Psi = \mathbb{A} \sum_{i=1}^I \phi_i \frac{1}{r} F_i + \sum_{j=1}^J c_j \Phi_j \quad (2.5)$$

where c_j are coefficients in this expansion and Φ_j are functions of bound-state type for the entire system [104, 110–112].

Because Equation 2.5 is a truncated expansion, as it consists of a finite number of terms, Ψ is not an exact solution of the Schrödinger equation given by Equation 2.1. The following variational condition can be used to derive the close coupling equations

$$(\delta\Psi | H - E | \Psi) = 0 \quad (2.6)$$

where $\delta\Psi$ is a variation in the wavefunction Ψ due to variations in the radial functions F_i and the close coupling expansion coefficients c_j . This results in a system of integro-differential equations that should be satisfied by F_i and c_j [110, 111].

The total energy of the whole system, E , in a certain state is given by

$$E = E_i + E_{e^-} \quad (2.7)$$

where E_i is the energy of the target in state i and E_{e^-} is the energy of the colliding electron. When the total energy results in a bound state for the whole system, the electron energy E_{e^-} is negative and the radial functions F_i exponentially decay to zero as r tends to infinity. However, for some i 's the collision states result in $E_{e^-} > 0$. Channel i is described as closed when $E_{e^-} < 0$ and open when $E_{e^-} > 0$.

If E_i 's are ordered increasingly: $E_1 < E_2 < \dots < E_I$, then for a given total energy E there are I_o open channels such that [112]

$$\begin{aligned} E_{e^-} > 0 & \quad \text{for} \quad i = 1 \quad \text{to} \quad I_o \\ E_{e^-} < 0 & \quad \text{for} \quad i = (I_o + 1) \text{ to } I \end{aligned} \quad (2.8)$$

where I is the total number of channels. A second subscript on the radial functions is normally used, when some channels are open, to denote boundary conditions. The numerical calculations start by computing real functions $F_{ii'}$ subject to certain boundary conditions on the reactance matrix

$$\begin{aligned} F_{ii'}(r) & \underset{r \rightarrow \infty}{\sim} s_i(r)\delta(i, i') + c_i(r)K(i, i') & \text{for} \quad i = 1 \quad \text{to} \quad I_o \\ F_{ii'}(r) & \underset{r \rightarrow 0}{\sim} 0 & \text{for} \quad i = (I_o + 1) \text{ to } I \end{aligned} \quad (2.9)$$

In the last equation, $s_i(r)$ and $c_i(r)$ are the components of the Coulomb functions ϑ^\pm having an asymptotic form, and $i' = 1 \dots I_o$. These functions are defined by

$$\vartheta^\pm(r) = c \pm is \quad (2.10)$$

where c and s represent cosine and sine functions respectively, and i is the imaginary unit. The \mathbf{S} -matrix functions also have asymptotic forms given by

$$\begin{aligned} F_{ii'}^-(r) &\sim \frac{1}{2} \{ \vartheta_i^-(r) \delta(i, i') - \vartheta_i^+(r) S(i, i') \} & \text{for } i = 1 & \text{ to } I_o \\ F_{ii'}^-(r) &\sim 0 & \text{for } i = (I_o + 1) & \text{ to } I \end{aligned} \quad (2.11)$$

It can be shown that the scattering matrix, \mathbf{S} , is related to the reactance matrix, \mathbf{K} , through the following relation

$$\mathbf{S} = \frac{\mathbf{I} + i\mathbf{K}}{\mathbf{I} - i\mathbf{K}} \quad (2.12)$$

where \mathbf{I} is the identity matrix and i is the imaginary unit. Moreover, the \mathbf{S} -matrix functions, \mathbf{F}^- , are related to the reactance matrix by

$$\mathbf{F}^- = \frac{-i\mathbf{F}^-}{\mathbf{I} - i\mathbf{K}} \quad (2.13)$$

It should be remarked that the complex conjugate of the \mathbf{S} -matrix functions, \mathbf{F}^+ , are used in the computation of photoionization cross sections [104, 110–112].

2.0.2 R-matrix Method

One way of solving the Schrödinger equation of the electron-atom system in the close coupling approximation is the \mathbf{R} -matrix method which is a computational technique based on the theory developed originally by Burke and Seaton to provide a suitable framework for analyzing scattering processes. The \mathbf{R} -matrix method is a computationally efficient way for solving the resulting close coupling equations. Its main feature is the partitioning of the space into two disjoint regions: inner and outer. These two regions are separated by a sphere centered at the system's center of mass. The computational connection between these regions is established

through the \mathbf{R} -matrix which links them at the boundary. The main task then is to find solutions for the inner region [111].

The \mathbf{R} -matrix method starts by selecting a value \mathcal{A} for the sphere radius r such that the functions ϕ_i and Φ_j are small outside the inner region. The focus of the method then is to find solutions in this region. A many-body Schrödinger equation should be solved when the incident electron is inside the inner region, while a solution of only a two-body equation is required in the outer region. This reduces the effort by restricting the mathematical and computational complexities to a small region of space. A complete discrete set of basis functions is used to express the wavefunction of the system in the scattering process. Initially, solutions that fulfill certain conditions on the boundary between the two regions are sought. Such solutions, $\Psi = \psi_n$, which contain radial functions $F_i(r) = f_{in}(r)$, do exist for a discrete set of energies $E = e_n$. A number of options are available for the boundary conditions. One choice is that $f'_{in}(\mathcal{A}) = 0$ where the prime indicates a derivative with respect to r . In this process, the functions ψ_n are normalized to

$$(\psi_n | \psi_{n'})_I = \delta(n, n') \quad (2.14)$$

with the evaluation of the matrix elements $(\dots)_I$ in the inner region. For a given energy E , the wavefunction Ψ_E with radial functions $F_{iE}(r)$ can be expressed as

$$\Psi_E = \sum_n \psi_n A_{nE} \quad (2.15)$$

where A_{nE} is given by

$$A_{nE} = (e_n - E)^{-1} \sum_i f_{in}(\mathcal{A}) F'_{iE}(\mathcal{A}) \quad (2.16)$$

In the last equation, $F'_{iE}(\mathcal{A})$ is chosen such that Ψ_E meets predefined boundary

and normalization conditions. On substituting 2.16 into 2.15 with some algebraic manipulation, the following relation can be obtained

$$F_{iE}(\mathcal{A}) = \sum_{i'} R_{ii'}(E) F'_{i'E}(\mathcal{A}) \quad (2.17)$$

where

$$R_{ii'}(E) = \sum_n f_{in}(\mathcal{A})(e_n - E)^{-1} f'_{i'n}(\mathcal{A}) \quad (2.18)$$

is the \mathbf{R} -matrix.

The target functions, ψ_n , are computed using expansions of the radial functions $f_{in}(r)$ with the inclusion of orthogonality conditions to obtain good convergence. The expansion coefficients are acquired from diagonalizing the Hamiltonian matrix with a truncation process. The Buttle correction is then employed to compensate for the truncation [104, 110–112].

2.0.2.1 Inner and Outer Regions

As indicated earlier, the inner region, which may also be called the \mathbf{R} -matrix box, is identified as the region inside a sphere of radius \mathcal{A} centered on the center of mass of the entire system and essentially contains all the target electrons, while the outer region is the rest of the configuration space. The essence of the \mathbf{R} -matrix method is to find solutions in the inner region where the system is considered a many-body problem. In the outer region, where electron correlation and exchange effects are less important and hence can be ignored, the system is treated as a two-body problem between the atomic target and incident electron, and the solution can then be acquired from an asymptotic expansion or by a perturbative treatment. In this region, the integro-differential equations are relegated to the following ordinary

differential equations

$$\left(\frac{d^2}{dr^2} - \frac{l_i(l_i + 1)}{r^2} + \frac{2z}{r} + \epsilon_i \right) F_i + \sum_{i'} V_{ii'} F_{i'} = 0 \quad (2.19)$$

where z is the ion's residual charge, ϵ_i is the energy of the free electron, and $V_{ii'}$ are multi-pole potentials [104, 110–112].

2.0.2.2 Matching of Solutions

The solutions in the inner and outer regions of the \mathbf{R} -matrix should be matched at the boundary between these regions $r = \mathcal{A}$. Depending on the nature of the available channels (some open or all closed), several matrices are defined and used to obtain and match the solutions. In this stage of the \mathbf{R} -matrix calculations, the reactance matrix \mathbf{K} is evaluated. This matrix, which symbolizes the asymptotic nature of the whole wavefunction, is real and symmetric and carries information from both regions [104, 112].

2.0.2.3 Bound States

Once the calculations of the inner-region of \mathbf{R} -matrix are carried out and the essential \mathbf{R} -matrix data $f_{in}(\mathcal{A})$ and e_n are obtained, as outlined already, speedy computations can be performed with minimum computational cost to find the energy and wavefunction of the bound states [110].

2.0.2.4 Resonances

On obtaining the reactance matrix \mathbf{K} and the scattering matrix \mathbf{S} which is given by Equation 2.12, resonances can be obtained following one of several approaches; some of which are outlined in § 3.2.1. An advantage of using the close coupling

method is that resonance effects are naturally delineated, since the interaction between closed and open channels is already incorporated in the scattering treatment.

2.0.2.5 Oscillator Strengths

The dipole operators in length and velocity form, \mathbf{D}^L and \mathbf{D}^V respectively, are given by

$$\mathbf{D}^L = \sum_n \mathbf{r}_n \quad \mathbf{D}^V = - \sum_n \nabla_n \quad (2.20)$$

where \mathbf{r} is the radius vector, ∇ is the del operator, and n is an index running over all electrons. Once these dipole operators are obtained, the line strength for a dipole transition between state a and state b can be computed in the following length and velocity forms

$$\begin{aligned} \mathcal{S}_{ba}^L &= |(b \parallel \mathbf{D}^L \parallel a)|^2 \\ \mathcal{S}_{ba}^V &= 4(E_b - E_a)^{-2} |(b \parallel \mathbf{D}^V \parallel a)|^2 \end{aligned} \quad (2.21)$$

where E_a and E_b are the energies of these states in Ryd. The oscillator strength, f_{ba} , which is a dimensionless quantity, can then be obtained [112]

$$f_{ba} = \frac{(E_b - E_a)\mathcal{S}_{ba}}{3g_a} \quad (2.22)$$

where g_a is the statistical weight of the initial state given by $g_a = (2S_a + 1)(2L_a + 1)$ for LS -coupling and $g_a = (2J_a + 1)$ for intermediate coupling. The oscillator strength f_{ba} can be in length or velocity form depending on the form of the line strength \mathcal{S}_{ba} . When exact functions are utilized in the equations, the two forms are equal, i.e. $\mathcal{S}^L = \mathcal{S}^V$ and $f^L = f^V$. The use of approximate functions would normally lead to differences between the two forms; the size of which may give a hint of the accomplished accuracy. However, agreement between the two forms

does not affirm accuracy as they can agree coincidentally [104, 112].

2.0.2.6 Photoionization Cross Sections

For a transition from an initial bound state to a free final state a generalized line strength \mathcal{S} , similar to that of Equation 2.21, can be introduced. The photoionization cross section is then given by

$$\sigma = \frac{4\pi^2 a_0^2 \alpha E_p \mathcal{S}}{3g} \quad (2.23)$$

where a_0 is Bohr radius, α is the fine structure constant, E_p is the photon energy in Ryd, and g is the degeneracy of the bound state. Again, in this formulation either the length or the velocity operator can be used [104, 112].

2.0.2.7 Relativistic Effects

To account for relativistic effects, the previously-outlined non-relativistic treatment of the \mathbf{R} -matrix method can be adjusted by adding terms from the relativistic Breit-Pauli Hamiltonian, H_{bp} , given by

$$H_{bp} = H_{nr} + H_{rc} \quad (2.24)$$

where H_{nr} is the non-relativistic Hamiltonian and H_{rc} is the relativistic correction terms which include the one body mass, Darwin and spin-orbit terms; the two body fine structure terms; and the two body non-fine structure terms. This is normally achieved by first computing the Hamiltonian matrices in LS -coupling followed by the application of a unitary transformation to convert to intermediate coupling. In the RMATRX-I code only some of these relativistic terms (i.e. mass correction, one body Darwin, and spin-orbit terms) are overtly held [104].

2.0.3 RMATRIX-I Code

The **R**-matrix theory for atomic scattering is implemented in a computer code called RMATRIX-I, which is a general-purpose program for analyzing atomic processes such as collision of free electrons with atoms and ions, radiative processes like transitions between bound states, polarizabilities, and photoionization cross sections. The **R**-matrix calculations can be performed in *LS*-coupling as well as in intermediate coupling, where the latter can be achieved through the inclusion of the one body correction terms from the Breit-Pauli relativistic Hamiltonian, as outlined earlier. The program consists of sequentially-coupled stages and is used in this study as the main tool for generating theoretical data for scattering, recombination and subsequent atomic processes. These stages fall into two major categories: inner region and outer region. The inner region code is composed of the following stages [104, 112, 113]

- STG1 to compute the bound and continuum orbital basis and the associated radial integrals. The target's radial functions should be provided as an input to this stage where they have been obtained from atomic structure codes such as Autostructure and CIV3, as will be discussed later.
- STG2 to calculate angular algebra. This stage reads radial integrals produced by STG1 and evaluates the Hamiltonian and dipole operator matrices. It can also diagonalize the Hamiltonian matrix of the target if required.
- STGJK which is an optional stage that runs between STG2 and STG3 to recouple the Hamiltonian in the case of intermediate coupling scheme by transforming the Hamiltonian matrix from *LS*-coupling to pair-coupling through the use of a unitary transformation to include Breit-Pauli relativistic effects.
- STG3 to diagonalize the Hamiltonian matrix in the continuum basis and

produce vital \mathbf{R} -matrix data required for the outer region stages.

The outer region code consists of the following stages

- STGB to calculate wavefunctions and energy levels for bound states and produce a data set required for radiative calculations of bound-bound and bound-free transitions.
- STGF to calculate wavefunctions of free states. It can also compute collision strengths for inelastic collisions and produce data needed for radiative calculations of free-free and bound-free transitions.
- STGGB to calculate oscillator strengths for bound-bound transitions.
- STGBF to calculate photoionization cross sections for bound-free transitions.

An extra stage called STGQB for finding and analyzing resonances was added to the \mathbf{R} -matrix code by Quigley and co-workers [114].

In Figure 2.1 a flow chart of the RMATRIX-I suite and its companions is presented. RMATRIX-I needs input data to define the atomic target. This can be provided either by CIV3 code of Hibbert [115], or by Superstructure code of Eissner *et al* [102], or by Autostructure code. The latter is a modified version of Superstructure that incorporates extensions and modifications such as those of Nussbaumer and Storey [103] and Badnell [41].

CIV3 is a general multi-configuration atomic structure code that calculates configuration interaction wavefunctions in LS and intermediate coupling schemes. The wavefunctions can then be used for further computations related to atomic processes such as finding oscillator strengths. CIV3 uses Slater Type Orbital (STO) formulation to specify the configuration interaction functions. The Slater Type

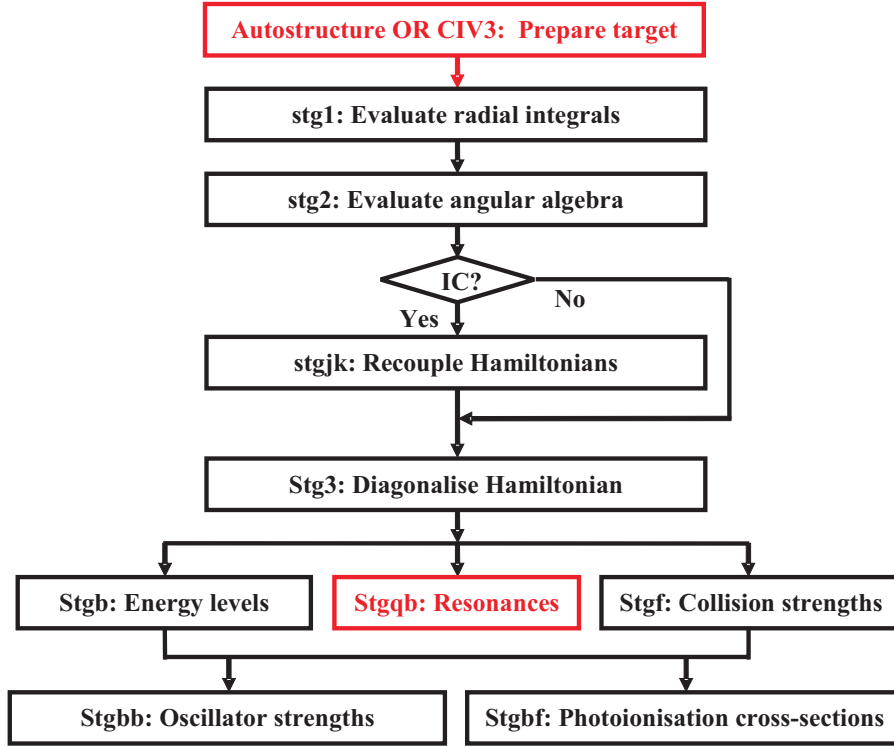


Figure 2.1: Flow chart of the RMATRIX-I suite.

Orbitals are defined by

$$P_{nl}(r) = \sum_i C_i r^{P_i} e^{-\xi_i r} \quad (2.25)$$

where $P_{nl}(r)$ is a radial function for the nl orbital, C_i is a coefficient and P_i and ξ_i are indicial parameters in this formulation, r is the radius, and i is a counting index that runs over the orbitals of interest.

Superstructure and Autostructure [41, 102, 103, 112] are automatic general-purpose atomic structure codes based on the Thomas-Fermi-Dirac formulation. They compute atomic radial functions using central potentials of the form

$$V(r) = -\frac{\zeta(r)}{r} \quad (2.26)$$

where $\zeta(r)$ is a radius-dependent effective charge. The programs produce large quantities of diverse atomic structure and transition data particularly useful for as-

tronomical applications. Minimum specification of the atomic system, the type of the requested data and the required degree of approximation is needed as an input to Superstructure and Autostructure. Among their many applications, they can be used to calculate the target functions for the **R**-matrix code and configuration mixing autoionization rates in *LS* or intermediate couplings, where Breit-Pauli terms are used to account for relativistic corrections. Superstructure and Autostructure can also be used to calculate term energies, atomic and ionic energy levels, term-coupling coefficients, cascade coefficients, atomic transition data such as forbidden and permitted radiative transition probabilities, and so on. The programs employ multi-configuration type for wavefunction expansions.

In our investigation of the C II recombination lines, we used target data generated by CIV3 for the scattering calculations as an input to STG1 of the **R**-matrix code, as presented in Table 3.1 and § D.1.1, while we used Autostructure to elaborate and investigate related issues. Autostructure was also used to find the oscillator strengths for the free-free transitions between resonance states since the available RMATRIX-I code does not contain a free-free stage. In this approach the free-free transitions were treated as bound-bound transitions. Autostructure was also used for generating *f*-values for free-bound and bound-bound transitions involving the 8 topmost bound states, namely the $1s^2 2s2p(^3P^\circ)3d$ $^4F^\circ$ and $^4D^\circ$ levels, as these quartets with their large effective quantum number for the outer electron are out of range of the **R**-matrix code validity. The Autostructure input data files for these calculations are given in § D.2 in Appendix D.

Chapter 3

Dielectronic Recombination Lines of C II

Carbon recombination lines are an important diagnostic tool that can provide valuable information on the physical conditions in various astrophysical environments such as planetary nebulae and the interstellar medium. Because the recombination rate depends on the electron temperature T_e and number density N_e , the variation of the carbon line intensities can be used in principle to determine the temperature and density in the line-emitting regions [116].

With regard to the recombination lines of C II, there are many theoretical and observational studies mainly within astronomical contexts. Examples are [2, 3, 8, 9, 17, 23, 46–51, 53–55, 57–62, 117, 118]. The aim of the current study is to treat the near-threshold resonances and subsequent radiative decays using the unified approach of the **R**-matrix method in intermediate coupling.

In this study we investigate the recombination lines of C II, that is the emission lines produced by the following recombination process



and the subsequent radiative cascade decay which persists until the atom reaches the ground or a metastable state. Our investigation includes all the autoionizing resonance states above the threshold of $C^{2+} 1s^2 2s^2 1S^e$ with a principal quantum number $n < 5$ for the captured electron as an upper limit. This condition was adopted mainly due to computational limitations. In total, 61 autoionizing states (27 doublets and 34 quartets) with this condition have been theoretically found by the **R**-matrix method. Of these 61 resonances, 55 are experimentally observed according to the NIST database [16]. More details will follow in the forthcoming sections.

The major work in this investigation can be split into three main parts

1. Autoionizing and bound states calculations to generate the required theoretical data for the resonances and bound states.
2. Calculation of oscillator strength, f -values, for various transitions.
3. Recombination and emissivity calculations and analysis to find the emissivity of various transition lines and compare the theoretical emissivity model to the observational data.

In the next section we provide a general theoretical background which will be followed by three sections in which we outline the theory and procedures that were followed in this investigation.

3.1 Theoretical Background

In a thermodynamic environment, an excited atomic state is populated by recombination and radiative cascade from higher states, and depopulated by autoionization

and radiative decay to lower states. Many recombination lines originate from dielectronic recombination with subsequent cascade decay of autoionizing resonance states just above the ionization threshold. These lines are dominated by low-temperature dielectronic recombination, as outlined in § 1.1.2. The population of these resonances is established by the balance between autoionization to the continuum and recombination with ensuing radiative decay to lower levels. When autoionization dominates, the population is determined by the Saha equation

$$N_{X_{(n-1)+}} = N_e N_{X_{n+}} \frac{g_{X_{(n-1)+}}}{2g_{X_{n+}}} \left(\frac{h^2}{2\pi m_e k T_e} \right)^{3/2} e^{-\Delta E_t / k T_e} \quad (3.2)$$

where $N_{X_{n+}}$ and $N_{X_{(n-1)+}}$ are the population of ions with effective positive charge n and $(n-1)$ respectively, N_e is the number density of electrons, g is the statistical weight of the indicated state, k and h are the constants of Boltzmann and Planck respectively, m_e is the electron mass, T_e is the electron temperature, and ΔE_t is the energy of the recombined electron in the $X_{(n-1)+}$ state relative to the ionization threshold [22, 119].

The Saha equation, which determines the degree of ionization of a gas, is only valid in local thermodynamic equilibrium situations where the equilibrium is established through thermal collision processes. In this case the velocity and energy distributions of the gas particles are described by the Maxwell and Boltzmann distributions respectively and local temperature can be defined. However, in many practical situations the assumption of local thermodynamic equilibrium is not applicable in the energy range of interest due to significant involvement of processes other than thermal collisions in establishing the particles distribution. Examples of these non-thermal processes are recombination, photoionization, autoionization, and radiative decay. These processes can shift the distribution significantly away from its thermodynamic equilibrium state if they have substantial contribution.

In these cases, particles distribution should be determined through more complex balance equations in which the effect of these processes on the energy and velocity of the particles is taken into account.

In the recombination calculations, to measure the departure of the state from its thermodynamic equilibrium a departure coefficient, b_u , is defined as the ratio of autoionization probability to the sum of radiative and autoionization probabilities, as given by Equation 3.8. The value of this coefficient is between 0 for radiative domination ($\Gamma^a \ll \Gamma^r$) and 1 for thermodynamic equilibrium where autoionization dominates ($\Gamma^a \gg \Gamma^r$). A large value of b_u ($\simeq 1$) is then required to justify the assumption of thermodynamic equilibrium and apply the relevant physics.

In thermodynamic equilibrium situation the rate of radiationless capture is equal to the rate of autoionization, yielding [120]

$$N_e N_i \varrho_c = N_u^S \Gamma_u^a \quad (3.3)$$

where N_e and N_i are the number density of electrons and ions respectively, ϱ_c is the recombination coefficient for the capture process, N_u^S is the Saha population of the doubly-excited autoionizing state and Γ_u^a is the autoionization transition probability of that state. In non-thermodynamic equilibrium situation, the balance is given by

$$N_e N_i \varrho_c = N_u (\Gamma_u^a + \Gamma_u^r) \quad (3.4)$$

where N_u is the non-thermodynamic equilibrium population of the indicated state and Γ_u^r is the total radiative transition probability of that state. The departure coefficient b_u is a gauge of the deviation of the population of an autoionizing state from its thermodynamic equilibrium value, and hence is the ratio of the non-thermodynamic equilibrium population to the Saha population. Comparing

Equations 3.3 and 3.4 gives

$$b_u = \frac{N_u}{N_u^S} = \frac{\Gamma_u^a}{\Gamma_u^a + \Gamma_u^r} \quad (3.5)$$

In the following we summarize the theoretical background for our recombination and emissivity calculations as implemented in the ‘Emissivity’ code [121]

- The calculations start by obtaining the radiative transition probability Γ_{ul}^r for all free-free transitions as given by

$$\Gamma_{ul}^r = \frac{\alpha^3 E_p^2 g_l f_{ul}}{2g_u \tau_o} \quad (3.6)$$

where α is the fine structure constant, E_p is the photon energy in Ryd, g_l and g_u are the statistical weights of the lower and upper states respectively, f_{ul} is the oscillator strength of the transition between the upper and lower states, and τ_o is the atomic time unit. This is followed by obtaining the radiative transition probability Γ_{ul}^r for all free-bound transitions, as in the case of free-free transitions.

- The total radiative transition probability Γ_u^r for all resonances is then found. This is the probability of radiative decay from an upper resonance state to all accessible lower resonances and bound states. This probability is found by summing up the individual probabilities Γ_{ul}^r over all lower free and bound states l for which a transition is possible according to the electric dipole rules, that is

$$\Gamma_u^r = \sum_l \Gamma_{ul}^r \quad (3.7)$$

- The departure coefficient, b_u , for all resonances is then obtained

$$b_u = \frac{\Gamma_u^a}{\Gamma_u^a + \Gamma_u^r} \quad (3.8)$$

where Γ_u^a and Γ_u^r are the autoionization and total radiative transition probabilities of state u respectively, and Γ^a is given by

$$\Gamma^a = \frac{\Delta_r}{\hbar} \quad (3.9)$$

where Δ_r is the full width at half maximum of the autoionizing state and \hbar is the reduced Planck's constant.

- The next step is to calculate the population of resonances by summing up two components: the Saha capture, and the radiative decay from all upper levels. In thermodynamic equilibrium the rate of radiationless capture and the rate of autoionization are equal, that is

$$N_e N_i \varrho_c = N_l^S \Gamma_l^a \quad (3.10)$$

where N_e and N_i are the number density of electrons and ions respectively, ϱ_c is the recombination coefficient for the capture process, N_l^S is the Saha population of the autoionizing state and Γ_l^a is the autoionization transition probability of that state. In non-thermodynamic equilibrium situation, the population and depopulation of the autoionizing state due to radiative decay from upper states and to lower states respectively should be included, and hence the balance is given by

$$N_e N_i \varrho_c + \sum_u N_u \Gamma_{ul}^r = N_l (\Gamma_l^a + \Gamma_l^r) \quad (3.11)$$

where N_l is the non-thermodynamic equilibrium population of the doubly-excited autoionizing state, Γ_l^r is the total radiative transition probability of that state, Γ_{ul}^r is the radiative transition probability from an upper state u to the autoionizing state l , and the sum is over all upper states that can decay to the autoionizing state. Combining Equations 3.10 and 3.11 yields

$$N_l^S \Gamma_l^a + \sum_u N_u \Gamma_{ul}^r = N_l (\Gamma_l^a + \Gamma_l^r) \quad (3.12)$$

On manipulating Equation 3.12 algebraically, the following relation can be obtained

$$\begin{aligned} N_l &= N_l^S \left(\frac{\Gamma_l^a}{\Gamma_l^a + \Gamma_l^r} \right) + \sum_u \frac{N_u \Gamma_{ul}^r}{\Gamma_l^r + \Gamma_l^a} \\ &= N_l^S b_l + \sum_u \frac{N_u \Gamma_{ul}^r}{\Gamma_l^r + \Gamma_l^a} \end{aligned} \quad (3.13)$$

where b_l is the departure coefficient of the autoionizing state.

- The next step is to calculate the radiative transition probabilities of the bound-bound transitions, Γ_{ul}^r . In these calculations the f -values can be in length form or velocity form; however the length form values may be more reliable as they converge rather quickly [122]. The ‘Emissivity’ code therefore uses the length form of the oscillator strengths where they are read from the f -value file ‘FVALUE’ produced by the **R**-matrix code. The calculation of Γ_{ul}^r for the bound-bound transitions is then followed by finding the total radiative transition probability of the bound states, Γ_u^r , by summing up Γ_{ul}^r over all lower bound states l accessible to an upper bound state u , as given earlier by Equation 3.7 for the case of autoionizing states.

- The population of the bound states is then obtained

$$N_l = \sum_u \frac{N_u \Gamma_{ul}^r}{\Gamma_l^r} \quad (3.14)$$

where the index u includes all upper free and bound states that can decay to the bound state l .

- Finally, all possible free-free, free-bound and bound-bound transitions which are allowed by the selection rules of electric dipole approximation are found. The emissivity, ε , of all the recombination lines that arise from a transition from an upper state u to a lower state l is then computed using the relation

$$\varepsilon_{ul} = N_u \Gamma_{ul}^r h\nu \quad (3.15)$$

where N_u is the population of the upper state, Γ_{ul}^r is the radiative transition probability between the upper and lower states, h is the Planck's constant, and ν is the frequency of the transition line. The equivalent effective recombination coefficient ϱ_f , which is linked to the emissivity by the following relation, can also be computed

$$\varrho_f = \frac{\varepsilon}{N_e N_i h\nu} \quad (3.16)$$

where N_e and N_i are the number density of the electrons and ions respectively.

3.2 Autoionizing and Bound States Calculations

The main computing tools that were used in this part to generate theoretical data is RMATRIX-I code and its companions (i.e. **K**-matrix implementation in stage STGF and STGQB code) though Autostructure was occasionally used to accom-

plish complementary tasks. In the first part of this section, three methods for finding and analyzing resonances are presented. However, the main focus will be on the two methods that were used in our investigation of the recombination lines of C II. The remaining parts will be dedicated to practical aspects.

3.2.1 Methods for Investigating Resonances

The resonance phenomenon is a highly important feature in atomic collisions as it plays a vital role in electron scattering with atoms, ions and molecules. The Auger effect is one of the early examples of the resonance effects that have been discovered and extensively investigated. There are several methods for finding and analyzing resonances that arise during the recombination processes. In the following sections we outline three of these methods; two of which are used in the current study to find and analyze resonances of C II. These two are the **K**-matrix method which was developed and implemented by modifying stage STGF of the **R**-matrix code as part of this study, and the **QB** method of Quigley and Berrington [123], which is implemented in the STGQB code of Quigley and coworkers [114] as an extension to the **R**-matrix code. The essence of the **K**-matrix method is to identify the resonance position and width from locating the poles of the **K**-matrix on the energy mesh, while the essence of the **QB** method is to apply a fitting procedure to the reactance matrix eigenphase near the resonance position using the analytic properties of the **R**-matrix theory. The third method is the Time-Delay of Stibbe and Tennyson [124] which is implemented in a computer code called TIMEDEL. This method is based on the use of the lifetime eigenvalues to locate the resonance position and identify its width. We tried to implement and use this method in an early stage of our investigation before developing the **K**-matrix method, but this attempt was abandoned in favor of the **K**-matrix method.

3.2.1.1 QB Method

A common approach for finding and analyzing resonances is to apply a fitting procedure to the reactance matrix, \mathbf{K} , or its eigenphase as a function of energy in the neighborhood of an autoionizing state. However, fitting the \mathbf{K} -matrix itself is complicated because the reactance matrix has a pole at the energy position of the autoionizing state. An easier alternative is to fit the arc-tangent of the reactance matrix. The latter approach was employed by Bartschat and Burke [125] in their fitting code RESFIT.

The eigenphase sum is defined by

$$\delta = \sum_{i=1}^N \arctan \Lambda_i \quad (3.17)$$

where Λ_i is an eigenvalue of the \mathbf{K} -matrix and the sum runs over all open channels interacting with the autoionizing state. The eigenphase sum is normally fitted to a Breit-Wigner form

$$\delta = \bar{\delta} + \arctan \left(\frac{\Delta_r}{2(E_r - E)} \right) \quad (3.18)$$

where $\bar{\delta}$ is the sum of the background eigenphase, Δ_r is the resonance width, E_r is the energy position of the resonance, and E is the energy. This approach was used by Tennyson and Noble [126] in their fitting code RESON [127].

In theory, an autoionizing state exhibits itself as a sharp increase by π radians in the eigenphase sum as a function of energy superimposed on a slowly-varying background. However, due to the finite width of resonances and the background variation over their profile, the increase may not be by π precisely in the actual calculations. A more practical approach then is to identify the position of the resonance from the energy location where the increase in the eigenphase sum is at its highest rate by having a maximum gradient with respect to the scattering

energy, i.e. $(d\delta/dE)_{max}$ [123, 126].

The **QB** method of Quigley and Berrington [123] is a computational technique for finding and analyzing autoionizing states that arise in atomic and molecular scattering processes using eigenphase fitting. The merit of the **QB** method over other eigenphase fitting procedures is that it utilizes the analytical properties of the **R**-matrix method to determine the variation of the reactance matrix with respect to the scattering energy analytically. This analytical approach can avoid possible weaknesses, linked to the calculations of **K**-matrix poles and arc-tangents, when numerical procedures are employed instead. The derivative of the reactance matrix with respect to the scattering energy in the neighborhood of a resonance can then be used in the fitting procedure to identify the energy position and width of the resonance.

The **QB** method begins by defining two matrices, **Q** and **B**, in terms of asymptotic solutions, the **R**-matrix and energy derivatives, such that

$$\frac{d\mathbf{K}}{dE} = \mathbf{B}^{-1}\mathbf{Q} \quad (3.19)$$

The eigenphase gradients of the **K**-matrix with respect to energy can then be calculated. This is followed by identifying the resonance position, E_r , from the point of maximum gradient at the energy mesh, and the resonance width, Δ_r , which is linked to the eigenphase gradient at the resonance position, $\delta'(E_r)$, by the relation

$$\Delta_r = \frac{2}{\delta'(E_r)} \quad (3.20)$$

This equation may be used to calculate the widths of a number of resonances in a first approximation. A background correction due to overlapping profiles can then be introduced on these widths individually to obtain a better estimate.

The **QB** method was implemented in the STGQB code of Quigley and coworkers

[114] as an extension to the **R**-matrix code. In the current study, STGQB was used as a supplementary tool for verifying the results of the **K**-matrix method.

3.2.1.2 Time-Delay Method

The Time-Delay method of Stibbe and Tennyson [124] is based on the time-delay theory of Smith [128]. According to this theory, the time-delay matrix **M** is defined in terms of the scattering matrix **S** by

$$\mathbf{M} = -i \hbar \mathbf{S}^* \frac{d\mathbf{S}}{dE} \quad (3.21)$$

where i is the imaginary unit, \hbar ($= h/2\pi$) is the reduced Planck's constant, \mathbf{S}^* is the complex conjugate of **S**, and E is the energy. It has been demonstrated by Smith [128] that the eigenvalues of the **M**-matrix represent the collision lifetimes and the largest of these eigenvalues corresponds to the longest time-delay of the scattered particle. For a resonance, the time-delay has a Lorentzian profile with a maximum precisely at the resonance position. By computing the energy-dependent time-delay from the reactance matrix, and fitting it to a Lorentzian peak shape, the resonance position can be located and its width is identified.

This method, as implemented in the TIMEDEL program of Stibbe and Tennyson [124], uses the reactance **K**-matrix as an input, either from a readily-available archived scattering calculations or from dynamically-performed computations on an adjustable mesh. The **S**-matrix is then formed using the relation

$$\mathbf{S} = \frac{\mathbf{I} + i\mathbf{K}}{\mathbf{I} - i\mathbf{K}} \quad (3.22)$$

where **I** is the identity matrix, and i is the imaginary unit. The time-delay **M**-matrix is then calculated from Equation 3.21, with numerical evaluation of the

S-matrix derivative, and diagonalized to find the eigenvalues and hence obtain the longest time-delay of the incident particle. Approximate resonance positions are then identified from the energy locations of the maxima in the time-delay profile, and the widths are estimated from the Lorentzian fit. On testing the degree of overlapping of neighboring resonances, TIMEDEL decides if the resonances should be fitted jointly or separately.

3.2.1.3 K-Matrix Method

Resonances arise from poles in the scattering matrix **S** which varies slowly with energy. The **K**-matrix method used in the current study is based on the fact that for the low-lying resonances just above the $C^{2+} 1s^2 2s^2 1S^e$ ionization threshold, the scattering matrix **S** has only one channel, and hence the reactance matrix, **K**, is a real scalar with a pole near the resonance position at the energy mesh.

According to the collision theory of Smith [128], the lifetime matrix **M** is related to the **S**-matrix by Equation 3.21. Now, a **K**-matrix with a pole at energy E_0 superimposed on a background K_o can be approximated by

$$K_i = K_o + \frac{g}{E_i - E_0} \quad (3.23)$$

where K_i is the value of the **K**-matrix at energy E_i and g is a physical parameter with dimension of energy. In Appendix A we revealed that in the case of single-channel scattering the **M**-matrix is real with a value given by

$$M = \frac{-2g}{(1 + K_o^2)(E - E_0)^2 + 2K_o g(E - E_0) + g^2} \quad (3.24)$$

Using the fact demonstrated by Smith [128] that the lifetime of the state is the expectation value of M , it can be shown from Equation 3.24 that the position of

the resonance peak E_r is given by

$$E_r = E_0 - \frac{K_o g}{1 + K_o^2} \quad (3.25)$$

while the full width at half maximum Δ_E is given by

$$\Delta_E = \frac{|2g|}{1 + K_o^2} \quad (3.26)$$

The two parameters of primary interest to our investigation are the resonance energy position E_r , and the resonance width Δ_r which equals the full width at half maximum Δ_E . However, for an energy point E_i with a \mathbf{K} -matrix value K_i , Equation 3.23 has three unknowns, K_o , g and E_0 , which are needed to find E_r and Δ_r . Hence, three energy points at the immediate neighborhood of E_0 are required to identify these unknowns. As the \mathbf{K} -matrix changes sign at the pole, the neighborhood of E_0 is located by testing the \mathbf{K} -matrix value at each point of the energy mesh for sign change. Consequently, the three points are obtained and used to find E_r and Δ_r . Complete derivation of the \mathbf{K} -matrix method is given in Appendix A.

3.2.2 Preparing Target

We used the \mathbf{R} -matrix code [104], and Autostructure [41, 102, 103] to compute the properties of autoionizing and bound states of C^+ . The first step in the \mathbf{R} -matrix is to have a target for the scattering calculations. In our study, orbitals describing the C^{2+} target for the \mathbf{R} -matrix scattering calculations were taken from Berrington *et al* [129], who used a target comprising the six terms $2s^2 \ ^1\text{S}^e$, $2s2p \ ^3\text{P}^o$, $\ ^1\text{P}^o$ and $2p^2 \ ^3\text{P}^e$, $\ ^1\text{D}^e$, $\ ^1\text{S}^e$, constructed from seven orthogonal orbitals; three physical and four pseudo orbitals. These orbitals are: $1s$, $2s$, $2p$, $\bar{3}s$, $\bar{3}p$, $\bar{3}d$ and $\bar{4}f$, where the bar

denotes a pseudo orbital. The purpose of including pseudo orbitals is to represent electron correlation effects and to improve the target wavefunctions. The radial parts, $P_{nl}(r)$, of these orbitals are Slater Type Orbital, defined by Equation 2.25, generated by the CIV3 program of Hibbert [115]. The values of these parameters are given in Table 3.1.

In this work we construct a scattering target of 26 terms which include the 6 terms of Berrington *et al* [129] plus all terms of the configurations $2s\bar{3}l$ and $2p\bar{3}l$, $l = 0, 1, 2$. This includes the terms outside the $n = 2$ complex which make the largest contribution to the dipole polarizability of the $2s^2\ ^1S^e$ and $2s2p\ ^3P^o$ states of C^{2+} . Autostructure was used to decide which terms of the target have the largest polarizability. This is based on the fact that the contribution to polarizability is proportional to the ratio of the oscillator strength of transition between levels i and j to the square of the corresponding energy difference (i.e. $C_p \propto f_{ij}/\Delta E_{ij}^2$). The Autostructure input data file for this calculation is given in § D.2.1 of Appendix D.

3.2.3 Developing and Implementing **K**-matrix Method

In the early stages of our theoretical investigation to C^+ autoionizing states, we experienced numerical instabilities, convergence difficulties and failures from the **QB** method as implemented in the STGQB code. It was necessary, therefore, to verify the results that we obtained from **QB** by an independent method and fill the gaps left by the failure of STGQB to converge in some cases due to limitation on the width of resonances as it was established afterwards. This motivated the development of **K**-matrix approach which we implemented in the STGF stage by searching for sign-change in the **K**-matrix at the poles. This came after an attempt to implement the time-delay method of Stibbe and Tennyson [124] once within STGF stage and another time as a stand-alone program that processes the data

produced by STGF. However, this attempt was abandoned in favor of the **K**-matrix approach which relies on the same physical principle as the time-delay method.

To improve the performance of the **K**-matrix method, which proved to be very successful and computationally efficient, an interactive graphical technique was also developed to read the **K**-matrix data directly and plot it against energy or arbitrary ordinal number while searching for poles. With a reasonably fine mesh, a positive or negative pulse in the graph appears even when the background is sufficiently large to prevent sign-change. As soon as this is detected, the search is stopped and resumed at higher resolution by focusing on a very narrow energy

Table 3.1: The seven orbitals used to construct the C^{2+} target and their Slater Type Orbital parameters. The bar marks the pseudo orbitals.

Orbital	C_i	P_i	ξ_i
1s	21.28251	1	5.13180
	6.37632	1	8.51900
	0.08158	2	2.01880
	-2.61339	2	4.73790
	-0.00733	2	1.57130
2s	-5.39193	1	5.13180
	-1.49036	1	8.51900
	5.57151	2	2.01880
	-5.25090	2	4.73790
	0.94247	2	1.57130
$\bar{3}s$	5.69321	1	1.75917
	-19.54864	2	1.75917
	10.39428	3	1.75917
2p	1.01509	2	1.47510
	3.80119	2	3.19410
	2.75006	2	1.83070
	0.89571	2	9.48450
$\bar{3}p$	14.41203	2	1.98138
	-10.88586	3	1.96954
$\bar{3}d$	5.84915	3	2.11997
$\bar{4}f$	9.69136	4	2.69086

band using a fine mesh, and hence very small number of energy points are needed to find the resonance. The strategy is to start the search with a coarse mesh over the suspected energy range. If the glitch failed to appear, the search is repeated with finer mesh until the glitch is observed. This graphical technique was essential for finding resonances in reasonably short time compared to the time required by STGQB. In a later stage, non-graphical tools for pole searching were developed and used. The purpose of these tools is to search for any sudden increase or decrease in the background of the **K**-matrix. As soon as this is detected, a search for poles with a finer mesh is resumed. These non-graphic tools proved to be more efficient than the graphic tools, and hence they helped substantially in finding most of the resonances with limited time and computational effort. It is noteworthy that the **K**-matrix method as implemented in STGF stage is completely automatic and can find and identify resonances without user interaction. The purpose of these graphic and non-graphic tools is to speed up the search and save the computing resources by reducing the required CPU time.

In this paragraph we present a brief comparison between these two methods (i.e. **K**-matrix and **QB**) and assess their roles in this study and any possible future investigation. The main results of these methods are presented in Table E.2. As seen, **K**-matrix and **QB** produce identical results in most cases. However, **K**-matrix is computationally superior in terms of the required computational resources, mainly CPU time, especially when coupled with the above-mentioned interactive graphic and non-graphic techniques. In fact we obtained most of the **QB** results guided by the **K**-matrix results which were obtained earlier. Without **K**-matrix it would be extremely hard and time consuming to obtain results for some resonances, especially the very narrow ones, by **QB** directly. In general, the purpose of obtaining **QB** results is to check the **K**-matrix results and compare the two methods. Another advantage of the **K**-matrix method is that it has a wider range of validity

with regard to the resonance width, that is in principle it can be used to find resonances with any width. The **QB** method fails to converge when the resonance width falls below a certain limit, whereas the only observable constraint on the **K**-matrix method is machine precision. Nevertheless, the **QB** method is more general as it deals with multi-channel resonances, as well as single-channel resonances, while the **K**-matrix method in its current formulation is restricted to single-channel resonances.

3.2.4 Calculations

Using the above-mentioned 26-term target, extensive calculations were carried out using the **R**-matrix code in intermediate coupling (IC) scheme by including the one-body terms of the Breit-Pauli Hamiltonian as outlined in Chapter 2. The IC was achieved by utilizing stage STGJK of the **R**-matrix code with the levels and $J\pi$ -symmetries identification. Sample calculations in LS -coupling were also performed in an early stage on typical case studies for validation and test. The intermediate coupling scheme is required for a comprehensive C II recombination lines investigation as many states and transitions do not exist within LS -coupling. An important case is the quartets as well as some doublet states which do not autoionize within LS -coupling scheme where the $LS\pi$ are not conserved. The requirement for the intermediate coupling arises from the fact that in LS -coupling the conserved quantities are $LS\pi$ and hence only the doublet states that conserve these quantities, such as $^2S^e$ and $^2P^o$, can autoionize. Therefore, in LS -coupling no autoionization is allowed for the quartet terms and some doublet states, such as $^2S^o$ and $^2P^e$. However, under intermediate coupling scheme the conserved quantities are $J\pi$, therefore the LS -allowed and LS -forbidden states with the same $J\pi$ mix up giving access to channels that were formerly inaccessible, and hence these states can autoionize. This is schematically depicted in Figure 3.1.

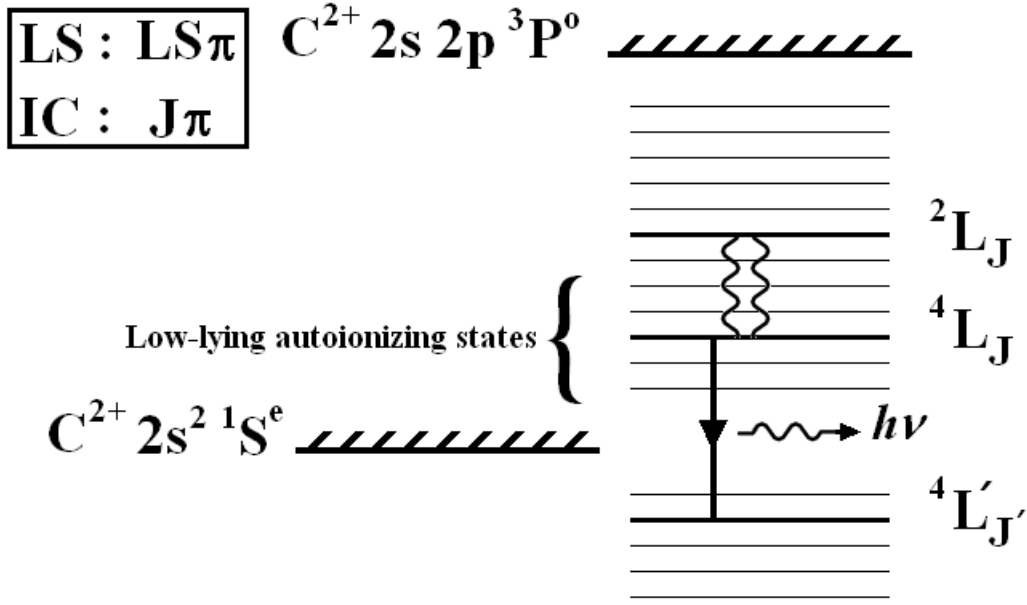


Figure 3.1: Schematic diagram of the low-lying autoionizing quartet and doublet states and their interaction in intermediate coupling scheme.

To investigate the convergence and numerical stability, the number of continuum basis orbitals used to express the wavefunction in the inner region (MAXC in STG1 of the \mathbf{R} -matrix code) was varied between 6-41 and the results were analyzed. It was noticed that increasing the number of basis functions, with all ensuing computational costs, does not necessarily improve the results; moreover a convergence instability may occur in some cases. It was decided therefore to use $\text{MAXC} = 16$ in all calculations as a compromise between the computational resources requirement and accuracy. The effect of varying the size of the inner region radius \mathcal{A} in the \mathbf{R} -matrix formulation was also investigated and a value of 10 atomic units was chosen on the basis of numerical stability and convergence, that is the resulting values do not change on increasing the radius.

Concerning the investigation of resonances, initially all computational work was carried out using the STGQB code since this was the only available tool before developing and implementing the \mathbf{K} -matrix approach. Several parameters of the \mathbf{QB} method were systematically inspected. The effect of varying the accuracy

parameter, AC , in STGQB was investigated and a value of 10^{-6} was chosen for all calculations as a deal between accuracy and speed. The effect of modifying the step size for the effective quantum number mesh was studied and beside missing some resonances when the step is not appropriately small as expected, it is observed that in some cases the resonance position and width may depend on the step size. Including the first order perturbation in the long-range coupling potentials when calculating the reactance matrix was also examined by turning ‘IPERT’ flag on and off (i.e. $IPERT = 1$ and 0) but no tangible change was observed. We therefore concluded that the perturbative treatment is not implemented in the STGQB code.

The development of the **K**-matrix method provided a way for checking and filling the gaps of the **QB** results. In the initial formulation of the **K**-matrix the background was ignored, and although there was good agreement between **QB** and **K**-matrix in some cases where the background is small, there was significant differences in the other cases. Consequently, the current formulation which takes into account the effect of background was developed after some checking using Autostructure. The results produced by the **K**-matrix method, which are presented in Table E.2, are perturbation-free, i.e. with ‘IPERT = NO’ in the stage STGF. Theoretical data with perturbative treatment was also produced for some resonances at an early stage, but this work was abandoned. The main reason is the highly time-consuming nature of the perturbative calculations. It is estimated that such calculations are by a factor of 5-10 times slower than that with the perturbative treatment off, i.e. when ‘IPERT=NO’ [113]. Our personal experience confirms this estimation.

With regard to sampling the three points for the **K**-matrix calculations, it was observed that sampling the points very close to the pole makes the energy position and width of resonances susceptible to fluctuations and instabilities. Therefore, a sampling scheme was adopted in which the points are selected from a broad

range not too close to the pole. This approach was implemented by generating two meshes, coarse and fine, around the pole as soon as the pole is found. To check the results, several different three-point combinations for each resonance were used to find the position and width of the resonance. In each case, the results from these different combinations were compared. In all cases they were identical within acceptable numerical errors. This verified that the sampling scheme is reliable. The results of **QB** confirm this conclusion as they agree with the **K**-matrix results as can be seen in Table E.2.

The results for all bound and autoionizing states are given in Tables E.1 and E.2. In total, 142 bound states belonging to 11 symmetries ($2J = 1, 3, 5, 7, 9$ even and $2J = 1, 3, 5, 7, 9, 11$ odd) and 61 resonances belonging to 11 symmetries ($2J = 1, 3, 5, 7, 9, 11$ even and $2J = 1, 3, 5, 7, 9$ odd) were theoretically identified. As seen in Tables E.1 and E.2, the theoretical results for both bound and resonance states agree very well with the available experimental data both in energy levels and in fine structure splitting. Experimental energies are not available for the very broad resonances as they are difficult to find experimentally. The maximum discrepancy between experiment and theory in the worst case does not exceed a few percent. Furthermore, the ordering of the energy levels is the same between the theoretical and experimental in most cases. Order reversal in some cases is indicated by a minus sign in the fine structure splitting. The input data for the **R**-matrix which are used to perform these calculations are given in § D.1 in Appendix D.

3.3 *f*-Values Calculations

The oscillator strengths for all types of transition (i.e. free-free, free-bound and bound-bound) are required to find the radiative probabilities for these transitions. In the following three sections we outline the procedures that we followed to produce

the *f*-values for FF, FB and BB transitions.

3.3.1 *f*-Values for Free-Free Transitions

As there is no free-free stage in the available **R**-matrix code, the *f*-values for the FF transitions were generated by Autostructure in the intermediate coupling scheme where 60 electron configurations were included in the atomic specification of the Autostructure input: $2s^2 nl$ ($2p \leq nl \leq 7s$), $2s2p nl$ ($2p \leq nl \leq 7s$), $2p^3$, and $2p^2 nl$ ($3s \leq nl \leq 7s$). An iterative procedure was followed to find the orbital scaling parameters (λ 's) for Autostructure before producing the required data. These scaling parameters are given in Table 3.2. The scaling parameters, which are obtained by Autostructure in an automated optimization variational process, are required to minimize the weighted energy sum of the included target states [32, 102, 130]. The Autostructure input data for generating the *f*-values for the free-free transitions is given in § D.2.3 in Appendix D. It should be remarked that Autostructure, with the same input data, was also used to generate *f*-values for the free-bound transitions and the bound-bound transitions that involve the 8 topmost bound states, namely the $1s^2 2s2p(^3P^o)3d ^4F^o$ and $^4D^o$ levels, as these states have large effective quantum number and hence are not accessible to the RMATRIX-I code. Because Autostructure produces data only to a certain level of approximation (i.e. the *f*-value is ignored when it falls below a certain limit) some of the entries were missing from the 'olg' file of the Autostructure output and hence zero was inserted for these missing entries in the oscillator strength files required by the 'Emissivity' code.

Table 3.2: Orbital scaling parameters (λ 's) for Autostructure input. The rows stand for the principal quantum number n , while the columns stand for the orbital angular momentum quantum number l .

	s	p	d	f	g	h
1	1.43240					
2	1.43380	1.39690				
3	1.25760	1.20290	1.35930			
4	1.25830	1.19950	1.35610	1.41460		
5	1.26080	1.20020	1.35770	1.41420	1.32960	
6	1.26370	1.20250	1.36210	1.41520	1.41420	2.34460
7	1.26790					

3.3.2 *f*-Values for Free-Bound Transitions

The *f*-values for more than 2500 free-bound transitions were computed by integrating the peaks of the photoionization cross sections (in mega barn) over the photon energy (in Rydberg). This was done for each bound state and for all resonances in the corresponding cross-section. The area under the cross-section curve comprises a background contribution, assumed linear with energy, and the contribution due to the resonance, which is directly related to the bound-free oscillator strength. The background contribution was therefore removed by subtracting the linear fit at the bottom of the profile from the peak. The computation of oscillator strengths from integrating the peaks of the photoionization cross sections is based on the fact that the contribution of a resonance to the recombination rate correlates to the area underneath, and hence it quantifies the oscillator strength between the resonance and the interacting state, while the width of a resonance depends on the strength of the interaction with the continuum [131]. Therefore, the first step in these computations is to obtain the photoionization cross section of a particular transition from a lower bound-state l to the continuum, $\sigma_{(l \rightarrow u)}$. Since the resonance contribution to a particular radiative process is proportional to the area beneath σ for that process, by integrating σ over energy the *f*-value for a transition from

an upper resonance state u to a lower bound state l is found.

In the following points we outline the general procedure that was followed to compute the oscillator strengths for the FB transitions:

- RESMESH program of P.J. Storey [private communication] was used to create an energy mesh that maps the resonances in the most precise way. The input data required by RESMESH are the position and width of resonances, the energy range of the mesh and an integral error index. In our case, the positions and widths of resonances were obtained by the **K**-matrix method as implemented in stage STGF of the **R**-matrix code. It should be remarked that a separate energy mesh was used to generate photoionization cross section data for each individual resonance with a refinement process to ensure correct mapping and to avoid peak overlapping from different resonances.
- The mesh generated by RESMESH was then used as an input to stage STGF of the **R**-matrix code to create F-files which contain the required data for resonances.
- Stage STGBF was then run to create ‘XSECTN’ file which contains the data for photoionization cross sections (in mega barn) versus photon energies (in Ryd). Plots of some representative cross-sections are shown in Figure 3.2 which displays a number of examples of photoionization cross sections of the indicated bound states close to the designated autoionizing states versus photon energy on linear-linear graphs.
- The peaks of the photoionization cross sections were extracted by graphic techniques. The numerical data were then used to obtain the f -values by integrating the photoionization cross sections over photon energy using a 3-point Simpson’s rule. A piece of code from P.J. Storey [private communication] was used to perform the integration with the required scaling. Visual

inspection to each peak during the extraction of data and computing the oscillator strengths was carried out to check the goodness of profile and verify that it contains sufficient number of points. In general, the data points that define the peak profile and which are used for the integrated cross sections were chosen to be as close as possible to the background on both sides considering some sort of symmetry and avoiding mixing with other resonances. The possibility of mixing between neighboring resonances was eliminated later on by producing photoionization cross section data ('XSECTN' files) for each resonance independently with the adoption of one-resonance mesh approach, as will be discussed next.

A refinement process was used to improve the positions of the resonances by inputting the results of one run to the next during mesh generation and data creation. The purpose of refinement is to optimize the position of resonances and obtain optimal resonance profiles. In the refinement process the RESMESH cycle, as outlined in the previous steps, was repeated several times (about five) where the results of one cycle was fed to the next. To find the positions in each cycle, all the peaks belonging to the resonance of interest are obtained from 'XSECTN' file created in that cycle. The energy position of the largest peak was then taken as an input to RESMESH in the next run. As the refinement progresses, the situation steadily improves in terms of peaks height and shape until it stabilizes where no improvement is observed on performing more iterations. Most of this process was carried out by automated procedures, and the results were thoroughly inspected and checked.

Initially a single mesh was used to optimize the position of all resonances in a single run. This is based on the assumption that the results will improve in general as the refinement progresses from one cycle to the next. However, it was observed that although the results generally do improve for some resonances they deteriorate

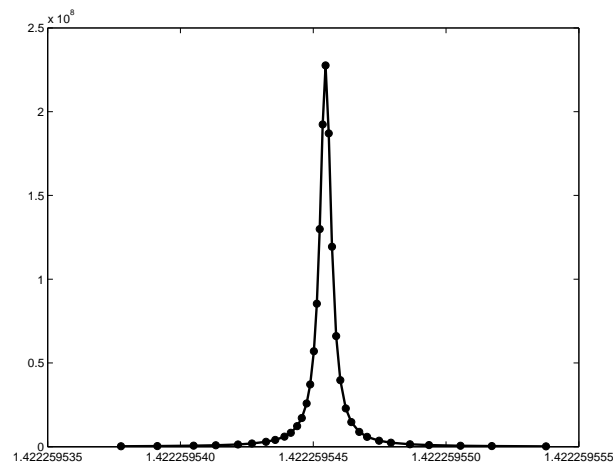
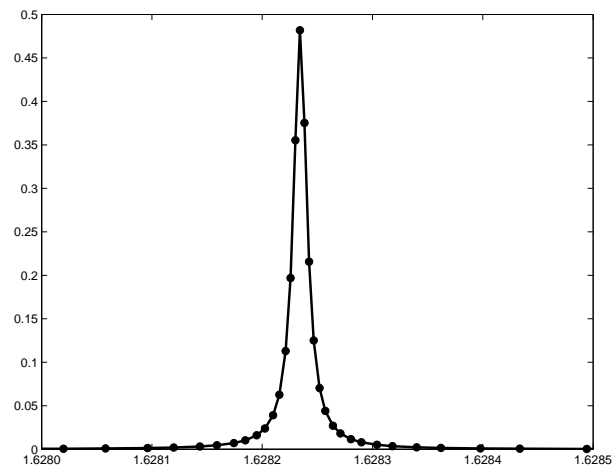
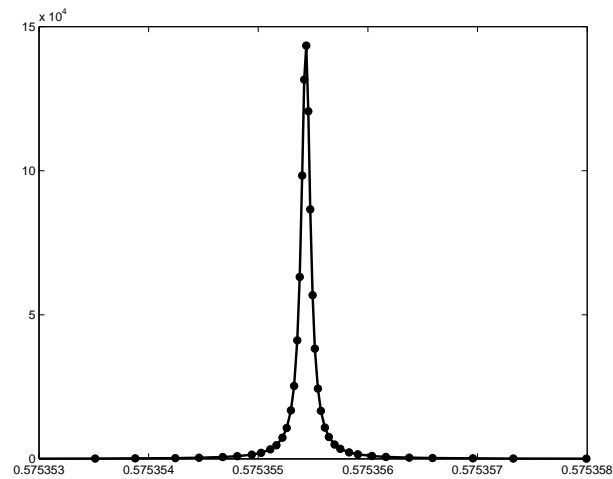
(a) $2s2p(^3P^o)3d\ ^4P^o_{1/2}$ resonance in $2s2p^2\ ^4P^e_{1/2}$ cross-section.(b) $2s2p(^3P^o)4d\ ^2F^o_{5/2}$ resonance in $2s2p^2\ ^4P^e_{3/2}$ cross-section.(c) $2s2p(^3P^o)4p\ ^2P^e_{3/2}$ resonance in $2p^3\ ^2D^o_{5/2}$ cross-section.

Figure 3.2: Examples of photoionization cross sections in mega barn (y -axis) of the indicated bound states near to the designated autoionizing states versus photon energy in Rydberg (x -axis).

for others. Moreover, there was a considerable overlap between some resonances especially for those from multiplets belonging to different symmetries.

A new approach of refinement was then started by continuing the refinement for the ones that continue to improve while holding the deteriorated ones at the position of their best photoionization cross section value. However, the results did not move in the anticipated direction and similar behavior to the previous (i.e. deterioration for some resonances) was observed. The apparent conclusion is that the resonances within a mesh interact, and therefore it is difficult to control the individual resonances within the mesh. Another serious problem with the single mesh is the size of the data files and the confusion created by the simultaneous presence of many resonances for each data set belonging to each bound state. Moreover, when resonances are too broad or too close to each other they mix up creating more reasons for confusion and error. These factors made processing the data without serious errors unfeasible.

A different approach was therefore adopted by generating a mesh for each individual resonance. The advantage of this approach is that it requires less effort in data extraction and produces more reliable results. Moreover, the extraction of data can be highly automated. The biggest advantage of the one-resonance mesh approach is that for the multiplets of the very broad resonances, such as the doublet $2s2p(^3P^o)4s\ ^2P^o_{1/2}$ and $^2P^o_{3/2}$, separate peak profiles are obtained for each level, whereas only one peak profile which combines the profiles of these two levels was obtained in the previous attempts using the single-mesh approach. However, the one-resonance mesh requires more preparation work since preparing the data and running the code are repeated as many times as the number of resonances. As indicated in § 3.3.1, Autostructure was used to produce *f*-values for the FB transitions that involve the 8 topmost bound states due to the **R**-matrix limitation related to the large effective quantum number of these states.

3.3.3 *f*-Values for Bound-Bound Transitions

No special effort was required to compute the *f*-values for the bound-bound transitions as these calculations were performed using stage STGGB of the **R**-matrix code. The input data for the **R**-matrix stages which were used to generate these data are given in § D.1 in Appendix D. As indicated in § 3.3.1, Autostructure was used to produce *f*-values for the BB transitions that involve the 8 topmost bound states due to the **R**-matrix limitation related to the large effective quantum number of these states.

3.4 Recombination and Emissivity Calculations

Emissivity and recombination calculations are the third major part of our work on the C II recombination lines. We are concerned with spectral lines formed by dielectronic capture followed by radiative decay. Including only these two processes and autoionization, the number density, N_l of a state l is given by

$$N_e N_i \varrho_c + \sum_u N_u \Gamma_{ul}^r = N_l (\Gamma_l^a + \Gamma_l^r) \quad (3.27)$$

where ϱ_c is the rate coefficient for dielectronic capture to state l and Γ_l^a is the autoionization probability of that state, related by

$$\varrho_c = \left(\frac{N_l}{N_e N_i} \right)_S \Gamma_l^a \quad (3.28)$$

where the subscript S refers to the value of the ratio given by the Saha equation, and N_e and N_i are the number densities of electrons and ions respectively. If state l lies below the ionization limit, $\varrho_c = \Gamma_l^a = 0$. Equation 3.27 can be solved for the populations l by a stepwise downward iteration using the ‘Emissivity’ code

[121]. Full account of the theoretical infrastructure of the ‘Emissivity’ code, which include the computation of the emissivities and their equivalent effective recombination coefficients which are the physical parameters of primary interest to this investigation, is given in § 3.1.

As part of this investigation, the C II lines from several observational line lists found in the literature, such as that of Sharpee *et al* [4] for the planetary nebula IC 418, were analyzed using our theoretical line list and all correctly-identified C II recombination lines in these observational lists were identified in our theoretical list apart from very few exceptions which are outside our wavelength range. The analysis also produced an electron temperature for the line-emitting regions of a number of astronomical objects in reasonably good agreement with the values obtained by other researchers using different data and employing other techniques. The details of this investigation are reported in Chapter 4.

3.4.1 Practical Aspects

Regarding the input data used in the transition lines calculations, all theoretical data for the energy of resonances and bound states were replaced with experimental data from NIST when such experimental data were available. This is based on the approach of Nussbaumer and Storey which was mentioned in Section 1.2.1. The use of experimental positions removes the uncertainty and errors which are usually introduced by *ab initio* calculations.

It should be remarked that all transitions in our calculations are subject to the electric dipole (E1) rules. Also, the data of SS1 list are generated assuming electron and ion number density of 10^{10} m^{-3} . Another remark is that the autoionization and radiative probabilities in the emissivity calculations as outlined in § 3.1 can also be obtained from Autostructure. In the early stages of this research such an approach

was adopted by producing some data by RMATRIX-I and some by Autostructure. According to the old approach, the widths of resonances are first obtained by the \mathbf{K} -matrix method; from which the autoionization transition probabilities, Γ^a , are computed. The corresponding radiative transition probabilities, Γ^r , are then found by Autostructure. The configurations that were used in the radiative calculations are the five most important ones for C^+ : $1s^2 2s^2 3d$, $1s^2 2s2p^2$, $1s^2 2s2p 3p$, $1s^2 2s2p 3d$ and $1s^2 2s2p 4s$. The Autostructure input data for these calculations are given in § D.2.2 in Appendix D. The departure coefficients, b_u , are then calculated and the states with $b_u \ll 1$ are excluded from further investigation because of their very low likelihood of existence. However, this approach was abandoned afterwards because a better treatment within a more comprehensive theory can be obtained from \mathbf{R} -matrix as we were able to produce all the required data by RMATRIX-I and ‘Emissivity’ codes. The main merit of the old approach is its simplicity and computational economy. Anyway, the method was useful in checking the \mathbf{R} -matrix results by comparing the departure coefficients from RMATRIX-I to those from Autostructure. Good agreement were found in most cases between the two methods on a sample data set.

3.5 Comparison to Previous Work

In this section we make a brief comparison of some of our results against a sample of similar results obtained by other researchers in previous studies. These include autoionization probabilities, given in Table 3.3, radiative transition probabilities, given in Table 3.4, and dielectronic recombination coefficients, given in Table 3.5.

In Table 3.3 we compare our calculated autoionization probabilities with those of De Marco *et al* [5]. They combined the LS -coupled autoionization probabilities calculated in the close coupling approximation by Davey *et al* [60] with one- and

two-body fine structure interactions computed with Superstructure [102] to obtain autoionization probabilities for four states that give rise to spectral lines seen in carbon-rich Wolf-Rayet stars. For the three larger probabilities, there is agreement within 25%, but for the $4f\ ^2G_{9/2}^e$ state there is a factor of about two difference. Because our autoionization probabilities are computed directly from the resonance widths (Equation 3.9) which are obtained from two independent methods (i.e. **K**-matrix and **QB**), we expect our values to be the more reliable ones.

Radiative transition probabilities, as seen in Table 3.4, generally show good agreement between the various calculations for the strongest electric dipole transitions. There are some significant differences for intercombination transitions, indicative of the increased uncertainty for these cases. There are also significant differences between the present results and those of Nussbaumer and Storey [117] for some of the allowed but two-electron transitions from the $1s^22s^23p$ configuration, where we would expect our results to be superior, given the larger scattering target.

In Table 3.5 we compare our results with effective recombination coefficients from Table (1) of Badnell [8]. His results are tabulated between terms, having been summed over the J of the upper and lower terms of the transition, so results for individual lines cannot be compared. Badnell only tabulates results for one transition in which the upper state is allowed to autoionize in LS -coupling ($1s^22s2p(^3P^o)3d\ ^2F^o$) and here the agreement is excellent as one might expect. On the other hand, the levels of $1s^22s2p(^3P^o)3d\ ^2D^o$ have small autoionization widths and our coefficients are generally smaller than Badnell's for transitions from this term. We note that the fine structure splitting of this term is well represented in our calculation as is its separation from neighboring states with large autoionization widths, giving us confidence in our result.

Table 3.3: Autoionization probabilities in s^{-1} of four resonance states as obtained in the current work (SS) compared to those obtained by De Marco *et al* [5] (DSB).

State	SS	DSB
$1s^2 2s 2p(^3P^o) 4f \ ^2D_{5/2}^e$	9.860e10	8.263e10
$1s^2 2s 2p(^3P^o) 4f \ ^2G_{9/2}^e$	8.601e08	1.623e09
$1s^2 2s 2p(^3P^o) 3d \ ^2P_{3/2}^o$	2.194e11	1.901e11
$1s^2 2s 2p(^3P^o) 3d \ ^2F_{7/2}^o$	1.196e12	1.488e12

Table 3.4: A sample of radiative transition probabilities in s^{-1} as obtained from this work compared to corresponding values found in the literature. The prime indicates an excited $1s^2 2s 2p ({}^3P^o)$ core. The $1s^2$ core is suppressed from all configurations.

Upper	Lower	λ_ν	SS	NS	LDHK	HST	GKMKW	FKWP	DT	DSB
$2s^2 2p^2 \ 4P^e_{1/2}$	$2s^2 2p \ 2P^o_{1/2}$	2325.40	52.8	55.3	74.4				42.5	
$2s^2 2p^2 \ 4P^e_{3/2}$	$2s^2 2p \ 2P^o_{1/2}$	2324.21	1.79	1.71	1.70				1.01	
$2s^2 2p^2 \ 4P^e_{1/2}$	$2s^2 2p \ 2P^o_{3/2}$	2328.84	60.6	65.5	77.8				40.2	
$2s^2 2p^2 \ 4P^e_{3/2}$	$2s^2 2p \ 2P^o_{3/2}$	2327.64	9.34	5.24	12.4				8.11	
$2s^2 2p^2 \ 4P^e_{5/2}$	$2s^2 2p \ 2P^o_{3/2}$	2326.11	36.7	43.2	53.9			51.2	34.4	
$2s^2 2p^2 \ 2D^e_{3/2}$	$2s^2 2p \ 2P^o_{1/2}$	1334.53	2.40e8	2.42e8	2.38e8				2.41e8	
$2s^2 2p^2 \ 2D^e_{5/2}$	$2s^2 2p \ 2P^o_{3/2}$	1335.71	2.87e8	2.88e8	2.84e8				2.89e8	
$2s^2 2p^2 \ 2D^e_{3/2}$	$2s^2 2p \ 2P^o_{3/2}$	1335.66	4.75e7	4.78e7	4.70e7				4.79e7	
$2s^2 2p^2 \ 2S^e_{1/2}$	$2s^2 2p \ 2P^o_{1/2}$	1036.34	7.75e8	7.74e8					7.99e8	
$2s^2 2p^2 \ 2S^e_{1/2}$	$2s^2 2p \ 2P^o_{3/2}$	1037.02	1.53e9	1.53e9					1.59e9	
$2s^2 2p^2 \ 2P^e_{1/2}$	$2s^2 2p \ 2P^o_{1/2}$	903.96	2.76e9	2.74e9					2.63e9	
$2s^2 2p^2 \ 2P^e_{3/2}$	$2s^2 2p \ 2P^o_{1/2}$	903.62	6.92e8	6.86e8					6.58e8	
$2s^2 2p^2 \ 2P^e_{3/2}$	$2s^2 2p \ 2P^o_{3/2}$	904.48	1.39e9	1.38e9					1.33e9	
$2s^2 2p^2 \ 2P^e_{1/2}$	$2s^2 2p \ 2P^o_{3/2}$	904.14	3.46e9	3.43e9					3.30e9	
$2s^2 3s \ 2S^e_{1/2}$	$2s^2 2p \ 2P^o_{1/2}$	858.09	1.26e8	1.31e8					3.69e7	
$2s^2 3s \ 2S^e_{1/2}$	$2s^2 2p \ 2P^o_{3/2}$	858.56	2.46e8	2.58e8					1.11e8	
$2s^2 3p \ 2P^o_{1/2}$	$2s^2 2p^2 \ 4P^e_{1/2}$	1127.13	36.3	55.5						
$2s^2 3p \ 2P^o_{3/2}$	$2s^2 2p^2 \ 4P^e_{1/2}$	1126.99	58.28	97.8						
$2s^2 3p \ 2P^o_{1/2}$	$2s^2 2p^2 \ 4P^e_{3/2}$	1127.41	21.8	20.3						
$2s^2 3p \ 2P^o_{3/2}$	$2s^2 2p^2 \ 4P^e_{3/2}$	1127.27		22.3						
$2s^2 3p \ 2P^o_{3/2}$	$2s^2 2p^2 \ 4P^e_{5/2}$	1127.63	1.86e2	2.60e2						
$2p^3 \ 4S^o_{3/2}$	$2s^2 2p^2 \ 4P^e_{1/2}$	1009.86	5.77e8	5.82e8					5.76e8	
$2p^3 \ 4S^o_{3/2}$	$2s^2 2p^2 \ 4P^e_{3/2}$	1010.08	1.15e9	1.16e9					1.15e9	
$2p^3 \ 4S^o_{3/2}$	$2s^2 2p^2 \ 4P^e_{5/2}$	1010.37	1.73e9	1.74e9					1.73e9	
$2s^2 3p \ 2P^o_{3/2}$	$2s^2 2p^2 \ 2D^e_{5/2}$	1760.40	3.77e7	3.75e7		4.3e7				
$2s^2 3p \ 2P^o_{1/2}$	$2s^2 2p^2 \ 2D^e_{3/2}$	1760.82	4.19e7	4.16e7		5.2e7				
$2s^2 3p \ 2P^o_{3/2}$	$2s^2 2p^2 \ 2D^e_{3/2}$	1760.47	4.18e6	4.16e6		4e6				
$2p^3 \ 4S^o_{3/2}$	$2s^2 2p^2 \ 2D^e_{5/2}$	1490.38	1.03e2	45.0						
$2p^3 \ 4S^o_{3/2}$	$2s^2 2p^2 \ 2D^e_{3/2}$	1490.44	10.5	11.9						
$2s^2 3p \ 2P^o_{1/2}$	$2s^2 2p^2 \ 2S^e_{3/2}$	2838.44	3.61e7	3.63e7		2.2e7				
$2s^2 3p \ 2P^o_{3/2}$	$2s^2 2p^2 \ 2S^e_{1/2}$	2837.54	3.61e7	3.64e7		2.2e7				
$2p^3 \ 4S^o_{3/2}$	$2s^2 2p^2 \ 2S^e_{1/2}$	2196.19	1.62	5.09						
$2s^2 3p \ 2P^o_{1/2}$	$2s^2 2p^2 \ 2P^e_{1/2}$	4739.29	5.85e4	7.70e4				<3.0e5		
$2s^2 3p \ 2P^o_{3/2}$	$2s^2 2p^2 \ 2P^e_{1/2}$	4736.79	7.98e3	1.19e4				<5e5		
$2s^2 3p \ 2P^o_{1/2}$	$2s^2 2p^2 \ 2P^e_{3/2}$	4748.61	2.35e4	3.23e4				<2.3e5		
$2s^2 3p \ 2P^o_{3/2}$	$2s^2 2p^2 \ 2P^e_{3/2}$	4746.09	6.08e4	8.28e4				<1.3e5		
$2p^3 \ 4S^o_{3/2}$	$2s^2 2p^2 \ 2P^e_{1/2}$	3184.42	16.4	14.9						
$2p^3 \ 4S^o_{3/2}$	$2s^2 2p^2 \ 2P^e_{3/2}$	3188.62	80.0	76.9						
$2s^2 3p \ 2P^o_{1/2}$	$2s^2 3s \ 2S^e_{1/2}$	6584.70	3.53e7	3.68e7		2.9e7	3.29e7			
$2s^2 3p \ 2P^o_{3/2}$	$2s^2 3s \ 2S^e_{1/2}$	6579.87	3.54e7	3.69e7		3.4e7	3.33e7			
$2p^3 \ 4S^o_{3/2}$	$2s^2 3s \ 2S^e_{1/2}$	3923.19	6.35	10.2						
$2s^2 3d \ 2D^e_{3/2}$	$2s^2 3p \ 2P^o_{1/2}$	7233.33	3.46e7				4.22e7			
$2s^2 3d \ 2D^e_{3/2}$	$2s^2 3p \ 2P^o_{3/2}$	7239.16	6.91e6				8.49e6			
$2s^2 3d \ 2D^e_{5/2}$	$2s^2 3p \ 2P^o_{3/2}$	7238.41	4.15e7				5.10e7			
$2s^2 3d \ 2D^e_{3/2}$	$2s^2 2p^2 \ 2P^o_{1/2}$	687.05	2.40e9						2.24e9	
$2s^2 3d \ 2D^e_{3/2}$	$2s^2 2p^2 \ 2P^o_{3/2}$	687.35	4.81e8						4.50e8	
$2s^2 3d \ 2D^e_{5/2}$	$2s^2 2p^2 \ 2P^o_{3/2}$	687.35	2.88e9						2.70e9	
$2p^3 \ 2D^o_{3/2}$	$2s^2 2p^2 \ 2D^e_{3/2}$	1323.91	4.33e8						4.53e8	
$2p^3 \ 2D^o_{5/2}$	$2s^2 2p^2 \ 2D^e_{3/2}$	1324.00	3.23e7						3.38e7	
$2p^3 \ 2D^o_{3/2}$	$2s^2 2p^2 \ 2D^e_{5/2}$	1323.86	4.91e7						5.10e7	
$2p^3 \ 2D^o_{5/2}$	$2s^2 2p^2 \ 2D^e_{5/2}$	1323.95	4.51e8						4.71e8	
$2p^3 \ 2D^o_{3/2}$	$2s^2 2p^2 \ 2P^e_{1/2}$	2509.88	4.53e7						5.38e7	
$2p^3 \ 2D^o_{3/2}$	$2s^2 2p^2 \ 2P^e_{3/2}$	2512.49	8.91e6						1.06e7	
$2p^3 \ 2D^o_{5/2}$	$2s^2 2p^2 \ 2P^e_{3/2}$	2512.81	5.40e7						6.43e7	
$4f' \ 2D^e_{5/2}$	$3d' \ 2P^o_{3/2}$	5115.07	1.18e8						6.94e7	
$4f' \ 2G^e_{9/2}$	$3d' \ 2F^o_{7/2}$	4620.54	2.29e8						1.84e8	
$3d' \ 2P^o_{3/2}$	$3p' \ 2P^e_{3/2}$	4966.12	3.14e7						2.89e7	
$3d' \ 2F^o_{7/2}$	$3p' \ 2D^e_{5/2}$	8796.49	2.03e7						1.99e7	

SS = current work, NS = Nussbaumer and Storey [117]; LDHK = Lennon *et al* [132]; HST = Huber *et al* [133]; GKMKW = Glenzer *et al* [134]; FKWP = Fang *et al* [135]; DT = Dankwort and Trefftz [136], DSB = De Marco *et al* [5].

Table 3.5: Effective dielectronic recombination rate coefficients in cm^3s^{-1} of a number of transitions for the given 10-based logarithmic temperatures. The first row for each transition corresponds to Badnell [8], while the second row is obtained from the current work. The superscripts denotes powers of 10. The prime indicates an excited $1s^22s2p(^3P^o)$ core. The $1s^2$ core is suppressed from all configurations.

Upper	Lower	log(T)									
		3.0	3.2	3.4	3.6	3.8	4.0	4.2	4.4	4.6	4.8
3d' $^4F^o$	3p' $^4D^e$	7.27 ⁻²⁴	5.73 ⁻²⁰	1.56 ⁻¹⁷	6.17 ⁻¹⁶	6.47 ⁻¹⁵	2.61 ⁻¹⁴	5.52 ⁻¹⁴	7.43 ⁻¹⁴	7.25 ⁻¹⁴	5.65 ⁻¹⁴
		6.74 ⁻²⁴	5.17 ⁻²⁰	1.29 ⁻¹⁷	4.33 ⁻¹⁶	3.90 ⁻¹⁵	1.33 ⁻¹⁴	2.31 ⁻¹⁴	2.57 ⁻¹⁴	2.13 ⁻¹⁴	1.47 ⁻¹⁴
3p' $^4D^e$	3s' $^4P^o$	1.90 ⁻¹⁶	3.21 ⁻¹⁶	8.53 ⁻¹⁶	4.95 ⁻¹⁵	1.93 ⁻¹⁴	4.90 ⁻¹⁴	8.51 ⁻¹⁴	1.05 ⁻¹³	9.91 ⁻¹⁴	7.57 ⁻¹⁴
		1.06 ⁻¹⁶	1.90 ⁻¹⁶	7.71 ⁻¹⁶	5.02 ⁻¹⁵	1.74 ⁻¹⁴	3.58 ⁻¹⁴	4.85 ⁻¹⁴	4.76 ⁻¹⁴	3.70 ⁻¹⁴	2.46 ⁻¹⁴
3d' $^2D^o$	3p' $^2P^e$	2.49 ⁻¹⁴	3.19 ⁻¹⁴	2.90 ⁻¹⁴	2.11 ⁻¹⁴	1.35 ⁻¹⁴	8.05 ⁻¹⁵	4.80 ⁻¹⁵	2.94 ⁻¹⁵	1.81 ⁻¹⁵	1.10 ⁻¹⁵
		4.67 ⁻¹⁵	5.99 ⁻¹⁵	5.44 ⁻¹⁵	3.97 ⁻¹⁵	2.58 ⁻¹⁵	1.68 ⁻¹⁵	1.17 ⁻¹⁵	8.31 ⁻¹⁶	5.54 ⁻¹⁶	3.41 ⁻¹⁶
3p' $^4P^e$	3s' $^4P^o$	3.08 ⁻¹⁶	5.09 ⁻¹⁶	9.86 ⁻¹⁶	4.02 ⁻¹⁵	1.08 ⁻¹⁴	1.73 ⁻¹⁴	2.04 ⁻¹⁴	1.97 ⁻¹⁴	1.61 ⁻¹⁴	1.14 ⁻¹⁴
		1.49 ⁻¹⁶	2.52 ⁻¹⁶	7.24 ⁻¹⁶	3.84 ⁻¹⁵	1.05 ⁻¹⁴	1.58 ⁻¹⁴	1.60 ⁻¹⁴	1.27 ⁻¹⁴	8.52 ⁻¹⁵	5.14 ⁻¹⁵
4f' $^2F^e$	3d' $^2D^o$	3.00 ⁻²⁷	6.39 ⁻²²	1.14 ⁻¹⁸	9.93 ⁻¹⁷	1.29 ⁻¹⁵	5.09 ⁻¹⁵	9.43 ⁻¹⁵	1.09 ⁻¹⁴	9.26 ⁻¹⁵	6.51 ⁻¹⁵
		1.64 ⁻²⁷	3.53 ⁻²²	6.33 ⁻¹⁹	5.54 ⁻¹⁷	7.22 ⁻¹⁶	2.82 ⁻¹⁵	5.18 ⁻¹⁵	5.88 ⁻¹⁵	4.94 ⁻¹⁵	3.43 ⁻¹⁵
4f' $^4D^e$	3d' $^4P^o$	2.56 ⁻²⁷	7.68 ⁻²²	1.70 ⁻¹⁸	1.70 ⁻¹⁶	2.40 ⁻¹⁵	9.95 ⁻¹⁵	1.90 ⁻¹⁴	2.21 ⁻¹⁴	1.89 ⁻¹⁴	1.33 ⁻¹⁴
		2.54 ⁻²⁷	7.63 ⁻²²	1.69 ⁻¹⁸	1.69 ⁻¹⁶	2.39 ⁻¹⁵	9.86 ⁻¹⁵	1.87 ⁻¹⁴	2.17 ⁻¹⁴	1.85 ⁻¹⁴	1.29 ⁻¹⁴
4s' $^4P^o$	3p' $^4P^e$	2.59 ⁻²⁰	1.23 ⁻¹⁷	4.65 ⁻¹⁶	3.58 ⁻¹⁵	1.01 ⁻¹⁴	1.51 ⁻¹⁴	1.51 ⁻¹⁴	1.18 ⁻¹⁴	7.80 ⁻¹⁵	4.67 ⁻¹⁵
		2.63 ⁻²⁰	1.25 ⁻¹⁷	4.72 ⁻¹⁶	3.63 ⁻¹⁵	1.02 ⁻¹⁴	1.53 ⁻¹⁴	1.53 ⁻¹⁴	1.19 ⁻¹⁴	7.83 ⁻¹⁵	4.68 ⁻¹⁵
4f' $^4F^e$	3d' $^4D^o$	5.39 ⁻²⁷	1.16 ⁻²¹	2.07 ⁻¹⁸	1.81 ⁻¹⁶	2.37 ⁻¹⁵	9.41 ⁻¹⁵	1.77 ⁻¹⁴	2.07 ⁻¹⁴	1.79 ⁻¹⁴	1.27 ⁻¹⁴
		3.48 ⁻²⁷	7.51 ⁻²²	1.35 ⁻¹⁸	1.19 ⁻¹⁶	1.55 ⁻¹⁵	6.07 ⁻¹⁵	1.11 ⁻¹⁴	1.26 ⁻¹⁴	1.06 ⁻¹⁴	7.37 ⁻¹⁵
4f' $^4G^e$	3d' $^4F^o$	5.42 ⁻²⁷	1.50 ⁻²¹	3.15 ⁻¹⁸	3.05 ⁻¹⁶	4.24 ⁻¹⁵	1.74 ⁻¹⁴	3.30 ⁻¹⁴	3.86 ⁻¹⁴	3.32 ⁻¹⁴	2.34 ⁻¹⁴
		2.98 ⁻²⁷	8.25 ⁻²²	1.73 ⁻¹⁸	1.68 ⁻¹⁶	2.33 ⁻¹⁵	9.49 ⁻¹⁵	1.78 ⁻¹⁴	2.06 ⁻¹⁴	1.75 ⁻¹⁴	1.22 ⁻¹⁴
4s' $^4P^o$	3p' $^4D^e$	2.86 ⁻²⁰	1.36 ⁻¹⁷	5.14 ⁻¹⁶	3.95 ⁻¹⁵	1.11 ⁻¹⁴	1.67 ⁻¹⁴	1.67 ⁻¹⁴	1.30 ⁻¹⁴	8.61 ⁻¹⁵	5.15 ⁻¹⁵
		3.15 ⁻²⁰	1.49 ⁻¹⁷	5.65 ⁻¹⁶	4.35 ⁻¹⁵	1.22 ⁻¹⁴	1.83 ⁻¹⁴	1.83 ⁻¹⁴	1.42 ⁻¹⁴	9.37 ⁻¹⁵	5.59 ⁻¹⁵
4d' $^4F^o$	3p' $^4D^e$	1.77 ⁻²⁶	1.71 ⁻²¹	1.85 ⁻¹⁸	1.18 ⁻¹⁶	1.30 ⁻¹⁵	4.85 ⁻¹⁵	9.35 ⁻¹⁵	1.18 ⁻¹⁴	1.10 ⁻¹⁴	8.31 ⁻¹⁵
		1.75 ⁻²⁶	1.69 ⁻²¹	1.83 ⁻¹⁸	1.17 ⁻¹⁶	1.24 ⁻¹⁵	4.28 ⁻¹⁵	7.25 ⁻¹⁵	7.83 ⁻¹⁵	6.37 ⁻¹⁵	4.34 ⁻¹⁵
2s2p 2 $^2D^e$	2s 2 2p $^2P^o$	2.45 ⁻¹²	5.89 ⁻¹²	8.34 ⁻¹²	8.17 ⁻¹²	6.33 ⁻¹²	4.36 ⁻¹²	3.01 ⁻¹²	2.21 ⁻¹²	1.66 ⁻¹²	1.19 ⁻¹²
		1.85 ⁻¹²	5.12 ⁻¹²	7.66 ⁻¹²	7.67 ⁻¹²	6.00 ⁻¹²	4.09 ⁻¹²	2.61 ⁻¹²	1.60 ⁻¹²	9.38 ⁻¹³	5.28 ⁻¹³
3d' $^2D^o$	2s2p 2 $^2P^e$	2.60 ⁻¹³	3.33 ⁻¹³	3.02 ⁻¹³	2.20 ⁻¹³	1.41 ⁻¹³	8.41 ⁻¹⁴	5.01 ⁻¹⁴	3.07 ⁻¹⁴	1.89 ⁻¹⁴	1.15 ⁻¹⁴
		4.50 ⁻¹⁴	5.78 ⁻¹⁴	5.24 ⁻¹⁴	3.83 ⁻¹⁴	2.49 ⁻¹⁴	1.62 ⁻¹⁴	1.13 ⁻¹⁴	8.01 ⁻¹⁵	5.34 ⁻¹⁵	3.29 ⁻¹⁵
4d' $^2D^o$	2s2p 2 $^2P^e$	6.56 ⁻²⁷	1.10 ⁻²¹	1.70 ⁻¹⁸	1.35 ⁻¹⁶	1.66 ⁻¹⁵	6.33 ⁻¹⁵	1.16 ⁻¹⁴	1.33 ⁻¹⁴	1.13 ⁻¹⁴	8.02 ⁻¹⁵
		1.98 ⁻²⁷	3.29 ⁻²²	5.03 ⁻¹⁹	3.97 ⁻¹⁷	4.85 ⁻¹⁶	1.82 ⁻¹⁵	3.26 ⁻¹⁵	3.64 ⁻¹⁵	3.03 ⁻¹⁵	2.09 ⁻¹⁵
2s2p 2 $^2P^e$	2s 2 2p $^2P^o$	2.68 ⁻¹³	3.99 ⁻¹³	5.05 ⁻¹³	5.45 ⁻¹³	4.87 ⁻¹³	3.95 ⁻¹³	3.37 ⁻¹³	3.09 ⁻¹³	2.75 ⁻¹³	2.21 ⁻¹³
		5.11 ⁻¹⁴	1.11 ⁻¹³	2.21 ⁻¹³	3.09 ⁻¹³	3.18 ⁻¹³	2.78 ⁻¹³	2.24 ⁻¹³	1.66 ⁻¹³	1.11 ⁻¹³	6.82 ⁻¹⁴
3d' $^2D^o$	2s2p 2 $^2D^e$	7.38 ⁻¹³	9.47 ⁻¹³	8.59 ⁻¹³	6.26 ⁻¹³	3.99 ⁻¹³	2.39 ⁻¹³	1.42 ⁻¹³	8.71 ⁻¹⁴	5.38 ⁻¹⁴	3.25 ⁻¹⁴
		1.36 ⁻¹³	1.75 ⁻¹³	1.59 ⁻¹³	1.16 ⁻¹³	7.53 ⁻¹⁴	4.90 ⁻¹⁴	3.43 ⁻¹⁴	2.42 ⁻¹⁴	1.61 ⁻¹⁴	9.95 ⁻¹⁵
3s' $^4P^o$	2s2p 2 $^4P^e$	1.36 ⁻¹⁵	2.22 ⁻¹⁵	3.36 ⁻¹⁵	1.07 ⁻¹⁴	3.30 ⁻¹⁴	7.13 ⁻¹⁴	1.12 ⁻¹³	1.32 ⁻¹³	1.21 ⁻¹³	9.09 ⁻¹⁴
		7.17 ⁻¹⁶	1.19 ⁻¹⁵	2.35 ⁻¹⁵	1.02 ⁻¹⁴	3.12 ⁻¹⁴	5.78 ⁻¹⁴	7.22 ⁻¹⁴	6.71 ⁻¹⁴	5.05 ⁻¹⁴	3.29 ⁻¹⁴
3d' $^2F^o$	2s2p 2 $^2D^e$	1.70 ⁻¹²	4.92 ⁻¹²	7.44 ⁻¹²	7.49 ⁻¹²	5.83 ⁻¹²	3.86 ⁻¹²	2.30 ⁻¹²	1.29 ⁻¹²	6.93 ⁻¹³	3.63 ⁻¹³
		1.71 ⁻¹²	4.94 ⁻¹²	7.48 ⁻¹²	7.53 ⁻¹²	5.86 ⁻¹²	3.88 ⁻¹²	2.32 ⁻¹²	1.30 ⁻¹²	6.97 ⁻¹³	3.65 ⁻¹³
4d' $^2D^o$	2s2p 2 $^2D^e$	2.30 ⁻²⁶	3.86 ⁻²¹	5.94 ⁻¹⁸	4.72 ⁻¹⁶	5.81 ⁻¹⁵	2.22 ⁻¹⁴	4.05 ⁻¹⁴	4.65 ⁻¹⁴	3.97 ⁻¹⁴	2.81 ⁻¹⁴
		9.59 ⁻²⁷	1.59 ⁻²¹	2.43 ⁻¹⁸	1.92 ⁻¹⁶	2.35 ⁻¹⁵	8.82 ⁻¹⁵	1.58 ⁻¹⁴	1.76 ⁻¹⁴	1.47 ⁻¹⁴	1.01 ⁻¹⁴
3d' $^4D^o$	2s2p 2 $^4P^e$	2.49 ⁻²⁴	2.83 ⁻²⁰	1.05 ⁻¹⁷	4.56 ⁻¹⁶	4.63 ⁻¹⁵	1.78 ⁻¹⁴	3.62 ⁻¹⁴	4.76 ⁻¹⁴	4.58 ⁻¹⁴	3.53 ⁻¹⁴
		2.34 ⁻²⁴	2.63 ⁻²⁰	9.38 ⁻¹⁸	3.84 ⁻¹⁶	3.62 ⁻¹⁵	1.23 ⁻¹⁴	2.11 ⁻¹⁴	2.32 ⁻¹⁴	1.91 ⁻¹⁴	1.31 ⁻¹⁴
3d' $^4P^o$	2s2p 2 $^4P^e$	6.71 ⁻¹⁴	1.08 ⁻¹³	1.13 ⁻¹³	9.07 ⁻¹⁴	6.36 ⁻¹⁴	4.86 ⁻¹⁴	4.61 ⁻¹⁴	4.51 ⁻¹⁴	3.87 ⁻¹⁴	2.84 ⁻¹⁴
		3.41 ⁻¹⁴	5.51 ⁻¹⁴	5.78 ⁻¹⁴	4.63 ⁻¹⁴	3.38 ⁻¹⁴	2.97 ⁻¹⁴	3.10 ⁻¹⁴	2.93 ⁻¹⁴	2.30 ⁻¹⁴	1.55 ⁻¹⁴
4s' $^4P^o$	2s2p 2 $^4P^e$	9.12 ⁻¹⁹	4.32 ⁻¹⁷	1.64 ⁻¹⁵	1.26 ⁻¹⁴	3.55 ⁻¹⁴	5.31 ⁻¹⁴	5.33 ⁻¹⁴	4.14 ⁻¹⁴	2.75 ⁻¹⁴	1.64 ⁻¹⁴
		1.13 ⁻¹⁹	5.37 ⁻¹⁷	2.03 ⁻¹⁵	1.56 ⁻¹⁴	4.40 ⁻¹⁴	6.58 ⁻¹⁴	6.59 ⁻¹⁴	5.12 ⁻¹⁴	3.38 ⁻¹⁴	2.02 ⁻¹⁴
4d' $^4D^o$	2s2p 2 $^4P^e$	4.87 ⁻²⁶	6.33 ⁻²¹	8.27 ⁻¹⁸	5.94 ⁻¹⁶	6.90 ⁻¹⁵	2.57 ⁻¹⁴	4.72 ⁻¹⁴	5.54 ⁻¹⁴	4.85 ⁻¹⁴	3.49 ⁻¹⁴
		1.73 ⁻²⁶	2.26 ⁻²¹	2.95 ⁻¹⁸	2.12 ⁻¹⁶	2.43 ⁻¹⁵	8.79 ⁻¹⁵	1.53 ⁻¹⁴	1.69 ⁻¹⁴	1.39 ⁻¹⁴	9.52 ⁻¹⁵
4d' $^4P^o$	2s2p 2 $^4P^e$	5.09 ⁻²⁷	9.49 ⁻²³	1.56 ⁻¹⁸	1.30 ⁻¹⁶	1.68 ⁻¹⁵	6.90 ⁻¹⁵	1.39 ⁻¹⁴	1.78 ⁻¹⁴	1.67 ⁻¹⁴	1.27 ⁻¹⁴
		4.37 ⁻²⁸	8.18 ⁻²³	1.34 ⁻¹⁹	1.11 ⁻¹⁷	1.40 ⁻¹⁶	5.37 ⁻¹⁶	9.70 ⁻¹⁶	1.09 ⁻¹⁵	9.13 ⁻¹⁶	6.32 ⁻¹⁶
3p' $^2P^e$	2s 2 2p $^2P^o$	1.91 ⁻¹⁴	2.70 ⁻¹⁴	3.11 ⁻¹⁴	3.17 ⁻¹⁴	2.97 ⁻¹⁴	2.65 ⁻¹⁴	2.26 ⁻¹⁴	1.81 ⁻¹⁴	1.34 ⁻¹⁴	9.18 ⁻¹⁵
		4.59 ⁻¹⁵	9.59 ⁻¹⁵	1.86 ⁻¹⁴	2.67 ⁻¹⁴	2.99 ⁻¹⁴	2.83 ⁻¹⁴	2.31 ⁻¹⁴	1.66 ⁻¹⁴	1.06 ⁻¹⁴	6.26 ⁻¹⁵
4p' $^2P^e$	2s 2 2p $^2P^o$	5.81 ⁻²³	3.67 ⁻¹⁹	7.12 ⁻¹⁷	1.53 ⁻¹⁵	8.24 ⁻¹⁵	1.85 ⁻¹⁴	2.40 ⁻¹⁴	2.19 ⁻¹⁴	1.61 ⁻¹⁴	1.03 ⁻¹⁴
		6.35 ⁻²³	3.96 ⁻¹⁹	7.62 ⁻¹⁷	1.63 ⁻¹⁵	8.74 ⁻¹⁵	1.96 ⁻¹⁴	2.52 ⁻¹⁴	2.30 ⁻¹⁴	1.68 ⁻¹⁴	1.07 ⁻¹⁴

Chapter 4

Electron Temperature of Astronomical Objects

The study of transition lines of carbon and its ions in the spectra of astronomical objects, such as planetary nebulae [137–139], has implications for carbon abundance determination [9, 52, 56, 58, 117, 140], probing the physical conditions in the interstellar medium [23, 51], and element enrichment in the CNO cycle [59, 140, 141]. The lines span large parts of the electromagnetic spectrum and originate from various processes under different physical conditions. Concerning C^+ , the subject of the current investigation, spectral lines of this ion have been observed in many astronomical objects such as planetary nebulae, Seyfert galaxies, stellar winds of Wolf-Rayet stars, symbiotic stars, and in the interstellar medium [3, 55, 56, 59, 60, 62, 142–144].

There are many observational and theoretical studies on the recombination lines of carbon related to the spectra of PNe [2, 9, 17, 46–52, 56, 57, 61]; some of which are linked to the C^+ ion [3, 8, 23, 53–55, 58–60, 62]. The latter, however, are limited in number and constrained in domain.

In this chapter we investigate the electron temperature in the emitting region of recombination lines of C^+ ion in the spectra of a number of astronomical objects, mainly planetary nebulae, using a least squares optimization method with theoretical data obtained from the recently-computed theoretical line list, SS1, of [116] and astronomical data gathered from the literature. The theoretical list was generated using the **R**-matrix [104], Autostructure [41, 102, 103] and Emissivity [121] codes with an intermediate coupling scheme where the transition lines are produced by dielectronic recombination processes originating from the low-lying autoionizing states with subsequent cascade decays.

The traditional method of identifying electron temperature in thin plasma, found for example in planetary nebulae, is by taking the intensity ratio of two transition lines [22]. The advantage of this method is simplicity and its reliance on limited data. The disadvantage is that the lines should have strong intensity. They should also have considerable energy gap, typically of several electron volts, if collisionally-excited transitions are employed. The method can be subject to large errors if the observed intensity is contaminated with significant errors. On the other hand, the least squares minimization is a collective method that normally involves a number of lines and hence can be more reliable in identifying the electron temperature. The objective of the least squares technique is to find the temperature at which the difference between the observed data and the calculated model is minimal and hence identifying the temperature of the line-emitting region. Least squares minimization is based on the fact that this difference tends to minimum when the temperature-dependent theoretical data approaches the unknown temperature of the observation. The main tool used in the emissivity analysis is the ‘Emissivity’ code [121]. The analysis is based on minimizing the sum of weighted squared differences between the normalized theoretical emissivity and the normalized observational flux of the C II lines.

4.1 Method

As indicated already, the theoretical data of the C II dielectronic recombination transitions and subsequent cascade decay are obtained from the SS1 line list of [116] which consists of 6187 optically-allowed transitions with their associated data such as emissivity and effective recombination coefficients. The autoionizing states involved in the transitions of this list consist of 64 resonances belonging to 11 symmetries ($J = 1, 3, 5, 7, 9, 11$ half even and $J = 1, 3, 5, 7, 9$ half odd) which are all the resonances above the threshold of $C^{2+} 1s^2 2s^2 1S^e$ with a principal quantum number $n < 5$ for the combined electron. These include 61 theoretically-found resonances by the **K**-matrix method plus 3 experimental ones which could not be found due to their very narrow width. The bound states involved in these transitions comprise 150 energy levels belonging to 11 symmetries ($J = 1, 3, 5, 7, 9$ half even and $J = 1, 3, 5, 7, 9, 11$ half odd). These include 142 theoretically found by **R**-matrix, which are all the bound states with effective quantum number between 0.1-13 for the outer electron and $0 \leq l \leq 5$, plus 8 experimental top states which are the levels of the $1s^2 2s 2p(^3P^o) 3d ^4F^o$ and $^4D^o$ terms.

The theoretical and computational backgrounds for the atomic transition calculations including the emissivity thermodynamic model are given in Chapters 2 and 3. The calculations were performed using an elaborate C^{+2} ionic target under an intermediate coupling scheme. The list has also been validated by various tests including comparison to literature data related to autoionization and radiative transition probabilities and effective dielectronic recombination coefficients. The theoretical data of the bound and resonance states were also compared to the available experimental data [16] and found to agree very well both in energy levels and in fine structure splitting.

It should be remarked that processes other than dielectronic recombination have

not been considered in the atomic scattering and transition model of SS1 list, so the results of SS1 are incomplete for states likely to be populated by radiative recombination or collisional excitation and de-excitation. Consequently, the results for free-free and free-bound transitions can be used directly to predict line intensities from low-density astrophysical plasmas such as gaseous nebulae but those between bound states underestimate the line intensities in general and hence can only be used as part of a larger ion population model including all relevant processes. Yes, there is an important exception for the bound-bound transitions that is when the upper level has a doubly-excited core and hence it occurs at the top of the cascade process where radiative contribution is minor. For these top-level transitions the contribution of processes other than dielectronic recombination is negligible and hence the theoretical data can be reliably used.

Therefore, with very few exceptions, only FF, FB, and BB with a doubly-excited upper state were used in the current study. The main exception about the bound-bound transitions with doubly-excited core is the $\lambda 4267 \text{ \AA}$ line which, being one of the strongest observed C II recombination lines and hence is a major line in almost all observational data sets, cannot be avoided altogether. Therefore, recombination coefficients in the form of case B from Davey *et al* [60], which are obtained within a more comprehensive theory that includes radiative contribution as well as dielectronic recombination, were used.

It should be remarked that the use in our analysis of the lines originating at the top of the cascade, which are excited in a very different and much simpler way than lines like $\lambda 4267 \text{ \AA}$ at the bottom of a complex cascade process, makes our analysis more reliable as it relies on a much simpler and better-understood decay process. Our analysis may also provide a way, in some cases at least, for testing and validating the results obtained from the low-lying transitions such as those obtained from line $\lambda 4267$. Hence agreement between electron temperatures obtained

without $\lambda 4267$ with those using $\lambda 4267$, may provide a validation of recombination theory for line $\lambda 4267$ and other low-lying transitions, as obtained previously by other researchers. For example, the possibility of the existence of some unknown mechanism that overpopulates the levels of the upper state of $\lambda 4267$ transition causing the enhancement of the ORL abundance may be ruled out if the results with $\lambda 4267$ are consistent with those obtained without $\lambda 4267$. This is one reason why in section 4.2 we computed electron temperature from least squares minimization once with and once without line $\lambda 4267$ when the selected observational data include this line.

With regard to the observational data, we carried out a fairly thorough research for C II recombination line data in the literature in which over 140 data sets related mainly to planetary nebulae were collected and archived. However, most of these data sets were eliminated for various reasons such as the failure in the reliability tests, the poor quality of the data, and the consistence of only a single line and hence the data cannot be used in a least squares minimization procedure which requires two lines at least. More important is that almost all data sets that comprise only bound-bound transitions with no doubly-excited core upper state have been removed.

On eliminating most of the data sets on the previous grounds, the remaining data sets were subjected to a refinement process in which the flux of all the observational lines in each data set were normalized to the flux of a reference observational line in the set, which is usually chosen as the brightest and most reliable, while the emissivity of all the theoretical lines in the set were normalized to the emissivity of the corresponding theoretical line. The observational flux and theoretical emissivity of the reference line were therefore unity. The ratio of the normalized observed flux to the normalized theoretical emissivity of each line were then plotted on common graphs as a function of temperature on log-linear scales. A sample of these graphs

is presented in Figure 4.5 for the planetary nebula NGC 5315. All lines that did not approach the ratio of the reference line within an arbitrarily-chosen factor of 3 were eliminated. Because the reference line was typically chosen as the brightest, and hence more reliable, any line whose normalized ratio deviates largely from the normalized ratio of this line should be deemed unreliable. The arbitrary factor of 3 was chosen as an appropriate limit considering practical factors that contribute to error in the collection of observational data. The refinement process also involved the utilization of graphs in which the ratio of theoretical emissivity to observational flux of all lines in a certain data set was plotted on a single graph as a function of electron temperature. A sample of these graphs are shown in Figures 4.2 and 4.11.

Some other lines were also eliminated for various reasons related mainly to an established or suspected misidentification of the line or its intensity. For example, the wavelength of the alleged C II line may not match with any known theoretical transition. Also, the absence of a strong line in the observational data associated with the presence of a much weaker line with no obvious reason, such as possible blending with a much stronger neighbor, casts doubt on the identification of the present line. The line may also be eliminated because its intensity ratio relative to another well-established line does not comply with the ratio obtained from theory. Very few lines were also out of the wavelength range of our line list and hence were eliminated due to lack of theoretical emissivity data. Other reasons for elimination include lack of intensity data, blending or close proximity to other non-C II lines.

The selected refined data sets were then subjected to a least squares optimization procedure which is outlined in the following section. It should be remarked that the observed flux used in the least squares procedure is the de-reddened flux obtained by correcting for extinction and other sources of error as stated by the data source and not the raw flux data. Therefore, there should be no ambiguity when we use ‘observed’ flux in the following sections.

4.1.1 Least Squares Minimization

The main method for generalizing and summarizing a set of data is by fitting it to a model that depends on adjustable parameters. A figure-of-merit function that measures the agreement between the data and the model for a particular choice of parameters is then chosen or designed so that small or large values indicate good agreement. The model parameters are then adjusted to achieve a minimum or maximum in the merit function, yielding best fit parameters. Least squares minimization is probably the most popular method in the physical sciences. It is widely used to determine the best set of parameters in a model to fit a set of observational data. The objective of the least squares technique is to minimize the difference between the observed data and the calculated model. The goodness-of-fit index χ^2 is one of the most suggestive and commonly accepted figures of merit. It is widely used as an indicator of the overall fit between a theoretical model and a set of observational data. In general terms, it is given by [145]

$$\chi^2 = \frac{\sum_i w_i (y_i^o - y_i^c)^2}{\eta} \quad (4.1)$$

where y_i^o and y_i^c are the observed and calculated values at step i , w_i is the corresponding weight, and η is the number of degrees of freedom given by $\eta = O - P$ where O and P are the number of observations and fitted parameters in the calculated model, respectively. The summation index i runs over all observed data points.

In our least squares calculations we have a single fitting parameter, which is the electron temperature of the line-emitting regions in the astronomical objects (e.g. NGC 5315 nebula), while the observations are the flux data of the C II recombination lines that we obtained from the literature (e.g. observational data of Peimbert *et al* [10]). The purpose of the least squares procedure is to find the optimal tem-

perature that gives the best fit of the theoretical model to the observational data, and hence identifying the temperature of the line-emitting region in the astronomical object. However, since the collected spectrum is usually integrated over some spatial part of the nebula and along the line of sight through a three-dimensional object, the obtained temperature normally is an average value. In the following we outline the least squares procedure

- The theoretical lines are mapped to their observational counterparts where the resolution of the observational data is considered for this mapping when such data are available, i.e. all theoretical lines within that resolution on both sides of the observational line are added up and mapped to the observational line. This mapping scheme is justified by the fact that the lines within the resolution limits are blended and hence cannot be identified separately by observational means. The resolution of the observational data can be estimated from the graphs of spectra when these graphs are available. Information reported in the data source, as well as other contextual evidence, may also be used to determine the observational resolution.
- All blended C II lines in the observational list are combined by considering them as a single line with a single flux, while C II lines blended with non-C II lines are eliminated.
- To compare the theoretical emissivity to the observational flux, the theoretical emissivity of each line is normalized to the total theoretical emissivity of all the lines involved in the least squares procedure, while the observational flux of that line is normalized to the total observational flux of these lines.
- When using line $\lambda 4267 \text{ \AA}$, the theoretical emissivity is obtained from Davey *et al* [60] in the form of case B effective recombination coefficients, and option ‘4’ of the ‘NormalizationChoice’ of the ‘Emissivity’ code is used, as explained

in Appendix C. The reason for this special treatment is that this important line, which is the most intense line of this ion in the visible part of the spectrum, comes from a BB transition, with no doubly-excited upper state, for which our emissivity model is not very accurate as it considers dielectronic contribution only.

- The normalized theoretical emissivities corresponding to a particular observational flux are added up when multiple mapping occurs, that is when the observational flux is given for a multiplet transition as a whole.
- The χ^2 defined by the following equation

$$\chi^2 = \sum_{i=1}^N \frac{(I_i^{no} - \varepsilon_i^{nt})^2}{\eta \sigma_{I_i^{no}}^2} \quad (4.2)$$

is then computed, where i is an index running over all the N lines involved in the least squares procedure, I_i^{no} and ε_i^{nt} are the normalized observational flux and normalized theoretical emissivity of line i respectively, η is the number of degrees of freedom, and $\sigma_{I_i^{no}}^2$ is the variance of I_i^{no} . This variance is computed from the formulae derived in Appendix B where for the data sets with given observational errors the reported errors were used in conjunction with formula B.6 while for the data sets with no reported error a Poisson distribution was assumed and hence Equation B.12 was used to estimate this variance. In some data sets, the observational error was given for some lines only, and hence the average of the given errors was assigned to the missing ones. In some cases when the reported error was unrealistically small resulting in large χ^2 , the χ^2 curve was scaled to unity at the minimum to obtain a more realistic error estimate. This scaling does not affect the temperature at minimum χ^2 but usually broadens the confidence interval.

- The temperature of the object is then identified from its value at the min-

imum χ^2 , while the confidence interval is identified from the values of the temperature corresponding to the values of $\chi_{min}^2 \pm 1$ on the lower and upper sides using linear interpolation. In some cases, the χ^2 curve was too shallow on one side and hence it resulted in a broad confidence interval on that side.

In the following section we present some astronomical objects that have been the subject of investigation in this study using the least squares minimization method.

4.2 Astronomical Objects

In this section we present a sample of the astronomical objects that have been investigated as part of the current study. The objects are mainly planetary nebulae and the physical parameter of interest is the electron temperature of the line emitting regions of the C II dielectronic recombination and subsequent cascade decay.

A Planetary Nebula (PN) is an expanding cloud of gas and dust ejected from a dying star due to instabilities at the end of its life. The cloud is ionized by the highly energetic radiation from the stellar core (progenitor). The spectra of planetary nebulae, which originate from various physical processes such as collisional excitation and recombination, are very rich and span large parts of the electromagnetic spectrum with manifestation in both emission and absorption. These spectra involve many atomic and ionic species across the periodic table especially the light ones such as helium, carbon, and nitrogen. The nebular spectra also contain transition lines from some compound molecular species such as CO and CN. The normal temperature range in PNe is 10^3 - 2×10^4 K with a typical value of 10^4 K, while the normal electron density range is 10^9 - 10^{11} m^{-3} with a typical value of 10^{10} m^{-3} . Figure 4.1 shows two prominent examples of planetary nebulae. The PNe are essential for astronomical and astrophysical studies because they are relatively

abundant in the Milky Way galaxy and hence provide imperative case studies. In other galaxies, they may be used to acquire useful information about the chemical composition and the thermodynamic conditions. For cosmic processes, the PNe are very important objects because they participate in the process of heavy element enrichment of the astronomical objects and interstellar medium [3, 67, 146–148].

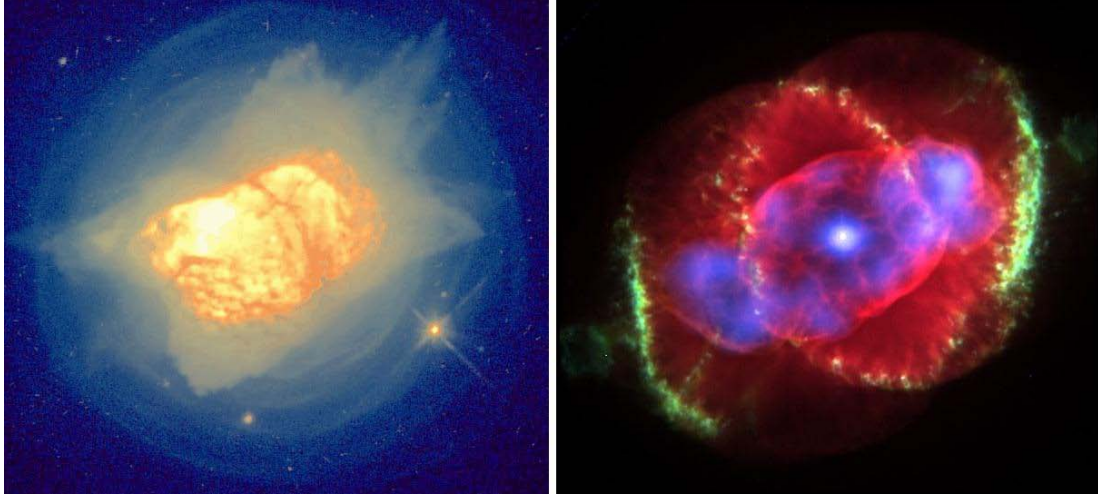


Figure 4.1: Two prominent planetary nebulae, NGC 7027 (left) and Cat's eye (right) [from NASA].

4.2.1 NGC 7009

NGC 7009, also called Saturn nebula, is a bright planetary nebula in the Aquarius constellation. This nebula has a double-ringed complex spatial structure with a rich recombination spectrum related to some elements like oxygen; therefore it is expected to be an ideal environment for recombination processes in general [1, 63, 69, 149]. The observational data of this object were obtained from Fang and Liu [1] who collected very deep CCD spectrum of this object in a wavelength range of 3040-11000Å. Their observational line list comprises about 1200 emission lines where approximately 80% of these lines are identified as originating from permitted transitions. On surveying this list for C II recombination lines we obtained about 64 lines attributed to C II transitions. Following the refinement process, outlined

in § 4.1, this list was reduced to just 9 lines. These lines are presented in Table 4.1. In this table, and other similar tables, λ_{lab} is the laboratory wavelength, and I is the flux (absolute or normalized to H_β), while the other columns stand for the lower and upper terms, the lower and upper statistical weights, and transition type (free-free, free-bound and bound-bound) respectively. For the multiplet transitions, the wavelength is given for the first line while the statistical weights represent the sum of the individual weights. The prime in the term designation indicates an excited core, i.e. $1s^22s2p(^3P^o)$. In Figure 4.2 the ratio of theoretical emissivity to observational flux is plotted against electron temperature on a linear-linear graph for the selected 9 lines. This graph, and other similar graphs for the other objects, were utilized to select the suitable lines.

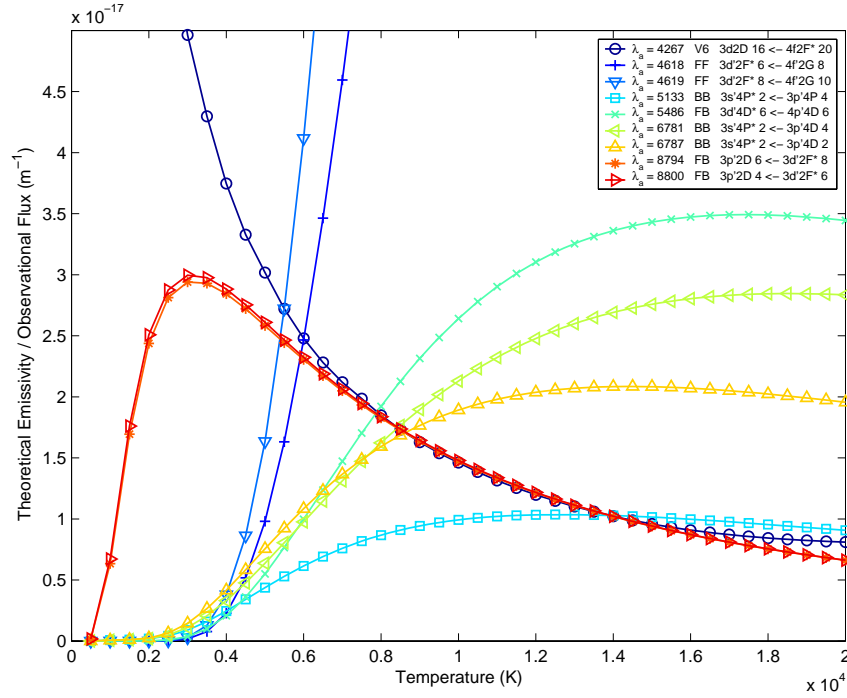


Figure 4.2: The ratio of theoretical emissivity to observational flux as a function of temperature for the selected C II lines of NGC 7009 spectra of Fang and Liu [1].

The observational data were normalized to the total observational flux while the theoretical to the total theoretical emissivity, and χ^2 was obtained and plotted against temperature over the range $T = 500 - 10000$ K in steps of 100 K. This

Table 4.1: The observational C II transition lines of Fang and Liu [1] that were used in the least squares minimization procedure to find the electron temperature of the line emitting region in the planetary nebula NGC 7009. The given flux is the normalized to the H_β flux.

λ_{lab}	I	Lower	Upper	g_l	g_u	Type
4267.00	0.8795	3d $^2D^e$	4f $^2F^o$	16	20	BB
4618.40	0.0021	3d' $^2F^o$	4f' $^2G^e$	6	8	FF
4619.23	0.0021	3d' $^2F^o$	4f' $^2G^e$	8	10	FF
5132.94	0.0088	3s' $^4P^o$	3p' $^4P^e$	2	4	BB
5485.90	0.0004	3d' $^4D^o$	4p' $^4D^e$	6	6	FB
6780.61	0.0070	3s' $^4P^o$	3p' $^4D^e$	2	4	BB
6787.22	0.0052	3s' $^4P^o$	3p' $^4D^e$	2	2	BB
8793.80	0.0320	3p' $^2D^e$	3d' $^2F^o$	6	8	FB
8799.90	0.0224	3p' $^2D^e$	3d' $^2F^o$	4	6	FB

process was repeated: once with inclusion of line $\lambda 4267$ and another with exclusion of this line. The reason for this was discussed in § 4.1. The χ^2 graphs for these two cases are given in Figures 4.3 and 4.4. As seen, the first indicates a temperature of about 5800 K while the second a temperature of about 5500 K, which are in good agreement.

In Table 4.2 we listed the electron temperature from different types of transitions related to various ions as obtained from the cited literature following a non-thorough research. As can be seen, the values that we obtained from our least squares method is in a broad agreement with the temperature obtained from several recombination lines. The lower electron temperature from optical recombination lines (ORL) compared to the values obtained from collisionally-excited lines (CEL) is consistent with the trend of the previous findings related to the long-standing problem of discrepancy between the abundance and temperature results of ORL and CEL (higher ORL abundance and lower electron temperature as compared to the CEL abundance and temperature), as outlined in § 1.3. In this table, and other similar ones, some types of transitions (e.g. C II) have been assigned more than one

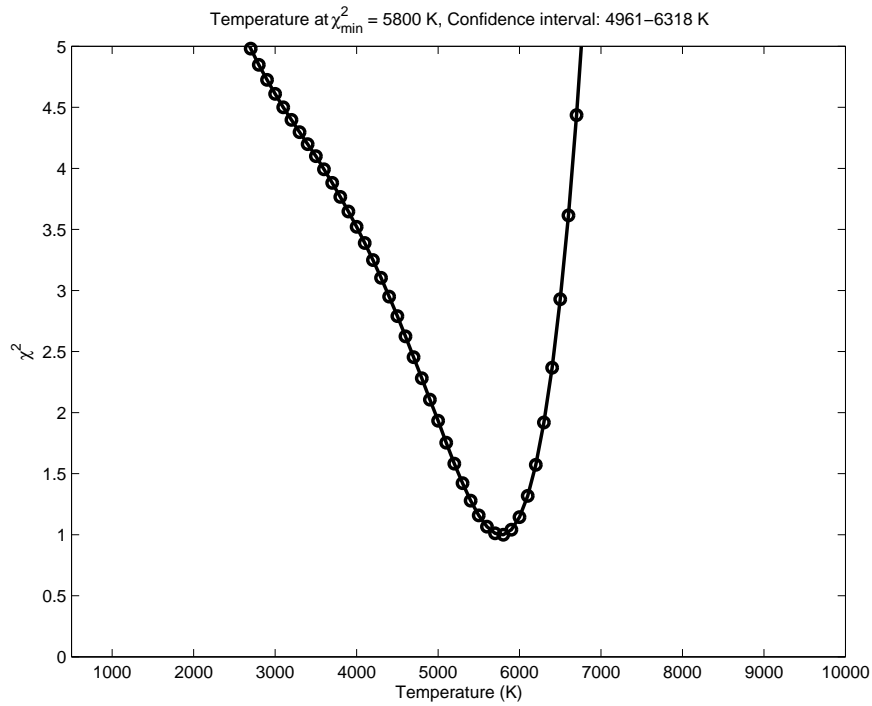


Figure 4.3: Temperature dependence of χ^2 for NGC 7009 with the inclusion of line $\lambda 4267$. The temperature at χ^2_{min} and the confidence interval are shown.

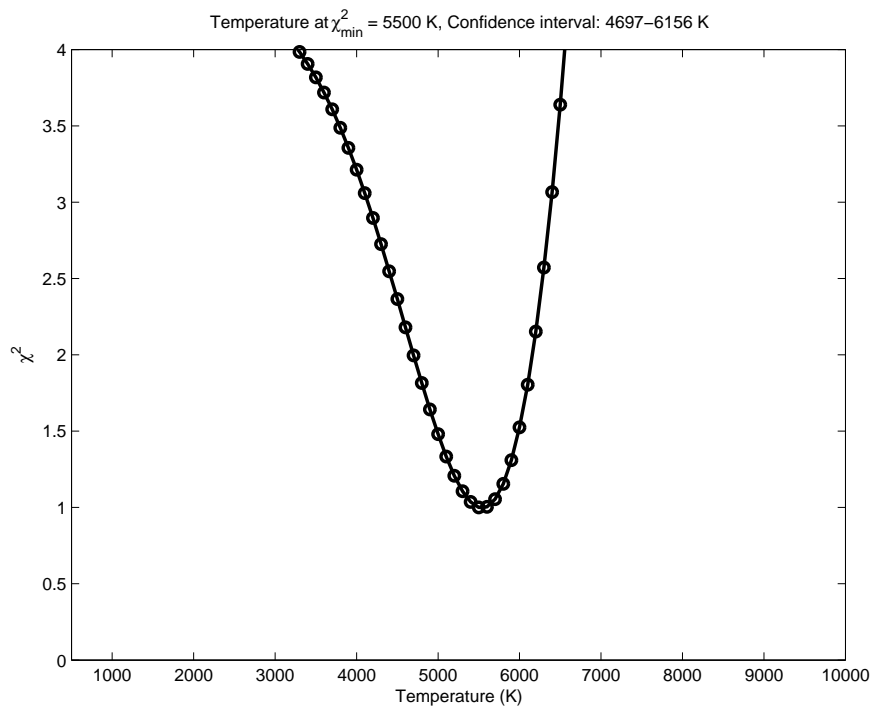


Figure 4.4: Temperature dependence of χ^2 for NGC 7009 with the exclusion of line $\lambda 4267$. The temperature at χ^2_{min} and the confidence interval are shown.

temperature value in the same cited reference; the reason normally is that more than one value has been obtained for that transition type using different spectral lines. These tables may also contain non-first hand data, as the purpose is to give a general idea about the values in the literature not to meticulously document the results obtained from previous works. There may also be some repetitive values as they are obtained from the same first hand source but reported in different literatures. It should be remarked that no error estimate is given in these tables due to the limited column space; the cited data sources should be consulted to obtain this information. Another remark is that we followed the apparent identification and labeling of the authors without meticulous verification of the lines and the type of transition they belong to. Since some authors use relaxed notation for ORL and CEL lines there may be some cases of inaccurate labeling of these lines. For more reliable verification our data sources, as cited in these tables, should be consulted to establish the origin of these lines.

Table 4.2: The electron temperature in Kelvin of NGC 7009 from different atoms, ions and transitions as obtained from the cited literature, where BJ stands for Balmer Jump and PJ for Paschen Jump. CW refers to the current work. For reference [9] we followed the apparent labeling of the authors although the temperatures may have been derived from CEL lines.

Source	[9]	[150]	[57]	[149]	[61]	[151]	[152]	[153]	[90]	CW
H I(BJ)					8150	7200	7200	7200		
H I(PJ)						5800				
He I					5380		5040	8000 6800 5040		
C II										5800 5500
C III]				8160 8350						
N II	10800									
[N II]		11040								
O II					1600					
O III	9600 8900									
O III]				9570 8730 10340 9870						
[O III]		9910		10380 9420 9740 9930	9980	9980 8350	9980	10000		
Mean			7419						10340	

4.2.2 NGC 5315

NGC 5315 is a young dense planetary nebula in the southern constellation Circinus located at a distance of about 2.6 kpc with an interesting complex flower shape appearance [10, 154]. The observational data of this object were obtained from Peimbert *et al* [10]. On inspecting this data source for C II recombination lines we obtained about 25 lines attributed to C II transitions. Following the refinement process, outlined in § 4.1, this list was reduced to just 4 lines. These lines are presented in Table 4.3. Figure 4.5 displays the ratio of the normalized observed flux to the normalized theoretical emissivity versus electron temperature for the selected 4 lines of NGC 5315 data. This graph, with similar graphs for the other objects were used in the refinement process to include and exclude lines from the original list into the final one, as explained in § 4.1.

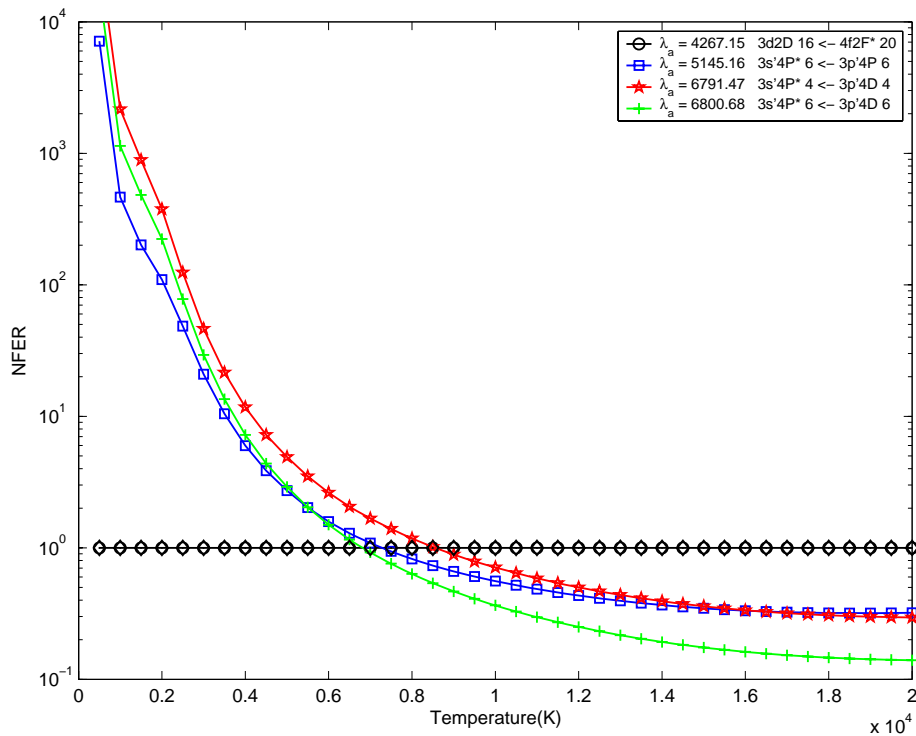


Figure 4.5: Ratio of normalized observed flux to normalized theoretical emissivity (NFER) versus temperature on log-linear scales for the planetary nebula NGC 5315.

Table 4.3: The observational C II transition lines of Peimbert *et al* [10] that were used in the least squares minimization procedure to find the electron temperature of the line emitting region in the planetary nebula NGC 5315. The given flux is the normalized to the H_β flux.

λ_{lab}	I	Lower	Upper	g_l	g_u	Type
4267.00	0.6559	3d $^2D^e$	4f $^2F^o$	16	20	BB
5145.16	0.0039	3s' $^4P^o$	3p' $^4P^e$	6	6	BB
6791.47	0.0068	3s' $^4P^o$	3p' $^4D^e$	4	4	BB
6800.68	0.0028	3s' $^4P^o$	3p' $^4D^e$	6	6	BB

The data were normalized to the total flux and emissivity, as outlined earlier, and χ^2 was computed and plotted against temperature over the range $T = 500 - 20000$ K in steps of 100 K. This process was performed with and without line $\lambda 4267$, as for NGC 7009. The χ^2 graphs for these two cases are given in Figures 4.6 and 4.7. As seen, the first minimizes at $T \simeq 7400$ K while the second at $T \simeq 6500$ K. The shape of these curves may indicate that the first value is more reliable. Table 4.4 presents some values of the electron temperature of NGC 5315 as reported in the cited literature. Our value of 7400 K compares very well with some of these values. Again, the temperature is lower than that derived from the collisionally-excited lines.

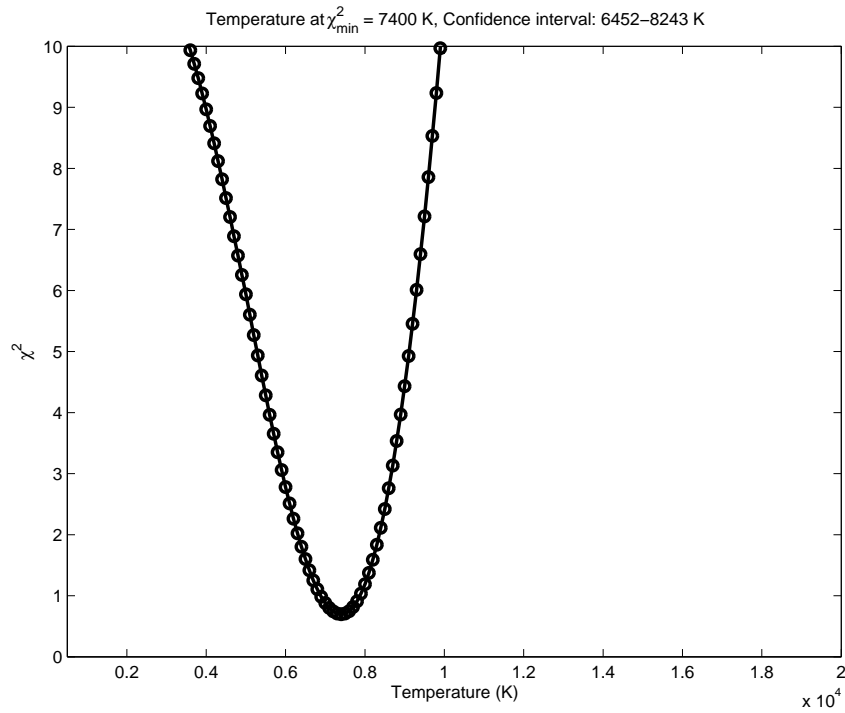


Figure 4.6: Temperature dependence of χ^2 for NGC 5315 with the inclusion of line $\lambda 4267$. The temperature at χ^2_{min} and the confidence interval are shown.

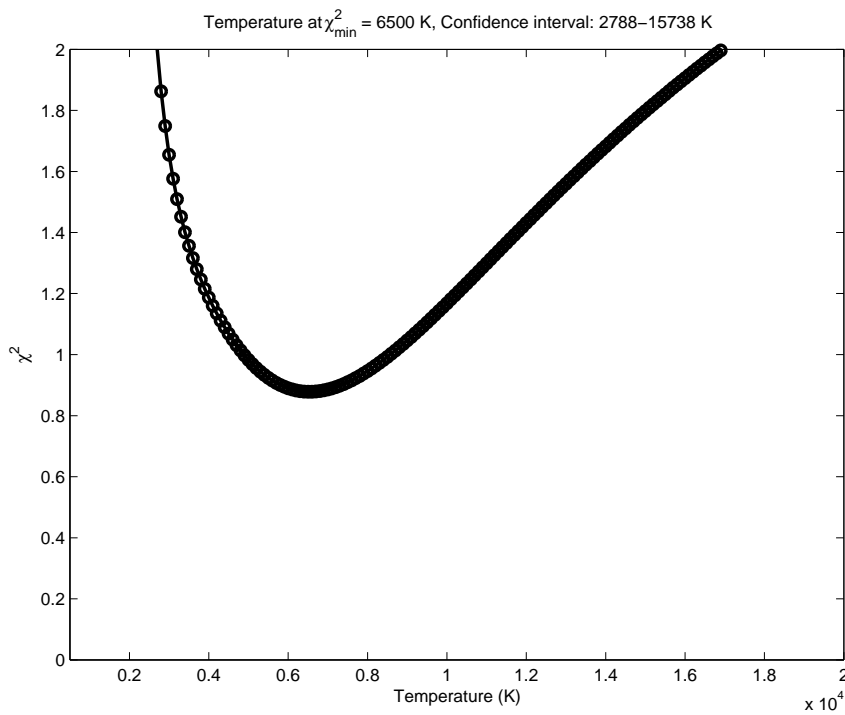


Figure 4.7: Temperature dependence of χ^2 for NGC 5315 with the exclusion of line $\lambda 4267$. The temperature at χ^2_{min} and the confidence interval are shown.

Table 4.4: The electron temperature in Kelvin of NGC 5315 from different atoms, ions and transitions as obtained from the cited literature, where BJ stands for Balmer Jump. CW refers to the current work.

Source	[150]	[57]	[149]	[88]	[89]	[10]	CW
H I(BJ)				8600	8600		
H II						7500	
He I					10000		
C II							7400 6500
N II						9600	
[N II]	9090			10800			
O I						7730	
O II				8100	5750 4350		
O III						8850	
O III]			10040				
[O III]	8150		10330	9000 18500 7800	9000		
Ne III						10700	
S II						9000	
S III						9150	
[S II]				11400			
Cl III						10500	
Cl IV						11200	
Ar III						8300	
Mean		7873					

4.2.3 NGC 7027

NGC 7027 is a compact, bright, young, high excitation planetary nebula with one of the hottest central stars known for a PN. Among the observed planetary nebulae, it has one of the richest lines emission which spans most parts of the electromagnetic spectrum and has been a challenge for observers as well as theorists. NGC 7027 is located about 0.9 kpc from the sun in the direction of the constellation Cygnus in the Milky Way. There is evidence on the existence of substantial quantities of heavy elements dust alongside the neutral and ionized nebular gas. Thanks to its luminosity and compactness, it can be easily observed despite the considerable extinction caused by interior and interstellar dust. It has been a reference object and the subject of several spectral surveys, and probably it is the best studied PN. There are several indications that the progenitor of NGC 7027 is a carbon-rich star [3, 67, 155].

Two observational data sets related to NGC 7027 were investigated: one obtained from Baluteau *et al* [2], and the other obtained from Zhang *et al* [3].

4.2.3.1 Baluteau *et al*

On surveying Baluteau *et al* [2] for C II recombination lines we obtained about 30 lines attributed to C II transitions. Following the refinement process, outlined in § 4.1, this list was reduced to just 8 lines. These lines are presented in Table 4.5.

Standard normalization process to the total flux and emissivity was carried out, and a χ^2 plot as a function of temperature over the range $T = 500 - 20000$ K in steps of 100 K was obtained. As seen in Figure 4.8, the χ^2_{min} occurs at a temperature of about 11100 K, in good agreement with values obtained by other researchers using different methods and various transitions from different atoms and ions; a sample of which is presented in Table 4.6. There are other estimates for

Table 4.5: The observational C II transition lines of Baluteau *et al* [2] that were used in the least squares minimization procedure to find the electron temperature of the line emitting region in the planetary nebula NGC 7027. The given flux is the normalized to the H_β flux.

λ_{lab}	I	Lower	Upper	g_l	g_u	Type
6779.93	11.8	$3s' \ ^4P^o$	$3p' \ ^4D^e$	4	6	BB
6783.91	2.1	$3s' \ ^4P^o$	$3p' \ ^4D^e$	6	8	BB
6787.22	3.7	$3s' \ ^4P^o$	$3p' \ ^4D^e$	2	2	BB
6791.47	4.9	$3s' \ ^4P^o$	$3p' \ ^4D^e$	4	4	BB
6798.10	0.7	$3s' \ ^4P^o$	$3p' \ ^4D^e$	4	2	BB
6812.28	0.5	$3s' \ ^4P^o$	$3p' \ ^4D^e$	6	4	BB
7112.48	4.7	$3p' \ ^4D^e$	$3d' \ ^4F^o$	6	10	BB
8793.80	11.8	$3p' \ ^2D^e$	$3d' \ ^2F^o$	6	8	FB

the electron temperature of the line emitting regions of NGC 7027 deduced from different methods, and they generally represent average values. For example, van Hoof *et al* [156] reported average electron temperatures in various line emitting regions of NGC 7027 obtained from a number of ions using their photoionization model; these temperatures range between $T = 10450 - 17990$ K with an average value of about 14100 K. This is very close to the value derived by Aller and Keyes [67] and Zhang *et al* [3] of about 14000 K.

4.2.3.2 Zhang *et al*

The observational data of this object were obtained from Zhang *et al* [3]. On surveying the observational list for C II recombination lines we obtained about 67 lines attributed to C II transitions. Following the refinement process, outlined in § 4.1, this list was reduced to just 20 lines. These lines are presented in Table 4.7.

The data were normalized to the total flux and emissivity with and without line $\lambda 4267$, as outlined earlier, and χ^2 was calculated and plotted against temperature over the range $T = 500 - 30000$ K in steps of 100 K. As seen in Figures 4.9

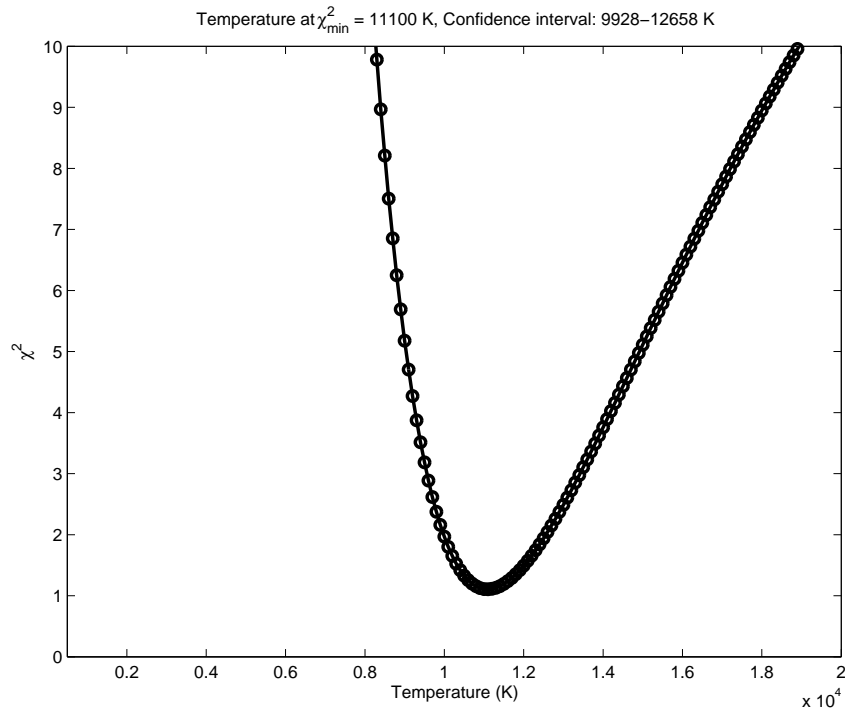


Figure 4.8: Temperature dependence of χ^2 for NGC 7027 of Baluteau *et al* [2]. The temperature at χ^2_{\min} and the confidence interval are shown.

and 4.10, the first minimizes at $T \simeq 12500$ K and the second at $T \simeq 12000$ K, which reasonably agree with some of the values reported in the literature as seen in Table 4.6. However, the confidence interval in both cases poorly constrains the temperature estimate limits especially on the upper end. It should be remarked that since no observational error estimate was given for these lines, an error estimate based on Poisson statistical distribution was used in the least squares procedure, as given by Equation B.12 in Appendix B.

Table 4.6: The electron temperature in Kelvin for NGC 7027 derived from different atoms, ions and transitions as obtained from the cited literature, where BJ stands for Balmer Jump and PJ for Paschen Jump. CW refers to the current work where the first value was obtained from Baluteau *et al* data while the other two are obtained from Zhang *et al* data.

Source	[150]	[57]	[149]	[61]	[151]	[98]	[153]	[100]	CW
H I(BJ)				12800	12000		12000	8000	
H I(PJ)					8000			8000	
He I				9260			10000 8200 10360		
C II									11100 12500 12000
C III]			12290						
[N I]								15000	
[N II]	12300								
O II				7100					
[O I]								11300	
O III]			13300						
[O III]	9260		14850	12600		14130	13000		
[Cl IV]								13700	
[Ar III]								12900	
[Ar IV]						13600			
Mean		11505 11124							

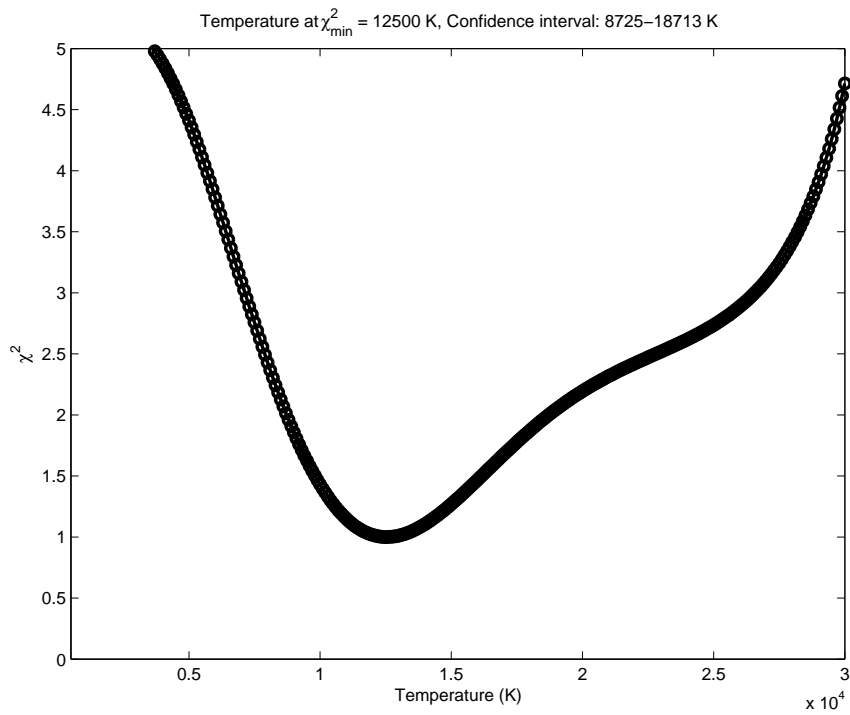


Figure 4.9: Temperature dependence of χ^2 for NGC 7027 of Zhang *et al* [3] with the inclusion of line $\lambda 4267$. The temperature at χ^2_{\min} and the confidence interval are shown.

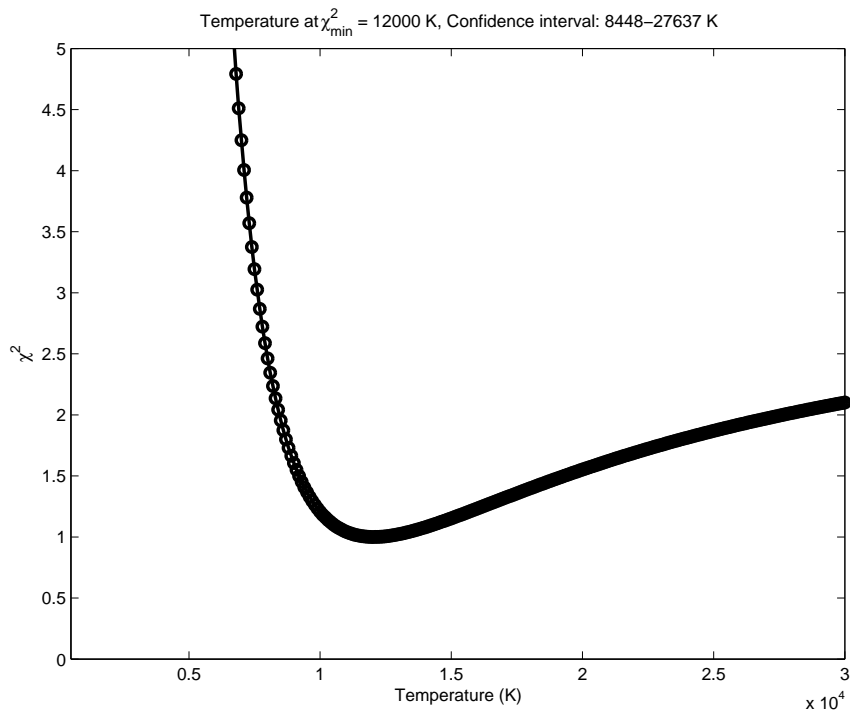


Figure 4.10: Temperature dependence of χ^2 for NGC 7027 of Zhang *et al* [3] with the exclusion of line $\lambda 4267$. The temperature at χ^2_{\min} and the confidence interval are shown.

Table 4.7: The observational C II transition lines of Zhang *et al* [3] that were used in the least squares minimization procedure to find the electron temperature of the line emitting region in the planetary nebula NGC 7027. The given flux is the normalized to the H_{β} flux.

λ_{lab}	I	Lower	Upper	g_l	g_u	Type
3588.92	0.018	$3p' \ ^4D^e$	$4s' \ ^4P^o$	2	2	FB
3590.86	0.059	$3p' \ ^4D^e$	$4s' \ ^4P^o$	10	6	FB
3876.66	0.026	$3d' \ ^4F^o$	$4f' \ ^4G^e$	6	8	FB
4267.00	0.575	$3d \ ^2D^e$	$4f \ ^2F^o$	16	20	BB
4323.11	0.004	$3p' \ ^4P^e$	$4s' \ ^4P^o$	2	2	FB
4372.35	0.026	$3d' \ ^4P^o$	$4f' \ ^4D^e$	4	4	FF
4376.56	0.031	$3d' \ ^4P^o$	$4f' \ ^4D^e$	4	6	FF
4411.16	0.019	$3d' \ ^2D^o$	$4f' \ ^2F^e$	4	6	FF
4618.40	0.009	$3d' \ ^2F^o$	$4f' \ ^2G^e$	6	8	FF
5133.28	0.013	$3s' \ ^4P^o$	$3p' \ ^4P^e$	4	6	BB
5143.38	0.013	$3s' \ ^4P^o$	$3p' \ ^4P^e$	4	2	BB
5151.09	0.009	$3s' \ ^4P^o$	$3p' \ ^4P^e$	6	4	BB
5259.06	0.009	$3d' \ ^4F^o$	$4p' \ ^4D^e$	8	6	FB
6779.93	0.034	$3s' \ ^4P^o$	$3p' \ ^4D^e$	4	6	BB
6783.90	0.004	$3s' \ ^4P^o$	$3p' \ ^4D^e$	6	8	BB
6787.22	0.008	$3s' \ ^4P^o$	$3p' \ ^4D^e$	2	2	BB
6791.47	0.012	$3s' \ ^4P^o$	$3p' \ ^4D^e$	4	4	BB
6800.68	0.009	$3s' \ ^4P^o$	$3p' \ ^4D^e$	6	6	BB
6812.29	0.001	$3s' \ ^4P^o$	$3p' \ ^4D^e$	6	4	BB
8793.80	0.015	$3p' \ ^2D^e$	$3d' \ ^2F^o$	6	8	FB

4.2.4 IC 418

IC 418, or Spirograph Nebula, is a bright, young, C-enhanced, low-excitation, highly symmetric, elliptically-shaped planetary nebula with apparent ring structure located at a distance of about 0.6 kpc in the constellation Lepus [52, 54, 64, 140, 157–161]. Due to its brightness and exceptional features, the nebula was, and is still, the subject of many theoretical and observational studies in the last decades. The observational data about IC 418 which we used in the current study come from Sharpee *et al* [4]. On surveying this source of data for C II recombination lines we obtained about 93 lines attributed to C II transitions. Following the refinement process, outlined in § 4.1, this list was reduced to just 23 lines. These lines are presented in Table 4.8. In Figure 4.11 the ratio of theoretical emissivity to observational flux is plotted against electron temperature on a linear-linear graph for the selected 23 lines. This graph, and other similar graphs for the other objects, were used to select the suitable lines.

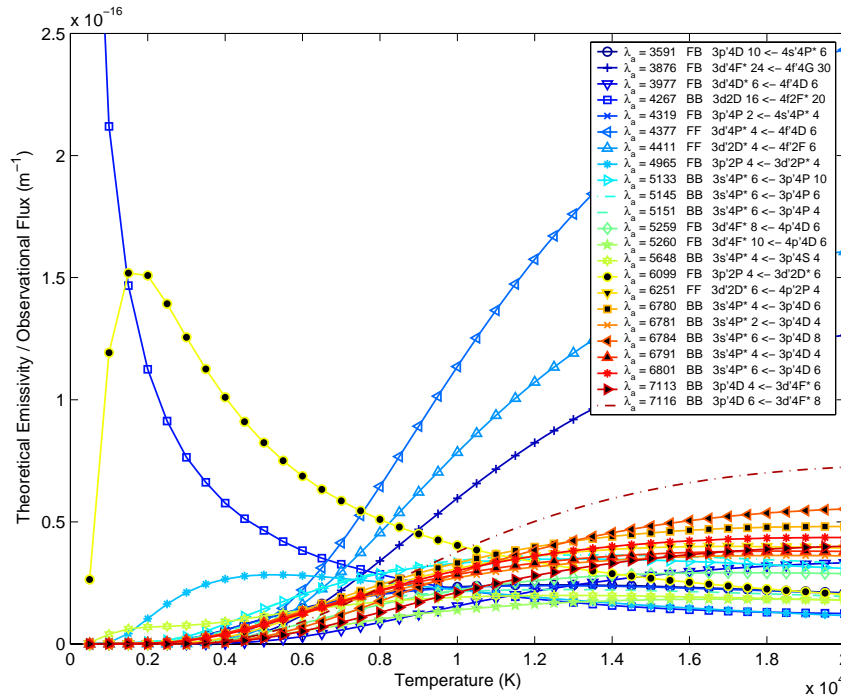


Figure 4.11: The ratio of theoretical emissivity to observational flux as a function of temperature for the selected C II lines of IC 418 spectra of Sharpee *et al* [4].

Table 4.8: The observational C II transition lines of Sharpee *et al* [4] that were used in the least squares minimization procedure to find the electron temperature of the line emitting region in the planetary nebula IC 418. The given flux is the normalized to the H_{β} flux.

λ_{lab}	I	Lower	Upper	g_l	g_u	Type
3590.757	0.0252	3p' $^4D^e$	4s' $^4P^o$	10	6	FB
3876.392	0.0069	3d' $^4F^o$	4f' $^4G^e$	24	30	FB
3977.250	0.0026	3d' $^4D^o$	4f' $^4D^e$	6	6	FB
4267.001	0.5712	3d $^2D^e$	4f $^2F^o$	16	20	BB
4318.606	0.0086	3p' $^4P^e$	4s' $^4P^o$	2	4	FB
4376.582	0.0016	3d' $^4P^o$	4f' $^4D^e$	4	6	FF
4411.152	0.0016	3d' $^2D^o$	4f' $^2F^e$	4	6	FF
4964.736	0.0211	3p' $^2P^e$	3d' $^2P^o$	4	4	FB
5132.947	0.0044	3s' $^4P^o$	3p' $^4P^e$	6	10	BB
5145.165	0.0040	3s' $^4P^o$	3p' $^4P^e$	6	6	BB
5151.085	0.0046	3s' $^4P^o$	3p' $^4P^e$	6	4	BB
5259.055	0.0031	3d' $^4F^o$	4p' $^4D^e$	8	6	FB
5259.664	0.0032	3d' $^4F^o$	4p' $^4D^e$	10	6	FB
5648.070	0.0014	3s' $^4P^o$	3p' $^4S^e$	4	4	BB
6098.510	0.0011	3p' $^2P^e$	3d' $^2D^o$	4	6	FB
6250.760	0.0015	3d' $^2D^o$	4p' $^2P^e$	6	4	FF
6779.940	0.0109	3s' $^4P^o$	3p' $^4D^e$	4	6	BB
6780.600	0.0055	3s' $^4P^o$	3p' $^4D^e$	2	4	BB
6783.910	0.0022	3s' $^4P^o$	3p' $^4D^e$	6	8	BB
6791.470	0.0066	3s' $^4P^o$	3p' $^4D^e$	4	4	BB
6800.680	0.0050	3s' $^4P^o$	3p' $^4D^e$	6	6	BB
7113.040	0.0052	3p' $^4D^e$	3d' $^4F^o$	4	6	BB
7115.630	0.0043	3p' $^4D^e$	3d' $^4F^o$	6	8	BB

The data, with and without $\lambda 4267$, were normalized to the total flux and emissivity and χ^2 was obtained and plotted against temperature over the range $T = 500 - 20000$ K in steps of 100 K. As seen in Figures 4.12 and 4.13, the first minimizes at $T \simeq 8700$ K while the second at $T \simeq 7700$ K. The electron temperature data reported in the literature, a sample of which is presented in Table 4.9, suffer from erratic scattering and hence no average broad value can be safely concluded. One possibility for this scattering, in addition to the differences arising from using different methods as well as different atoms, ions and transitions, is the

type of spectral data and the range to which they belong as they originate from different parts in the nebula. For example, using the visible part originating in one part of the nebula should produce a temperature different to that obtained from radio frequency or far-infrared originating from another part. It should be remarked that Sharpee *et al* [4] give the signal-to-noise (S/N) ratio instead of giving observational error; therefore the error (i.e. standard deviation) on flux was computed as the product of the line flux times the reciprocal of S/N ratio.

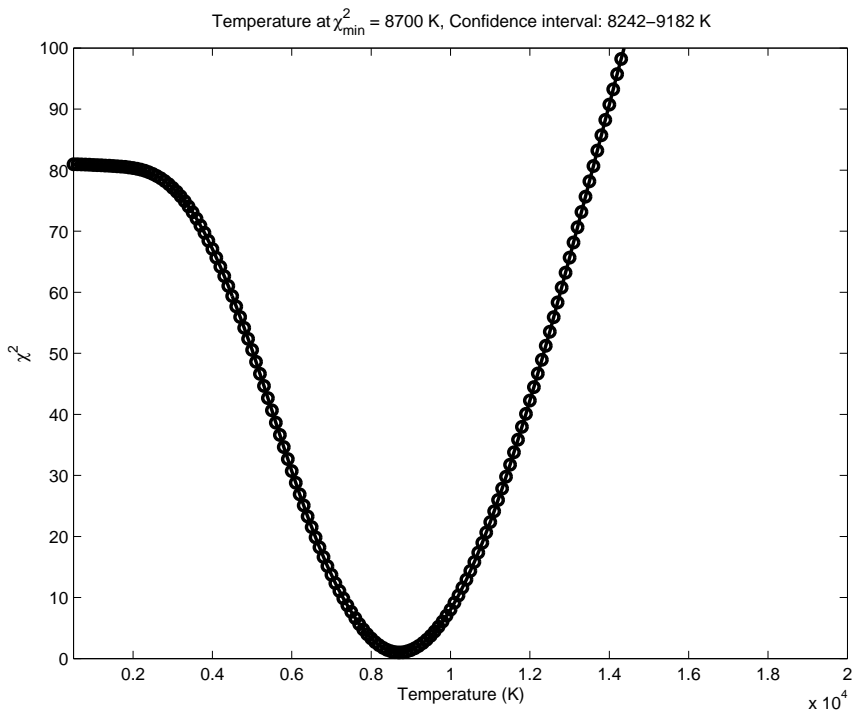


Figure 4.12: Temperature dependence of χ^2 for IC 418 with the inclusion of line $\lambda 4267$. The temperature at χ^2_{\min} and the confidence interval are shown.

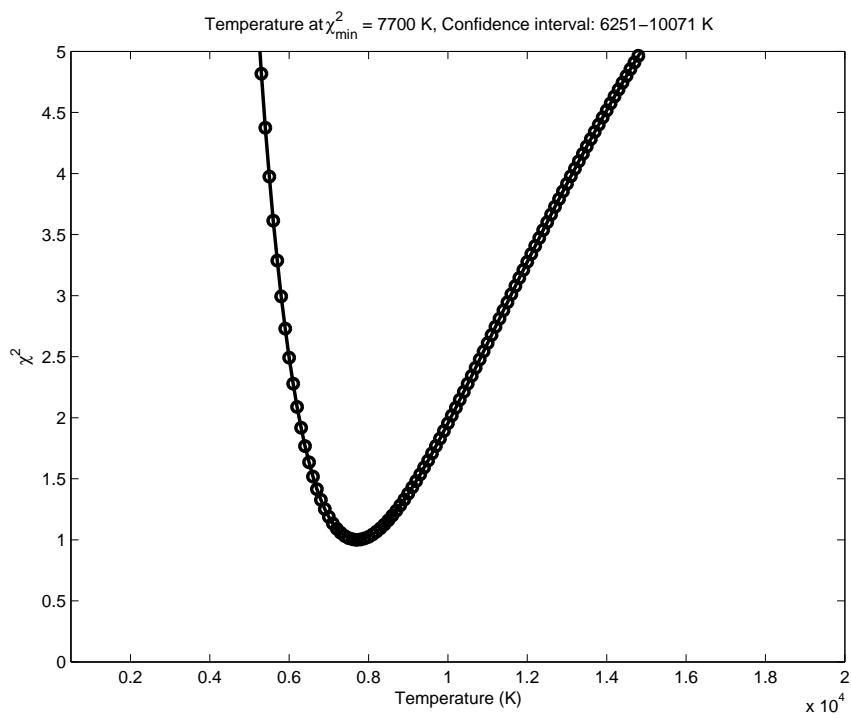


Figure 4.13: Temperature dependence of χ^2 for IC 418 with the exclusion of line $\lambda 4267$. The temperature at χ^2_{\min} and the confidence interval are shown.

Table 4.9: The electron temperature in Kelvin of IC 418 from different atoms, ions and transitions as obtained from the cited literature, where BD stands for Balmer Discontinuity and RF for Radio Frequency. CW refers to the current work.

Source	[157]	[162]	[163]	[164]	[165]	[52]	[140]	[160]	[150]	[161]	[64]	CW
H I(BD)	>15000											
He I								9800 9800				
C II								9600				8700 7700
C III								9800				
C III]							8700					
N I								8500				
N II								9600				
[N II]						8300 8200	8200		8510	9400		
[N III]										8500		
O I								8500				
O II								9600				
O III								9800				
[O II]							8200					
[O III]	7000		11200			9100 10300	9800 9500 9600		9360	9100 9400		
Ne II								8500				
Ne III								9800				
[Ne III]										8000		
Mg II								8500				
S II								8500 8500				
S III								9800				
[S III]										9500 9200		
Cl II								8500				
Cl III								9800				
Ar II								8500				
Ar III								9800 9800				
[Ar III]										9100		
RF				12500 23000 7100	6600							
Mean		20000									10000	

4.2.5 NGC 2867

NGC 2867, or Caldwell 90, is a compact planetary nebula with comparatively small size and fairly strong surface brightness located at a distance of about 0.5 kpc in the southern constellation Carina. It has a rather warm (~ 145000 K) Wolf-Rayet central star of WC6 or early WO type with evidence of being relatively rich in nitrogen. The rich spectrum of this nebula and its star has been the subject of investigation for many studies in the last few decades with some emphasis on the optical and ultraviolet transitions [11, 166–168].

The observational data of this object were obtained from García-Rojas *et al* [11] where two knots have been studied: one labeled NGC 2867-1 and the other NGC 2867-2. On surveying this data source for C II recombination lines we obtained about 8 lines attributed to C II transitions. Following the refinement process, outlined in § 4.1, this list was reduced to just 2 lines. These lines are presented in Table 4.10 where the first value of I belongs to the first knot while the second (inside the brackets) belongs to the second.

Table 4.10: The observational C II transition lines of García-Rojas *et al* [11] that were used in the least squares minimization procedure to find the electron temperature of the line emitting region in the planetary nebula NGC 2867. The given flux is the normalized to the H_β flux. The first I value belongs to knot 1 and the second to knot 2.

λ_{lab}	I	Lower	Upper	g_l	g_u	Type
4267.15	0.814(1.246)	3d $^2D^e$	4f $^2F^o$	16	20	BB
6779.93	0.045(0.079)	3s' $^4P^o$	3p' $^4D^e$	4	6	BB

These data sets were normalized to the total flux and emissivity and χ^2 was obtained and plotted against temperature in the range $T = 500 - 30000$ K with a step size of 100 K. These plots are presented in Figures 4.14 and 4.15. As seen, NGC 2867-1 graph indicates a temperature of about 14300 K while NGC 2867-2

graph a temperature of about 16000 K. The difference in temperature value may be caused by the difference in the physical conditions of the two knots. Table 4.11 presents electron temperatures derived in previous works from transitions of different species. As seen, our values are significantly higher than most of the values reported in the literature. However, this may be explained by the complex structure of this nebula and the possibility of different lines being originating from different regions with very different physical conditions.

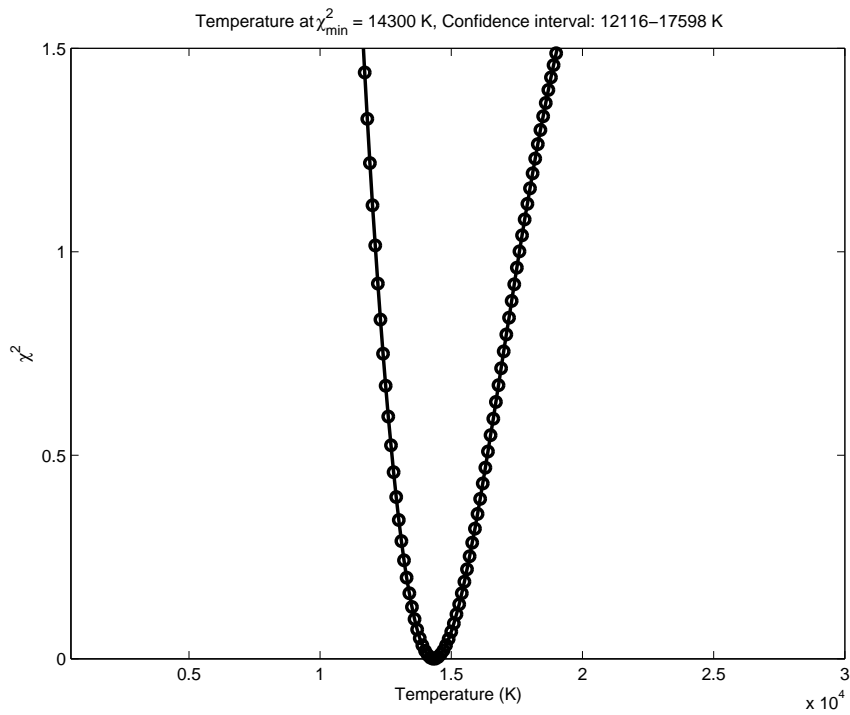


Figure 4.14: Temperature dependence of χ^2 for NGC 2867-1. The temperature at χ^2_{\min} and the confidence interval are shown.

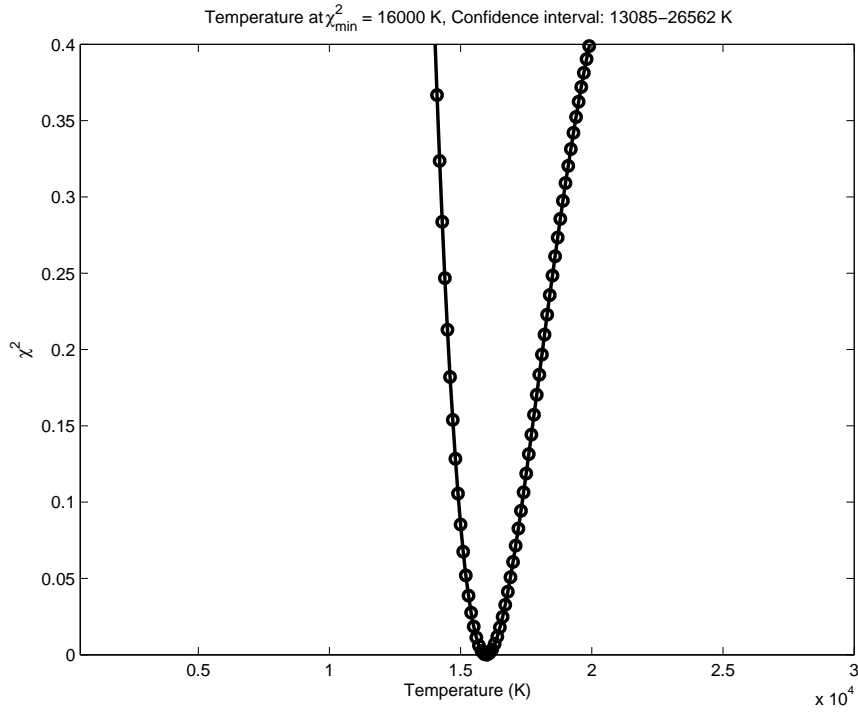


Figure 4.15: Temperature dependence of χ^2 for NGC 2867-2. The temperature at χ^2_{\min} and the confidence interval are shown.

Table 4.11: The electron temperature in Kelvin of NGC 2867 from different species and transitions as obtained from the cited literature, where BD stands for Balmer Decrement and K1 and K2 for knot 1 and knot 2. CW refers to the current work where the first value is related to knot 1 and the second to knot 2.

Source	[166]	[150]	[57]	[149]	[11] K1	[11] K2	CW
H I(BD)					8950	8950	
He I					10900	10250	
C II							14300 16000
C III]				10750			
[N II]	8800	9000			11750	11750	
O III]				10580			
[O III]	11100	10520		11340	11850	11600	
[S II]					8450	8250	
[Ar III]					10800	11350	
[Ar IV]					15400	>19870	
[N II]+[O III]					11850	11600	
Mean			10592				

4.2.6 DQ Herculis 1934

This is a peculiar old classical galactic nova originating from an accreting cataclysmic variable binary system which apparently consists of a white and a red dwarfs. It is located in the Hercules constellation at an estimated distance of about 0.2-0.4 kpc. DQ Her is characterized by its 71 s periodically pulsating spectrum which occurs mainly in the visible, ultraviolet and X-ray regions. The strange features of this nova include a very low electron temperature and an enhanced CNO abundance. The former seems to correlate to the latter since low electron temperatures usually characterize metal rich nebulae. Thanks to its reasonable brightness, pulsation, and peculiar properties, it is one of the most observed and best studied novae [12, 68, 169–175].

The observational data of DQ Her which we used in the current study were obtained from Ferland *et al* [12]. On surveying the data source for C II recombination lines we obtained 2 lines attributed to C II transitions. These lines are presented in Table 4.12. The observational and theoretical data were then normalized to the total flux and emissivity respectively and χ^2 was obtained and plotted against temperature in the range $T = 500 - 5000$ K with a step size of 100 K. The χ^2 plot is shown in Figure 4.16. As seen in this figure the deduced electron temperature is about 1600 K.

It should be remarked that the use of $\lambda 1335$ Å line is a second exception (the first is $\lambda 4267$ Å) to our rule of using the BB transitions only if the upper state has a doubly-excited core. The justification of this exception is that the upper state of the $\lambda 1335$ transition is $1s^2 2s 2p^2$ which is connected to the $C^{2+} 1s^2 2s^2$ continuum and $1s^2 2s^2 nl$ Rydberg states by two-electron radiative processes which are usually very weak. Another remark is that since no observational error estimate was given for these lines, an error estimate based on Poisson statistical distribution was used

in the least squares procedure, as given by Equation B.12 in Appendix B.

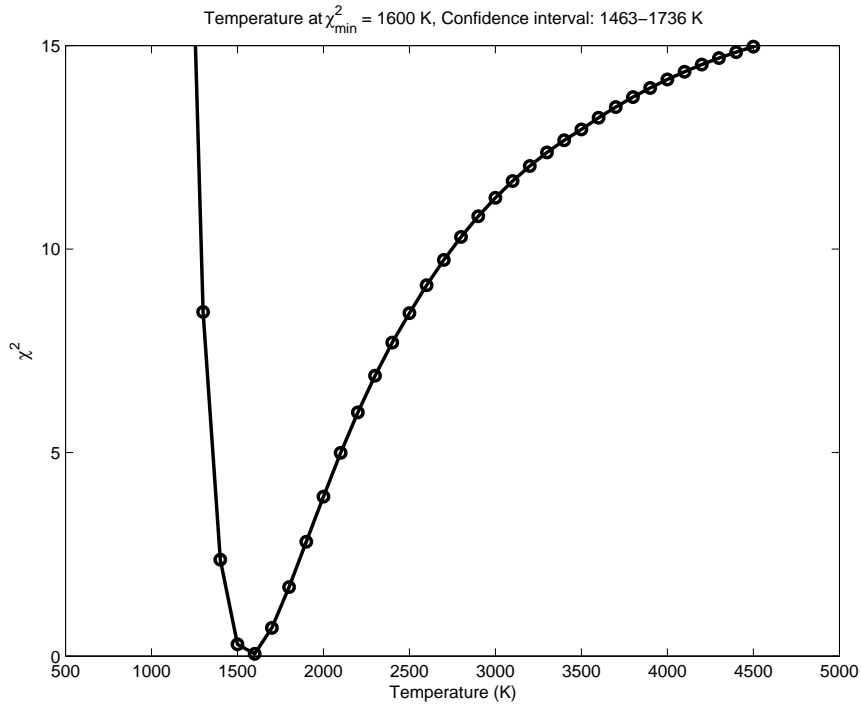


Figure 4.16: Temperature dependence of χ^2 for DQ Herculis 1934. The temperature at χ^2_{\min} and the confidence interval are shown.

Table 4.13 presents some of the electron temperature values for DQ Her collected from the literature. Our value of 1600 K reasonably agrees with the values of Smits [176] and Davey [13] which are also derived from C II recombination lines but with different method using the flux ratio of $\lambda 1335$ to $\lambda 4267$. Itoh [173] seems to conclude different temperature values derived from various species and may originate from different parts of DQ Her; some of these values are lower than 500 K while some are much higher and may even reach 20000 K or higher although some of these derived values are based on tentative models. The higher temperatures may also belong to the hot inner disk region, rather than the cool outer nebula shell, where much higher temperatures have been derived for the disk [177–179].

Table 4.12: The observational C II transition lines of Ferland *et al* [12] that were used in the least squares minimization procedure to find the electron temperature of the line emitting region in DQ Hercules 1934. The given flux is the normalized to the H_{β} flux.

λ_{lab}	I	Lower	Upper	g_l	g_u	Type
1335	270	2p $^2P^o$	2s2p 2 $^2D^e$	10	14	BB
4267	29	3d $^2D^e$	4f $^2F^o$	16	20	BB

Table 4.13: The electron temperature in Kelvin of DQ Hercules 1934 from different species and transitions as obtained from the cited literature, where BC stands for Balmer Continuum. CW refers to the current work.

Source	[180]	[181]	[12]	[68]	[176]	[13]	CW
H I(BC)	500	1000		450			
C II			700		1300	1450	1600
[N II]				2500 2400			
Mean			500				

4.2.7 CPD - 56°8032

CPD - 56°8032 is a cool late-type Wolf-Rayet star that is usually classified as WC10 or WC11. The star, which is located at about 1.3-1.5 kpc, is surrounded by a young planetary nebula with complex visible structure. The low-excitation spectrum of CPD - 56°8032, which has been described as unique, shows bright C II and C III emission lines indicating the star is carbon-rich. Observational studies suggest that the star is encircled by a disk or torus of dust [182–192].

Here, we try to infer the electron temperature of the stellar nebular wind surrounding CPD - 56°8032. The observational data of this object were obtained from De Marco *et al* [5]. On surveying this data source we obtained about 16 C II lines. Following the refinement process, outlined in § 4.1, this list was reduced to 13 lines. These lines are presented in Table 4.14.

The data were normalized to the total flux and emissivity and χ^2 was computed and plotted against temperature over the range $T = 500 - 30000$ K in steps of 100 K. As seen in Figure 4.17, the plot indicates a temperature of about 17300 K. This agrees, within the reported error bars, with the temperature of De Marco *et al* [193, 194] who deduced a value of 18500 ± 1500 K for this object using a similar least squares approach. Table 4.15 presents electron temperatures derived previously in the cited literature. As seen there is a large scattering in the reported values. The main reason for this may be the large temperature variations across the line emitting regions, where the high temperature lines originate from the inner ring next to the central star while the low temperature lines come from the relatively cold region at the perimeter of the nebula. Differences in the derivation methods and the type of transitions used in these derivations (e.g. CEL versus ORL), as well as observational and theoretical errors, should also contribute to the scattering. However, our value agrees reasonably with some of these reported values.

Table 4.14: The observational C II transition lines of De Marco *et al* [5] that were used in the least squares minimization procedure to find the electron temperature of the line emitting region in the planetary nebula CPD - 56°8032. The given flux is the absolute value in units of $\text{erg.s}^{-1}.\text{cm}^{-2}$.

λ_{lab}	I	Lower	Upper	g_l	g_u	Type
4618.73	4.194E-12	3d' ² F ^o	4f' ² G ^e	6	8	FF
4619.23	6.167E-12	3d' ² F ^o	4f' ² G ^e	8	10	FF
4627.63	1.850E-13	3d' ² F ^o	4f' ² G ^e	8	8	FF
4953.85	1.437E-12	3p' ² P ^e	3d' ² P ^o	2	2	FB
4958.67	7.183E-13	3p' ² P ^e	3d' ² P ^o	4	2	FB
4959.92	7.183E-13	3p' ² P ^e	3d' ² P ^o	2	4	FB
4964.73	3.592E-12	3p' ² P ^e	3d' ² P ^o	4	4	FB
5107.97	5.906E-13	3d' ² P ^o	4f' ² D ^e	4	4	FF
5113.69	3.384E-12	3d' ² P ^o	4f' ² D ^e	4	6	FF
5114.26	2.888E-12	3d' ² P ^o	4f' ² D ^e	2	4	FF
8793.80	1.926E-12	3p' ² D ^e	3d' ² F ^o	6	8	FB
8799.90	1.347E-12	3p' ² D ^e	3d' ² F ^o	4	6	FB
8826.98	9.426E-14	3p' ² D ^e	3d' ² F ^o	6	6	FB

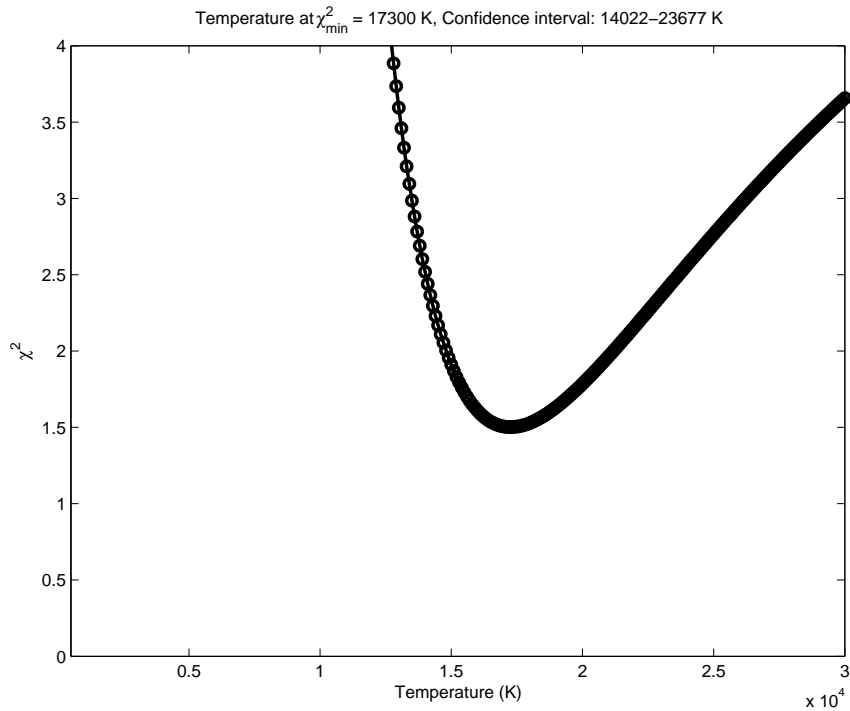


Figure 4.17: Temperature dependence of χ^2 for CPD - 56°8032. The temperature at χ^2_{min} and the confidence interval are shown.

Table 4.15: The electron temperature in Kelvin of the stellar wind of the CPD - 56°8032 Wolf-Rayet star from different species and transitions as obtained from the cited literature. CW refers to the current work. Also Davey [13] seems to support the value of 12800 K derived by Barlow and Storey [14].

Source	[184]	[195]	[196]	[14]	[197]	[186]	[193, 194]	[5]	[198]	CW
He I					20100					
He II					20800					
C II				12800		20000	18500	21300 18900 21000 21700	21300	17300
[N II]		11000								
General	10000		7000							

4.2.8 He 2-113

He 2-113 is a late-type WC10 Wolf-Rayet star surrounded by a planetary nebula with an apparent ring structure. There are many physical similarities between CPD - 56°8032 and He 2-113 such as age, flux and distance. These similarities are reflected in the strong resemblance of their observed spectra and hence they are normally investigated jointly [5, 191–193, 199–202].

Here, we investigate the electron temperature of the stellar wind surrounding He 2-113 using observational data from De Marco *et al* [5]. On surveying this data source we obtained about 16 C II recombination lines. Following the refinement process, outlined in § 4.1, this list was reduced to 13 lines. These lines are presented in Table 4.16.

Table 4.16: The observational C II transition lines of De Marco *et al* [5] that were used in the least squares minimization procedure to find the electron temperature of the line emitting region in the planetary nebula He 2-113. The given flux is the absolute value in units of $\text{erg.s}^{-1}.\text{cm}^{-2}$.

λ_{lab}	I	Lower	Upper	g_l	g_u	Type
4618.73	2.271E-12	3d' ² F ^o	4f' ² G ^e	6	8	FF
4619.23	3.339E-12	3d' ² F ^o	4f' ² G ^e	8	10	FF
4627.63	1.002E-13	3d' ² F ^o	4f' ² G ^e	8	8	FF
4953.85	7.141E-13	3p' ² P ^e	3d' ² P ^o	2	2	FB
4958.67	3.571E-13	3p' ² P ^e	3d' ² P ^o	4	2	FB
4959.92	3.571E-13	3p' ² P ^e	3d' ² P ^o	2	4	FB
4964.73	1.785E-12	3p' ² P ^e	3d' ² P ^o	4	4	FB
5107.97	1.973E-13	3d' ² P ^o	4f' ² D ^e	4	4	FF
5113.69	1.130E-12	3d' ² P ^o	4f' ² D ^e	4	6	FF
5114.26	9.646E-13	3d' ² P ^o	4f' ² D ^e	2	4	FF
8793.80	9.342E-13	3p' ² D ^e	3d' ² F ^o	6	8	FB
8799.90	6.533E-13	3p' ² D ^e	3d' ² F ^o	4	6	FB
8826.98	4.573E-14	3p' ² D ^e	3d' ² F ^o	6	6	FB

The data were normalized to the total flux and emissivity, as outlined previously, and χ^2 was computed and plotted against temperature over the range $T = 500 -$

30000 K in steps of 100 K. As seen in Figure 4.18, the plot indicates a temperature of about 16200 K which agrees very well with some previously-deduced values notably those of De Marco *et al* [5, 198]. Table 4.17 presents electron temperatures derived previously in the cited literature. As seen there is some scattering in these values. Similar arguments to those presented in the CPD - 56°8032 section may be given to explain this scattering in the derived electron temperatures.

Table 4.17: The electron temperature in Kelvin of the stellar wind of the He 2-113 Wolf-Rayet star as obtained from the cited literature. CW refers to the current work.

Source	[195]	[193, 194]	[5]	[198]	CW
C II		13600	16400 17000	16400	16200
General	8800				

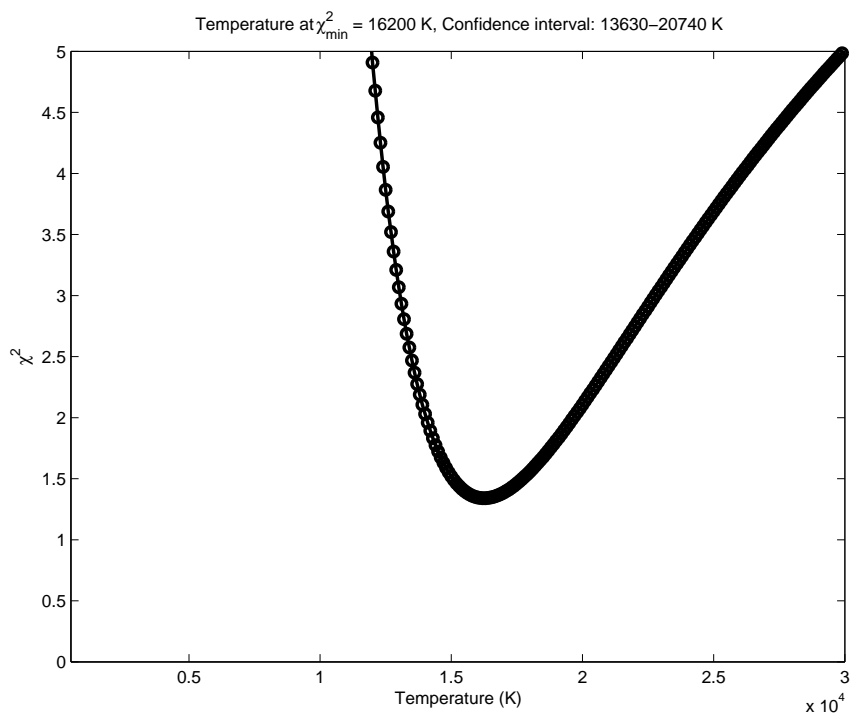


Figure 4.18: Temperature dependence of χ^2 for He 2-113. The temperature at χ^2_{\min} and the confidence interval are shown.

4.3 Electron Distribution

As discussed in 1.3, it has been suggested [109] that the discrepancy between the results of ORLs and those of CELs is based on the assumption of a Maxwell-Boltzmann (MB) for the electron distribution in the nebulae. Therefore by assuming a different type of distribution, e.g. κ -distribution, the ORLs and CELs should yield very similar results for the abundance and electron temperature. One way for testing this proposal is to obtain the electron distribution from the transition lines obtained from the spectra of nebulae and compare to the MB and other distributions. Since we have sufficient theoretical data for the C II dielectronic recombination with some observational data, we decided to put this proposal to test. To obtain the electron distribution from the observed spectra, the observed flux in conjunction with theoretical data such as recombination coefficient, are used as outlined in the following for the cases in which the transition originates from an autoionizing upper state.

The dielectronic recombination coefficient, $\alpha(\lambda)$, is related to the fraction of electrons per unit energy, f , in the energy range ϵ to $\epsilon + d\epsilon$ by the following relation

$$\alpha(\lambda) = 2\pi a_0^3 \frac{\omega_r}{\omega_+} R \left(\frac{R}{\epsilon} \right)^{1/2} \Gamma^r b f \quad (4.3)$$

where a_0 is the Bohr radius, ω_r is the statistical weight of resonance, ω_+ is the statistical weight of the recombined ion, R is the Rydberg constant, Γ^r is the radiative probability of the transition, and b is the departure coefficient of the autoionizing state. Now MB distribution is given by

$$f_{MB} = \frac{2}{(kT)^{3/2}} \sqrt{\frac{\epsilon}{\pi}} e^{-\frac{\epsilon}{kT}} \quad (4.4)$$

where k is the Boltzmann constant, and T is the electron temperature. Because

there is a proportionality between the de-reddened flux, I , and the dielectronic recombination coefficient multiplied by the photon energy, $\frac{hc}{\lambda}$, we can write

$$\alpha = CI\lambda \quad (4.5)$$

where C is a proportionality factor. On substituting α from Equation 4.5 into Equation 4.3 and solving for f we obtain

$$f = DI \frac{\omega_+}{\omega_r} \left(\frac{\epsilon}{R} \right)^{1/2} \frac{\lambda}{\Gamma r b} \quad (4.6)$$

where D is another proportionality factor. Full derivation of the electron sampling formulation can be found in [142].

By obtaining the f observational data points related to the FF and FB transitions for a particular object, where ϵ in Equation 4.6 stands for the energy of resonance, and plotting them as a function of energy alongside the MB distribution, as given by Equation 4.4, for suitably-chosen temperatures, the observational electron distribution can be compared to the MB theoretical distribution.

As part of the current investigation, we carried out these calculations on the data sets that contain more than one FF or FB transition to be useful for comparison to the MB distribution. The resonance data required for these calculations are given in Table 4.18. In Figures 4.19-4.23 the results of the calculations are presented where the \sqrt{E} -scaled Maxwell-Boltzmann electron distribution for the given temperature, which is chosen as the temperature that we obtained for that object from our least squares procedure, is plotted against electron energy on a log-linear graph alongside the \sqrt{E} -scaled observed data points representing the electron fraction in the given energy range for the FF and FB transitions of the selected lines from the indicated object and cited data source. The \sqrt{E} -scaled κ and Druyvesteyn distributions are also plotted in these figures for comparison

using typical values for the parameters of these functions which are given by the following equations [203]

$$f_{\kappa, E_{\kappa}}(E) = \frac{2}{\sqrt{\pi} \kappa^{3/2} E_{\kappa}} \sqrt{\frac{E}{E_{\kappa}}} \frac{\Gamma(\kappa + 1)}{\Gamma(\kappa - \frac{1}{2})} \left(1 + \frac{E}{\kappa E_{\kappa}}\right)^{-(\kappa+1)} \quad (4.7)$$

and

$$f_{x, E_x}(E) = \frac{x}{E_x^{3/2}} \frac{\Gamma(\frac{5}{2}x)^{3/2}}{\Gamma(\frac{3}{2}x)^{5/2}} \sqrt{E} \exp\left(-\left[\frac{E\Gamma(\frac{5}{2}x)}{E_x\Gamma(\frac{3}{2}x)}\right]^x\right) \quad (4.8)$$

where κ and x are parameters characterizing these distributions, while E_{κ} and E_x are characteristic energies.

As seen, there is in general a few observed data points to constrain the trend and determine decisively if the observed electron distribution is MB or not. However, the scattering of these data points is not far from MB, although in some cases the observational data may also broadly resemble a Druyvesteyn distribution and this similarity may even improve for carefully chosen Druyvesteyn parameters. An interesting point is that the fit between the observational data points and the MB curve generally improves as the temperature of the curve approaches the broadly-known temperature of the object.

Table 4.18: The 64 autoionizing states of C^+ used in the current study with their energy in Ryd, departure coefficient, and autoionization probability in s^{-1} . The $1s^2$ core is suppressed from all configurations.

Index	Configuration	Level	E	b	Γ^a
1	2s2p($^3P^o$)3d	$^2D_{3/2}^o$	0.0160449523	0.0056778500	1.240914E+07
2	2s2p($^3P^o$)3d	$^2D_{5/2}^o$	0.0161440982	0.0261058105	5.390253E+07
3	2s2p($^3P^o$)3d	$^4P_{5/2}^o$	0.0198592428	0.0002217072	4.494221E+05
4	2s2p($^3P^o$)3d	$^4P_{3/2}^o$	0.0200528871	0.0109357666	2.600220E+07
5	2s2p($^3P^o$)3d	$^4P_{1/2}^o$	0.0201782774	0.0044633618	1.054050E+07
6	2s2p($^3P^o$)3d	$^2F_{5/2}^o$	0.0298595786	0.9981159635	1.159802E+12
7	2s2p($^3P^o$)3d	$^2F_{7/2}^o$	0.0302407616	0.9981660633	1.195966E+12
8	2s2p($^3P^o$)3d	$^2P_{3/2}^o$	0.0502577447	0.9925373136	2.193909E+11
9	2s2p($^3P^o$)3d	$^2P_{1/2}^o$	0.0504825543	0.9928976298	2.304847E+11

Table 4.18: continued.

Index	Configuration	Level	E	b	Γ^a
10	2s2p(³ P ^o)4s	⁴ P ^o _{1/2}	0.1174409992	0.9062462126	5.264264E+09
11	2s2p(³ P ^o)4s	⁴ P ^o _{3/2}	0.1176606145	0.9595276889	1.292497E+10
12	2s2p(³ P ^o)4s	⁴ P ^o _{5/2}	0.1180785216	0.0000000000	0.000000E+00
13	2s2p(³ P ^o)4s	² P ^o _{1/2}	0.1378830490	0.9999959170	1.267096E+14
14	2s2p(³ P ^o)4s	² P ^o _{3/2}	0.1383845207	0.9999959515	1.270574E+14
15	2s2p(³ P ^o)4p	² P ^e _{1/2}	0.1616554031	0.5081258069	4.383575E+08
16	2s2p(³ P ^o)4p	² P ^e _{3/2}	0.1618888697	0.8281132233	2.043629E+09
17	2s2p(³ P ^o)4p	⁴ D ^e _{1/2}	0.1648956865	0.0166709970	1.096506E+06
18	2s2p(³ P ^o)4p	⁴ D ^e _{3/2}	0.1650135133	0.9428663460	1.059104E+09
19	2s2p(³ P ^o)4p	⁴ D ^e _{5/2}	0.1652179105	0.9575548715	1.436774E+09
20	2s2p(³ P ^o)4p	⁴ D ^e _{7/2}	0.1655322976	0.0000000000	0.000000E+00
21	2s2p(³ P ^o)4p	⁴ S ^e _{3/2}	0.1740799826	0.0023540601	1.361289E+05
22	2s2p(³ P ^o)4p	⁴ P ^e _{1/2}	0.1795026594	0.9721418782	1.500088E+09
23	2s2p(³ P ^o)4p	⁴ P ^e _{3/2}	0.1796552966	0.9802394591	2.134176E+09
24	2s2p(³ P ^o)4p	⁴ P ^e _{5/2}	0.1798464804	0.9965561757	1.249636E+10
25	2s2p(³ P ^o)4p	² D ^e _{3/2}	0.1854199383	0.9999806616	2.450767E+13
26	2s2p(³ P ^o)4p	² D ^e _{5/2}	0.1846436636	0.9999809896	2.436138E+13
27	2s2p(³ P ^o)4p	² S ^e _{1/2}	0.1997648585	0.9999637714	8.854266E+12
28	2s2p(¹ P ^o)3s	² P ^o _{1/2}	0.2058921572	0.9999507406	6.254162E+13
29	2s2p(¹ P ^o)3s	² P ^o _{3/2}	0.2059121732	0.9999505223	6.218950E+13
30	2s2p(³ P ^o)4d	⁴ F ^o _{3/2}	0.2086057952	0.0130742833	1.050972E+06
31	2s2p(³ P ^o)4d	⁴ F ^o _{5/2}	0.2087298186	0.5207186031	8.735439E+07
32	2s2p(³ P ^o)4d	⁴ F ^o _{7/2}	0.2089176308	0.6046487195	1.231846E+08
33	2s2p(³ P ^o)4d	⁴ F ^o _{9/2}	0.2091829917	0.0000000000	0.000000E+00
34	2s2p(³ P ^o)4d	⁴ D ^o _{1/2}	0.2137906313	0.0240817145	4.770103E+07
35	2s2p(³ P ^o)4d	⁴ D ^o _{3/2}	0.2138393841	0.0111774423	2.183347E+07
36	2s2p(³ P ^o)4d	⁴ D ^o _{5/2}	0.2139172974	0.0140469244	2.749728E+07
37	2s2p(³ P ^o)4d	⁴ D ^o _{7/2}	0.2140182658	0.0623175129	1.279541E+08
38	2s2p(³ P ^o)4d	² D ^o _{3/2}	0.2181284447	0.3163623529	4.111112E+08
39	2s2p(³ P ^o)4d	² D ^o _{5/2}	0.2182467272	0.1161936608	1.173714E+08
40	2s2p(³ P ^o)4d	⁴ P ^o _{5/2}	0.2200435636	0.0044332899	5.029955E+06
41	2s2p(³ P ^o)4d	⁴ P ^o _{3/2}	0.2202300088	0.0095968218	1.099796E+07
42	2s2p(³ P ^o)4d	⁴ P ^o _{1/2}	0.2203477445	0.0066028492	7.552275E+06
43	2s2p(³ P ^o)4f	² F ^e _{5/2}	0.2225695047	0.4062779057	1.887721E+08
44	2s2p(³ P ^o)4f	² F ^e _{7/2}	0.2226518832	0.0014994709	4.083866E+05
45	2s2p(³ P ^o)4f	⁴ F ^e _{3/2}	0.2226157059	0.3253636102	1.231093E+08
46	2s2p(³ P ^o)4f	⁴ F ^e _{5/2}	0.2226627273	0.3227642510	1.220007E+08

Table 4.18: continued.

Index	Configuration	Level	E	b	Γ^a
47	2s2p($^3P^o$)4f	$^4F_{7/2}^e$	0.2227230532	0.0414199477	1.122416E+07
48	2s2p($^3P^o$)4f	$^4F_{9/2}^e$	0.2227599595	0.0926167497	2.606316E+07
49	2s2p($^3P^o$)4d	$^2F_{5/2}^o$	0.2259594181	0.9967124124	3.003092E+11
50	2s2p($^3P^o$)4d	$^2F_{7/2}^o$	0.2263462510	0.9968281849	3.121474E+11
51	2s2p($^3P^o$)4f	$^4G_{5/2}^e$	0.2267242446	0.0410695674	1.127515E+07
52	2s2p($^3P^o$)4f	$^4G_{7/2}^e$	0.2268078989	0.3627478405	1.492546E+08
53	2s2p($^3P^o$)4f	$^4G_{9/2}^e$	0.2270049148	0.3399201973	1.350812E+08
54	2s2p($^3P^o$)4f	$^4G_{11/2}^e$	0.2272718249	0.0000000000	0.000000E+00
55	2s2p($^3P^o$)4f	$^2G_{7/2}^e$	0.2271098017	0.6893371371	5.331860E+08
56	2s2p($^3P^o$)4f	$^2G_{9/2}^e$	0.2274615507	0.7843011811	8.601144E+08
57	2s2p($^3P^o$)4f	$^4D_{7/2}^e$	0.2281245886	0.0002600797	6.139194E+04
58	2s2p($^3P^o$)4f	$^4D_{5/2}^e$	0.2282086986	0.9951533708	4.934209E+10
59	2s2p($^3P^o$)4f	$^4D_{3/2}^e$	0.2284089951	0.9846397825	1.519940E+10
60	2s2p($^3P^o$)4f	$^4D_{1/2}^e$	0.2285283711	0.0000000000	0.000000E+00
61	2s2p($^3P^o$)4f	$^2D_{5/2}^e$	0.2284110910	0.9979488054	9.860173E+10
62	2s2p($^3P^o$)4f	$^2D_{3/2}^e$	0.2286146681	0.9984868233	1.359512E+11
63	2s2p($^3P^o$)4d	$^2P_{3/2}^o$	0.2332306002	0.9986068098	5.007744E+11
64	2s2p($^3P^o$)4d	$^2P_{1/2}^o$	0.2334757310	0.9986193975	5.083958E+11

4.4 Epilogue

In the end of this chapter, an important issue should be addressed that is how to justify the large discrepancy in the temperature values obtained by different investigators from different atoms, ions, and types of transition. In the following points we propose some possible reasons for this discrepancy.

- Differences in theoretical, observational and numerical techniques used to infer electron temperatures. Since the frameworks of these techniques are different the results may also differ.
- The astronomical objects in general and planetary nebulae in particular are extensive objects with complex structure of varying physical conditions.

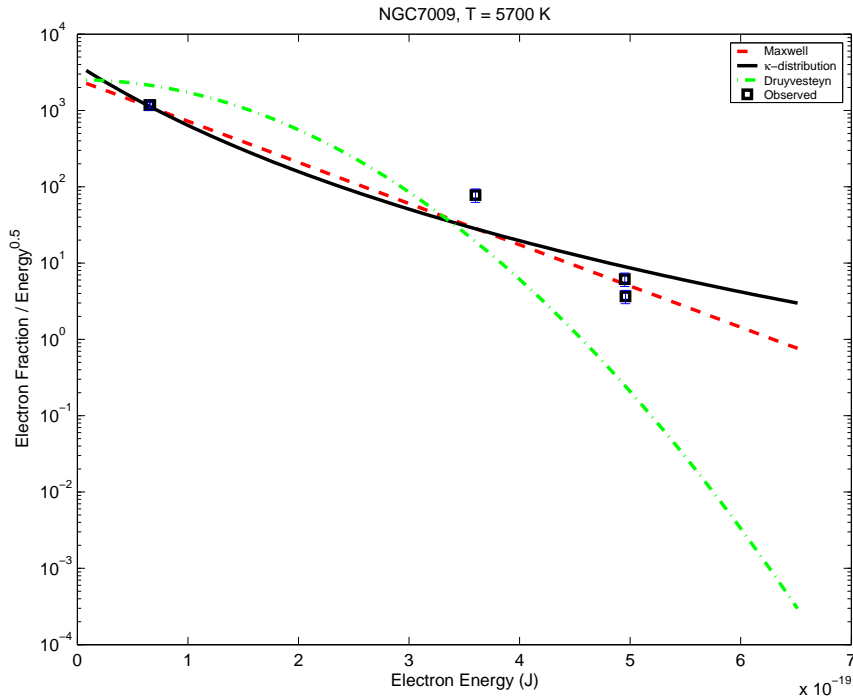


Figure 4.19: Electron distribution plot for NGC 7009 data of Fang and Liu [1], alongside Maxwell-Boltzmann, κ ($= 5.0$) and Druyvesteyn (with $x = 2.0$) distributions for $T = 5700$ K. The y -axis is in arbitrary units.

Hence, the collected spectrum normally originates from different regions in the object which are subject to different physical conditions, including temperature. Therefore, there is no contradiction in some cases of varying electron temperatures as they can be deduced from transitions originating from different regions.

- Selectivity of electron temperature by different types of transition (e.g. forbidden or recombination) from the same or different species. Because each type of transition of a particular species is optimal at certain ranges of electron energy, the deduced temperature is dependent on these factors [156].
- Finally, observational and theoretical errors (gross, systematic, random, etc.) should also be considered as a possible reason in some cases especially for some eccentric results.

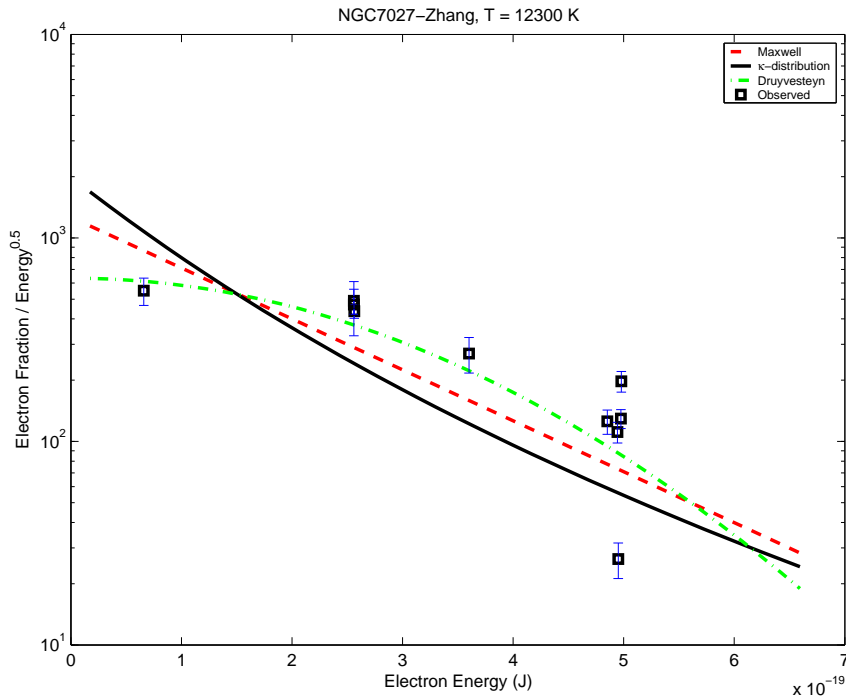


Figure 4.20: Electron distribution plot for NGC 7027 data of Zhang *et al* [3], alongside Maxwell-Boltzmann, κ ($= 5.0$) and Druyvesteyn (with $x = 2.0$) distributions for $T = 12300$ K. The y -axis is in arbitrary units.

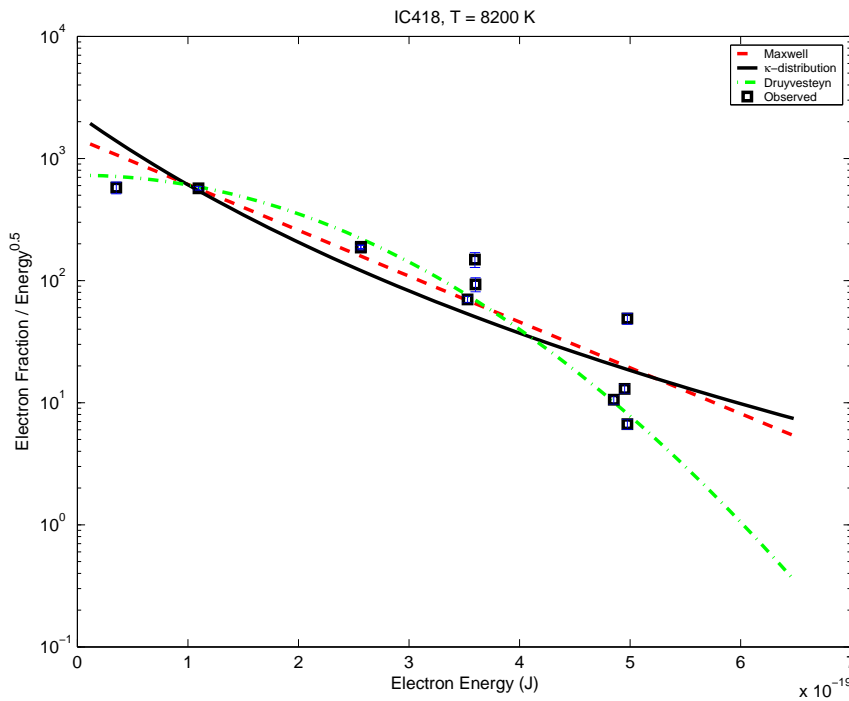


Figure 4.21: Electron distribution plot for IC 418 data of Sharpee *et al* [4], alongside Maxwell-Boltzmann, κ ($= 5.0$) and Druyvesteyn (with $x = 2.0$) distributions for $T = 8200$ K. The y -axis is in arbitrary units.

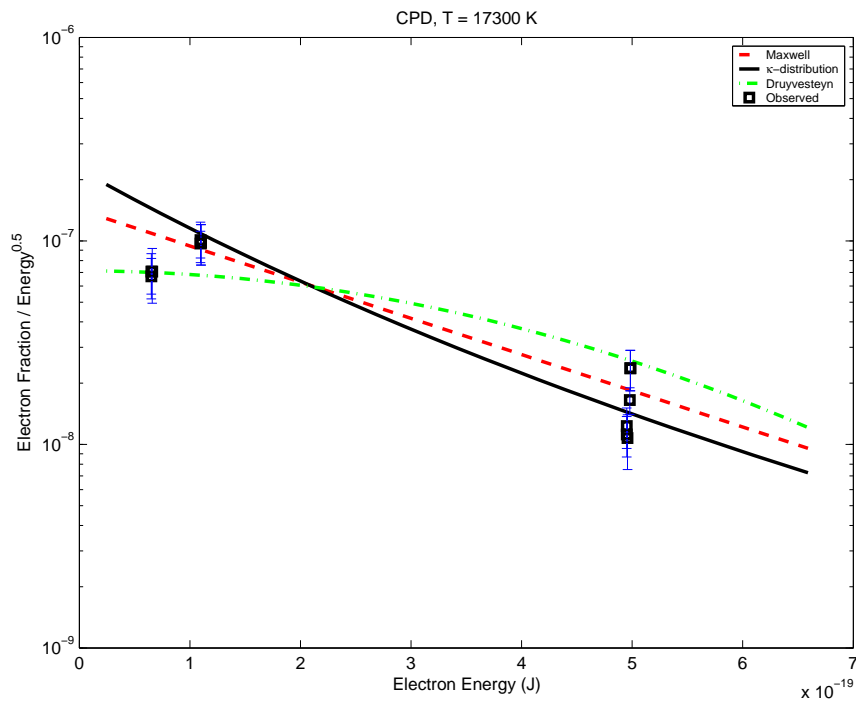


Figure 4.22: Electron distribution plot for CPD - 56°8032 data of De Marco *et al* [5], alongside Maxwell-Boltzmann, κ ($= 5.0$) and Druyvesteyn (with $x = 2.0$) distributions for $T = 17300$ K. The y -axis is in arbitrary units.

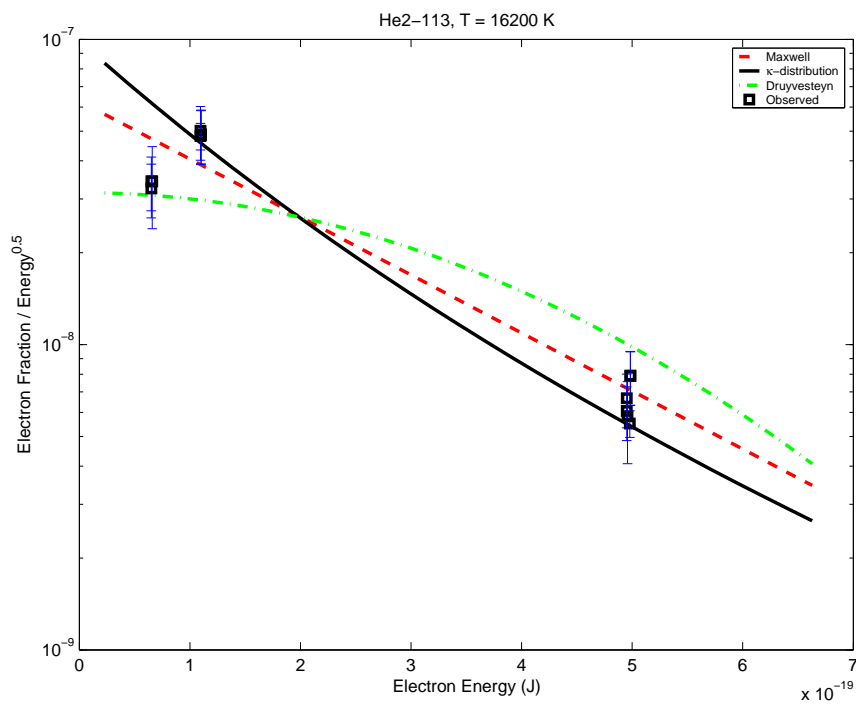


Figure 4.23: Electron distribution plot for He 2-113 data of De Marco *et al* [5], alongside Maxwell-Boltzmann, κ ($= 5.0$) and Druyvesteyn (with $x = 2.0$) distributions for $T = 16200$ K. The y -axis is in arbitrary units.

Part II

Molecular Physics:

A Computed Line List for Molecular Ion



Chapter 5

Computed Line List for H_2D^+

In this part of the thesis, we present our comprehensive, highly-accurate calculated line list of frequencies and transition probabilities for the singly deuterated isotopologue of H_3^+ , H_2D^+ . The list, called ST1, contains over 22 million rotational-vibrational transitions occurring between more than 33 thousand energy levels and covers frequencies up to 18500 cm^{-1} . Due to its simplicity and cosmological and astrophysical importance, H_2D^+ has been the subject of a substantial number of spectroscopic and astronomical studies in the last three decades. We hope that our line list and the associated conclusions presented in this thesis will be a valuable contribution in this direction that other researchers will benefit from [204].

5.1 Introduction

H_2D^+ is one of the simplest polyatomic quantum systems and the lightest asymmetric top molecular ion. It has a substantial permanent electric dipole moment of about 0.6 Debye due to the displacement of the center of charge from the center of mass. It consists of two electrons bound to three nuclei (two protons and one deuteron) forming a triangular shape at equilibrium. The molecule is a pro-

late top with three normal vibrational modes: a symmetric breathing mode ν_1 , a bending mode ν_2 , and an asymmetric stretch ν_3 . All these modes are infrared active. Depending on the spin alignment of its protons, it has two different species, ortho and para, with a spin weight ratio of 3:1. Because H_2D^+ has a permanent dipole moment, it possesses pure rotational transitions which mainly occur in the sub-millimeter region (far infrared and microwave) and hence it can be observed in emission or absorption from ground-based detectors. This all contrasts strongly with the non-deuterated H_3^+ molecular ion which has no allowed rotational spectrum and only one infrared active vibrational mode [205–208].

In cool astrophysical environments, where this molecule is mostly found and where it plays very important role, the molecule is formed by several reactions; the main one is



Because this and other similar formation reactions are exothermic, the formation of H_2D^+ in the cold interstellar environment is favored. Consequently, the abundance of this species is enhanced relative to the D/H ratio.

H_2D^+ possesses very rich rotational and roto-vibrational spectra. As an isotopomer of H_3^+ , H_2D^+ is a major participant in chemical reactions taking place in the interstellar medium. In particular, it plays a key role in the deuteration processes in these environments [209]. Although the existence of H_2D^+ in the interstellar medium (ISM) and astrophysical objects was contemplated decades ago [205, 210] with some reported tentative sighting [211–213], it is only relatively recently that the molecule was firmly detected in the ISM via one of its rotational transition lines [214]. There have been many subsequent astronomical studies related to H_2D^+ spectra [215–222]. In particular these spectra have been used to investigate the mid-plane of proto-planetary disks [223], the kinematics of the cen-

ters of pre-stellar cores [224], and the suggestion of possible use as a probe for the presence of the hypothetical cloudlets forming the baryonic dark matter [225]. Vibrational transitions of H_2D^+ have yet to be observed astronomically.

The important role of H_2D^+ in the astrophysical molecular chemistry, especially in the deuterium fractionation processes, was recognized since the early stages of radio astronomy development. Because H_3^+ lacks a permanent dipole moment and hence cannot be detected via radio astronomy, its asymmetrical isotopomers, namely H_2D^+ and D_2H^+ , are the most promising tracers of the extremely cold and highly dense interstellar clouds. These species are the last to remain in gaseous state under these extreme conditions with observable pure rotational spectra [205, 226]. Of these two isotopomers, H_2D^+ is the more abundant and easier to observe and hence it is the main species to utilize in such astrophysical investigations.

H_2D^+ is the key molecular ion that drives deuterium fractionation of various molecular species by isotope exchange processes in the interstellar medium especially at low temperatures. This results in considerable enhancement of deuterated molecules that may also participate in other deuteration processes by passing their deuterium content to other species. At very low temperatures (~ 10 K), where abundant species, such as CO, N_2 and O_2 , that consume H_2D^+ freeze out onto the surface of interstellar dust grains, and where the destruction channels of H_2D^+ in the H/D exchange reactions are blocked due to zero-point energy effects, the formation of H_2D^+ is strongly enhanced. This can lead to H_2D^+ becoming more abundant than H_3^+ although the cosmic abundance of deuterium is only about 2×10^{-5} that of hydrogen. In these conditions H_2D^+ becomes the main source of deuterium fractionation as it is more abundant than any other deuterated species, with subsequent effective deuteration of other species [148, 209, 214, 226–228].

The potential importance of H_2D^+ spectroscopy for cosmology is obvious as it is a primordial molecular species that could have a considerable abundance in the

early universe. In particular, it may have played a role in the cooling of primordial proto-objects [229–233]. Its significance is highlighted by a number of studies which consider the role of H_2D^+ in spectral distortions of Cosmic Microwave Background Radiation and whether this can be used to determine the H_2D^+ and deuterium abundances at different epochs [230]. Finally the H_2D^+ 372 GHz line has been considered as a probe for the presence of dark matter [225].

In the following we present a short literature review summarizing some landmarks in the investigation of this molecule.

5.1.1 Literature Review

H_2D^+ is a highly important molecule and hence it was the subject of extensive studies both at laboratory and astrophysical levels in the last few decades. It is regarded as one of the benchmark systems for theoretical and experimental molecular investigations [205, 228, 234, 235].

The first successful spectroscopic investigation of H_2D^+ was carried out by Shy *et al* [227] where nine rotational-vibrational transitions were measured in the infrared region between 1800 and 2000 cm^{-1} using Doppler-tuned fast-ion laser technique, but no specific spectroscopic assignments were made. This was followed by other spectroscopic investigations which include the observation and identification of the strong and highly-important rotational $1_{10} - 1_{11}$ transition line of ortho- H_2D^+ at 372 GHz in 1984 by Bogey *et al* [207] and Warner *et al* [228] using discharge techniques. The three fundamental vibrational bands of the H_2D^+ ion were also detected and identified by Amano and Watson [206], Amano [236] and Foster *et al* [237] using laser spectroscopy.

Fárník *et al* [208] measured transitions to overtones $2\nu_2$ and $2\nu_3$ and to combination $\nu_2 + \nu_3$ in jet-cooled H_2D^+ ions using high-resolution infrared spectroscopic

technique. Amano and Hirao [238] also measured the transition frequency of the $1_{10} - 1_{11}$ line of H_2D^+ at 372 GHz with improved accuracy [372.421385(10) GHz]. Moreover, the transition frequency of the $3_{21} - 3_{22}$ line of H_2D^+ was observed and measured [646.430293(50) GHz] for the first time in this investigation. Hlavenka *et al* [239] measured second overtone transition frequencies of H_2D^+ in the infrared region using cavity ringdown absorption spectroscopy. Other examples of spectroscopic investigations include those of Asvany *et al* [15], who detected 20 lines with full spectroscopic assignment using laser induced reaction techniques, and the relatively recent work of Yonezu *et al* [240], who reported precise measurement of the transition frequency of the H_2D^+ $2_{12} - 1_{11}$ line at 2.363 THz, alongside three more far-infrared lines of H_2D^+ , using tunable far-infrared spectrometry. However, none of these studies measured absolute line intensities, although the work of Fárník *et al* [208] and Asvany *et al* [15] give relative intensities.

On the astronomical side, a tentative observation of the $1_{10} - 1_{11}$ transition line of ortho- H_2D^+ at 372 GHz from NGC 2264 has been reported by Phillips *et al* [211]. This line is the strongest and the most important of the H_2D^+ lines as it involves some of the lowest rotational levels and is the main one that can be observed from ground-based telescopes. Pagani *et al* [212] have also searched for this line in several dark clouds with no success; nonetheless they derived upper limits for the ortho- H_2D^+ column density. A similar failed attempt to observe this line in a number of interstellar clouds including NGC 2264 was made by van Dishoeck *et al* [210]. In their search for the rotational transitions of H_2D^+ , Boreiko and Betz [213] detected an absorption feature toward the IRc2 region of M42. The feature was suspected to be from the lowest rotational $1_{01} - 0_{00}$ transition at 1370 GHz of para- H_2D^+ .

The first confirmed astronomical observation of H_2D^+ was made in 1999 by Stark *et al* [214] who reported the detection of the $1_{10} - 1_{11}$ ground-state transition

line of ortho- H_2D^+ at 372 GHz in emission from the young stellar object NGC 1333 IRAS 4A. This was followed by the detection of this line towards the pre-stellar core L1544 by Caselli *et al* [215] and the detection of the same line toward another pre-stellar core 16293E by Vastel *et al* [216]. The 372 GHz line of H_2D^+ was also detected toward a disk source DM Tau, and tentatively detected toward TW Hya by Ceccarelli *et al* [217]. Other confirmed or tentative sightings of this line include the observation toward I16293A [218], toward L1544 and L183 [241, 242], in the starless core Barnard 68 [219], and in a massive pre-stellar core in Orion B [220]. H_2D^+ has also been detected in absorption toward Sgr B2 in the galactic center through the far-infrared $2_{12} - 1_{11}$ transition of ortho- H_2D^+ at 2363.325 GHz [221]. Recently, H_2D^+ has been observed through the 372 GHz $1_{10} - 1_{11}$ line in seven starless cores and four protostellar cores by Caselli *et al* [222].

5.1.2 Line Lists

Several synthetic H_2D^+ line lists have been generated from *ab initio* calculations in the last few decades. Prominent examples include the line list of Miller *et al* [234] and another one generated by Tennyson and co-workers as part of the work reported by Asvany *et al* [15]. Miller *et al*'s list extends to rotational quantum number $J = 30$ and covers all levels up to 5500 cm^{-1} above the ground state. These lists were used in a number of studies for various purposes such as spectroscopic assignment of energy levels and transition lines from astronomical observations, and for computation of low-temperature partition functions [6]. The line lists also played an important role in motivating and steering the experimental and observational work in this field [15, 234]. Nonetheless, the previous H_2D^+ line lists suffered from limitations that include low energy cut-off and the inclusion of a limited number of levels especially at high J . These limitations, alongside the recent developments in computing technology and the availability of high accuracy *ab initio* models of

H_3^+ and its isotopologues, including H_2D^+ , represented by the potential and dipole surfaces of Polyansky and Tennyson [243], provided the motivation to generate a more comprehensive and accurate line list. The intention is that the new list will both fill the previous gaps and provide data of better quality.

The H_2D^+ line list presented in this thesis, called ST1, consists of 22164810 transition lines occurring between 33330 rotational-vibrational levels. These are all the energy levels with rotational quantum number $J \leq 20$ and frequencies below 18500 cm^{-1} as an upper cut-off limit for both levels and transitions. This line list can be seen as a companion to the H_3^+ line list of Neale *et al* [7] which has been extensively used for astrophysical studies; although for reasons explained below, the ST1 line list is actually expected to be more accurate. More details about ST1 will follow.

5.2 Method

As indicated already, the main code used to generate the H_2D^+ line list is the DVR3D code of Tennyson *et al* [244] which is a suite of programs for performing rotational-vibrational calculations on triatomic molecules. The code calculates, among other things, wavefunctions, energy levels, transition lines, dipole moments, and transition probabilities. DVR3D is based on a discrete variable representation (DVR) approach by using Gauss-Jacobi and Gauss-Laguerre quadrature schemes for representing the internal coordinates. The code uses an exact Hamiltonian, within the Born-Oppenheimer approximation, and requires potential energy and dipole surfaces to be supplied as an input. In general, it is these surfaces which largely determine the accuracy of the resulting calculations [245] assuming a good choice of DVR3D input parameters. The DVR3D code consists of four main stages: vibration, rotation, dipole and spectra. These stages are fully documented by Ten-

nyson *et al* [244], and hence the following discussion about these stages is restricted to what is necessary to clarify the method that we followed in generating the ST1 list. In general, the parameters of these stages were chosen following extensive consistency and convergence tests, some of which are outlined. The results were regularly compared to the available experimental and observational data and the theoretical results from previous investigations. A sample of these comparisons, validations and preliminary results will follow in the subsequent sections.

The vibrational stage of the DVR3D suite requires an accurate model for the variation of electronic potential as a function of nuclear geometry. This potential energy surface, which is supplied through a fortran subroutine, is usually obtained from *ab initio* calculations enhanced by empirical adjustment to improve the fit to experimental data. For the generation of ST1 list, we used the H_3^+ global potential surface of Polyansky *et al* [246], who used the ultra-high accurate *ab initio* data of Cencek *et al* [247] supplemented by extra data points to reach about 200 data points in total. The surface was constrained at high energy by the data of Schinke *et al* [248]. We complemented this surface by adding the H_2D^+ adiabatic correction term fitted by Polyansky and Tennyson [243]. To allow for non-adiabatic corrections to the Born-Oppenheimer approximation, we employed Polyansky and Tennyson's [243] vibrational mass scaling where different values for the reduced nuclear mass were used for modeling vibrational and rotational motions. We used $\mu_{\text{H}} = 1.0075372$ u and $\mu_{\text{D}} = 2.0138140$ u for the vibrational atomic masses, and $\mu_{\text{H}} = 1.00727647$ u and $\mu_{\text{D}} = 2.01355320$ u for the rotational atomic masses. The accuracy of this model will be assessed below.

Calculations were performed in Jacobi scattering coordinate system (r_1, r_2, θ) , schematically presented in Figure 5.1, to depict the triatomic H_2D^+ molecule, where r_1 represents the diatomic distance (H-H), r_2 is the separation of the D atom from the center of mass of the diatom, and θ is the angle between r_1 and r_2 . This

coordinate system is believed to be more appropriate for an asymmetric molecule like H_2D^+ . Radial basis functions of Morse oscillator type were used to model r_1 [249], while spherical oscillators were used to model r_2 [250]. Following Polyansky and Tennyson [243], the Morse parameters for r_1 were set to $r_e = 1.71$, $D_e = 0.10$ and $\omega_e = 0.0108$, with 20 Gauss-Laguerre grid points. Parameters of the spherical oscillator functions were set to $\alpha = 0.0$ and $\omega_e = 0.0075$ with 44 Gauss-Laguerre grid points, following extensive tests on convergence of the vibrational band origins. The essence of these tests is to vary these parameters systematically to minimize the sum of the energy of the rotation-less states. 36 Gauss-Legendre grid points were used to represent the angular motion. The final vibrational Hamiltonian matrix used was of dimension 2000. In this investigation six combinations of α and ω_e ($\alpha = 0.0, 0.5$ and 1.0 with $\omega_e = 0.0075$ and 0.0095) were used for test in conjunction with 16 different values (30, 32, ..., 60) for the number of r_2 mesh points (NPNT2).

The vibrational stage requires the maximum dimension of the largest intermediate 2D Hamiltonian, MAX2D, and the maximum dimension of the final Hamiltonian, MAX3D, as an input. For these parameters we used values of 1000 and 2000 respectively. The vibrational stage also requires the number of eigenvalues and eigenvectors to be archived for use in the rotational stage (NEVAL). A value of 4000 were chosen for this parameter based on the results of convergence tests. For the number of DVR mesh points in r_2 from Gauss-associated Laguerre quadrature (NPNT2) a value of 44 were chosen, while values of 36 and 20 were used for the number of mesh points in θ (NALF) and in r_1 (NPNT1) respectively. The selection of these values was mainly based on the results obtained from previous investigations and our own convergence tests.

In the rotational stage, a value of 2000 was used for the number of vibrational levels for each k to be read and used (NVIB). The size of the Hamiltonian matrix in

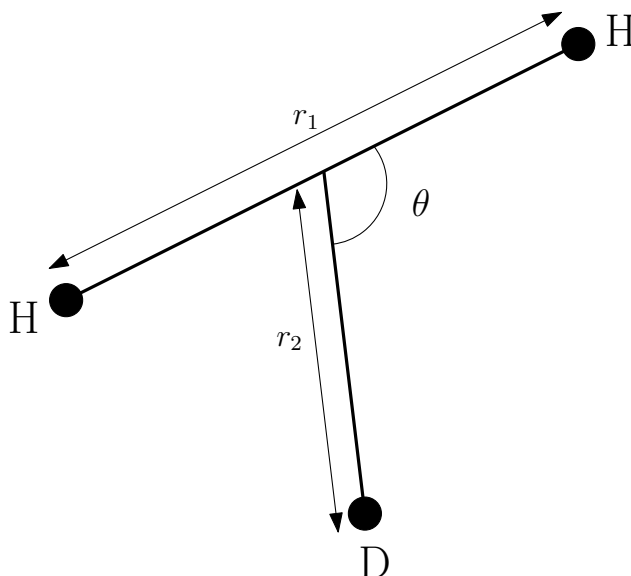


Figure 5.1: Jacobi scattering coordinate system.

this stage (IBASS), which is a function of J , was set to $1800(J+1)$ following a series of tests on $J = 3$ and $J = 15$ in which this parameter was varied incrementally until convergence within an error margin of 0.01 cm^{-1} was reached. These tests demonstrated that choosing sufficiently large values for the size of rotational Hamiltonian (IBASS), although computationally very expensive, is crucial for obtaining reliable results. Our aim was to obtain convergence to within 0.01 cm^{-1} for all rotation-vibration levels considered. Our tests suggest we achieved this except, possibly, for some of the highest lying levels. For these levels our basic model, and in particular our corrections to the Born-Oppenheimer approximation, are not expected to be reliable to this accuracy. Recently, an improved *ab initio* adiabatic potential energy surfaces for H_3^+ and its isotopomers have been developed by Pavanello *et al* [251]. These surfaces include diagonal Born-Oppenheimer corrections calculated from precise wavefunctions. The use of these surfaces in the future should improve the accuracy of these levels.

To compute the intensity of the vibration-rotation transitions, the transition dipole moments between the states concerned must be known. Therefore, a dipole

moment surface, supplied to the dipole stage in the form of an independent fortran subroutine, is required. This surface is usually obtained from *ab initio* calculations without empirical adjustment due to limitation on the quality of experimental data if such data are available at all. For ST1 generation, we used the *ab initio* dipole surface of Röhse *et al* [252] to calculate the components of the H₂D⁺ dipole. In the DIPOLE3 module of DVR3D we set the number of Gauss-Legendre quadrature points used for evaluating the wavefunctions and dipole surface (NPOT) to 50. This choice is consistent with the requirement that this parameter should be slightly larger than the number of DVR points used to calculate the underlying wavefunctions.

Finally, the last stage, spectra, is for producing the list of transition lines. The data of each line in this list include the attributes of the upper and lower levels, the frequency of the line in cm⁻¹, the line strength, the temperature-dependent absolute and relative intensities, and the Einstein *A* coefficient. The actual transitions file of the ST1 list represents a summary of the transitions file produced by spectra stage, where the upper and lower levels in the ST1 file are identified by a unique index from the levels file alongside the Einstein *A* coefficient. These data augmented with the data in the levels file are sufficient to find the intensity and other temperature-dependent quantities. The purpose of this compact form presentation of the transition data is to reduce file size and avoid possible errors and confusion.

The final ST1 line list consists of two main files: one for the levels and the other for the transitions. These two files are constructed and formatted according to the method and style of the BT2 water line list of Barber *et al* [253]. The total amount of CPU time spent in producing the ST1 list including preparation, convergence tests, and verifying the final results was about 8000 hours. We used the serial version of the DVR3D suite on PC platforms running Linux (Red Hat)

operating system, as part of the computing network of the Physics Department, University College London. Both 32- and 64-bit machines were used in this work although the final data were produced mainly on 64-bit machines due to the huge memory requirement of the DVR3D code especially for the high- J calculations. Large samples of data produced by these machines were compared and found to be identical.

It should be remarked that the outlined variational nuclear motion procedure used for these calculations provides rigorous quantum numbers: J , ortho/para and parity p , but not the standard approximate quantum numbers in normal mode, rigid rotor notation. We therefore hand labeled those levels for which such quantum numbers could be assigned in a fairly straightforward fashion. 5000 of these levels are fully designated with 3 rotational (J, K_a, K_c) and 3 vibrational (v_1, v_2, v_3) quantum numbers, while 341 levels are identified with rotational quantum numbers only. The assignments were made by first identifying 176 experimentally-assigned levels. The rotation-less levels are then assigned by taking $K_a = K_c = 0$ when $J = 0$. This is followed by the assignment of the vibrational ground state levels which are obtained mainly from Polyansky *et al* [254]. All these assignments can then provide a guess for many other levels. For example, the energy of the ($v_1, v_2, v_3, J, K_a, K_c$) level can be estimated from the energy of the ($0, 0, 0, J, K_a, K_c$) and ($v_1, v_2, v_3, 0, 0, 0$) levels. Many gaps can then be filled as the missing levels can be uniquely identified from the identified ones in their neighborhood. Some of these assignments are made as a tentative guess and hence the assignments in general should be treated with caution. Tables 5.1 and 5.2 present samples of the ST1 levels and transitions files respectively. A sample of the input data files used as an input to the DVR3D code in various stages of production of ST1, as well as the input files of Spectra-BT2 code used to generate the synthetic spectra, is given in Appendix F.

Table 5.1: Sample of the ST1 levels file. The columns from left to right are for: index of level in file, J , symmetry, index of level in block, frequency in cm^{-1} , v_1 , v_2 , v_3 , J , K_a , K_c . We used -2 to mark unassigned quantum numbers.

720	1	4	89	17645.80538	-2	-2	-2	1	1	0
721	1	4	90	17699.90283	-2	-2	-2	1	1	0
722	1	4	91	17712.30089	-2	-2	-2	1	1	0
723	1	4	92	17778.46381	-2	-2	-2	1	1	0
724	1	4	93	17840.99975	-2	-2	-2	1	1	0
725	1	4	94	17902.76377	-2	-2	-2	1	1	0
726	1	4	95	18005.04261	-2	-2	-2	1	1	0
727	1	4	96	18113.51953	-2	-2	-2	1	1	0
728	1	4	97	18163.92137	-2	-2	-2	1	1	0
729	1	4	98	18226.60371	-2	-2	-2	1	1	0
730	1	4	99	18265.61525	-2	-2	-2	1	1	0
731	1	4	100	18379.99989	-2	-2	-2	1	1	0
732	1	4	101	18499.05736	-2	-2	-2	1	1	0
733	2	1	1	131.63473	0	0	0	2	0	2
734	2	1	2	223.86306	0	0	0	2	2	0
735	2	1	3	2318.35091	0	1	0	2	0	2
736	2	1	4	2427.09231	0	1	0	2	2	0
737	2	1	5	2490.93374	0	0	1	2	1	2
738	2	1	6	3123.27957	1	0	0	2	0	2
739	2	1	7	3209.80678	1	0	0	2	2	0
740	2	1	8	4407.78525	0	2	0	2	0	2
741	2	1	9	4512.34757	0	2	0	2	2	0
742	2	1	10	4563.25961	0	1	1	2	1	2
743	2	1	11	4761.25784	0	0	2	2	0	2
744	2	1	12	4845.07742	0	0	2	2	2	0
745	2	1	13	5157.02577	1	1	0	2	0	2
746	2	1	14	5256.75108	1	1	0	2	2	0
747	2	1	15	5392.06999	1	0	1	2	1	2
748	2	1	16	6006.36278	2	0	0	2	0	2
749	2	1	17	6088.92801	2	0	0	2	2	0
750	2	1	18	6404.39091	0	3	0	2	0	2
751	2	1	19	6514.12841	0	3	0	2	2	0
752	2	1	20	6536.82044	0	2	1	2	1	2
753	2	1	21	6730.08074	0	1	2	2	0	2
754	2	1	22	6881.05077	0	1	2	2	2	0
755	2	1	23	6988.69291	-2	-2	-2	2	-2	-2
756	2	1	24	7123.16702	1	2	0	2	0	2
757	2	1	25	7211.77759	1	2	0	2	2	0
758	2	1	26	7333.23873	-2	-2	-2	2	-2	-2
759	2	1	27	7564.78576	-2	-2	-2	2	-2	-2

Table 5.2: Sample of the ST1 transitions file. The first two columns are for the indices of the two levels in the levels file, while the third column is for the A coefficients in s^{-1} .

30589	29553	7.99E-04
19648	18049	8.37E-03
8943	7423	5.55E-01
8490	7981	2.18E-03
20620	22169	6.91E-04
17613	15937	5.62E-03
13046	11400	1.15E+00
20639	20054	7.26E-03
14433	17117	2.49E-03
25960	28074	1.92E-03
10371	8748	3.80E-02
10380	12978	2.61E-04
6353	6778	4.34E-04
12834	14507	8.68E-04
19391	18843	2.05E-03
29648	27652	9.58E-05
25891	26331	3.67E-04
16727	19473	1.23E-03
17387	14665	1.63E-03
9227	11797	9.18E-06

5.3 Validation and Primary Results

In this section we present a number of comparisons that we made between the ST1 list and data sets found in the literature to validate our list. We also present some preliminary results that we obtained from ST1.

5.3.1 Comparison to Experimental and Theoretical Data

To validate our results, a number of comparisons between the ST1 line list and experimental data found in the literature were carried out. The main data sources of laboratory measurements that have been used in these comparisons are presented in Table 5.3. The table also gives statistical information about the discrepancy

between the calculated line frequencies and their experimental counterparts. Table 5.4 presents a rather detailed account of this comparison for a sample data extracted from one of these data sets, specifically that of Asvany *et al* [15]. This table also contains a comparison of relative Einstein B coefficients between theoretical values from ST1 and measured values from Asvany *et al*. The theoretical values in this table are obtained from the calculated A coefficients using the relation [148]

$$B_{lu} = \frac{(2J' + 1)c^3 A_{ul}}{(2J'' + 1)8\pi h\nu^3} \quad (5.2)$$

where A_{ul} and B_{lu} are the Einstein A and B coefficients respectively for transition between upper (u) and lower (l) states, J' and J'' are the rotational quantum numbers for upper and lower states, c is the speed of light, h is Planck's constant, and ν is the transition frequency.

Tables 5.5 and 5.6 present more comparisons to Asvany *et al* [15] data. As seen, in all cases the ST1 values agree very well with the measured values of Asvany *et al* within acceptable experimental errors. Other comparisons to previous theoretical data, such as that of Polyansky and Tennyson [243], were also made and the outcome was satisfactory in all cases.

5.3.2 Partition Function

The partition function of a system consisting of an ensemble of particles in thermodynamic equilibrium is given by

$$\mathcal{P}(T) = \sum_i (2J_i + 1) g_i e^{\left(\frac{-E_i}{kT}\right)} \quad (5.3)$$

where i is an index running over all energy states of the ensemble, E_i is the energy of state i above the ground level which has rotational angular momentum J_i , k

Table 5.3: The main experimental data sources used to validate the ST1 list. Columns 2 and 3 give the number of data points and the frequency range of the experimental data respectively, while the last four columns represent the minimum, maximum, average, and standard deviation of discrepancies (i.e. observed minus calculated) in cm^{-1} between the ST1 and the experimental data sets.

Source	N	Range (cm^{-1})	Min.	Max.	Ave.	SD
Shy <i>et al</i> [227]	9	1837 – 1953	−0.014	0.116	0.033	0.052
Amano and Watson [206]	27	2839 – 3179	−0.315	0.054	0.033	0.065
Amano [236]	37	2839 – 3209	−0.024	0.054	0.022	0.019
Foster <i>et al</i> [237]	73	1837 – 2603	−0.134	0.213	0.072	0.067
Fárník <i>et al</i> [208]	8	4271 – 4539	0.046	0.172	0.104	0.050
Asvany <i>et al</i> [15]	25	2946 – 7106	0.008	0.242	0.120	0.088

Table 5.4: Comparison between measured (Asvany *et al* [15]) and calculated (ST1) frequencies and relative Einstein B coefficients for a number of transition lines of H_2D^+ . These coefficients are normalized to the last line in the table. The absolute B coefficients, as obtained from the A coefficients of ST1 list using Equation 5.2, are also shown in column 5 as multiples of 10^{14} and in units of m.kg^{-1} .

Transition		Freq. (cm^{-1})		B	Relative B	
Vib.	Rot.	Obs.	ST1	ST1	Obs.	ST1
(0,3,0)	$1_{10} \leftarrow 1_{11}$	6303.784	6303.676	8.05	0.29	0.29
(0,3,0)	$1_{01} \leftarrow 0_{00}$	6330.973	6330.850	8.59	0.32 ± 0.02	0.31
(0,2,1)	$0_{00} \leftarrow 1_{11}$	6340.688	6340.456	7.36	0.27 ± 0.03	0.27
(0,2,1)	$2_{02} \leftarrow 1_{11}$	6459.036	6458.794	9.17	0.35 ± 0.04	0.34
(0,2,1)	$1_{11} \leftarrow 0_{00}$	6466.532	6466.300	27.3	1.00	1.00

is Boltzmann's constant, T is temperature, and g_i is the nuclear spin degeneracy factor which is 1 for para states and 3 for ortho ones.

Using the ST1 energy levels we calculated the partition function of H_2D^+ for a range of temperatures and compared the results to those obtained by Sidhu *et al* [6]. Table 5.7 presents these results for a temperature range of 5 – 4000 K. The results are also graphically presented in Figure 5.2. The table and figure reveal that although our results and those of Sidhu *et al* agree very well at low temperatures (below 1200 K), they differ significantly at high temperatures and the deviation increases as the temperature rises. This can be explained by the fact that ST1 contains more energy levels, particularly at high energy, which contribute

Table 5.5: Asvany [15] data for the second overtone and combination transitions of H_2D^+ compared to the corresponding data as calculated from the ST1 list.

Transition		ν (cm^{-1})		A (s^{-1})		B (s^{-1})	
Vib.	Rot.	Asv	ST1	Asv	ST1	Asv	ST1
(0,3,0)	$0_{00} \leftarrow 1_{01}$	6241.966	6241.854	7.08	7.08	0.21	0.21
(0,3,0)	$1_{11} \leftarrow 1_{10}$	6270.392	6270.272	2.13	2.13	0.19	0.19
(0,3,0)	$1_{10} \leftarrow 1_{11}$	6303.784	6303.676	3.36	3.36	0.29	0.29
(0,3,0)	$1_{01} \leftarrow 0_{00}$	6330.973	6330.850	1.21	1.21	0.31	0.31
(0,2,1)	$0_{00} \leftarrow 1_{11}$	6340.688	6340.456	9.36	9.37	0.27	0.27
(0,2,1)	$1_{01} \leftarrow 1_{10}$	6369.460	6369.219	6.04	6.04	0.51	0.51
(0,2,1)	$1_{10} \leftarrow 1_{01}$	6433.742	6433.514	4.64	4.64	0.38	0.38
(0,2,1)	$2_{02} \leftarrow 1_{11}$	6459.036	6458.794	2.47	2.47	0.34	0.34
(0,2,1)	$1_{11} \leftarrow 0_{00}$	6466.532	6466.300	4.10	4.10	1.00	1.00
(0,2,1)	$3_{03} \leftarrow 2_{12}$	6483.576	6483.335	3.86	3.86	0.44	0.44
(0,2,1)	$2_{12} \leftarrow 1_{01}$	6491.349	6491.124	4.49	4.49	0.60	0.60
(0,2,1)	$2_{21} \leftarrow 1_{10}$	6573.837	6573.616	3.64	3.64	0.47	0.47
(0,2,1)	$2_{20} \leftarrow 1_{11}$	6589.412	6589.193	2.49	2.49	0.32	0.32
(1,2,0)	$0_{00} \leftarrow 1_{01}$	6945.877	6945.831	10.25	10.30	0.22	0.23
(1,2,0)	$1_{11} \leftarrow 1_{10}$	6974.252	6974.199	5.54	5.54	0.36	0.36
(1,2,0)	$1_{10} \leftarrow 1_{11}$	7004.803	7004.759	5.10	5.10	0.33	0.33
(1,2,0)	$1_{01} \leftarrow 0_{00}$	7039.362	7039.309	3.72	3.72	0.70	0.70
(1,2,0)	$2_{12} \leftarrow 1_{11}$	7066.839	7066.777	3.60	3.60	0.37	0.37
(1,2,0)	$2_{02} \leftarrow 1_{01}$	7077.529	7077.470	4.05	4.05	0.42	0.42
(1,2,0)	$2_{11} \leftarrow 1_{10}$	7105.518	7105.464	3.38	3.38	0.35	0.35

Table 5.6: Asvany [15] data for the transitions of the (1,0,0) band of H_2D^+ detected with an optical parametric oscillator systems compared to the corresponding data as calculated from the ST1 list.

Transition	ν (cm^{-1})		A (s^{-1})		B (s^{-1})	
	Asv	ST1	Asv	ST1	Asv	ST1
$0_{00} \leftarrow 1_{01}$	2946.805	2946.790	53.167	53.200	0.318	0.318
$1_{10} \leftarrow 1_{11}$	3003.279	3003.267	27.509	27.500	0.466	0.465
$1_{01} \leftarrow 0_{00}$	3038.182	3038.158	20.353	20.400	1.000	1.000
$2_{12} \leftarrow 1_{11}$	3068.850	3068.817	20.088	20.100	0.532	0.531
$2_{20} \leftarrow 1_{01}$	3164.118	3164.110	1.5976	1.6000	0.040	0.039

increasingly at high temperatures. Moreover, the Sidhu list has a lower limit for the upper cut-off energy and hence the levels at the top cannot contribute to the high-energy transitions beyond a certain limit. We therefore expect our partition

function to be the more reliable one for $T > 1200$ K.

Using a Levenberg-Marquardt nonlinear curve-fitting routine, we fitted the ST1 partition function curve in the indicated range to a fifth order polynomial in temperature

$$\mathcal{P}(T) = \sum_{i=0}^5 a_i T^i \quad (5.4)$$

and obtained the following coefficients for T in Kelvin:

$$\begin{aligned} a_0 &= -0.300315 \\ a_1 &= +0.094722 \\ a_2 &= +0.000571 \\ a_3 &= -3.24415 \times 10^{-7} \\ a_4 &= +2.01240 \times 10^{-10} \\ a_5 &= -1.94176 \times 10^{-14} \end{aligned} \quad (5.5)$$

The fitting curve is not shown on Figure 5.2 because it is virtually identical to the ST1 curve within the graph resolution. The root-mean-square of the percentage error between the polynomial fit and the line list values, as given in Table 5.7, is about 0.18. It should be remarked that the fitting polynomial is valid only within the fitting temperature range (5 – 4000 K) and hence cannot be extrapolated beyond this range. Moreover, we recommend using the line list directly to obtain more reliable values for the partition function because the purpose of the fitting polynomial is to show the trend rather than to be a substitute for the line list.

5.3.3 Cooling Function

ST1 was also used to compute the cooling function of H_2D^+ as a function of temperature. The cooling function W which quantifies the rate of cooling per molecule

Table 5.7: The partition function of H_2D^+ for a number of temperatures as obtained from Sidhu *et al* [6] and ST1 line lists.

$T(\text{K})$	Partition Function		$T(\text{K})$	Partition Function	
	Sidhu	ST1		Sidhu	ST1
5	1.00	1.00	800	347.58	347.53
10	1.01	1.01	900	426.24	426.24
20	1.07	1.28	1000	515.43	516.31
30	2.15	2.15	1200	731.43	737.61
40	3.46	3.46	1400	1004.25	1026.84
50	5.05	5.05	1600	1339.43	1401.52
60	6.82	6.82	1800	1738.89	1881.33
70	8.73	8.73	2000	2203.94	2487.98
80	10.76	10.76	2200	2735.31	3244.83
90	12.90	12.89	2400	3327.58	4176.19
100	15.12	15.12	2600	3983.83	5306.36
150	27.56	27.55	2800	4698.51	6658.69
200	42.03	42.02	3000		8254.62
300	76.49	76.46	3200		10112.90
400	117.48	117.44	3400		12249.00
500	164.51	164.53	3600		14674.90
600	218.11	217.98	3800		17398.90
700	278.66	278.58	4000		20425.60

for dense gas in local thermodynamic equilibrium is given by

$$W(T) = \frac{1}{\mathcal{P}} \left(\sum_{u,l} A_{ul}(E_u - E_l)(2J_u + 1)g_u e^{\left(\frac{-E_u}{kT}\right)} \right) \quad (5.6)$$

where \mathcal{P} is the partition function as given by Equation 5.3, A is the spontaneous transition probability, E is the energy of the state above the ground level, J is the rotational angular momentum quantum number, k is Boltzmann's constant, T is the temperature, g is the nuclear spin degeneracy factor which, for H_2D^+ , is 1 for para states and 3 for ortho states, and u and l stand for the upper and lower levels respectively.

Figure 5.3 graphically presents ST1 cooling function (upper curve) as a function of temperature for a certain temperature range alongside the cooling function of

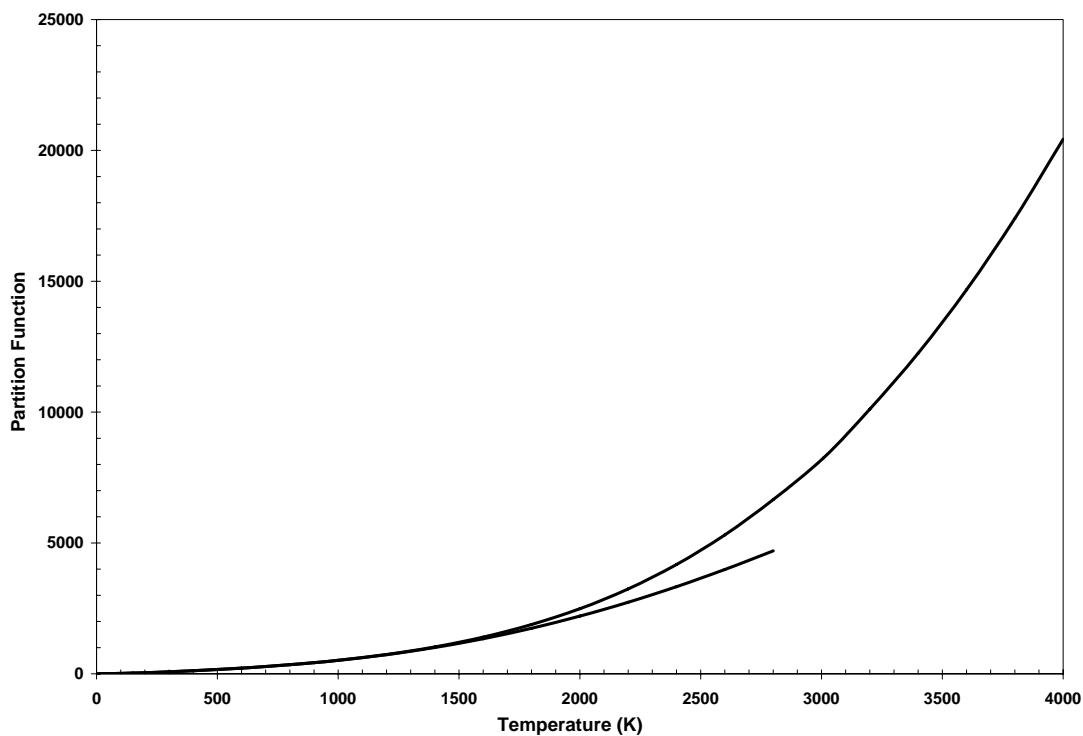


Figure 5.2: The H_2D^+ partition functions of ST1 (upper curve) and Sidhu *et al* [6] (lower curve).

Neale *et al* [7] for H_3^+ ion as obtained from a digitized image. As seen, the two curves match very well on the main part of the common temperature range ($T > 600$ K). However the H_2D^+ cooling function continues to be significant at lower temperatures, whereas at these temperatures the cooling curve of H_3^+ was not given by Neale *et al* [7] because they considered it too small to be of significance. This shows why the cooling properties of H_2D^+ could be important in the cold interstellar clouds. The larger values of ST1 can be explained by the inclusion of more energy states and the higher upper cut-off energy of this list. It should be remarked that Miller *et al* [255] have recently improved significantly the H_3^+ cooling function of Neale *et al* [7] by improving the fit to the calculated values of the partition function used in the original computations.

Using a Levenberg-Marquardt curve-fitting routine, we fitted our H_2D^+ cooling function curve to a fourth order polynomial in temperature over the range 10 –

4000 K and obtained

$$W(T) = \sum_{i=0}^4 b_i T^i \quad (5.7)$$

where

$$\begin{aligned} b_0 &= -1.34302 \times 10^{-16} \\ b_1 &= +1.56314 \times 10^{-17} \\ b_2 &= -2.69764 \times 10^{-19} \\ b_3 &= +7.03602 \times 10^{-22} \\ b_4 &= -1.10821 \times 10^{-25} \end{aligned} \quad (5.8)$$

The fit was essentially perfect on a linear scale.

5.3.4 Synthetic Spectra

One of the main uses of line lists such as ST1 is to generate temperature-dependent synthetic spectra. These spectra were generated from ST1 using the Spectra-BT2 code, which is described by Barber *et al* [253] and is a modified version of the original spectra code of Tennyson *et al* [256]. A Gaussian line profile with 10 data points per cm^{-1} was used in these computations. In Figure 5.4 a sample of these spectra for the temperatures $T = 100, 500, 1000$ and 2000 K over the frequency range $0 - 10000 \text{ cm}^{-1}$ is presented. Figure 5.4 (a) shows a temperature-dependent H_2D^+ absorption spectrum for the region largely associated with pure rotational transitions, while Figures 5.4 (b), (c) and (d) show the corresponding spectrum for the vibrational region. As is usual with rotation-vibration spectra, H_2D^+ spectra show a strong dependence on temperature.

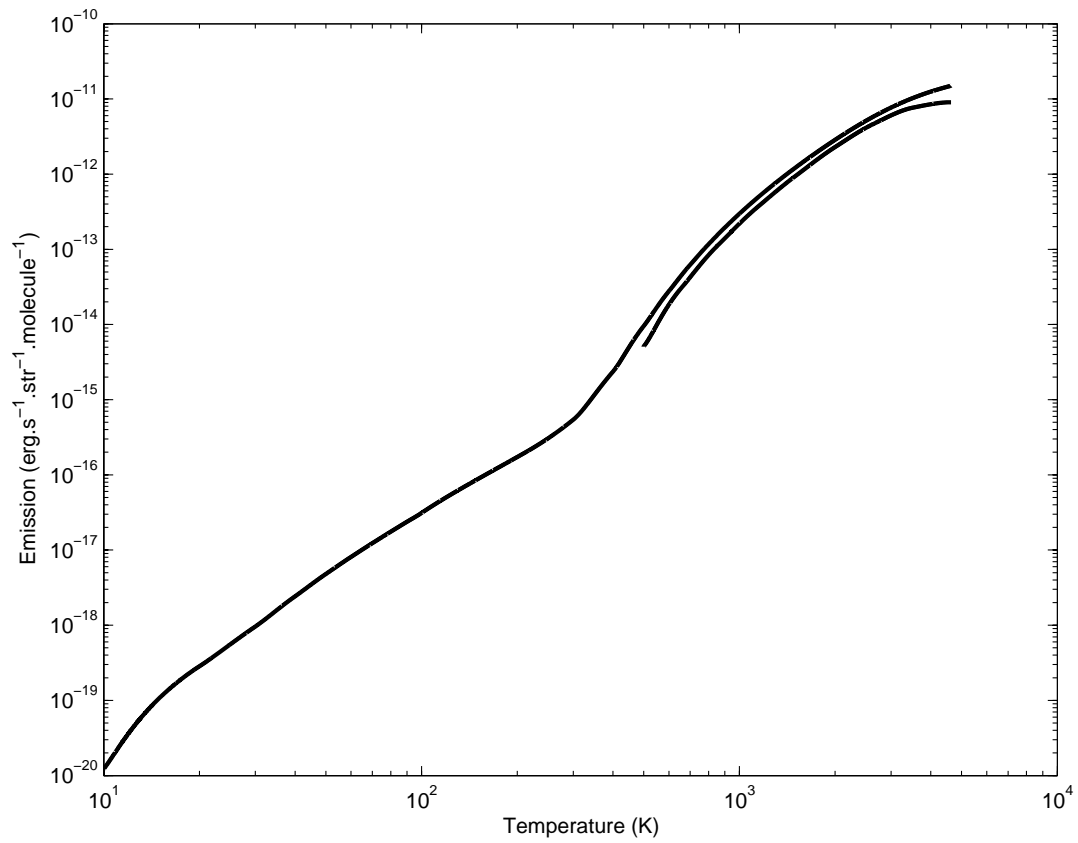


Figure 5.3: A graph of per molecule emission of H_2D^+ (upper curve) and H_3^+ (lower curve) as a function of temperature on a log-log scale. The H_2D^+ curve is obtained from ST1 while the H_3^+ curve is obtained from a digitized image from Neale *et al* [7].

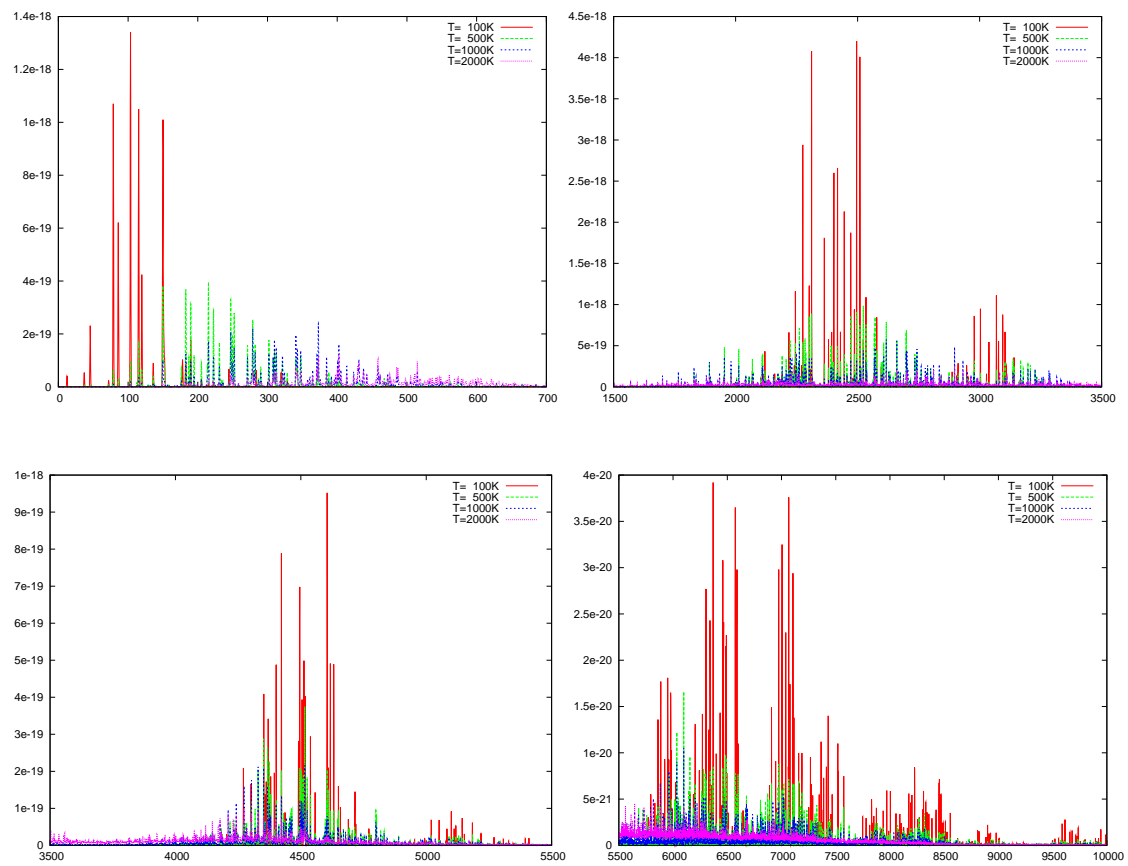


Figure 5.4: A graph of integrated absorption coefficient in cm.molecule^{-1} (on y axis) as a function of wave number in cm^{-1} (on x axis) within the range $0 - 10000 \text{ cm}^{-1}$ for $T = 100, 500, 1000$ and 2000 K .

Chapter 6

Conclusions and Future Work

6.1 Conclusions

In the first part of our atomic investigation, a list of line effective recombination coefficients is generated for the atomic ion C^+ using the **R**-matrix [104], Autostructure [41, 102, 103] and Emissivity [121] codes. These lines are produced by dielectronic capture and subsequent radiative decays of the low-lying autoionizing states above the threshold of $C^{2+} 1s^2 2s^2 1S^e$ with a principal quantum number $n < 5$ for the captured electron. The line list, called SS1, contains 6187 optically-allowed transitions which include many C II lines observed in astronomical spectra. Beside the effective recombination coefficients, the list also includes detailed data of level energies for bound and resonance states, and oscillator strengths. The theoretical results for energy and fine structure splitting agree very well with the available experimental data for both resonances and bound states. In the course of this investigation, a novel method, namely the **K**-matrix method, for finding and analyzing resonances was developed as an alternative to the **QB** [114, 123] and Time-Delay [124] methods. The **K**-matrix and **QB** methods produce virtually identical results; however, as far as the one-channel resonances related to the search for the low-lying autoion-

izing states is concerned, the **K**-matrix method offers a superior alternative to the **QB** method in terms of numerical stability, computational viability and comprehensiveness. The big advantage of **QB** is that it is more general and can be used for multi-channel as well as single-channel resonances. The **K**-matrix method was implemented, elaborated and used in the production of the atomic data leading to this investigation. The theoretical results of our line list were validated by a number of tests such as comparing the energy and fine structure splitting to the available experimental data [16] of autoionizing and bound states. A conclusive comparison to theoretical data previously reported in the literature; which include radiative transition probabilities, effective dielectronic recombination rate coefficients and autoionization probabilities; was carried out to verify our data. All these tests indicate the reliability of our line list. We expect SS1 to fill some of the existing gaps in the theoretical data needed for spectroscopic and astronomical applications.

In the second part of our atomic investigation, we studied the electron temperature of the emitting region of recombination lines in a number of astronomical objects, mainly planetary nebulae, by analyzing the transition lines of C II which originate from dielectronic recombination processes from the low-lying autoionizing states and subsequent cascade decays. The investigation is based on the use of theoretical data from SS1 list, and observational data from several sources in the refereed literature. In the emissivity analysis we used a least squares minimization method to find the electron temperature of the line emitting region in the investigated objects. Our results were broadly consistent with the reported findings of other studies in the literature, which are mainly obtained from other spectral lines with the use of different analysis techniques. The investigation was concluded by proposing and applying a method for determining electron energy distribution from observational data supplemented by theoretical data from SS1 to investigate the

long-standing problem in the nebular studies related to the dichotomy between the results of abundance and temperature obtained from ORLs and CELs. Although no definite conclusion has been reached, due to the limited quantity of the available pertinent observational data, the observational data seem to suggest a Maxwell-Boltzmann electron distribution opposite to what has been suggested recently in the literature of a κ -distribution.

In the molecular part of this study we investigated the generation of a new line list, called ST1, for the highly-important triatomic ion H_2D^+ . The list, which can be obtained from the Centre de Données astronomiques de Strasbourg (CDS) database, comprises over 33 thousand rotational-vibrational energy levels and more than 22 million transition lines archived within two files. Various rigorous tests were performed during all stages of production and after. All these tests confirmed that, although ST1 is based entirely on *ab initio* quantum mechanics, it is sufficiently accurate for almost all astronomical purposes. The one possible exception is for predicting the frequency of pure rotational transitions which are often needed to high accuracy and which are therefore better obtained from measured frequencies using combination differences. A number of comparisons to the available experimental and theoretical data were made. Several primary results, which include partition and cooling functions as well as temperature-dependent synthetic spectra, were also drawn from this list and presented in this thesis. These comparisons and results also confirmed the reliability of the list. We expect ST1 to be a helpful tool in analyzing and understanding physical processes in various H_2D^+ systems at spectroscopic and astronomical levels.

6.2 Recommendations for Future Work

There are many aspects of the current work that can be elaborated and extended in the future; some of these prospectives are outlined in the following points

- Extending the theoretical and computational treatments of the atomic investigation by employing more comprehensive theory to incorporate processes and phenomena other than dielectronic recombination, such as radiative recombination and collisional processes. Some of these treatments are already developed and implemented within existing codes while others require developing novel tools.
- Extending the **K**-matrix method to include multi-channel resonances and implementing it within the **R**-matrix code or as a stand alone code.
- Pushing the current limit on the principal quantum number of the active electron in the autoionizing states beyond the $n < 5$ condition which is adopted in the present work. This extension becomes more important at higher temperatures, as the contribution of resonances arising from the $n \geq 5$ levels increases.
- Extending the electron temperature analysis to more data sets and including even the bound-bound transition lines. This depends on the availability of a more comprehensive C II list generated on the base of a more comprehensive theoretical foundation which includes processes other than dielectronic recombination, as indicated earlier.
- Improving the least squares method for electron temperature analysis and performing more tests and validations by application to more data sets to identify and fix any possible weaknesses. One of the objectives is to reduce the

temperature dependency of the χ^2 curve shape which affects the confidence interval.

- Extending the H₂D⁺ line list beyond its current limits of $J \leq 20$ for rotational quantum number and $\nu < 18500 \text{ cm}^{-1}$ for frequency.

Bibliography

- [1] Fang X.; Liu X.-W. Very deep spectroscopy of the bright Saturn nebula NGC 7009 - I. Observations and plasma diagnostics. *Monthly Notices of the Royal Astronomical Society*, 415(1):181–198, 2011.
- [2] Baluteau J.P.; Zavagno A.; Morisset C.; Péquignot D. The 654-1046 NM line spectrum of the planetary nebula NGC 7027. *Astronomy and Astrophysics*, 303:175–203, 1995.
- [3] Zhang Y.; Liu X.-W.; Luo S.-G.; Péquignot D.; Barlow M.J. Integrated spectrum of the planetary nebula NGC 7027. *Astronomy and Astrophysics*, 442(1):249–262, 2005.
- [4] Sharpee B.; Williams R.; Baldwin J.A.; van Hoof P.A.M. Introducing EMILI: Computer-aided Emission Line Identification . *The Astrophysical Journal Supplement Series*, 149:157–187, 2003.
- [5] De Marco O.; Storey P.J.; Barlow M.J. The WC10 central stars CPD-56 degrees 8032 and He 2-113 - III. Wind electron temperatures and abundances. *Monthly Notices of the Royal Astronomical Society*, 297(4):999–1014, 1997.
- [6] Sidhu K.S.; Miller S.; Tennyson J. Partition functions and equilibrium constants for h3p and H₂D⁺. *Astronomy and Astrophysics*, 255(1-2):453–456, 1992.
- [7] Neale L.; Miller S.; Tennyson J. Spectroscopic Properties of the H₃⁺ Molecule: A New Calculated Line List. *The Astrophysical Journal*, 464:516–520, 1996.
- [8] Badnell N.R. The influence of core fine-structure interactions on dielectronic recombination at low temperatures: B-like C, N and O recombined ions. *Journal of Physics B*, 21(5):749–767, 1988.
- [9] Harrington J.P.; Lutz J.H.; Seaton M.J. Ultraviolet spectra of planetary nebulae. IV - The C III λ 2297 dielectronic recombination line and dust absorption in the C IV λ 1549 resonance doublet. *Monthly Notices of the Royal Astronomical Society*, 195:21P–26P, 1981.
- [10] Peimbert M.; Peimbert A.; Ruiz M.T.; Esteban C. Physical Conditions of the Planetary Nebula NGC 5315 Derived from VLT Echelle Observations and

- the t^2 Problem. *The Astrophysical Journal Supplement Series*, 150:431–454, 2004.
- [11] García-Rojas J.; Pena M.; Peimbert A. Faint recombination lines in Galactic PNe with a [WC] nucleus. *Astronomy and Astrophysics*, 496(1):139–152, 2009.
- [12] Ferland G.J.; Williams R.E.; Lambert D.L.; Shields G.A.; Slovak M.; Gondhalekar P.M.; Truran J.W. IUE observations of DQ Herculis and its nebula, and the nature of the cold nova shells. *The Astrophysical Journal*, 281:194–204, 1984.
- [13] Davey A.R. *The recombination spectrum of carbon* II. PhD thesis, University College London, 1995.
- [14] Barlow M.J.; Storey P.J. In: *Planetary Nebulae; Proceedings of the International Astronomical Union Symposium, Innsbruck, Austria, July 13-17, 1992*, volume 155. Kluwer Academic Publishers, 1993.
- [15] Asvany O.; Hugo E.; Müller F.; Kühnemann F.; Schiller S.; Tennyson J.; Schlemmer S. Overtone spectroscopy of H_2D^+ and D_2H^+ using laser induced reactions. *Journal of Chemical Physics*, 127:154317(1–11), 2007.
- [16] National Institute of Standards and Technology (NIST). URL: <http://www.nist.gov>. 2010.
- [17] Péquignot D.; Petitjean P.; Boisson C. Total and effective radiative recombination coefficients. *Astronomy and Astrophysics*, 251(2):680–688, 1991.
- [18] Nahar S.N.; Pradhan A.K.; Zhang H.L. Electron-Ion Recombination Rate Coefficients and Photoionization Cross Sections for Astrophysically Abundant Elements. IV. Relativistic Calculations for C IV and C V for Ultraviolet and X-Ray Modeling . *The Astrophysical Journal Supplement Series*, 131(1):375–389, 2000.
- [19] Badnell N.R.; O’Mullane M.G.; Summers H.P.; Altun Z.; Bautista M.A.; Colgan J.; Gorczyca T.W.; Mitnik D.M.; Pindzola M.S.; Zatsarinny O. Dielectronic recombination data for dynamic finite-density plasmas I. Goals and methodology. *Astronomy and Astrophysics*, 406(3):1151–1165, 2003.
- [20] Aldrovandi S.M.V.; Péquignot D. Radiative and Dielectronic Recombination Coefficients for Complex Ions. *Astronomy and Astrophysics*, 25:137–140, 1973.
- [21] Aldrovandi S.M.V.; Péquignot D. Ionization and Heating of a Low Density Plasma by Energetic Particles. *Astronomy and Astrophysics*, 26:33–43, 1973.
- [22] Ferland G.J. Quantitative Spectroscopy of Photoionized Clouds. *Annual Review of Astronomy and Astrophysics*, 41:517–554, 2003.

- [23] Peng Y.-L.; Han X.-Y.; Wang M.-S.; Li J.-M. A theoretical study of dielectronic recombination processes of C^{2+} ions in planetary nebulae. *Journal of Physics B*, 38(21):3825–3839, 2005.
- [24] Massey H.S.W; Bates D.R. The properties of neutral and ionized atomic oxygen and their influence on the upper atmosphere. *Reports on Progress in Physics*, 9(1):62–74, 1942.
- [25] Bates D.R.; Massey H.S.W. The Negative Ions of Atomic and Molecular Oxygen. *Philosophical Transactions of the Royal Society of London, Series A*, 239(806):269–304, 1943.
- [26] Burgess A. Dielectronic recombination and the temperature of the solar corona. *The Astrophysical Journal*, 139:776–780, 1964.
- [27] Goldberg L. In: *Interstellar Ionized Hydrogen, Proceedings of NRAO-AIO H II Region Symposium*. W.A. Benjamin Inc., New York, 1968.
- [28] Seaton M.J. Quantum defect theory VII. Analysis of resonance structures. *Journal of Physics B*, 2(1):5–11, 1969.
- [29] Davies P.C.W; Seaton M.J. Radiation damping in the optical continuum. *Journal of Physics B*, 2(7):757–765, 1969.
- [30] Presnyakov L.P.; Urnov A.M. Asymptotic approach to the theory of excitation of multiply-charged ions by electron impact. *Journal of Physics B*, 8(8):1280–1288, 1975.
- [31] Beigman I.L.; Chichkov B.N. Dielectronic recombination through the forbidden levels. *Journal of Physics B*, 13(3):565–569, 1980.
- [32] Storey P.J. Dielectronic recombination at nebular temperatures. *Monthly Notices of the Royal Astronomical Society*, 195:27P–31P, 1981.
- [33] Nussbaumer H.; Storey P.J. Dielectronic recombination at low temperatures. *Astronomy and astrophysics*, 126(1):75–79, 1983.
- [34] Bell R.H.; Seaton M.J. Dielectronic recombination. I. General theory. *Journal of Physics B*, 18(8):1589–1629, 1985.
- [35] Harmin D.A. Precise Theory of Field Enhancement of Dielectronic Recombination. *Physical Review Letters*, 57(13):1570–1573, 1986.
- [36] Nussbaumer H.; Storey P.J. Dielectronic recombination at low temperatures. IV. Recombination coefficients for neon. *Astronomy and Astrophysics Supplement Series*, 69:123–133, 1987.
- [37] Badnell N.R. Di-electronic recombination of He-like ions: Fe^{24+} . *Journal of Physics B*, 19:1541–1552, 1986.

- [38] Badnell N.R. Electron impact excitation of He. *Journal of Physics B*, 17(19):4013–4032, 1984.
- [39] Badnell N.R. Dielectronic recombination of Fe²²⁺ and Fe²⁴⁺. *Journal of Physics B*, 19:3827–3835, 1986.
- [40] Badnell N.R. Dielectronic recombination of Fe¹³⁺: benchmarking the M-shell. *Journal of Physics B*, 39(23):4825–4852, 2006.
- [41] Badnell N.R. Autostructure writeup on the world wide web. URL: <http://amdpp.phys.strath.ac.uk/autos/ver/WRITEUP>. 2011.
- [42] LaGattuta K.; Nasser I.; Hahn Y. The effect of static electric fields on dielectronic recombination: I. Basic theory. *Journal of Physics B*, 20(7):1565–1576, 1987.
- [43] Sakimoto K. Dielectronic recombination in electric fields: a quantum-defect theory approach. *Journal of Physics B*, 20(4):807–819, 1987.
- [44] Nahar S.N.; Pradhan A.K. Unified treatment of electron-ion recombination in the close-coupling approximation. *Physical Review A*, 49(3):1816–1835, 1994.
- [45] Nahar S.N.; Pradhan A.K. Unified Electron-Ion Recombination Rate Coefficients of Silicon and Sulfur Ions. *The Astrophysical Journal*, 447:966–979, 1995.
- [46] Leibowitz E.M. The emission spectrum of the ion C IV in planetary nebulae. *Monthly Notices of the Royal Astronomical Society*, 157:97–102, 1972.
- [47] Leibowitz E.M. Polarization of C IV emission lines in planetary nebulae. *Monthly Notices of the Royal Astronomical Society*, 157:115–120, 1972.
- [48] Balick B.; Gammon R.H.; Doherty L.H. The Structure of the Orion Nebula. I. Observations of the C 85 α Recombination Line. *The Astrophysical Journal*, 188:45–52, 1974.
- [49] Nussbaumer H.; Storey P.J. The Ionization Balance of C⁰ to C⁺⁴. *Astronomy and astrophysics*, 44:321–327, 1975.
- [50] Nussbaumer H.; Storey P.J. Dielectronic recombination at low temperatures. II. Recombination coefficients for lines of C, N, O. *Astronomy and Astrophysics Supplement Series*, 56:293–312, 1984.
- [51] Boughton W.L. Carbon recombination lines and the neutral hydrogen clouds near the Orion Nebula. *The Astrophysical Journal*, 222:517–526, 1978.
- [52] Harrington J.P.; Lutz J.H.; Seaton M.J.; Stickland D.J. Ultraviolet spectra of planetary nebulae - I. The abundance of carbon in IC 418. *Monthly Notices of the Royal Astronomical Society*, 191:13–22, 1980.

- [53] Clavel J.; Flower D.R.; Seaton M.J. Ultraviolet spectra of planetary nebulae. V - The C II λ 1335 dielectronic recombination lines in IC 418. *Monthly Notices of the Royal Astronomical Society*, 197:301–311, 1981.
- [54] Clegg R.E.S.; Seaton M.J.; Peimbert M.; Torres-Peimbert S. Analysis of nebulosity in the planetary nebula NGC 40. *Monthly Notices of the Royal Astronomical Society*, 205:417–434, 1983.
- [55] Hayes M.A.; Nussbaumer H. The C II infrared and ultraviolet lines. *Astronomy and Astrophysics*, 134(1):193–197, 1984.
- [56] Kholtygin A.F. Carbon Abundance in planetary nebulas. *Astrofizika*, 20(3):503–511, 1984.
- [57] Kholtygin A.F. Inhomogeneous planetary nebulae: carbon and oxygen abundances. *Astronomy and Astrophysics*, 329:691–703, 1998.
- [58] Bogdanovich P.O.; Nikitin A.A.; Rudzikas Z.B.; Kholtygin A.F. Lines of carbon, nitrogen, and oxygen ions in the spectra of planetary nebulas. II - Intensities of the C II and N III recombination lines and abundances of the C III and N IV ions. *Astrofizika*, 23(2):427–435, 1985.
- [59] Rola C.; Stasińska G. The carbon abundance problem in planetary nebulae. *Astronomy and Astrophysics*, 282(1):199–212, 1994.
- [60] Davey A.R.; Storey P.J.; Kisielius R. Recombination coefficients for C II lines. *Astronomy and Astrophysics Supplement Series*, 142:85–94, 2000.
- [61] Liu Y.; Liu X.-W.; Barlow M.J.; Luo S.-G. Chemical abundances of planetary nebulae from optical recombination lines - II. Abundances derived from collisionally excited lines and optical recombination lines. *Monthly Notices of the Royal Astronomical Society*, 353(4):1251–1285, 2004.
- [62] Peng Y.-L.; Wang M.-S.; Han X.-Y.; Li J.-M. Theoretic Study of C II Recombination Line. *Chinese Physics Letters*, 21(9):1723–1726, 2004.
- [63] Liu X.-W.; Luo S.-G.; Barlow M.J.; Danziger I.J.; Storey P.J. Chemical abundances of planetary nebulae from optical recombination lines - III. The Galactic bulge PN M 1-42 and M 2-36. *Monthly Notices of the Royal Astronomical Society*, 327(1):141–168, 2001.
- [64] Sharpee B.; Baldwin J.A.; Williams R. Identification and Characterization of Faint Emission Lines in the Spectrum of the Planetary Nebula IC 418. *The Astrophysical Journal*, 615(1):323–343, 2004.
- [65] Flower D.R. Ultraviolet spectra of planetary nebulae. VIII - The C/O abundance ratio in the Ring nebula. *Monthly Notices of the Royal Astronomical Society*, 199:15P–18P, 1982.

- [66] Barker T. The ionization structure of planetary nebulae. VII. New observations of the Ring Nebula. *The Astrophysical Journal*, 322:922–929, 1987.
- [67] Aller L.H.; Keyes C.D. The spectrum of NGC 7027 (367-650 nm). *Proceedings of the National Academy of Sciences of the United States of America*, 85(8):2417–2421, 1988.
- [68] Petitjean P.; Boisson C.; Péquignot D. A photoionization model study of the old nova shell DQ Herculis 1934. *Astronomy and astrophysics*, 240(2):433–452, 1990.
- [69] Liu X.-W.; Storey P.J.; Barlow M.J.; Clegg R.E.S. The rich O II recombination spectrum of the planetary nebula NGC 7009: new observations and atomic data. *Monthly Notices of the Royal Astronomical Society*, 272(2):369–388, 1995.
- [70] Liu X.-W.; Storey P.J.; Barlow M.J.; Danziger I.J.; Cohen M.; Bryce M. NGC 6153: a super-metal-rich planetary nebula? *Monthly Notices of the Royal Astronomical Society*, 312(3):585–628, 2000.
- [71] Liu X.-W.; Barlow M.J.; Zhang Y.; Bastin R.J.; Storey P.J. Chemical abundances for Hf 2-2, a planetary nebula with the strongest-known heavy-element recombination lines. *Monthly Notices of the Royal Astronomical Society*, 368(4):1959–1970, 2006.
- [72] Esteban C.; Peimbert M.; Torres-Peimbert S.; Escalante V. Faint Emission Lines in the Orion Nebula: C and O Abundances. *Revista Mexicana de Astronomia y Astrofisica Serie de Conferencias*, 3:241–244, 1995. The Fifth Mexico-Texas Conference on Astrophysics: Gaseous Nebulae and Star Formation, Tequesquitengo, Mor., Mexico, April 3-5.
- [73] Esteban C.; Peimbert M.; Torres-Peimbert S.; Escalante V. Chemical composition of the Orion nebula derived from echelle spectrophotometry. *Monthly Notices of the Royal Astronomical Society*, 295(2):401–422, 1998.
- [74] Esteban C.; Peimbert M.; Torres-Peimbert S.; Rodríguez M. Optical Recombination Lines of Heavy Elements in Giant Extragalactic H II Regions. *The Astrophysical Journal*, 581(1):241–257, 2002.
- [75] Esteban C.; Peimbert M.; García-Rojas J.; Ruiz M.T.; Peimbert A.; Rodríguez M. A reappraisal of the chemical composition of the Orion nebula based on Very Large Telescope echelle spectrophotometry. *Monthly Notices of the Royal Astronomical Society*, 355(1):229–247, 2004.
- [76] Esteban C.; Bresolin F.; Peimbert M.; García-Rojas J.; Peimbert A.; Mesa-Delgado A. Keck HIRES Spectroscopy of Extragalactic H II Regions: C and O Abundances from Recombination Lines. *The Astrophysical Journal*, 700(1):654–678, 2009.

- [77] Garnett D.R.; Dinerstein H.L. Spatially Resolved O II Recombination Line Observations of the Ring Nebula, NGC 6720. *The Astrophysical Journal*, 558(1):145–156, 2001.
- [78] Bernard-Salas J.; Pottasch S.R.; Beintema D.A.; Wesselius P.R. The ISO-SWS spectrum of planetary nebula NGC 7027. *Astronomy and Astrophysics*, 367(3):949–958, 2001.
- [79] Bernard-Salas J.; Pottasch S.R.; Feibelman W.A.; Wesselius P.R. An ISO and IUE study of planetary nebula NGC 2440. *Astronomy and Astrophysics*, 387(1):301–309, 2002.
- [80] Bernard-Salas J.; Pottasch S.R.; Wesselius P.R.; Feibelman W.A. Abundances of Planetary Nebulae BD+30 3639 and NGC 6543. *Astronomy and Astrophysics*, 406(1):165–174, 2003.
- [81] Bernard-Salas J.; Pottasch S.R.; Beintema D.A.; Wesselius P.R. *Erratum* The ISO-SWS spectrum of planetary nebula NGC7027. *Astronomy and Astrophysics*, 406(1):175, 2003.
- [82] Peimbert A. The Chemical Composition of the 30 Doradus Nebula Derived from Very Large Telescope Echelle Spectrophotometry. *The Astrophysical Journal*, 584:735–750, 2003.
- [83] Wesson R.; Liu X.-W.; Barlow M.J. Physical conditions in the planetary nebula Abell 30. *Monthly Notices of the Royal Astronomical Society*, 340(1):253–263, 2003.
- [84] Wesson R.; Liu X.-W. Physical conditions in the planetary nebula NGC 6543. *Monthly Notices of the Royal Astronomical Society*, 351(3):1026–1042, 2004.
- [85] Wesson R.; Liu X.-W.; Barlow M.J. The abundance discrepancy - recombination line versus forbidden line abundances for a northern sample of galactic planetary nebulae. *Monthly Notices of the Royal Astronomical Society*, 362(2):424–454, 2005.
- [86] Wesson R.; Barlow M.J.; Liu X.-W.; Storey P.J.; Ercolano B.; De Marco O. The hydrogen-deficient knot of the ‘born-again’ planetary nebula Abell 58 (V605 Aql). *Monthly Notices of the Royal Astronomical Society*, 383(4):1639–1648, 2008.
- [87] Tsamis Y.G.; Barlow M.J.; Liu X.-W.; Danziger I.J.; Storey P.J. Heavy elements in Galactic and Magellanic Cloud HII regions: recombination-line versus forbidden-line abundances. *Monthly Notices of the Royal Astronomical Society*, 338(3):687–710, 2003.
- [88] Tsamis Y.G.; Barlow M.J.; Liu X.-W.; Danziger I.J.; Storey P.J. A deep survey of heavy element lines in planetary nebulae - I. Observations and

- forbidden-line densities, temperatures and abundances. *Monthly Notices of the Royal Astronomical Society*, 345(1):186–220, 2003.
- [89] Tsamis Y.G.; Barlow M.J.; Liu X.-W.; Storey P.J.; Danziger I.J. A deep survey of heavy element lines in planetary nebulae - II. Recombination-line abundances and evidence for cold plasma. *Monthly Notices of the Royal Astronomical Society*, 353(3):953–979, 2004.
- [90] Tsamis Y.G.; Walsh J.R.; Péquignot D.; Barlow M.J.; Danziger I.J.; Liu X.-W. Integral field spectroscopy of planetary nebulae: mapping the line diagnostics and hydrogen-poor zones with VLT FLAMES. *Monthly Notices of the Royal Astronomical Society*, 386(1):22–46, 2008.
- [91] Ruiz M.Te.; Peimbert A.; Peimbert M.; Esteban C. Very Large Telescope Echelle Spectrophotometry of the Planetary Nebula NGC 5307 and Temperature Variations. *The Astrophysical Journal*, 595(1):247–258, 2003.
- [92] García-Rojas J.; Esteban C.; Peimbert M.; Rodríguez M.; Ruiz M.T.; Peimbert A. Chemical Abundances of the Galactic H II Region NGC 3576 Derived from Very Large Telescope Echelle Spectrophotometry. *The Astrophysical Journal Supplement Series*, 153(2):501–522, 2004.
- [93] García-Rojas J.; Esteban C.; Peimbert A.; Peimbert M.; Rodríguez M.; Ruiz M.T. Deep echelle spectrophotometry of S 311, a Galactic H II region located outside the solar circle. *Monthly Notices of the Royal Astronomical Society*, 362(1):301–312, 2005.
- [94] García-Rojas J.; Esteban C.; Peimbert M.; Costado M.T.; Rodríguez M.; Peimbert A.; Ruiz M.T. Faint emission lines in the Galactic H II regions M16, M20 and NGC 3603. *Monthly Notices of the Royal Astronomical Society*, 368(1):253–279, 2006.
- [95] García-Rojas J.; Esteban C.; Peimbert A.; Rodríguez M.; Peimbert M.; Ruiz M.T. The chemical composition of the Galactic regions M8 and M17. A revision based on deep VLT echelle spectrophotometry. *Revista Mexicana de Astronomía y Astrofísica*, 43:3–31, 2007.
- [96] Ercolano B.; Wesson R.; Zhang Y.; Barlow M.J.; De Marco O.; Rauch T.; Liu X.-W. Observations and three-dimensional photoionization modelling of the Wolf-Rayet planetary nebula NGC 1501. *Monthly Notices of the Royal Astronomical Society*, 354(2):558–574, 2004.
- [97] Stasińska G.; Gräfener G.; Pena M.; Hamann W.-R.; Koesterke L.; Szczerba R. Comprehensive modelling of the planetary nebula LMC-SMP 61 and its [WC]-type central star. *Astronomy and Astrophysics*, 413(1):329–342, 2004.
- [98] Robertson-Tessi M.; Garnett D.R. Recombination line versus forbidden line abundances in planetary nebulae. *The Astrophysical Journal Supplement Series*, 157:371–395, 2005.

- [99] Wang W.; Liu X.-W. Elemental abundances of Galactic bulge planetary nebulae from optical recombination lines. *Monthly Notices of the Royal Astronomical Society*, 381(2):669–701, 2007.
- [100] Sharpee B.; Zhang Y.; Williams R.; Pellegrini E.; Cavagnolo K.; Baldwin J.A.; Phillips M.; X.-W. Liu. *s*-Process Abundances in Planetary Nebulae. *The Astrophysical Journal*, 659(2):1265–1290, 2007.
- [101] Williams R.; Jenkins E.B.; Baldwin J.A.; Zhang Y.; Sharpee B.; Pellegrini E.; Phillips M. Independent Emission and Absorption Abundances for Planetary Nebulae. *The Astrophysical Journal*, 677(2):1100–1119, 2008.
- [102] Eissner W.; Jones M.; Nussbaumer H. Techniques for the calculation of atomic structures and radiative data including relativistic corrections. *Computer Physics Communications*, 8(4):270–306, 1974.
- [103] Nussbaumer H.; Storey P.J. The C III transition probabilities. *Astronomy and Astrophysics*, 64(1-2):139–144, 1978.
- [104] Berrington K.A.; Eissner W.B.; Norrington P.H. RMATRX1: Belfast atomic R-matrix codes. *Computer Physics Communications*, 92(2):290–420, 1995.
- [105] Kisielius R.; Storey P.J.; Davey A.R.; Neale L.T. Recombination coefficients for Ne II lines at nebular temperatures and densities. *Astronomy and Astrophysics Supplement*, 133:257–269, 1998.
- [106] Liu X.-W. Optical Recombination Lines and Temperature Fluctuations. *Proceedings of the Conference to Celebrate the 60th Birthdays of Silvia Torres-Peimbert and Manuel Peimbert, Mexico City*, 12:70–76, 2002.
- [107] Tsamis Y.G.; Walsh J.R.; Péquignot D.; Barlow M.J.; Liu X.-W.; Danziger I.J. Integral-field Spectroscopy of Galactic Planetary Nebulae with VLT FLAMES. *The Messenger*, 127:53–57, 2007.
- [108] Garnett D.R.; Dinerstein H.L. The O II Recombination Line Abundance Problem in Planetary Nebulae. *Revista Mexicana de Astronomía y Astrofísica (Serie de Conferencias)*, 10:13–18, 2001.
- [109] Nicholls D.C.; Dopita M.A.; Sutherland R.S. Resolving the electron temperature discrepancies in H II regions and planetary nebulae: κ -distributed electrons. *The Astrophysical Journal*, 752(2):148, 2012.
- [110] Seaton M.J. Use of the R-matrix method for bound-state calculations: I. General theory. *Journal of Physics B*, 18(11):2111–2131, 1985.
- [111] Berrington K.A.; Eissner W.B.; Saraph H.E.; Seaton M.J.; Storey P.J. A comparison of close-coupling calculations using UCL and QUB codes. *Computer Physics Communications*, 44(1-2):105–119, 1987.

- [112] Berrington K.A.; Burke P.G.; Butler K.; Seaton M.J.; Storey P.J.; Taylor K.T.; Yu Yan. Atomic data for opacity calculations: II. Computational methods. *Journal of Physics B*, 20(23):6379–6397, 1987.
- [113] Badnell N.R. RMATRIX-I writeup on the world wide web. URL: http://amdpp.phys.strath.ac.uk/UK_RmaX/codes/serial/WRITEUP. 2009.
- [114] Quigley L.; Berrington K.A.; Pelan J. The QB program: Analysing resonances using R-matrix theory. *Computer Physics Communications*, 114(1-3):225–235, 1998.
- [115] Hibbert A. CIV3 - A general program to calculate configuration interaction wave functions and electric-dipole oscillator strengths. *Computer Physics Communications*, 9(3):141–172, 1975.
- [116] Sochi T.; Storey P.J. Dielectronic Recombination Lines of C⁺. *Atomic Data and Nuclear Data Tables (Accepted)*, 2012.
- [117] Nussbaumer H.; Storey P.J. C II two-electron transitions. *Astronomy and Astrophysics*, 96(1-2):91–95, 1981.
- [118] Yan Y.; Seaton M.J. Atomic data for opacity calculations. IV. Photoionisation cross sections for C II. *Journal of Physics B*, 20(23):6409–6429, 1987.
- [119] Benoy D.A.; Mullen J.A.M.; Schram D.C. Radiative energy loss in a non-equilibrium argon plasma. *Journal of Physics D*, 26(9):1408–1413, 1993.
- [120] Seaton M.J.; Storey P.J. Di-electronic recombination. *In: Atomic Processes and Applications; North-Holland Publishing Company*, pages 133–197, 1976.
- [121] Sochi T. Emissivity: A program for atomic transition calculations. *Communications in Computational Physics*, 7(5):1118–1130, 2010.
- [122] Hibbert A. Oscillator strengths of transitions in the beryllium sequence. *Journal of Physics B*, 7(12):1417–1434, 1974.
- [123] Quigley L.; Berrington K.A. The QB method: analysing resonances using R-matrix theory. Applications to C⁺, He and Li. *Journal of Physics B*, 29(20):4529–4542, 1996.
- [124] Stibbe D.T.; Tennyson J. TIMEDEL: A program for the detection and parameterization of resonances using the time-delay matrix. *Computer Physics Communications*, 114(1-3):236–242, 1998.
- [125] Bartschat K.; Burke P.G. Resfit - A multichannel resonance fitting program. *Computer Physics Communications*, 41(1):75–84, 1986.

- [126] Tennyson J.; Noble C.J. RESON-A program for the detection and fitting of Breit-Wigner resonances. *Computer Physics Communications*, 33(4):421–424, 1984.
- [127] Stibbe D.T.; Tennyson J. Time-delay matrix analysis of resonances in electron scattering: e^- - H_2 and H_2^+ . *Journal of Physics B*, 29:4267–4283, 1996.
- [128] Smith F.T. Lifetime Matrix in Collision Theory. *Physical Review*, 118(1):349–356, 1960.
- [129] Berrington K.A.; Burke P.G.; Dufton P.L.; Kingston A.E. Electron collisional excitation of C III and O V. *Journal of Physics B*, 10(8):1465–1475, 1977.
- [130] Eissner W.; Nussbaumer H. A programme for calculating atomic structures. *Journal of Physics B*, 2(10):1028–1043, 1969.
- [131] Storey P.J. Recombination coefficients for O II lines at nebular temperatures and densities. *Astronomy and Astrophysics*, 282(3):999–1013, 1994.
- [132] Lennon D.J.; Dufton P.L.; Hibbert A.; Kingston A.E. C II emission lines formed in optically thin plasmas. *The Astrophysical Journal*, 294:200–206, 1985.
- [133] Huber M.C.E.; Sandeman R.J.; Tozzi G.P. Branching Ratios of the $2s^23p\ ^2P^0$ Term of Singly-Ionized Carbon. *Physica Scripta*, T8:95–99, 1984.
- [134] Glenzer S.; Kunze H.-J.; Musielok J.; Kim Y.-K.; Wiese W.L. Investigation of LS coupling in boronlike ions. *Physical Review A*, 49(1):221–227, 1994.
- [135] Fang Z.; Kwong V.H.S.; Wang J. Measurements of radiative-decay rates of the $2s^22p(^2P^o)$ - $2s2p^2(^4P)$ intersystem transitions of C II. *Physical Review A*, 48(2):1114–1122, 1993.
- [136] Dankwort W.; Trefftz E. Breit-Pauli approximation for highly ionized boronlike ions, up to Fe XXII. *Astronomy and Astrophysics*, 65(1):93–98, 1978.
- [137] Pottasch S.R.; Wesselius P.R.; van Duinen R.J. Ultraviolet observations of planetary nebulae. IV. The C IV lines at $\lambda 1550\ \text{\AA}$. *Astronomy and Astrophysics*, 70:629–634, 1978.
- [138] Nikitin A.A.; Sapar A.A.; Feklistove T.H.; Kholtygin A.F. Emission-line spectra and the abundance of carbon and nitrogen ions in planetary nebulae. *Soviet Astronomy*, 25(1):56–58, 1981.
- [139] Bogdanovich P.O.; Lukoshiavichius R.A.; Nikitin A.A.; Rudzikas Z.B.; Kholtygin A.F. Lines of carbon, nitrogen, and oxygen ions in the spectra of planetary nebulas. I. Transition probabilities and oscillator strengths. *Astrophysics*, 22(3):326–334, 1985.

- [140] Adams S.; Seaton M.J. Ultraviolet spectra of planetary nebulae. VII - The abundance of carbon in the very low excitation nebula He 2-131. *Monthly Notices of the Royal Astronomical Society*, 200:7P–12P, 1982.
- [141] Clegg R.E.S.; Storey P.J.; Walsh J.R.; Neale L. Measurement of the $^{12}\text{C}/^{13}\text{C}$ ratio in planetary nebulae. *Monthly Notices of the Royal Astronomical Society*, 284(2):348–358, 1997.
- [142] Storey P.J.; Sochi T. Electron Temperature of Planetary Nebulae from C II Recombination Lines. *Submitted*, 2012.
- [143] Nikitin A.A.; Yakubovskii O.A. The Investigation of the N III Recombination Spectrum in Stellar Envelopes and Nebulae. VI. The Equations of Statistical Equilibrium for the Lower Excited Levels of C II, N III, and O IV. *Soviet Astronomy*, 7(2):189–198, 1963.
- [144] Stanghellini L.; Shaw R.A.; Gilmore D. Space Telescope Imaging Spectrograph Ultraviolet Spectra of Large Magellanic Cloud Planetary Nebulae: A Study of Carbon Abundances and Stellar Evolution. *The Astrophysical Journal*, 622(1):294–318, 2005.
- [145] Press W.H.; Teukolsky S.A.; Vetterling W.T.; Flannery B.P. *Numerical Recipes in C++ The Art of Scientific Computing*. Cambridge University Press, 2nd edition, 2002.
- [146] Illingworth V.; Clark J., editor. *Collins Dictionary of Astronomy*. Harper-Collins Publishers, 2000.
- [147] Matzner R.A., editor. *Dictionary of Geophysics, Astrophysics and Astronomy*. CRC Press, 2001.
- [148] Tennyson J. *Astronomical Spectroscopy: An Introduction to the Atomic and Molecular Physics of Astronomical Spectra*. Imperial College Press, 1st edition, 2005.
- [149] Mathis J.S.; Torres-Peimbert S.; Peimbert M. Temperature and Density Fluctuations in Planetary Nebulae. *The Astrophysical Journal*, 495(1):328–336, 1998.
- [150] McKenna F.C.; Keenan F.P.; Kaler J.B.; Wickstead A.W.; Bell K.L.; Agarwal K.M. [N II] and [O III] Mean Electron Temperatures in Planetary Nebulae. *Publications of the Astronomical Society of the Pacific*, 108:610–614, 1996.
- [151] Zhang Y.; Liu X.-W.; Wesson R.; Storey P.J.; Liu Y.; Danziger I.J. Electron temperatures and densities of planetary nebulae determined from the nebular hydrogen recombination spectrum and temperature and density variations. *Monthly Notices of the Royal Astronomical Society*, 351(3):935–955, 2004.

- [152] Liu X-W. Optical recombination lines as probes of conditions in planetary nebulae. *Proceedings of the International Astronomical Union Symposium S234*, 2:219–226, 2006.
- [153] Peimbert M.; Peimbert A. Temperature Variations and Chemical Abundances in Planetary Nebulae. In Barlow M.J. and Méndez R.H., editors, *Planetary Nebulae in our Galaxy and Beyond*, Proceedings of the International Astronomical Union Symposia and Colloquia No. 234, pages 227–234. Cambridge University Press, 2006.
- [154] Liu X.-W.; Barlow M.J.; Cohen M.; Danziger I.J.; Luo S.-G.; Baluteau J.P.; Cox P.; Emery R.J.; Lim T.; Péquignot D. ISO LWS observations of planetary nebula fine-structure lines. *Monthly Notices of the Royal Astronomical Society*, 323(2):343–361, 2001.
- [155] Péquignot D.; Baluteau J.P. The 680-1050 nm recombination spectrum of hydrogen and helium in the planetary nebula NGC 7027. *Astronomy and Astrophysics*, 206(2):298–315, 1988.
- [156] van Hoof P.A.M.; Beintema D.A.; Verner D.A.; Ferland G.J. The collision strength of the [Ne V] infrared fine-structure lines. *Astronomy and Astrophysics*, 354:L41–L44, 2000.
- [157] Minkowski R. The Electron Temperature in the Planetary Nebula IC 418. *Publications of the Astronomical Society of the Pacific*, 65(384):161–162, 1953.
- [158] Pottasch S.R.; Beintema D.A.; Raimond E.; Baud B.; van Duinen R.J.; Habing H.J.; Houck J.R.; de Jong T.; Jennings R.E.; Olnon F.M.; Weselius P.R. IRAS spectra of planetary nebulae. *The Astrophysical Journal*, 278:L33–L35, 1984.
- [159] Phillips J.P.; Riera A.; Mampaso A. A carbon star outflow envelope about IC 418. *Astrophysics and Space Science*, 171(1-2):173–176, 1990.
- [160] Hyung S.; Aller L.H.; Feibelman W.A. The spectrum of the planetary nebula IC 418. *Astronomical Society of the Pacific*, 106(701):745–755, 1994.
- [161] Pottasch S.R.; Bernard-Salas J.; Beintema D.A.; Feibelman W.A. Abundances of Planetary Nebulae IC 418, IC 2165 and NGC 5882. *Astronomy and Astrophysics*, 423(2):593–605, 2004.
- [162] Seaton M.J. Electron temperatures and electron densities in planetary nebulae. *Monthly Notices of the Royal Astronomical Society*, 114:154–171, 1954.
- [163] Kaler J.B. Hydrogen and Helium Spectra of Gaseous Nebulae. *The Astrophysical Journal*, vol. 143, p., 143:722–742, 1966.

- [164] Le Marne A.E.; Shaver P.A. The electron temperature of the planetary nebula IC 418. *Proceedings of the Astronomical Society of Australia*, 1:216–217, 1969.
- [165] Miller J.S. Planetary Nebulae. *Annual Review of Astronomy and Astrophysics*, 12:331–358, 1974.
- [166] Aller L.H.; Keyes C.D.; Ross J.E.; O’Mara B.J. An analysis of the planetary nebula NGC 2867. *Monthly Notices of the Royal Astronomical Society*, 197:647–658, 1981.
- [167] Kaler J.B.; Jacoby G.H. Central star temperatures of optically thick planetary nebulae and a distance-independent test of dredge-up theory. *The Astrophysical Journal*, 345:871–880, 1989.
- [168] Feibelman W.A. The Complex *IUE* Spectrum of the “O VI Sequence” Planetary Nebula NGC 2867. *The Astrophysical Journal Supplement Series*, 114(2):263–267, 1998.
- [169] Bath G.T.; Evans W.D.; Pringle J.E. An oblique rotator model for DQ Herculis. *Monthly Notices of the Royal Astronomical Society*, 166:113–121, 1974.
- [170] Nelson M.R. Mass transfer in DQ Herculis. *The Astrophysical Journal*, 209:168–170, 1976.
- [171] Gallagher J.S.; Hege E.K.; Kopriva D.A.; Butcher H.R.; Williams R.E. Spectrophotometry of the nebula surrounding nova T Aurigae 1891. *The Astrophysical Journal*, 237:55–60, 1980.
- [172] Ferland G.J. On the distance and luminosity of nova DQ Herculis. *The Observatory*, 100:166–167, 1980.
- [173] Itoh H. Physical Conditions in the Shell around the Old Nova DQ Herculis 1934. *Publications of the Astronomical Society of Japan*, 33:743–747, 1981.
- [174] King A.R. The origin of soft X-ray pulsations in dwarf novae at outburst and the DQ Herculis phenomenon. *Nature*, 313:291–292, 1985.
- [175] Canalle J.B.G.; Opher R. The accretion column of DQ Herculis binaries. *Revista Mexicana de Astronomia y Astrofisica*, 21:433–436, 1990.
- [176] Smits D.P. Low-temperature recombination coefficients and nova-shell abundances. *Monthly Notices of the Royal Astronomical Society*, 248:193–216, 1991.
- [177] Kraft R.P. The Binary System Nova DQ Herculis. II. An Interpretation of the Spectrum during the Eclipse Cycle. *The Astrophysical Journal*, 130:110–122, 1959.

- [178] Starrfield S.G. The Rate of Mass Exchange in DQ Herculis. *The Astrophysical Journal*, 161:361–363, 1970.
- [179] Saito R.K.; Baptista R.; Horne K.; Martell P. Spectral Mapping of the Intermediate Polar DQ Herculis. *The Astronomical Journal*, 139(6):2542–2556, 2010.
- [180] Williams R.E.; Woolf N.J.; Hege E.K.; Moore R.L.; Kopriva D.A. The shell around nova DQ Herculis 1934. *The Astrophysical Journal*, 224:171–181, 1978.
- [181] Gallagher J.S.; Starrfield S. Theory and Observations of Classical Novae. *Annual Review of Astronomy and Astrophysics*, 16:171–214, 1978.
- [182] I.S. Webster B.L.; Glass. The coolest Wolf-Rayet stars. *Monthly Notices of the Royal Astronomical Society*, 166:491–497, 1974.
- [183] Thackeray A.D. The red/infrared spectrum of CPD - 56°8032. *The Observatory*, 97:165–169, 1977.
- [184] Houziaux L.; Heck A. Carbon abundance in the WC 11 star CPD - 56°8032. *In: Wolf-Rayet stars: Observations, physics, evolution; Proceedings of the Symposium, Cozumel, Mexico, September 18-22, 1981*, pages 139–145, 1982.
- [185] Pollacco D.L.; Kilkenny D.; Marang F.; van Wyk F.; Roberts G. The discovery of photometric variations in the prototype WC11 star CPD - 56°8032. *Monthly Notices of the Royal Astronomical Society*, 256(4):669–672, 1992.
- [186] Crowther P.A.; De Marco O.; Barlow M.J.; Storey P.J. A quantitative analysis of the prototype [WCL] star CPD - 56°8032. *Astrophysics and Space Science*, 238(1):119–123, 1996.
- [187] Cohen M.; Barlow M.J.; Sylvester R.J.; Liu X.-W.; Cox P.; Lim T.; Schmitt B.; Speck A.K. Silicate and ice emission bands in the ISO spectrum of the PAH-emitting carbon-rich planetary nebula CPD - 56°8032. *In: Proceedings of the 191st Symposium of the International Astronomical Union, Montpellier, France, 27 August to 1 September, 1998*, pages 291–296, 1999.
- [188] Cohen M.; Barlow M.J.; Sylvester R.J.; Liu X.-W.; Cox P.; Lim T.; Schmitt B.; Speck A.K. Water Ice, Silicate, and Polycyclic Aromatic Hydrocarbon Emission Features in the Infrared Space Observatory Spectrum of the Carbon-rich Planetary Nebula CPD - 56°8032. *The Astrophysical Journal Letters*, 513(2):L135–L138, 1999.
- [189] Cohen M.; Barlow M.J.; Liu X.-W.; Jones A.F. The dual dust chemistries of planetary nebulae with [WCL] central stars. *Monthly Notices of the Royal Astronomical Society*, 332(4):879–890, 2002.

- [190] De Marco O.; Jones A.F.; Barlow M.J.; Cohen M.; Bond H.E.; Harmer D. The dual dust chemistry - Binarity connection. *In: ASP Conference Series, Asymmetric Planetary Nebulae III*, 313:100–103, 2004.
- [191] Chesneau O. High spatial resolution study of the inner environment around two young planetary nebulae. *In: ASP Conference Series, Stars with the B[e] Phenomenon*, 355:117–123, 2006.
- [192] Chesneau O.; Collioud A.; De Marco O.; Wolf S.; Lagadec E.; Zijlstra A.A.; Rothkopf A.; Acker A.; Clayton G.C.; Lopez B. A close look into the carbon disk at the core of the planetary nebula CPD - 56°8032. *Astronomy and Astrophysics*, 455(3):1009–1018, 2006.
- [193] De Marco O.; Barlow M.J.; Storey P.J. The winds of WC10 central stars of planetary nebulae. *Astrophysics and Space Science*, 238(1):91–96, 1996.
- [194] De Marco O.; Storey P.J.; Barlow M.J. A method for the direct determination of the wind electron temperature of WC10 central stars of planetary nebulae. *In: Proceedings of the 2nd International Colloquium on Hydrogen-Deficient Stars, Bamberg, Germany, 28 August to 1 September, 1995*, 96:145–148, 1996.
- [195] Rao N.K. Nebular spectrum of CPD - 56°8032 and He 2-113. *Quarterly Journal of the Royal Astronomical Society*, 28:261–263, 1987.
- [196] N.K.; Giridhar S.; Nandy K. Rao. The UV spectrum of the WC 11 star CPD - 56°8032. *Astronomy and Astrophysics*, 234(1-2):410–418, 1990.
- [197] Crowther P.A.; Hillier D.J.; Smith L.J. Fundamental parameters of Wolf-Rayet stars. I. Ofpe/WN9 stars. *Astronomy and Astrophysics*, 293:172–197, 1995.
- [198] De Marco O.; Barlow M.J. Abundances of [WC] central stars and their planetary nebulae. *Astrophysics and Space Science*, 275(1-2):53–66, 2001.
- [199] Cohen M. Infrared observations of southern WC9 stars and He 2-113. *Monthly Notices of the Royal Astronomical Society*, 173:489–496, 1975.
- [200] Sahai R.; Nyman L.-Å.; Wootten A. He 2-113: A multipolar planetary nebula with rings around a cool wolf-rayet star. *The Astrophysical Journal*, 543(2):880–888, 2000.
- [201] Soker N. Formation of Double Rings around Evolved Stars. *The Astrophysical Journal*, 577(2):839–844, 2002.
- [202] Lagadec E.; Chesneau O.; Matsuura M.; De Marco O.; de Freitas Pacheco J.A.; Zijlstra A.A.; Acker A.; Clayton G.C.; Lopez B. New insights on the complex planetary nebula Hen 2-113. *Astronomy and Astrophysics*, 448(1):203–212, 2006.

- [203] Bryans P. *On the Spectral Emission of Non-Maxwellian Plasmas*. PhD thesis, University of Strathclyde, 2005.
- [204] Sochi T.; Tennyson J. A computed line list for the H_2D^+ molecular ion. *Monthly Notices of the Royal Astronomical Society*, 405(4):2345–2350, 2010.
- [205] Dalgarno A.; Herbst E.; Novick S.; Klemperer W. Radio Spectrum of H_2D^+ . *The Astrophysical Journal*, 183:L131–L133, 1973.
- [206] Amano T.; Watson J.K.G. Observation of the ν_1 fundamental band of H_2D^+ . *Journal of Chemical Physics*, 81(7):2869–2871, 1984.
- [207] Bogey M.; Demuyne C.; Denis M.; Destombes J.L.; Lemoine B. Laboratory measurement of the $1_{10} - 1_{11}$ submillimeter line of H_2D^+ . *Astronomy and Astrophysics*, 137:L15–L16, 1984.
- [208] Fárník M.; Davis S.; Kostin M.A.; Polyansky O.L.; Tennyson J.; Nesbitt D.J. Beyond the Born-Oppenheimer approximation: High-resolution overtone spectroscopy of H_2D^+ and D_2H^+ . *Journal of Chemical Physics*, 116(14):6146–6158, 2002.
- [209] Millar T.J. Deuterium Fractionation in Interstellar Clouds. *Space Science Reviews*, 106:73–86, 2003.
- [210] van Dishoeck E.F.; Phillips T.G.; Keene J.; Blake G.A. Ground-based searches for interstellar H_2D^+ . *Astronomy and Astrophysics*, 261(1):L13–L16, 1992.
- [211] Phillips T.G.; Blake G.A.; Keene J.; Woods R.C.; Churchwell E. Interstellar H_3^+ : Possible detection of the $1_{10} - 1_{11}$ transition of H_2D^+ . *The Astrophysical Journal*, 294:L45–L48, 1985.
- [212] Pagani L.; Wannier P.G.; Frerking M.A.; Kuiper T.B.H.; Gulkis S.; Zimmermann P.; Encrenaz P.J.; Whiteoak J.B.; Destombes J.L.; Pickett H.M. Search for H_2D^+ at 372 GHz in dense interstellar clouds. *Astronomy and Astrophysics*, 258(2):472–478, 1992.
- [213] Boreiko R.T.; Betz A.L. A search for the rotational transitions of H_2D^+ at 1370 GHz and H_3O^+ at 985 GHz. *The Astrophysical Journal*, 405(1):L39–L42, 1993.
- [214] Stark R.; van der Tak F.F.S.; van Dishoeck E.F. Detection of Interstellar H_2D^+ Emission. *The Astrophysical Journal*, 521:L67–L70, 1999.
- [215] Caselli P.; van der Tak F.F.S.; Ceccarelli C.; Bacmann A. Abundant H_2D^+ in the pre-stellar core L1544. *Astronomy and Astrophysics*, 403(3):L37–L41, 2003.
- [216] Vastel C.; Phillips T.G.; Yoshida H. Detection of D_2H^+ in the Dense Interstellar Medium. *The Astrophysical Journal*, 606:L127–L130, 2004.

- [217] Ceccarelli C.; Dominik C.; Lefloch B.; Caselli P.; Caux E. Detection of H_2D^+ : Measuring the Midplane Degree of Ionization in the Disks of DM Tauri and TW Hydrae. *The Astrophysical Journal*, 607:L51–L54, 2004.
- [218] Stark R.; Sandell G.; Beck S.C.; Hogerheijde M.R.; van Dishoeck E.F.; van der Wal P.; van der Tak F.F.S.; Schäfer F.; Melnick G.J.; Ashby M.L.N.; de Lange G. Probing the Early Stages of Low-Mass Star Formation in LDN 1689N: Dust and Water in IRAS 16293-2422A, B, and E. *The Astrophysical Journal*, 608:341–364, 2004.
- [219] Hogerheijde M.R.; Caselli P.; Emprechtinger M.; van der Tak F.F.S.; Alves J.; Belloche A.; Güsten R.G.; Lundgren A.A.; Nyman L.-Å.; Volgenau N.; Wiedner M.C. Probable detection of H_2D^+ in the starless core Barnard 68. *Astronomy and Astrophysics*, 454(2):L59–L62, 2006.
- [220] Harju J.; Haikala L.K.; Lehtinen K.; Juvela M.; Mattila K.; Miettinen O.; Dumke M.; Güsten R.; Nyman L.-Å. Detection of H_2D^+ in a massive prestellar core in Orion B. *Astronomy and Astrophysics*, 454(2):L55–L58, 2006.
- [221] Cernicharo J.; Polehampton E.; Goicoechea J.R. Far-Infrared Detection of H_2D^+ toward Sgr B2. *The Astrophysical Journal*, 657:L21–L24, 2007.
- [222] Caselli P.; Vastel C.; Ceccarelli C.; van der Tak F.F.S.; Crapsi A.; Bacmann A. Survey of ortho- H_2D^+ ($1_{1,0} - 1_{1,1}$) in dense cloud cores. *Astronomy and Astrophysics*, 492(3):703–718, 2008.
- [223] Ramos A.A.; Ceccarelli C.; Elitzur M. H_2D^+ line emission in Proto-Planetary Disks. *Astronomy and Astrophysics*, 471(1):187–192, 2007.
- [224] van der Tak F.F.S.; Caselli P.; Ceccarelli C. Line profiles of molecular ions toward the pre-stellar core LDN 1544. *Astronomy and Astrophysics*, 439(1):195–203, 2005.
- [225] Ceccarelli C.; Dominik C. H_2D^+ : A Light on Baryonic Dark Matter? *The Astrophysical Journal*, 640:L131–L134, 2006.
- [226] Herbst E.; Millar T.J. *The Chemistry of Cold Interstellar Cloud Cores: Low Temperatures and Cold Molecules*. World Scientific Publishing, 2008.
- [227] Shy J.-T.; Farley J.W.; Wing W.H. Observation of the infrared spectrum of the triatomic molecular ion H_2D^+ . *Physical Review A*, 24:1146–1149, 1981.
- [228] Warner H.E.; Conner W.T.; Petrmichl R.H.; Woods R.C. Laboratory detection of the $1_{10} - 1_{11}$ submillimeter wave transition of the H_2D^+ ion. *Journal of Chemical Physics*, 81(5):2514, 1984.
- [229] Dubrovich V.K. Blurring of spatial microwave background fluctuations by molecular line scattering. *Astronomy Letters*, 19(1):53–54, 1993.

- [230] Dubrovich V.K.; Lipovka A.A. Distortions of the cosmic blackbody spectrum due to luminescence of H_2D^+ molecules. *Astronomy and Astrophysics*, 296:301–306, 1995.
- [231] Dubrovich V.; Partridge B. Line and continuum emission from high redshift objects and proto-objects. *Astronomical and Astrophysical Transactions*, 19:233–251, 2000.
- [232] Galli D.; Palla F. The chemistry of the early Universe. *Astronomy and Astrophysics*, 335:403–420, 1998.
- [233] Schleicher D.R.G.; Galli D.; Palla F.; Camenzind M.; Klessen R.S.; Bartelmann M.; Glover S.C.O. Effects of primordial chemistry on the cosmic microwave background. *Astronomy and Astrophysics*, 490(2):521–535, 2008.
- [234] Miller S.; Tennyson J.; Sutcliffe B.T. First principles calculation of rotational and ro-vibrational line strengths Spectra for H_2D^+ and D_2H^+ . *Molecular Physics*, 66(2):429–456, 1989.
- [235] Dinelli B.M.; Neale L.; Polyansky O.L.; Tennyson J. New Assignments for the Infrared Spectrum of H_3^+ . *Journal of Molecular Spectroscopy*, 181(1):142–150, 1997.
- [236] Amano T. Difference-frequency laser spectroscopy of molecular ions with a hollow-cathode cell: extended analysis of the ν_1 band of H_2D^+ . *Journal of the Optical Society of America B*, 2(5):790–793, 1985.
- [237] Foster S.C.; McKellar A.R.W.; Peterkin I.R.; Watson J.K.G.; Pan F.S.; Crofton M.W.; Altman R.S.; Oka T. Observation and analysis of the ν_2 and ν_3 fundamental bands of the H_2D^+ ion. *Journal of Chemical Physics*, 84(1):91–99, 1986.
- [238] Amano T.; Hirao T. Accurate rest frequencies of submillimeter-wave lines of H_2D^+ and D_2H^+ . *Journal of Molecular Spectroscopy*, 233(1):7–14, 2005.
- [239] Hlavenka P.; Korolov I.; Plašil R.; Varju J.; Kotrík T.; Glosík.
- [240] Yonezu T.; Matsushima F.; Moriwaki Y.; Takagi K.; Amano T. THz spectroscopy of H_2D^+ . *Journal of Molecular Spectroscopy*, 256(2):238–241, 2009.
- [241] Vastel C.; Caselli P.; Ceccarelli C.; Phillips T.; Wiedner M.C.; Peng R.; Houde M.; Dominik C. The Distribution of Ortho- $\text{H}_2\text{D}^+(1_{10} - 1_{11})$ in L1544: Tracing the Deuteration Factory in Prestellar Cores. *The Astrophysical Journal*, 645:1198–1211, 2006.
- [242] Vastel C.; Phillips T.G.; Caselli P.; Ceccarelli C.; Pagani L. Deuterium enhancement in H_3^+ in pre-stellar cores. *Philosophical Transactions of the Royal Society A*, 364(1848):3081–3090, 2006.

- [243] Polyansky O.L.; Tennyson J. Ab initio calculation of the rotation-vibration energy levels of H_3^+ and its isotopomers to spectroscopic accuracy. *Journal of Chemical Physics*, 110(11):5056–5064, 1999.
- [244] Tennyson J.; Kostin M.A.; Barletta P.; Harris G.J.; Polyansky O.L.; Ramanlal J.; Zobov N.F. DVR3D: a program suite for the calculation of rotation-vibration spectra of triatomic molecules. *Computer Physics Communications*, 163(2):85–116, 2004.
- [245] Polyansky O.L.; Császár A.G.; Shirin S.V.; Zobov N.F.; Barletta P.; Tennyson J.; Schwenke D.W.; Knowles P.J. High accuracy *ab initio* rotation-vibration transitions of water. *Science*, 299:539–542, 2003.
- [246] Polyansky O.L.; Prosmi R.; Klopper W.; Tennyson J. An accurate, global, *ab initio* potential energy surface for the H_3^+ molecule. *Molecular Physics*, 98(5):261–273, 2000.
- [247] Cencek W.; Rychlewski J.; Jaquet R.; Kutzelnigg W. Sub-micro-Hartree accuracy potential energy surface for H_3^+ including adiabatic and relativistic effects. I. Calculation of the potential points. *Journal of Chemical Physics*, 108:2831–2836, 1998.
- [248] Schinke R.; Dupuis M.; Lester Jr. W.A. Proton- H_2 scattering on an *ab initio* CI potential energy surface. I. Vibrational excitation at 10 eV. *Journal of Chemical Physics*, 72(7):3909–3915, 1980.
- [249] Tennyson J.; Sutcliffe B.T. The *ab initio* calculation of the vibration-rotation spectrum of triatomic systems in the close-coupling approach with KCN and H_2Ne as examples. *Journal of Chemical Physics*, 77(8):4061–4072, 1982.
- [250] Tennyson J.; Sutcliffe B.T. Variationally exact ro-vibrational levels of the floppy CH_2^+ molecule. *Journal of Molecular Spectroscopy*, 101(1):71–82, 1983.
- [251] Pavanello M.; Adamowicz L.; Alijah A.; Zobov N.F.; Mizus I.I.; Polyansky O.L.; Tennyson J.; Szidarovszky T.; Császár A.G. Calibration-quality adiabatic potential energy surfaces for H_3^+ and its isotopologues. *Journal of Chemical Physics*, 136(18):184303–184316, 2012.
- [252] Röhse R.; Kutzelnigg W.; Jaquet R.; Klopper W. Potential energy surface of the H_3^+ ground state in the neighborhood of the minimum with microhartree accuracy and vibrational frequencies derived from it. *Journal of Chemical Physics*, 101(3):2231–2243, 1994.
- [253] Barber R.J.; Tennyson J.; Harris G.J.; Tolchenov R.N. A high-accuracy computed water line list. *Monthly Notices of the Royal Astronomical Society*, 368(3):1087–1094, 2006.

- [254] Polyansky O.L.; Miller S.; Tennyson J. Rotational Levels of H_2D^+ : Variational Calculations and Assignments. *Journal of Molecular Spectroscopy*, 157(1):237–247, 1993.
- [255] Miller S.; Stallard T.; Melin H.; Tennyson J. H_3^+ cooling in planetary atmospheres. *Faraday Discussions*, 147:283–291, 2010.
- [256] Tennyson J.; Miller S.; Le Sueur C.R. TRIATOM: programs for the calculation of ro-vibrational spectra of triatomic molecules. *Computer Physics Communications*, 75:339–364, 1993.

Appendix A

Using Lifetime Matrix to Investigate Single-Channel Resonances

In this Appendix we present the \mathbf{K} -matrix method of P.J. Storey which is based on using the lifetime matrix \mathbf{M} expressed in terms of the reactance matrix \mathbf{K} to investigate single-channel resonances. This method is used in this study to investigate the low-lying autoionizing states of C^+ .

According to Smith [128], the \mathbf{M} -matrix is given, in terms of the scattering matrix \mathbf{S} , by

$$\mathbf{M} = -i\hbar \mathbf{S}^* \frac{d\mathbf{S}}{dE} \quad (\text{A.1})$$

where \mathbf{S} -matrix is defined, in terms of \mathbf{K} -matrix, by

$$\mathbf{S} = \frac{\mathbf{I} + i\mathbf{K}}{\mathbf{I} - i\mathbf{K}} \quad (\text{A.2})$$

with \mathbf{I} being the identity matrix. In the case of single-channel states, \mathbf{M} , \mathbf{S} and \mathbf{K} are one-element matrices. To indicate this fact we annotate them with M , S and K . From A.1 and A.2, the following relation may be derived

$$M = \frac{2}{1 + K^2} \frac{dK}{dE} \quad (\text{A.3})$$

where $\hbar = 1$ in atomic units. It is noteworthy that since K is real, M is real as it should be.

Smith [128] has demonstrated that the expectation value of M is the lifetime of the state, τ . Now if K has a simple pole at energy E_0 , given by

$$K = \frac{g}{E - E_0} \quad (\text{A.4})$$

where g is a parameter with dimensions of energy, then from A.3 we obtain

$$\begin{aligned} M(E) &= \frac{-2g}{(1 + K^2)(E - E_0)^2} \\ &= \frac{-2g}{(E - E_0)^2 + g^2} \end{aligned} \quad (\text{A.5})$$

and hence the maximum value of $M(E)$ is $M(E_0) = -2/g$. On substituting the half maximum, $-1/g$, into Equation A.5 we find

$$E - E_0 = \pm g \quad (\text{A.6})$$

and therefore, the full width at half maximum is

$$\Delta_E = |2g| \quad (\text{A.7})$$

According to Smith [128], the lifetime of the state τ , and the FWHM Δ_E are related by

$$\tau = \frac{1}{\Delta_E} \quad (\text{au}) \quad (\text{A.8})$$

Hence, for a \mathbf{K} -matrix pole given by A.4 the autoionization probability, Γ^a , which by definition equals the reciprocal of the lifetime, is given in atomic units by

$$\Gamma^a = \frac{1}{\tau} = \Delta_E = |2g| \quad (\text{au}) \quad (\text{A.9})$$

Now if we consider a \mathbf{K} -matrix with a pole superimposed on a background K_o

$$K = K_o + \frac{g}{E - E_0} \quad (\text{A.10})$$

then from A.3 we find

$$\begin{aligned} M(E) &= \frac{-2g}{(1 + K^2)(E - E_0)^2} \\ &= \frac{-2g}{(1 + K_o^2)(E - E_0)^2 + 2K_o g(E - E_0) + g^2} \end{aligned} \quad (\text{A.11})$$

The maximum value of $M(E)$ occurs when the denominator has a minimum, that is when

$$E = E_0 - \frac{K_o g}{1 + K_o^2} \quad (\text{A.12})$$

and hence

$$M_{max} = -\frac{2(1 + K_o^2)}{g} \quad (\text{A.13})$$

This reveals that by including a non-vanishing background the peak of M is shifted relative to the pole position, $E = E_0$, and the peak value is modified. If we now calculate the FWHM, Δ_E , by locating the energies where $M = \frac{1}{2}M_{max}$ from solving the quadratic

$$(1 + K_o^2)(E - E_0)^2 + 2K_o g(E - E_0) - \frac{g^2(1 - K_o^2)}{(1 + K_o^2)} = 0 \quad (\text{A.14})$$

we find

$$\Delta_E = \frac{|2g|}{1 + K_o^2} \quad (\text{A.15})$$

As FWHM and autoionization probability are numerically equal in atomic units, we obtain

$$\Gamma^a = \frac{|2g|}{1 + K_o^2} \quad (\text{au}) \quad (\text{A.16})$$

The two parameters of primary interest are the resonance position E_r and the resonance width Δ_r . However, for an energy point E_i with a \mathbf{K} -matrix value K_i , Equation A.10 has three unknowns, K_o , g and E_0 which are needed to find E_r and Δ_r , and hence three energy points at the immediate neighborhood of E_0 are required to identify the unknowns. Since the \mathbf{K} -matrix changes sign at the pole, the neighborhood of E_0 is located by testing the \mathbf{K} -matrix value at each point of the energy mesh for sign change and hence the three points are obtained accordingly. Now, if we take the three consecutive values of K

$$K_i = K_o + \frac{g}{E_i - E_0} \quad (i = 1, 2, 3) \quad (\text{A.17})$$

and define

$$\Delta E_{jk} = E_j - E_k \quad \& \quad \Delta K_{jk} = K_j - K_k \quad (\text{A.18})$$

then from A.17 we obtain

$$\Delta K_{12} = g \left(\frac{1}{\Delta E_{10}} - \frac{1}{\Delta E_{20}} \right) = g \left(\frac{\Delta E_{21}}{\Delta E_{10} \Delta E_{20}} \right) \quad (\text{A.19})$$

$$\Delta K_{23} = g \left(\frac{1}{\Delta E_{20}} - \frac{1}{\Delta E_{30}} \right) = g \left(\frac{\Delta E_{32}}{\Delta E_{20} \Delta E_{30}} \right) \quad (\text{A.20})$$

and

$$\frac{\Delta K_{12}}{\Delta K_{23}} = \frac{\Delta E_{30} \Delta E_{21}}{\Delta E_{10} \Delta E_{32}} \quad (\text{A.21})$$

Therefore

$$\frac{\Delta E_{30}}{\Delta E_{10}} = \frac{E_3 - E_0}{E_1 - E_0} = \frac{\Delta K_{12} \Delta E_{32}}{\Delta K_{23} \Delta E_{21}} \quad (\text{A.22})$$

On algebraically manipulating A.22 we find

$$E_0 = \frac{E_1 \Delta K_{12} \Delta E_{32} - E_3 \Delta K_{23} \Delta E_{21}}{\Delta K_{12} \Delta E_{32} - \Delta K_{23} \Delta E_{21}} \quad (\text{A.23})$$

Having located the pole position, E_0 , the following relation can be obtained from A.19

$$\boxed{g = \frac{\Delta K_{12} \Delta E_{10} \Delta E_{20}}{\Delta E_{21}}} \quad (\text{A.24})$$

Similarly, from A.17 we obtain

$$\boxed{K_o = K_1 - \frac{g}{\Delta E_{10}}} \quad (\text{A.25})$$

Finally, E_r and Δ_r can be computed from Equation A.12 and Equation A.15 respectively.

Appendix B

Error Analysis

In this Appendix we present the formulae of P.J. Storey to account for the errors in the observational data used in the least squares optimization method where the flux of each line is normalized to the total flux of all lines involved in the optimization process.

In the following we define the symbols used in these formulae

f_i is the observed flux of line i

f is the sum of observed flux of all N lines involved in the least squares process

$$y_i^O = \frac{f_i}{f}$$

y_i^C is the ratio of the theoretical emissivity of line i to the sum of the theoretical emissivity of all N lines

$\sigma_{y_i^O}^2$ is the variance of the observed ratio y_i^O

σ_{f_i} is the standard deviation of the observed flux of line i

In the following, we adopt a basic definition of χ^2 based on a least squares difference and a statistical weight given by the reciprocal of variance, and hence other factors that may enter in the definition of χ^2 , such as scaling factors like degrees of freedom, are not included for the sake of simplicity. The method therefore is based on minimizing χ^2 given by

$$\chi^2 = \sum_{i=1}^N \frac{(y_i^O - y_i^C)^2}{\sigma_{y_i^O}^2} \quad (\text{B.1})$$

From the definition of y_i^O it can be shown that

$$\sigma_{y_i^O}^2 = \left(\frac{\partial y_i^O}{\partial f_i} \right)^2 \sigma_{f_i}^2 + \left(\frac{\partial y_i^O}{\partial f} \right)^2 \sigma_f^2 = \left(\frac{1}{f} \right)^2 \sigma_{f_i}^2 + \left(-\frac{f_i}{f^2} \right)^2 \sigma_f^2 \quad (\text{B.2})$$

Dividing through by $(y_i^O)^2$ we get

$$\frac{\sigma_{y_i^O}^2}{(y_i^O)^2} = \frac{\left(\frac{1}{f} \right)^2 \sigma_{f_i}^2}{\left(\frac{f_i}{f} \right)^2} + \frac{\left(\frac{f_i}{f^2} \right)^2 \sigma_f^2}{\left(\frac{f_i}{f} \right)^2} \quad (\text{B.3})$$

that is

$$\sigma_{y_i^O}^2 = (y_i^O)^2 \left(\frac{\sigma_{f_i}^2}{f_i^2} + \frac{\sigma_f^2}{f^2} \right) \quad (\text{B.4})$$

Now, since f_i 's are mutually independent

$$\sigma_f^2 = \sum_j^N \left(\frac{\partial f}{\partial f_j} \right)^2 \sigma_{f_j}^2 = \sum_j^N \sigma_{f_j}^2 \quad (\text{B.5})$$

On substituting, we obtain

$$\boxed{\sigma_{y_i^O}^2 = (y_i^O)^2 \left(\frac{\sigma_{f_i}^2}{f_i^2} + \frac{\sum_j^N \sigma_{f_j}^2}{f^2} \right)} \quad (\text{B.6})$$

In the following, we investigate three types of error.

B.1 Observed Error

In this case, Equation B.6 should be used as it stands where σ_{f_i} and σ_{f_j} are the errors given by the observer as standard deviations on the observed flux of lines i and j respectively.

B.2 Fixed Percentage Error

If we assume a constant percentage error on the flux of all lines, that is

$$\sigma_{f_i} = \gamma f_i \quad (\text{B.7})$$

then from Equation B.6 we obtain

$$\sigma_{y_i^O}^2 = (y_i^O)^2 \left(\gamma^2 \frac{f_i^2}{f_i^2} + \gamma^2 \frac{\sum_j^N f_j^2}{f^2} \right) \quad (\text{B.8})$$

that is

$$\boxed{\sigma_{y_i^O}^2 = (y_i^O)^2 \gamma^2 \left(1 + \frac{\sum_j^N f_j^2}{f^2} \right)} \quad (\text{B.9})$$

B.3 Poisson Error

Now if we assume, based on Poisson counting statistics, that the error on the observed flux is proportional to the square root of flux, i.e.

$$\sigma_{f_i}^2 = \beta f_i \quad (\text{B.10})$$

where β is an unknown proportionality factor with the same dimensionality as f_i , then equation B.6 becomes

$$\sigma_{y_i^O}^2 = \beta \frac{f_i^2}{f^2} \left(\frac{1}{f_i} + \frac{1}{f} \right) \quad (\text{B.11})$$

that is

$$\boxed{\sigma_{y_i^O}^2 = \frac{\beta f_i}{f^2} \left(1 + \frac{f_i}{f} \right)} \quad (\text{B.12})$$

Since β is unknown, χ^2 may be normalized to its value at the minimum to

obtain a more realistic error estimate.

Appendix C

Emissivity Program Documentation

‘Emissivity’ code is a command line program that was developed during this investigation to implement the atomic transition and emissivity model. Its main functionality is to find all possible transitions and calculate the emissivity and recombination coefficients of the transition lines from dielectronic recombination and cascade decay all the way down to the ground or a metastable state, that is all free-free, free-bound and bound-bound transitions. ‘Emissivity’ is written in C++ computer language and mixes procedural with object oriented programming. The program was compiled successfully with no errors or warnings using Dev-C++ compiler on Windows, and g++ compiler on Cygwin and Red Hat Linux. Sample results produced by these three versions were compared and found to be identical. Elaborate checks were carried out in all stages of writing and debugging the program and the output was verified. Thorough independent checks on sample emissivity data produced by ‘Emissivity’ were performed and found to be consistent.

C.1 Theoretical background

In thermodynamic environments, an excited atomic state is populated by recombination and radiative decay from accessible higher states, and depopulated by autoionization and radiative decay to lower states. The population of a resonance state is, therefore, determined by the balance between recombination, autoionization and radiative decay. In thermodynamic equilibrium situations, autoionization dominates and the population is described by Saha equation. In non-thermodynamic equilibrium situations, processes other than autoionization have significant contribution to the population and hence detailed equilibrium calculations are required to account for these processes. In these situations, a departure coefficient, defined as the ratio of autoionization probability to the sum of autoionization and total radiative probabilities, is used to measure the departure from thermodynamic equilibrium and quantify the contribution of various processes.

The first step in the transition lines calculations is to find the radiative transition probabilities of all types of transitions (free-free, free-bound and bound-bound) which, for a given photon energy and statistical weights of the upper and lower states, can be obtained from the oscillator strengths. The total radiative transition probability of each state can then be obtained by summing up the transition probabilities of the given state to all optically-accessible lower states. The population of all states can then be computed. For autoionizing states, the population is obtained by summing up the Saha capture term, given by Saha population times the departure coefficient, and the radiative decay term given by the sum over all accessible upper states of the population of these states times the ratio of the radiative probability of the transition to the sum of total radiative and autoionizing probabilities of the lower state. For bound states, the population is simply computed by summing up over all accessible upper states the population of these states times the ratio of the radiative probability of the transition to the total radiative

probability of the lower state.

On finding all optically-allowed transitions, the emissivity of lines arising from these transitions can be obtained from

$$\varepsilon_{ul} = N_u \Gamma_{ul}^r E_p \quad (\text{C.1})$$

while the equivalent effective recombination coefficient is computed from

$$\varrho_f = \frac{\varepsilon_{ul}}{N_e N_i E_p} \quad (\text{C.2})$$

In the last equations, N_u is the population of upper state, Γ_{ul}^r is the radiative transition probability from upper to lower state, E_p is the photon energy, and N_e and N_i are the number density of electrons and ions respectively.

This theoretical model, with some other extensions and elaborations, represent the basic framework of ‘Emissivity’ code [121] which was the main tool used by the author of this thesis to perform the calculations of dielectronic recombination transition lines using the raw atomic data generated mainly by **R**-matrix and Autostructure programs. The ‘Emissivity’ calculations include identifying the allowed electric dipole transitions, vacuum and air wavelengths, radiative transition probabilities, dimensional and normalized emissivities, effective recombination coefficients, decay routes, and so on. The code can also perform comparison to observational data and analyze the results using a least squares optimization procedure. Moreover, it can produce electron energy distribution for the FF and FB transitions of the observed spectra. Some practical details about these calculations and how to be performed by ‘Emissivity’ will be highlighted in the subsequent sections of this appendix.

C.2 Input and Output Files

‘Emissivity’ code reads from plain text input files and writes the results to a main plain text output file called ‘Transitions’. The structure of this output file is explained in section C.2.4. Other secondary output data files are also produced for particular purposes. The required input text files are ‘Input’, ‘ResEmis’, ‘ELEVEmis’ and ‘FVALUE’. The structure of these files, apart from the ‘FVALUE’ file which is produced by the STGGB stage of the **R**-matrix code and is used by ‘Emissivity’ program with no modification, apart from possible inclusion of additional data, is outlined below. Two other input data files are also required if comparison and analysis to observational data are needed. One of these is a data file that contains astronomical observations while the other includes mapping information of the observational lines to their theoretical counterparts using their indices. In the following subsections we outline the files used by the ‘Emissivity’ code for input and output.

C.2.1 ‘Input’ Data File

The program uses a keyword based input file called ‘Input’ which controls the program flow and its main parameters. All keywords are optional with no order required. If keywords are omitted, default values will be used. Comments can be inserted in any part of the input file as long as they do not intrude between a keyword and its parameter(s) or between the parameters. No commentary line should be initiated with a keyword. Each keyword must occur first on its line of text followed by its parameter(s) in the order that will be given. There is no restriction on using spaces and new lines as long as they obey the aforementioned rules.

1. ‘Temperature(K)’

The first entry after this keyword is a boolean flag to choose one of the two available schemes, followed by the number of temperature entries in K. If the flag is on (i.e. '1'), this must be followed by the initial temperature and the interval between the temperature points in this order; and if it is off, it should be followed by the temperature points. The first scheme is most suitable for a large and regularly spaced temperature vector, while the second is more suitable for small or irregularly spaced temperature vector. If this keyword is omitted, the default is a single temperature entry of 10000.

2. 'Ni(m⁻³)'

This is the number density of the ions in m⁻³. If this keyword is omitted, the default value is 10¹⁰.

3. 'Ne(m⁻³)'

This is the number density of the electrons in m⁻³. If this keyword is omitted, the default value is 10¹⁰.

4. 'ResidualCharge'

This is the residual charge of the ion. It is required for scaling some of the data obtained from the **R**-matrix code output files. If this keyword is omitted, the default value is 2.

5. 'AstronomicalData'

This keyword requires a boolean flag to read astronomical data from a data file ('0' for 'No' and '1' for 'Yes'). If the flag is on, a second entry, which is the name of the data file to read the data from, will be required. The structure of the astronomical data file requires the file to start with a comment that can occupy any number

of text lines but it should be terminated with ‘EndOfComment’ string to mark the end. This should be followed by the transition lines data organized in sets preferably each set on a single line of text. When the normalization is on, as will be explained later on, the program will normalize the astronomical data to the first data set. This facilitates the normalization as the user can simply normalize to any line in the astronomical data by copying the data of that line and paste at the front. The data for each line usually consist of the observed and laboratory wavelengths, the observed flux (normally after correcting for dust extinction and normalizing such that $I(H_\beta) = 100$), the observed error (standard deviation as percentage), the ionic identification, the type of transition (FF, FB or BB), the lower spectral term of the transition, the upper spectral term of the transition, the statistical weight of the lower level, and the statistical weight of the upper level. There is another option for normalization that is normalizing the observational fluxes to the total flux and the theoretical emissivities to the total emissivity.

If the user chooses to read astronomical data, the data lines will be inserted between the theoretical lines in the ‘Transitions’ output file according to their observed wavelength. If this keyword is omitted, the default value is 0.

6. ‘TestsFlag’

This keyword requires one entry which is a flag for carrying the first (in-out) and second (ground-metastable) consistency tests. These tests are described in section C.3 of this appendix. The options for this flag are: ‘1’ for running the first test only, ‘2’ for running the second test only and ‘3’ for running both tests. Any other value means that no test will be carried out. If this keyword is omitted, the default value is 0.

7. ‘NormalizationChoice’

This keyword controls the generation and writing of normalization data for theoretical and observational lines to the ‘Transitions’ output file alongside the original emissivity data. The options for this keyword are

- ‘0’ for no normalization. In this case no normalization data will be written to the ‘Transitions’ file. Any invalid normalization choice will also be treated like zero.
- ‘1’ for internal normalization with the theoretical data of one of the transition lines produced by the program. In this case this should be followed by the index of the normalization line.
- ‘2’ for normalizing with respect to an outside set of emissivity values corresponding to the temperatures included under the ‘Temperature(K)’ keyword. The emissivity values should be on the next line(s) of text and in the SI units (i.e. in $\text{J}\cdot\text{s}^{-1}\cdot\text{m}^{-3}$).
- ‘3’ for normalizing with respect to an outside set of emissivity data in the form of effective recombination coefficients corresponding to the specified temperatures. In this case the recombination coefficients should be followed by the wavelength of the line to be normalized to. The recombination coefficients in the input data file should be in $\text{cm}^3\cdot\text{s}^{-1}$ while the wavelength, which follows the recombination coefficients, should be in nanometer. The reason for this choice is to avoid potential error in conversion as the available data in the literature are mostly given in these units rather than SI units. These values should be entered on the next line(s) of text in the data file.
- ‘4’ for normalizing with respect to an outside set of emissivity data in the form of effective recombination coefficients corresponding to a set of temperatures that may be different from those included under the ‘Temperature(K)’

keyword. In this case, the recombination coefficients corresponding to the temperature values of the ‘Temperature(K)’ keyword are obtained by interpolation or extrapolation using ‘polint’ algorithm [145]. This algorithm is a polynomial interpolation routine which implements Nevilles interpolating method and is regarded as an improvement to the classical Lagrange’s formula for polynomial interpolation. For this option, the normalization choice should be followed by the number of points which identify the order of interpolation (e.g. ‘3’ for 3-point second order interpolation and so on). The recommended value for the number of points is ‘3’ or ‘4’. Going beyond this should be for a good reason, otherwise the interpolation may fail to produce reasonable results. The details should be sought in the literature of numerical methods. An initial investigation suggests that the optimal number of points may depend on the proximity to the tabulated data points and the nature of the process, i.e. interpolation vs. extrapolation. It may be a good idea to have a trial run inspecting the estimated errors which can be found in the ‘Transitions’ output file before choosing the order of interpolation. The required data entries, which should follow the number of points, are the number of data pairs (i.e. temperature in K and recombination coefficient in $\text{cm}^3.\text{s}^{-1}$) followed by the data pairs followed by the wavelength of the line of normalization in nanometer. These values should be included on the next line(s) of text in the data file.

If this keyword is omitted, the default value is 0.

8. ‘RecCoefficient’

This keyword controls the production and writing of the effective recombination coefficients, ρ_f , which are equivalent to the given emissivities. Vacuum wavelength of the transition line will be used in these calculations as the air wavelength is not

available for $\lambda < 2000 \text{ \AA}$. The keyword should be followed by a boolean flag, i.e. ‘1’ for ‘Yes’ and ‘0’ for ‘No’. Any other choice will be treated as zero. The written recombination coefficients to the ‘Transitions’ file will be in the SI units ($\text{m}^3.\text{s}^{-1}$). If this keyword is omitted, the default value is 0.

9. ‘TheoAstroLS’

This keyword controls the algorithm to obtain the sum of weighted square differences between the observational lines and their theoretical counterparts over the input temperature range. This sum, in its basic form, is given by

$$\chi^2 = \sum_{i=1}^N w_i (I_i^{no} - \varepsilon_i^{nt})^2 \quad (\text{C.3})$$

where I_i^{no} is the normalized observational flux of line i , ε_i^{nt} is the normalized theoretical emissivity, w_i is a statistical weight which mainly accounts for error, and N is the number of lines involved in the least squares procedure. This algorithm also offers the possibility of computing the temperature confidence interval.

The keyword requires a boolean flag to compute χ^2 or not. If the flag is on, the name of the file that maps the indices of the theoretical and observational lines should follow. The structure of the mapping file requires that the index of the observational line should be followed by the index of its theoretical counterpart. If an observational line corresponds to more than one theoretical line, which occurs when observational lines from the same multiplet are blended or when the lines are too close to be entirely resolved observationally, the mapping should be repeated independently for each theoretical line. The rest of the file can be used for commenting or storing other data if the index mapping is terminated with ‘-999’.

The results of the least squares minimization algorithm are written to a file called ‘TNV’. This file contains information on χ^2 , temperature at minimum χ^2 , and the temperature limits for the confidence interval. This is followed by the

temperatures with the corresponding least squares residuals.

10. ‘DecayRoutes’

This keyword is for finding the decay routes to a particular state, bound or free, from all upper states. The parameters required are a boolean flag to run this algorithm or not (‘1’ for ‘Yes’ and ‘0’ for ‘No’). In the first case, the configuration, term and $2J$ of the state should follow. As the number of decay routes can be very large (millions and even billions) especially for the low bound states, another parameter is used to control the maximum number of detected routes, and this parameter should follow. The results (number of decay routes and the routes themselves grouped in complete and non-complete) are output to ‘DecayRoutes’ file. If the number of detected routes exceeds the maximum number, say n , only the first n routes will be written to the ‘DecayRoutes’ file. The scheme is that the program keeps detecting the routes as long as the total number of complete and uncomplete routes detected at any point during the program execution does not exceed the maximum number. The algorithm follows the routes from the given state upwards, and hence the number of detected routes, complete and uncomplete, steadily increases as iteration progresses. Consequently, to find a substantial number of complete routes or all of them if this is feasible, the maximum number should be set to a sufficiently large value. It is recommended that for the bound states and low resonances the maximum number should be increased in steps until the output satisfies the user need. If the maximum number was set to a very large value the program may fail or take very long time to complete; moreover the data produced will become virtually useless thanks to its massive size.

The states of each decay route are identified by their configuration, term and $2J$. For resonances, the Saha capture term and the radiative decay term are also given when relevant. These temperature-dependent data are given for a single

temperature, that is the first value in the temperature array.

C.2.2 ‘ResEmis’ Input Data File

This is the file containing the data for resonances. The file contains four main sections:

1. The first line in the file is a comment line. This is followed by the number of resonances followed by a number of text lines matching the number of resonances. Each one of these lines contains an index identifying the resonance, the energy position of the resonance in z -scaled Ryd, the width in z -scaled Ryd, the configuration, term, $2J$, parity, a flag for marking the energy position data as experimental (1) or theoretical (0), and a flag marking the resonances, according to their departure coefficients b , as ‘good’ (1) or not (0) so that the bad ones with low b can be excluded from computations if required. Each of the configuration and term should be a single string with no space in between.
2. After the resonances data, a comment is expected. This comment, which can span any number of text lines, should be terminated by the string ‘EndOf-Comment’ to mark the end. Next, the number of the bound-state symmetries is expected. This is followed, possibly, by a comment to the end of the line. The oscillator strengths (f -values) for the free-bound transitions then follow in sections according to the symmetries of the bound states, so the number of the f -values sections is the same as the number of bound state symmetries. Each section of the f -values is headed by a line containing $2J$, parity and the number of bound states in that symmetry. This is followed by a two-dimensional array of f -values where the columns stand for the resonances as ordered previously, whereas the rows are for the bound states of the given

symmetry. For the transitions which are forbidden by the electric dipole rules for J and parity, the f -values should be set to zero. This convention is adopted to accommodate possible future extension to include optically-forbidden transitions.

3. Next a comment is expected which should be terminated by the ‘EndOfComment’ string to mark the end. The data for the photon energy at resonance position which correspond to the f -value data in the previous section, then follow, sectioned and formatted as for the f -value data. The photon energy data, which are obtained from the ‘XSECTN’ file produced by stage STGBF of the **R**-matrix code, are in Ryd.
4. The last section starts with a comment terminated by the ‘EndOfComment’ string. The f -value data for the free-free transitions are then included in a two-dimensional array where the columns stand for the odd resonances while the rows stand for the even ones. This section is required only if the resonances are of mixed parity.

C.2.3 ‘ELEVEmis’ Input Data File

This file contains the bound states data. The file starts with a comment terminated by the ‘EndOfComment’ marker. Next, the number of bound states symmetries are expected. This is followed by a data block for each symmetry. Each block is headed by a line containing $2J$, parity and the number of bound states in that symmetry. Next, a number of text lines as the number of bound states in that symmetry are expected. Each line contains (in the following order) an index identifying the state, the energy of the bound state in z -scaled Ryd, the effective quantum number, the configuration, term and a flag for marking the energy data as experimental (1) or theoretical (0). Each of the configuration and term should be a single string with no

space in between. The effective quantum number, though not used in the program, is included because the original data come from the ‘ELEV’ data file generated by the STGB stage of the **R**-matrix code. It is kept for possible use in the future.

C.2.4 ‘Transitions’ Output Data File

This is the main output file of ‘Emissivity’ program. The file starts with a number of text lines summarizing the input data used and the output results, followed by a few commentary lines explaining the symbols and units. This is followed by a number of data lines matching the number of transitions. The data for each transition includes (in the following order) an index identifying the transition, status (FF, FB or BB transition), two joined boolean flags describing the experimental state of the energy data of the upper and lower levels (‘0’ for theoretical data and ‘1’ for experimental), the attributes of the upper and lower levels (configuration, term, $2J$ and parity), wavelength in vacuum, wavelength in air (only for $\lambda > 2000$ Å), the radiative transition probability, the emissivities corresponding to the given temperatures, the normalized emissivities and the effective recombination coefficients corresponding to the given emissivities. Writing the normalized emissivities and the effective recombination coefficients is optional and can be turned off, as described under ‘NormalizationChoice’ and ‘RecCoefficient’ keywords. As mentioned earlier, if the user chooses to read the astronomical data, the observational lines will be inserted in between the theoretical lines according to their lab wavelength.

C.3 Tests

Apart from the normal debugging and testing of the program components to check that they do what they are supposed to do, two physical tests are incorporated within the program to validate its functionality and verify that no serious er-

rors have occurred in processing and computing the data. These tests are the population-balance test and the ground-metastable test. The first test relies on the fact that the population of each state should equal the depopulation. This balance is given by the relation

$$\sum_{j>i} N_j \Gamma_{ji}^r = N_i \sum_{k<i} \Gamma_{ik}^r \quad (\text{C.4})$$

where N is the population of the indicated state, Γ^r is the radiative transition probability, i is the index for the state of concern, j is an index for the states above state i , and k is an index for the states below state i .

The second test is based on the fact that the total number of the electrons leaving the resonances in radiative decay should equal the total number arriving at the ground and metastable states. This balance is given by the relation

$$\sum_{\forall j} N_j \Gamma_j^r = \sum_{\forall i, k>i} N_k \Gamma_{ki}^r \quad (\text{C.5})$$

where i is an index for ground and metastable states and j is an index for resonances.

Appendix D

Input Data for **R**-matrix and Autostructure

In this appendix we include the input data files that we used to generate our theoretical results from **R**-matrix and Autostructure. This is for the purpose of thoroughness and to enable the interested researcher to regenerate and check our results. It should be remarked that the structure of the **R**-matrix and Autostructure data files is fully explained in the write-up of these codes as given by Badnell [41, 113].

D.1 **R**-matrix Input Data

In this section we present our input data files for each stage of **R**-matrix.

D.1.1 STG1

The input data file for this stage is:

```
STO-
&STG1A RAD='YES' RELOP='YES' ISMITN=1 &END
&STG1B NZED=6 NELC=4 MAXORB=7 MAXLA=3 MAXLT=10 MAXC=16 ISMIT(1)=30 ISMIT(2)=31 ISMIT(3)=32 ISMIT(4)=43 MAXE=8 IBC=1 &END
1 0 2 0 2 1 3 0 3 1 3 2 4 3
5
1 1 2 2 2
5.13180 8.51900 2.01880 4.73790 1.57130
21.28251 6.37632 0.08158 -2.61339 -0.00733
5
1 1 2 2 2
```

5.13180	8.51900	2.01880	4.73790	1.57130
-5.39193	-1.49036	5.57151	-5.25090	0.94247
3				
1	2	3		
1.75917	1.75917	1.75917		
5.69321	-19.54864	10.39428		
4				
2	2	2	2	
1.47510	3.19410	1.83070	9.48450	
1.01509	3.80119	2.75006	0.89571	
2				
2	3			
1.98138	1.96954			
14.41203	-10.88586			
1				
3				
2.11997				
5.84915				
1				
4				
2.69086				
9.69136				
10.0000000	0.0			
5				
1	1	2	2	2
5.13180	8.51900	2.01880	4.73790	1.57130
21.28251	6.37632	0.08158	-2.61339	-0.00733
5				
1	1	2	2	2
5.13180	8.51900	2.01880	4.73790	1.57130
-5.39193	-1.49036	5.57151	-5.25090	0.94247
3				
1	2	3		
1.75917	1.75917	1.75917		
5.69321	-19.54864	10.39428		
4				
2	2	2	2	
1.47510	3.19410	1.83070	9.48450	
1.01509	3.80119	2.75006	0.89571	
2				
2	3			
1.98138	1.96954			
14.41203	-10.88586			
1				
3				
2.11997				
5.84915				
1				
4				
2.69086				
9.69136				
10.0000000	0.0			

D.1.2 STG2

The input data file for this stage is:

```

STG-
&STG2A RAD='YES' RELOP='YES' &END
&STG2B MAXORB=7 NELC=4 NAST=26 INAST=0 MINST=2 MAXST=4 MINLT=0 MAXLT=8 &END
1 0 2 0 2 1 3 0 3 1 3 2 4 3
18
2 0 0 0 0 0 0
2 2 2 2 2 2 2
2 2 0 0 0 0 0 0
2 0 2 0 0 0 0 0
2 1 0 1 0 0 0 0
2 0 0 2 0 0 0 0
2 0 1 0 1 0 0 0
2 0 0 0 2 0 0 0
2 0 0 0 2 0 0 0
2 1 1 0 0 0 0 0
2 1 0 0 1 0 0 0
2 0 0 1 1 0 0 0
2 0 1 1 0 0 0 0
2 0 1 0 0 1 0 0
2 0 0 0 1 1 0 0
2 0 0 0 1 1 0 0
2 1 0 0 0 1 0 0
2 0 0 1 0 1 0 0
2 0 1 0 0 0 1 0
2 0 0 0 1 0 1 0
0 1 0
1 3 1
1 1 1
1 3 0

```

```

2 1 0
0 1 0
0 3 0
0 1 0
1 1 1
1 3 1
1 3 1
2 3 0
1 1 1
1 1 0
2 1 0
2 3 0
0 3 0
3 3 1
2 1 1
1 3 1
1 3 0
2 3 1
2 1 0
3 1 1
1 1 1
0 1 0
48
2 0 0 0 0 0
2 2 3 2 3 3 1
2 2 1 0 0 0 0 0
2 2 0 1 0 0 0 0
2 2 0 0 1 0 0 0
2 2 0 0 0 1 0 0
2 2 0 0 0 0 1 0
2 1 2 0 0 0 0 0
2 0 3 0 0 0 0 0
2 0 2 1 0 0 0 0
2 0 2 0 1 0 0 0
2 0 2 0 0 1 0 0
2 0 2 0 0 0 1 0
2 1 1 1 0 0 0 0
2 1 0 2 0 0 0 0
2 1 0 1 1 0 0 0
2 1 0 1 0 1 0 0
2 1 0 1 0 0 1 0
2 0 1 2 0 0 0 0
2 0 0 2 1 0 0 0
2 0 0 2 0 1 0 0
2 0 0 2 0 1 1 0
2 1 1 0 1 0 0 0
2 0 1 1 1 0 0 0
2 0 1 0 2 0 0 0
2 0 1 0 1 1 0 0
2 0 1 0 1 0 1 0
2 1 0 0 2 0 0 0
2 0 0 1 2 0 0 0
2 0 0 0 3 0 0 0
2 0 0 0 2 1 0 0
2 0 0 0 2 0 1 0
2 1 0 0 0 2 0 0
2 0 1 0 0 2 0 0
2 0 0 1 0 2 0 0
2 0 0 0 1 2 0 0
2 0 0 0 0 3 0 0
2 0 0 0 0 2 1 0
2 1 1 0 0 1 0 0
2 1 1 0 0 0 1 0
2 1 0 0 1 1 0 0
2 1 0 0 1 0 1 0
2 0 0 1 1 1 0 0
2 0 0 1 1 0 1 0
2 0 1 1 0 1 0 0
2 0 1 1 0 0 1 0
2 0 1 0 0 1 1 0
2 0 0 0 1 1 1 0
2 1 0 0 0 1 1 0
2 0 0 1 0 1 1 0

```

D.1.3 STGJK

The input data file for this stage is:

```

S.S.
&STGJA RAD='YES' &END
&STGJB JNAST=46 IJNAST=12 &END
0 0
0 1
2 1
4 1
2 1

```



```

0 0
2 0
4 0
4 0
0 0
2 0
0 0
2 1
0 1
2 1
4 1
2 0
4 0
6 0
0 1
2 1
4 1
4 0
2 1
2 0
4 1
6 1
8 1
2 0
4 0
6 0
4 1
2 0
0 1
2 1
4 1
2 1
4 1
6 1
0 0
2 0
4 0
4 0
2 1
6 1
0 0
1 0
3 0
5 0
7 0
9 0
11 0
1 1
3 1
5 1
7 1
9 1
11 1

```

D.1.4 STG3

The input data file for this stage is:

```

S.S.
&STG3A RAD='YES' &END
&STG3B &END

```

D.1.5 STGF

The parameters in the input data file with a sample data is:

```

&STGF IMODE = 0 IPRKM = 1 IQDT = 0 IRDO = 99 IMESH = 1 IEQ = -1 PERT = 'NO'
      LRGLAM = -1 IBIGE = 0 IPRINT = 3 IRAD = 1 IOPT1 = 2 &END
&MESH1 MXE = 1000 E0 = 0.0298042 EINCR = 5.0E-8 &END
0 3 1
-1 -1 -1

```

D.1.6 STGB

The input file for this stage is:

```
&STGB IPERT=0 IRAD=1 &END
  0 1 0
0.1 13.0 0.001
  0 3 0
0.1 13.0 0.001
  0 5 0
0.1 13.0 0.001
  0 7 0
0.1 13.0 0.001
  0 9 0
0.1 13.0 0.001
  0 1 1
0.1 13.0 0.001
  0 3 1
0.1 13.0 0.001
  0 5 1
0.1 13.0 0.001
  0 7 1
0.1 13.0 0.001
  0 9 1
0.1 13.0 0.001
  0 11 1
0.1 13.0 0.001
-1 -1 -1
```

D.1.7 STGBF

For this stage, default values are used, that is:

```
&STGBF &END
```

D.1.8 STGBB

The input data file for this stage is:

```
&STGBB IPRINT=0 IBUT=0 &END
  0 1 0 0 1 1
  0 1 0 0 3 1
  0 3 0 0 1 1
  0 3 0 0 3 1
  0 3 0 0 5 1
  0 5 0 0 3 1
  0 5 0 0 5 1
  0 5 0 0 7 1
  0 7 0 0 5 1
  0 7 0 0 7 1
  0 7 0 0 9 1
  0 9 0 0 7 1
  0 9 0 0 9 1
  0 9 0 0 11 1
  0 11 0 0 9 1
  0 11 0 0 11 1
-1 -1 -1 -1 -1 -1
```

D.1.9 STGQB

The parameters in the input data file with a sample data is:

```
0 0 0
  1
0 3 1
2.945 4.1 1.0E-8
```

D.2 Autostructure Input Data

Autostructure code was used in various stages to produce required theoretical atomic data or to check the results of **R**-matrix. In the next sections we present some of these input data files.

D.2.1 Polarizability

The following input data file was used to decide which terms of the target are the most important ones by having the largest polarizability, as explained in § 3.2.2.

```
S.S.
123456789 22 12513 23 12514 12515 12516 13514 13515 13516
          10 20 21
&SALGEB RUN=' ' RAD='YES' CUP='IC' TITLE='C III_9'
          KORB1=1 KORB2=1 KUTSO=0 &END
&SMINIM NZION=6 INCLUD=6 PRINT='FORM' NLAM=6 RADOUT='YES' &END
          1.00000 1.00000 1.00000 -1.00000 -1.00000 -1.00000
```

D.2.2 Transition Probabilities

The following input data were used to compute the radiative transition probabilities, as discussed in § 3.4.1.

```
S.S.
123456789 12513516 12513515 12523 22516 12513517
          10 20 21 30 31 32
&SALGEB RUN=' ' RAD='YES' CUP='IC' TITLE='Resonance'
          KORB1=1 KORB2=1 KUTSO=0 &END
&SMINIM NZION=6 INCLUD=6 PRINT='FORM' NLAM=6 RADOUT='YES' &END
          1.00000 1.00000 1.00000 1.00000 1.00000 1.00000
```

D.2.3 f -values

The following input data file was used to generate f -values for all FF transitions. It was also used to generate f -values for the free-bound and bound-bound transitions for the topmost bound states, namely the $1s^2 2s 2p(^3P^o) 3d^4 F^o$ and $4D^o$ levels, as these quartets with their large effective quantum number are out of range of RMATRIX-I validity.

```
S.S. 2s2 nl (2s<nl<7p); 2s 2p nl (2s<nl<7p); 2p3; 2p2 nl (2p<nl<7p)
123456789 22513 22514 22515 22516 22517 22518 22519 2251A 2251B 2251C
          2251D 2251E 2251F 2251G 2251H 2251I 2251J 2251K 2251L 2251M
          12523 12513514 12513515 12513516 12513517 12513518 12513519
          1251351A 1251351B 1251351C 1251351D 1251351E 1251351F 1251351G
          1251351H 1251351I 1251351J 1251351K 1251351L 1251351M 33
          23514 23515 23516 23517 23518 23519 2351A 2351B 2351C 2351D
          2351E 2351F 2351G 2351H 2351I 2351J 2351K 2351L 2351M
```

20 21
30 31 32
40 41 42 43
50 51 52 53 54
60 61 62 63 64 65
70

```
&SALGEB RUN=' ' RAD='YES' CUP='IC' TITLE='Resonance'  
KORB1=1 KORB2=1 KUTSO=0 &END  
&SMINIM NZION=6 INCLUD=500 PRINT='FORM' NLAM=22 NVAR=22 RADOUT='YES' &END  
1.43240 1.43380 1.39690 1.25760 1.20290 1.35930 1.25830 1.19950 1.35610 1.41460 1.26080  
1.20020 1.35770 1.41420 1.32960 1.26370 1.20250 1.36210 1.41520 1.41420 2.34460 1.26790  
1 2 3 4 5 6 7 8 9 10 11 12 13 14 15 16 17 18 19 20 21 22
```

Appendix E

Tables

In this appendix, we present a sample of the data produced during this investigation. In Table E.1 the theoretical results for the energies of the bound states of C^+ below the $C^{2+} \ 1S_0^e$ threshold are given alongside the available experimental data from the NIST database [16]. Similarly, Table E.2 presents the energy and autoionization width data for the resonances as obtained by the **K**-matrix and **QB** methods. In these tables, a negative fine structure splitting indicates that the theoretical levels are in reverse order compared to their experimental counterparts. It is noteworthy that due to limited precision of figures in these tables, some data may appear inconsistent, e.g. a zero fine structure splitting from two levels with different energies. Full-precision data in electronic format are available from the author of this thesis on request.

Regarding the bound states, all levels with effective quantum number n_f between 0.1-13 for the outer electron and $0 \leq l \leq 5$ (142 states) are sought and found by **R**-matrix. The 8 uppermost bound states in Table E.1, i.e. the levels of $1s^2 2s 2p(^3P^o) 3d \ 4F^o$ and $4D^o$, have quantum numbers higher than 13 and hence are out of range of the **R**-matrix approximation validity; therefore only experimental data are included for these states. Concerning the resonances, we searched for all

states with $n < 5$ where n is the principal quantum number of the active electron. 61 levels were found by the **K**-matrix method and 55 by the **QB** method.

Tables E.3-E.5 present a sample of the f -values of the free-bound transitions for some bound symmetries as obtained by integrating photoionization cross section over photon energy where these data are obtained from stage STGBF of the **R**-matrix code. The columns in these tables stand for the bound states identified by their indices as given in Table E.1 while the rows stand for the resonances represented by their indices as given in Table E.2. The superscript denotes the power of 10 by which the number is to be multiplied. An entry of ‘0’ in the f -value tables indicates that no peak was observed in the photoionization cross section data.

The reason for presenting a sample of the f -values for the free-bound transitions only is that they require considerable effort to produce. No data belonging to f -values for the bound-bound transitions are given here because they can be easily obtained from the ‘FVALUE’ file generated by the **R**-matrix code using the input data files given in § D.1 in Appendix D. Similarly, no data related to the f -values for the free-free transitions are provided in this appendix because they can be easily generated by Autostructure using the input data file supplied in § D.2.3 in Appendix D.

Finally, Table E.6 contains a sample of the effective recombination coefficients for transitions extracted from our list, SS1, in a wavelength range where several lines have been observed in the spectra of planetary nebulae. It should be remarked that the data of SS1 are generated assuming electron and ion number density of 10^{10} m^{-3} .

Table E.1: The available experimental data from NIST for the bound states of C^+ below the C^{2+} $1S_0^e$ threshold alongside the theoretical results from **R**-matrix calculations.

In. ^a	Config. ^b	Level	NEEW ^c	NEER ^d	FSS ^e	TER ^f	FSSR ^g
1	2s ² 2p	$2P_{1/2}^o$	0	-1.792141		-1.792571	
2	2s ² 2p	$2P_{3/2}^o$	63.42	-1.791563	63.4	-1.791994	63.3
3	2s2p ²	$4P_{1/2}^e$	43003.3	-1.400266		-1.401292	
4	2s2p ²	$4P_{3/2}^e$	43025.3	-1.400065		-1.401090	
5	2s2p ²	$4P_{5/2}^e$	43053.6	-1.399807	50.3	-1.400755	59.0
6	2s2p ²	$2D_{5/2}^e$	74930.1	-1.109327		-1.105247	
7	2s2p ²	$2D_{3/2}^e$	74932.62	-1.109304	2.5	-1.105266	-2.1
8	2s2p ²	$2S_{1/2}^e$	96493.74	-0.912825		-0.899439	
9	2s2p ²	$2P_{1/2}^e$	110624.17	-0.784059		-0.772978	
10	2s2p ²	$2P_{3/2}^e$	110665.56	-0.783682	41.4	-0.772570	44.8
11	2s ² 3s	$2S_{1/2}^e$	116537.65	-0.730171		-0.727698	
12	2s ² 3p	$2P_{1/2}^o$	131724.37	-0.591780		-0.592081	
13	2s ² 3p	$2P_{3/2}^o$	131735.52	-0.591678	11.1	-0.591980	11.1
14	2p ³	$4S_{3/2}^o$	142027.1	-0.497894		-0.487491	
15	2s ² 3d	$2D_{3/2}^e$	145549.27	-0.465798		-0.466024	
16	2s ² 3d	$2D_{5/2}^e$	145550.7	-0.465785	1.4	-0.466005	2.1
17	2p ³	$2D_{5/2}^o$	150461.58	-0.421034		-0.412359	
18	2p ³	$2D_{3/2}^o$	150466.69	-0.420987	5.1	-0.412388	-3.1
19	2s ² 4s	$2S_{1/2}^e$	157234.07	-0.359318		-0.358955	
20	2s ² 4p	$2P_{1/2}^o$	162517.89	-0.311169		-0.310784	
21	2s ² 4p	$2P_{3/2}^o$	162524.57	-0.311108	6.7	-0.310723	6.6
22	2s2p(³ P ^o)3s	$4P_{1/2}^o$	166967.13	-0.270624		-0.268893	
23	2s2p(³ P ^o)3s	$4P_{3/2}^o$	166990.73	-0.270409		-0.268645	
24	2s2p(³ P ^o)3s	$4P_{5/2}^o$	167035.71	-0.269999	68.6	-0.268229	72.9
25	2s ² 4d	$2D_{3/2}^e$	168123.74	-0.260084		-0.260084	
26	2s ² 4d	$2D_{5/2}^e$	168124.45	-0.260078	0.7	-0.260074	1.1
27	2p ³	$2P_{1/2}^o$	168729.53	-0.254564		-0.245329	
28	2p ³	$2P_{3/2}^o$	168748.3	-0.254393	18.8	-0.245083	27.1
29	2s ² 4f	$2F_{5/2}^o$	168978.34	-0.252297		-0.252162	
30	2s ² 4f	$2F_{7/2}^o$	168978.34	-0.252297	0.0	-0.252160	0.2
31	2s ² 5s	$2S_{1/2}^e$	173347.84	-0.212479		-0.212278	
32	2s ² 5p	$2P_{1/2}^o$	175287.39	-0.194804		-0.190099	

Table E.1: continued.

In.	Config.	Level	NEEW	NEER	FSS	TER	FSSR
33	2s ² 5p	² P _{3/2} ^o	175294.75	-0.194737	7.4	-0.190072	3.0
34	2s2p(³ P ^o)3s	² P _{1/2} ^o	177774.59	-0.172139		-0.165330	
35	2s2p(³ P ^o)3s	² P _{3/2} ^o	177793.54	-0.171967	19.0	-0.165143	20.5
36	2s ² 5d	² D _{3/2} ^e	178495.11	-0.165573		-0.165606	
37	2s ² 5d	² D _{5/2} ^e	178495.71	-0.165568	0.6	-0.165599	0.8
38	2s ² 5f	² F _{5/2} ^o	178955.94	-0.161374		-0.161296	
39	2s ² 5f	² F _{7/2} ^o	178955.94	-0.161374	0.0	-0.161295	0.1
40	2s ² 5g	² G _{7/2} ^e	179073.05	-0.160307		-0.160184	
41	2s ² 5g	² G _{9/2} ^e	179073.05	-0.160307	0.0	-0.160184	0.0
42	2s ² 6s	² S _{1/2} ^e	181264.24	-0.140339		-0.140231	
43	2s2p(³ P ^o)3p	⁴ D _{1/2} ^e	181696.66	-0.136399		-0.136848	
44	2s2p(³ P ^o)3p	⁴ D _{3/2} ^e	181711.03	-0.136268		-0.136699	
45	2s2p(³ P ^o)3p	⁴ D _{5/2} ^e	181736.05	-0.136040		-0.136454	
46	2s2p(³ P ^o)3p	⁴ D _{7/2} ^e	181772.41	-0.135709	75.8	-0.136115	80.4
47	2s2p(³ P ^o)3p	² P _{1/2} ^e	182023.86	-0.133417		-0.133095	
48	2s2p(³ P ^o)3p	² P _{3/2} ^e	182043.41	-0.133239	19.6	-0.132896	21.8
49	2s ² 6p	² P _{1/2} ^o	182993.23	-0.124584		-0.124376	
50	2s ² 6p	² P _{3/2} ^o	182993.66	-0.124580	0.4	-0.124351	2.7
51	2s ² 6d	² D _{3/2} ^e	184074.59	-0.114730		-0.114739	
52	2s ² 6d	² D _{5/2} ^e	184075.28	-0.114723	0.7	-0.114729	1.0
53	2s ² 6f	² F _{5/2} ^o	184376.06	-0.111982		-0.111924	
54	2s ² 6f	² F _{7/2} ^o	184376.06	-0.111982	0.0	-0.111924	0.1
55	2s ² 6g	² G _{7/2} ^e	184449.27	-0.111315		-0.111264	
56	2s ² 6g	² G _{9/2} ^e	184449.27	-0.111315	0.0	-0.111264	0.0
57	2s ² 6h	² H _{9/2} ^o	184466.5	-0.111158		-0.111122	
58	2s ² 6h	² H _{11/2} ^o	184466.5	-0.111158	0.0	-0.111122	0.0
59	2s2p(³ P ^o)3p	⁴ S _{3/2} ^e	184690.98	-0.109113		-0.108410	
60	2s ² 7s	² S _{1/2} ^e	185732.93	-0.099618		-0.099537	
61	2s2p(³ P ^o)3p	⁴ P _{1/2} ^e	186427.35	-0.093290		-0.092097	
62	2s2p(³ P ^o)3p	⁴ P _{3/2} ^e	186443.69	-0.093141		-0.091950	
63	2s2p(³ P ^o)3p	⁴ P _{5/2} ^e	186466.02	-0.092937	38.7	-0.091717	41.8
64	2s ² 7p	² P _{1/2} ^o	186745.9	-0.090387		-0.090313	
65	2s ² 7p	² P _{3/2} ^o	186746.3	-0.090383	0.4	-0.090302	1.1

Table E.1: continued.

In.	Config.	Level	NEEW	NEER	FSS	TER	FSSR
66	2s ² 7d	² D _{3/2} ^e	187353	-0.084854		-0.084804	
67	2s ² 7d	² D _{5/2} ^e	187353	-0.084854	0.0	-0.084764	4.4
68	2s ² 7f	² F _{5/2} ^o	187641.6	-0.082225		-0.082171	
69	2s ² 7f	² F _{7/2} ^o	187641.6	-0.082225	0.0	-0.082171	0.0
70	2s ² 7g	² G _{7/2} ^e	187691.4	-0.081771		-0.081744	
71	2s ² 7g	² G _{9/2} ^e	187691.4	-0.081771	0.0	-0.081744	0.0
72	2s ² 7h	² H _{9/2} ^o	187701	-0.081683		-0.081645	
73	2s ² 7h	² H _{11/2} ^o	187701	-0.081683	0.0	-0.081645	0.0
74	2s ² 8s	² S _{1/2} ^e	—	—		-0.074324	
75	2s2p(³ P ^o)3p	² D _{3/2} ^e	188581.25	-0.073662		-0.071901	
76	2s2p(³ P ^o)3p	² D _{5/2} ^e	188615.07	-0.073354	33.8	-0.071582	34.9
77	2s ² 8p	² P _{1/2} ^o	—	—		-0.068349	
78	2s ² 8p	² P _{3/2} ^o	—	—		-0.068343	0.7
79	2s ² 8f	² F _{5/2} ^o	—	—		-0.062873	
80	2s ² 8f	² F _{7/2} ^o	—	—		-0.062872	0.0
81	2s ² 8g	² G _{7/2} ^e	189794.2	-0.062609		-0.062580	
82	2s ² 8g	² G _{9/2} ^e	189794.2	-0.062609	0.0	-0.062580	0.0
83	2s ² 8h	² H _{11/2} ^o	—	—		-0.062511	
84	2s ² 8h	² H _{9/2} ^o	—	—		-0.062511	0.0
85	2s ² 8d	² D _{3/2} ^e	—	—		-0.062612	
86	2s ² 8d	² D _{5/2} ^e	—	—		-0.062564	5.3
87	2s ² 9s	² S _{1/2} ^e	—	—		-0.057638	
88	2s ² 9p	² P _{1/2} ^o	—	—		-0.053490	
89	2s ² 9p	² P _{3/2} ^o	—	—		-0.053486	0.4
90	2s ² 9d	² D _{3/2} ^e	—	—		-0.049942	
91	2s ² 9d	² D _{5/2} ^e	—	—		-0.049935	0.8
92	2s ² 9f	² F _{5/2} ^o	—	—		-0.049651	
93	2s ² 9f	² F _{7/2} ^o	—	—		-0.049650	0.0
94	2s ² 9g	² G _{7/2} ^e	—	—		-0.049441	
95	2s ² 9g	² G _{9/2} ^e	—	—		-0.049441	0.0
96	2s ² 9h	² H _{9/2} ^o	—	—		-0.049392	
97	2s ² 9h	² H _{11/2} ^o	—	—		-0.049392	0.0
98	2s ² 10s	² S _{1/2} ^e	—	—		-0.046050	

Table E.1: continued.

In.	Config.	Level	NEEW	NEER	FSS	TER	FSSR
99	2s ² 10p	² P _{1/2} ^o	—	—		-0.042990	
100	2s ² 10p	² P _{3/2} ^o	—	—		-0.042987	0.3
101	2s ² 10d	² D _{3/2} ^e	—	—		-0.040487	
102	2s ² 10d	² D _{5/2} ^e	—	—		-0.040484	0.3
103	2s ² 10f	² F _{5/2} ^o	—	—		-0.040198	
104	2s ² 10f	² F _{7/2} ^o	—	—		-0.040198	0.0
105	2s ² 10g	² G _{7/2} ^e	—	—		-0.040044	
106	2s ² 10g	² G _{9/2} ^e	—	—		-0.040044	0.0
107	2s ² 10h	² H _{9/2} ^o	—	—		-0.040007	
108	2s ² 10h	² H _{11/2} ^o	—	—		-0.040007	0.0
109	2s ² 11s	² S _{1/2} ^e	—	—		-0.037746	
110	2s ² 11p	² P _{1/2} ^o	—	—		-0.035300	
111	2s ² 11p	² P _{3/2} ^o	—	—		-0.035298	0.2
112	2s ² 11d	² D _{3/2} ^e	—	—		-0.033449	
113	2s ² 11d	² D _{5/2} ^e	—	—		-0.033448	0.2
114	2s ² 11f	² F _{5/2} ^o	—	—		-0.033209	
115	2s ² 11f	² F _{7/2} ^o	—	—		-0.033209	0.0
116	2s ² 11g	² G _{7/2} ^e	—	—		-0.033092	
117	2s ² 11g	² G _{9/2} ^e	—	—		-0.033092	0.0
118	2s ² 11h	² H _{9/2} ^o	—	—		-0.033064	
119	2s ² 11h	² H _{11/2} ^o	—	—		-0.033064	0.0
120	2s ² 12s	² S _{1/2} ^e	—	—		-0.031953	
121	2s ² 12p	² P _{1/2} ^o	—	—		-0.029501	
122	2s ² 12p	² P _{3/2} ^o	—	—		-0.029499	0.2
123	2s2p(³ P ^o)3p	² S _{1/2} ^e	—	—		-0.028972	
124	2s ² 12d	² D _{3/2} ^e	—	—		-0.028090	
125	2s ² 12d	² D _{5/2} ^e	—	—		-0.028089	0.1
126	2s ² 12f	² F _{5/2} ^o	—	—		-0.027895	
127	2s ² 12f	² F _{7/2} ^o	—	—		-0.027895	0.0
128	2s ² 12g	² G _{7/2} ^e	—	—		-0.027804	
129	2s ² 12g	² G _{9/2} ^e	—	—		-0.027804	0.0
130	2s ² 12h	² H _{9/2} ^o	—	—		-0.027783	
131	2s ² 12h	² H _{11/2} ^o	—	—		-0.027783	0.0

Table E.1: continued.

In.	Config.	Level	NEEW	NEER	FSS	TER	FSSR
132	2s ² 13s	² S _{1/2} ^e	—	—		-0.025758	
133	2s ² 13p	² P _{1/2} ^o	—	—		-0.025021	
134	2s ² 13p	² P _{3/2} ^o	—	—		-0.025020	0.1
135	2s ² 13d	² D _{3/2} ^e	—	—		-0.023920	
136	2s ² 13d	² D _{5/2} ^e	—	—		-0.023919	0.1
137	2s ² 13f	² F _{5/2} ^o	—	—		-0.023762	
138	2s ² 13f	² F _{7/2} ^o	—	—		-0.023762	0.0
139	2s ² 13g	² G _{7/2} ^e	—	—		-0.023690	
140	2s ² 13g	² G _{9/2} ^e	—	—		-0.023690	0.0
141	2s ² 13h	² H _{9/2} ^o	—	—		-0.023673	
142	2s ² 13h	² H _{11/2} ^o	—	—		-0.023673	0.0
143	2s2p(³ P ^o)3d	⁴ F _{3/2} ^o	195752.58	-0.008312			
144	2s2p(³ P ^o)3d	⁴ F _{5/2} ^o	195765.85	-0.008191			
145	2s2p(³ P ^o)3d	⁴ F _{7/2} ^o	195785.74	-0.008010			
146	2s2p(³ P ^o)3d	⁴ F _{9/2} ^o	195813.66	-0.007755	61.1		
147	2s2p(³ P ^o)3d	⁴ D _{1/2} ^o	196557.87	-0.000974			
148	2s2p(³ P ^o)3d	⁴ D _{3/2} ^o	196563.41	-0.000923			
149	2s2p(³ P ^o)3d	⁴ D _{5/2} ^o	196571.82	-0.000846			
150	2s2p(³ P ^o)3d	⁴ D _{7/2} ^o	196581.96	-0.000754	24.1		

^a Index.

^b Configuration. The 1s² core is suppressed from all configurations.

^c NIST Experimental Energy in Wavenumbers (cm⁻¹) relative to the ground state.

^d NIST Experimental Energy in Rydberg relative to the C²⁺ ¹S₀^e limit.

^e Fine Structure Splitting from experimental values in cm⁻¹.

^f Theoretical Energy in Rydberg from **R**-matrix calculations relative to the C²⁺ ¹S₀^e limit.

^g Fine Structure Splitting from **R**-matrix in cm⁻¹. The minus sign indicates that the theoretical levels are in reverse order compared to the experimental.

Table E.2: The available experimental data from NIST for the resonance states of C^+ above the $C^{2+} 1s_0^e$ threshold alongside the theoretical results as obtained by **K**-matrix and **QB** methods.

In. ^a	Config. ^b	Level	NEEW ^c	NEER ^d	FSS ^e	TERK ^f	FSSK ^g	FWHMK ^h	TERQ ⁱ	FSSQ ^j	FWHMQ ^k
1	2s2p(³ P ^o)3d	² D _{3/2} ^o	198425.43	0.016045		0.017012		6.00E-10	0.017012		6.00E-10
2	2s2p(³ P ^o)3d	² D _{5/2} ^o	198436.31	0.016144	10.9	0.017124	12.3	2.61E-09	0.017124	12.3	2.61E-09
3	2s2p(³ P ^o)3d	⁴ P _{5/2} ^o	198844	0.019859		0.020655		2.17E-11	—		—
4	2s2p(³ P ^o)3d	⁴ P _{3/2} ^o	198865.25	0.020053		0.020849		1.26E-09	0.020849		1.26E-09
5	2s2p(³ P ^o)3d	⁴ P _{1/2} ^o	198879.01	0.020178	35.0	0.020968	34.3	5.10E-10	0.020968		5.10E-10
6	2s2p(³ P ^o)3d	² F _{5/2} ^o	199941.41	0.029860		0.031693		5.61E-05	0.031689		5.61E-05
7	2s2p(³ P ^o)3d	² F _{7/2} ^o	199983.24	0.030241	41.8	0.032109	45.6	5.79E-05	0.032106	45.8	5.79E-05
8	2s2p(³ P ^o)3d	² P _{3/2} ^o	202179.85	0.050258		0.053787		1.06E-05	0.053787		1.06E-05
9	2s2p(³ P ^o)3d	² P _{1/2} ^o	202204.52	0.050483	24.7	0.054019	25.5	1.12E-05	0.054019	25.5	1.12E-05
10	2s2p(³ P ^o)4s	⁴ P _{1/2} ^o	209552.36	0.117441		0.118682		2.55E-07	0.118682		2.55E-07
11	2s2p(³ P ^o)4s	⁴ P _{3/2} ^o	209576.46	0.117661		0.118938		6.25E-07	0.118938		6.25E-07
12	2s2p(³ P ^o)4s	⁴ P _{5/2} ^o	209622.32	0.118079	70.0	0.119304	68.3	<1.0E-16	—		—
13	2s2p(³ P ^o)4s	² P _{1/2} ^o	—	—		0.137883		6.13E-03	0.137866		6.02E-03
14	2s2p(³ P ^o)4s	² P _{3/2} ^o	—	—		0.138385	55.0	6.15E-03	0.138365	54.8	6.03E-03
15	2s2p(³ P ^o)4p	² P _{1/2} ^e	214404.33	0.161655		0.162743		2.12E-08	0.162743		2.12E-08
16	2s2p(³ P ^o)4p	² P _{3/2} ^e	214429.95	0.161889	25.6	0.162996	27.7	9.89E-08	0.162996	27.8	9.89E-08
17	2s2p(³ P ^o)4p	⁴ D _{1/2} ^e	214759.91	0.164896		0.165629		5.30E-11	0.165629		5.31E-11
18	2s2p(³ P ^o)4p	⁴ D _{3/2} ^e	214772.84	0.165014		0.165760		5.12E-08	0.165760		5.12E-08
19	2s2p(³ P ^o)4p	⁴ D _{5/2} ^e	214795.27	0.165218		0.165984		6.95E-08	0.165984		6.95E-08
20	2s2p(³ P ^o)4p	⁴ D _{7/2} ^e	214829.77	0.165532	69.9	—	—	—	—	—	—
21	2s2p(³ P ^o)4p	⁴ S _{3/2} ^e	215767.77	0.174080		0.174625		6.59E-12	—		—
22	2s2p(³ P ^o)4p	⁴ P _{1/2} ^e	216362.84	0.179503		0.180780		7.26E-08	0.180780		7.26E-08
23	2s2p(³ P ^o)4p	⁴ P _{3/2} ^e	216379.59	0.179655		0.180931		1.03E-07	0.180931		1.03E-07
24	2s2p(³ P ^o)4p	⁴ P _{5/2} ^e	216400.57	0.179846	37.7	0.181145	40.0	6.05E-07	0.181145	40.0	6.05E-07
25	2s2p(³ P ^o)4p	² D _{3/2} ^e	—	—		0.185420		1.19E-03	0.185422		1.18E-03
26	2s2p(³ P ^o)4p	² D _{5/2} ^e	216927	0.184644		0.185859	48.2	1.18E-03	0.185859	48.0	1.18E-03
27	2s2p(³ P ^o)4p	² S _{1/2} ^e	—	—		0.199765		4.28E-04	0.199765		4.28E-04
28	2s2p(¹ P ^o)3s	² P _{1/2} ^o	—	—		0.205892		3.03E-03	0.205889		3.02E-03
29	2s2p(¹ P ^o)3s	² P _{3/2} ^o	—	—		0.205912	2.2	3.01E-03	0.205909	2.2	3.01E-03
30	2s2p(³ P ^o)4d	⁴ F _{3/2} ^o	219556.54	0.208606		0.208824		5.08E-11	0.208824		5.08E-11
31	2s2p(³ P ^o)4d	⁴ F _{5/2} ^o	219570.15	0.208730		0.208968		4.23E-09	0.208968		4.23E-09
32	2s2p(³ P ^o)4d	⁴ F _{7/2} ^o	219590.76	0.208918		0.209174		5.96E-09	0.209174		5.96E-09
33	2s2p(³ P ^o)4d	⁴ F _{9/2} ^o	219619.88	0.209183	63.3	—	—	—	—	—	—
34	2s2p(³ P ^o)4d	⁴ D _{1/2} ^o	220125.51	0.213791		0.214804		2.31E-09	0.214804		2.31E-09
35	2s2p(³ P ^o)4d	⁴ D _{3/2} ^o	220130.86	0.213839		0.214847		1.06E-09	0.214847		1.06E-09
36	2s2p(³ P ^o)4d	⁴ D _{5/2} ^o	220139.41	0.213917		0.214923		1.33E-09	0.214923		1.33E-09
37	2s2p(³ P ^o)4d	⁴ D _{7/2} ^o	220150.49	0.214018	25.0	0.215042	26.1	6.19E-09	0.215042	26.1	6.19E-09
38	2s2p(³ P ^o)4d	² D _{3/2} ^o	220601.53	0.218128		0.219325		1.99E-08	0.219325		1.99E-08
39	2s2p(³ P ^o)4d	² D _{5/2} ^o	220614.51	0.218247	13.0	0.219441	12.7	5.68E-09	0.219441	12.7	5.68E-09
40	2s2p(³ P ^o)4d	⁴ P _{5/2} ^o	220811.69	0.220044		0.220495		2.43E-10	0.220495		2.43E-10
41	2s2p(³ P ^o)4d	⁴ P _{3/2} ^o	220832.15	0.220230		0.220680		5.32E-10	0.220680		5.32E-10
42	2s2p(³ P ^o)4d	⁴ P _{1/2} ^o	220845.07	0.220348	33.4	0.220796	33.0	3.65E-10	0.220796	33.0	3.65E-10
43	2s2p(³ P ^o)4f	² F _{5/2} ^e	221088.88	0.222570		0.223542		9.13E-09	0.223542		9.13E-09
44	2s2p(³ P ^o)4f	² F _{7/2} ^e	221097.92	0.222652	9.0	0.223626	9.2	1.98E-11	—		—
45	2s2p(³ P ^o)4f	⁴ F _{3/2} ^e	221093.95	0.222616		0.223626		5.96E-09	0.223626		5.96E-09

Table E.2: continued.

In.	Config.	Level	NEEW	NEER	FSS	TERK	FSSK	FWHMK	TERQ	FSSQ	FWHMQ
46	2s2p(³ P ^o)4f	⁴ F _{5/2} ^e	221099.11	0.222663		0.223658		5.90E-09	0.223658		5.90E-09
47	2s2p(³ P ^o)4f	⁴ F _{7/2} ^e	221105.73	0.222723		0.223725		5.43E-10	0.223725		5.43E-10
48	2s2p(³ P ^o)4f	⁴ F _{9/2} ^e	221109.78	0.222760	15.8	0.223779	16.8	1.26E-09	0.223779	16.8	1.26E-09
49	2s2p(³ P ^o)4d	² F _{5/2} ^o	221460.88	0.225959		0.227144		1.45E-05	0.227144		1.45E-05
50	2s2p(³ P ^o)4d	² F _{7/2} ^o	221503.33	0.226346	42.4	0.227556	45.1	1.51E-05	0.227556	45.1	1.51E-05
51	2s2p(³ P ^o)4f	⁴ G _{5/2} ^e	221544.81	0.226724		0.227648		5.45E-10	0.227648		5.46E-10
52	2s2p(³ P ^o)4f	⁴ G _{7/2} ^e	221553.99	0.226808		0.227757		7.22E-09	0.227757		7.22E-09
53	2s2p(³ P ^o)4f	⁴ G _{9/2} ^e	221575.61	0.227005		0.227966		6.53E-09	0.227966		6.54E-09
54	2s2p(³ P ^o)4f	⁴ G _{11/2} ^e	221604.9	0.227272	60.1	—	—	—	—	—	—
55	2s2p(³ P ^o)4f	² G _{7/2} ^e	221587.12	0.227110		0.228164		2.58E-08	0.228164		2.58E-08
56	2s2p(³ P ^o)4f	² G _{9/2} ^e	221625.72	0.227462	38.6	0.228541	41.4	4.16E-08	0.228541	41.4	4.16E-08
57	2s2p(³ P ^o)4f	⁴ D _{7/2} ^e	221698.48	0.228125		0.229105		2.97E-12	—		—
58	2s2p(³ P ^o)4f	⁴ D _{5/2} ^e	221707.71	0.228209		0.229229		2.39E-06	0.229229		2.39E-06
59	2s2p(³ P ^o)4f	⁴ D _{3/2} ^e	221729.69	0.228409		0.229418		7.35E-07	0.229418		7.35E-07
60	2s2p(³ P ^o)4f	⁴ D _{1/2} ^e	221742.79	0.228528	44.3	0.229529	46.5	<1.0E-16	—		—
61	2s2p(³ P ^o)4f	² D _{5/2} ^e	221729.92	0.228411		0.229459		4.77E-06	0.229459		4.77E-06
62	2s2p(³ P ^o)4f	² D _{3/2} ^e	221752.26	0.228615	22.3	0.229695	25.9	6.58E-06	0.229696	25.9	6.58E-06
63	2s2p(³ P ^o)4d	² P _{3/2} ^o	222258.8	0.233231		0.234626		2.42E-05	0.234626		2.42E-05
64	2s2p(³ P ^o)4d	² P _{1/2} ^o	222285.7	0.233476	26.9	0.234870	26.8	2.46E-05	0.234870	26.8	2.46E-05

^a Index.

^b Configuration. The 1s² core is suppressed from all configurations.

^c NIST Experimental Energy in Wavenumbers (cm⁻¹) relative to the ground state.

^d NIST Experimental Energy in Rydberg relative to the C²⁺ ¹S₀^e limit.

^e Fine Structure Splitting from experimental values in cm⁻¹.

^f Theoretical Energy in Rydberg from **K**-matrix calculations relative to the C²⁺ ¹S₀^e limit.

^g Fine Structure Splitting from **K**-matrix in cm⁻¹.

^h Full Width at Half Maximum from **K**-matrix in Rydberg.

ⁱ Theoretical Energy in Rydberg from **QB** calculations relative to the C²⁺ ¹S₀^e limit.

^j Fine Structure Splitting from **QB** in cm⁻¹.

^k Full Width at Half Maximum from **QB** in Rydberg.

Table E.3: Free-bound f -values for bound symmetry $J^\pi = 1/2^p$ obtained by integrating photoionization cross sections from \mathbf{R} -matrix calculations. The superscript denotes the power of 10 by which the number is to be multiplied.

In.	1	12	20	22	27	32	34	49	64	77	88	99	110	121	133
15	6.12 ⁻³	1.57 ⁻³	5.60 ⁻⁴	4.58 ⁻⁵	1.92 ⁻²	1.01 ⁻³	2.89 ⁻²	3.93 ⁻³	1.55 ⁻³	8.99 ⁻⁴	5.98 ⁻⁴	4.26 ⁻⁴	3.17 ⁻⁴	2.44 ⁻⁴	1.92 ⁻⁴
16	3.18 ⁻³	8.30 ⁻⁴	2.69 ⁻⁴	1.21 ⁻⁵	9.72 ⁻³	5.02 ⁻⁴	1.47 ⁻²	2.02 ⁻³	7.92 ⁻⁴	4.63 ⁻⁴	3.07 ⁻⁴	2.20 ⁻⁴	1.64 ⁻⁴	1.26 ⁻⁴	9.93 ⁻⁵
17	1.70 ⁻⁵	4.69 ⁻⁶	1.59 ⁻⁶	1.34 ⁻²	5.91 ⁻⁵	2.92 ⁻⁶	8.14 ⁻⁵	1.09 ⁻⁵	4.27 ⁻⁶	2.47 ⁻⁶	1.64 ⁻⁶	1.16 ⁻⁶	8.63 ⁻⁷	6.60 ⁻⁷	5.15 ⁻⁷
18	8.53 ⁻⁶	3.43 ⁻⁶	4.94 ⁻⁷	1.35 ⁻²	1.19 ⁻⁵	7.05 ⁻⁷	2.68 ⁻⁵	5.00 ⁻⁶	1.95 ⁻⁶	1.19 ⁻⁶	8.00 ⁻⁷	5.89 ⁻⁷	4.64 ⁻⁷	3.50 ⁻⁷	2.90 ⁻⁷
21	4.43 ⁻⁷	1.39 ⁻⁷	5.34 ⁻⁸	1.78 ⁻³	1.67 ⁻⁶	7.21 ⁻⁸	2.04 ⁻⁶	2.71 ⁻⁷	1.04 ⁻⁷	5.92 ⁻⁸	3.88 ⁻⁸	2.71 ⁻⁸	1.99 ⁻⁸	1.51 ⁻⁸	1.18 ⁻⁸
22	4.48 ⁻⁷	3.87 ⁻⁷	4.64 ⁻⁹	2.22 ⁻⁴	6.57 ⁻¹³	7.26 ⁻⁸	8.82 ⁻⁷	1.54 ⁻⁷	7.90 ⁻⁸	5.31 ⁻⁸	3.85 ⁻⁸	2.95 ⁻⁸	2.41 ⁻⁸	1.91 ⁻⁸	1.53 ⁻⁸
23	2.44 ⁻⁶	1.65 ⁻⁶	6.16 ⁻⁷	1.01 ⁻³	1.65 ⁻⁷	5.61 ⁻⁸	7.62 ⁻⁷	5.76 ⁻⁷	3.75 ⁻⁷	2.74 ⁻⁷	2.08 ⁻⁷	1.61 ⁻⁷	1.27 ⁻⁷	1.02 ⁻⁷	8.32 ⁻⁸
25	1.81 ⁻²	1.13 ⁻²	3.63 ⁻³	3.44 ⁻⁷	2.22 ⁻³	1.01 ⁻³	1.66 ⁻²	7.00 ⁻³	4.20 ⁻³	2.96 ⁻³	2.20 ⁻³	1.69 ⁻³	1.32 ⁻³	1.05 ⁻³	8.50 ⁻⁴
27	1.81 ⁻³	2.76 ⁻³	7.42 ⁻⁴	3.83 ⁻⁸	1.55 ⁻³	4.26 ⁻⁴	2.16 ⁻³	4.12 ⁻⁴	2.69 ⁻⁴	1.98 ⁻⁴	1.52 ⁻⁴	1.20 ⁻⁴	9.55 ⁻⁵	7.73 ⁻⁵	6.32 ⁻⁵
45	1.31 ⁻⁹	3.51 ⁻⁸	1.80 ⁻⁸	7.18 ⁻⁷	3.61 ⁻⁶	6.21 ⁻⁶	1.84 ⁻⁵	6.64 ⁻⁷	1.40 ⁻⁷	6.59 ⁻⁸	4.25 ⁻⁸	2.98 ⁻⁸	2.26 ⁻⁸	1.82 ⁻⁸	1.53 ⁻⁸
59	8.42 ⁻⁷	3.47 ⁻⁶	1.84 ⁻⁶	6.24 ⁻⁴	4.20 ⁻⁴	6.82 ⁻⁴	1.99 ⁻³	6.74 ⁻⁵	1.46 ⁻⁵	6.42 ⁻⁶	3.64 ⁻⁶	2.34 ⁻⁶	1.61 ⁻⁶	1.17 ⁻⁶	8.82 ⁻⁷
60	1.93 ⁻¹⁰	1.70 ⁻¹⁰	2.09 ⁻¹¹	5.12 ⁻⁴	1.07 ⁻⁹	1.51 ⁻⁹	3.28 ⁻⁹	2.78 ⁻¹⁰	7.52 ⁻¹³	2.96 ⁻¹³	2.36 ⁻¹³	1.88 ⁻¹³	5.71 ⁻¹³	4.68 ⁻¹³	3.86 ⁻¹³
62	8.30 ⁻⁶	1.94 ⁻⁵	1.09 ⁻⁵	6.60 ⁻⁵	3.76 ⁻³	6.16 ⁻³	1.74 ⁻²	5.94 ⁻⁴	1.29 ⁻⁴	5.62 ⁻⁵	3.17 ⁻⁵	2.03 ⁻⁵	1.39 ⁻⁵	1.00 ⁻⁵	7.51 ⁻⁶

Table E.4: Free-bound f -values for bound symmetry $J^\pi = 3/2^0$ obtained by integrating photoionization cross sections from \mathbf{R} -matrix calculations. The superscript denotes the power of 10 by which the number is to be multiplied.

In.	2	13	14	18	21	23	28	33	35	50	65	78	89	100	111	122	134
15	1.49 ⁻³	3.73 ⁻⁴	3.75 ⁻¹⁰	2.32 ⁻³	1.45 ⁻⁴	6.09 ⁻⁶	4.82 ⁻³	2.45 ⁻⁴	7.17 ⁻³	9.78 ⁻⁴	3.82 ⁻⁴	2.21 ⁻⁴	1.47 ⁻⁴	1.04 ⁻⁴	7.77 ⁻⁵	5.97 ⁻⁵	4.69 ⁻⁵
16	7.53 ⁻³	1.91 ⁻³	1.58 ⁻⁹	4.40 ⁻⁴	7.03 ⁻⁴	2.70 ⁻⁵	2.39 ⁻²	1.23 ⁻³	3.60 ⁻²	4.91 ⁻³	1.92 ⁻³	1.11 ⁻³	7.36 ⁻⁴	5.25 ⁻⁴	3.91 ⁻⁴	2.99 ⁻⁴	2.35 ⁻⁴
17	4.15 ⁻⁶	1.12 ⁻⁶	1.96 ⁻¹⁰	6.73 ⁻⁶	4.15 ⁻⁷	1.33 ⁻³	1.48 ⁻⁵	7.06 ⁻⁷	2.02 ⁻⁵	2.73 ⁻⁶	1.06 ⁻⁶	6.09 ⁻⁷	4.02 ⁻⁷	2.85 ⁻⁷	2.11 ⁻⁷	1.61 ⁻⁷	1.26 ⁻⁷
18	9.38 ⁻⁶	2.33 ⁻⁶	1.26 ⁻⁹	2.57 ⁻⁷	9.49 ⁻⁷	8.54 ⁻³	3.96 ⁻⁵	1.87 ⁻⁶	5.00 ⁻⁵	6.55 ⁻⁶	2.40 ⁻⁶	1.38 ⁻⁶	9.09 ⁻⁷	6.43 ⁻⁷	4.53 ⁻⁷	3.45 ⁻⁷	2.68 ⁻⁷
19	8.52 ⁻⁷	6.35 ⁻⁷	2.88 ⁻⁹	1.31 ⁻⁸	6.29 ⁻⁸	1.70 ⁻²	3.61 ⁻⁷	1.17 ⁻⁷	4.99 ⁻⁷	4.47 ⁻⁷	2.97 ⁻⁷	2.18 ⁻⁷	1.67 ⁻⁷	1.30 ⁻⁷	1.03 ⁻⁷	8.24 ⁻⁸	6.72 ⁻⁸
21	1.07 ⁻⁶	3.31 ⁻⁷	9.71 ⁻⁹	7.28 ⁻⁸	1.41 ⁻⁷	1.75 ⁻³	4.13 ⁻⁶	1.77 ⁻⁷	5.05 ⁻⁶	6.70 ⁻⁷	2.56 ⁻⁷	1.45 ⁻⁷	9.47 ⁻⁸	6.65 ⁻⁸	4.88 ⁻⁸	3.70 ⁻⁸	2.88 ⁻⁸
22	8.46 ⁻⁸	1.94 ⁻⁷	3.34 ⁻⁶	2.59 ⁻⁸	8.10 ⁻⁸	6.20 ⁻⁴	5.42 ⁻⁷	5.30 ⁻⁸	2.18 ⁻⁸	3.66 ⁻⁸	3.16 ⁻⁸	2.63 ⁻⁸	2.16 ⁻⁸	1.76 ⁻⁸	1.44 ⁻⁸	1.18 ⁻⁸	8.36 ⁻⁹
23	8.05 ⁻⁷	3.16 ⁻⁷	6.69 ⁻⁶	3.12 ⁻⁷	7.82 ⁻⁸	1.75 ⁻⁴	8.71 ⁻⁷	5.77 ⁻⁸	1.69 ⁻⁶	3.10 ⁻⁷	1.41 ⁻⁷	8.84 ⁻⁸	6.13 ⁻⁸	4.48 ⁻⁸	3.38 ⁻⁸	2.61 ⁻⁸	2.06 ⁻⁸
24	1.21 ⁻⁵	7.19 ⁻⁶	1.02 ⁻⁵	1.33 ⁻⁷	1.97 ⁻⁶	5.70 ⁻⁴	1.39 ⁻⁶	9.26 ⁻⁷	9.35 ⁻⁶	4.66 ⁻⁶	2.71 ⁻⁶	1.93 ⁻⁶	1.44 ⁻⁶	1.11 ⁻⁶	8.68 ⁻⁷	6.92 ⁻⁷	5.60 ⁻⁷
25	2.17 ⁻³	1.34 ⁻³	4.07 ⁻¹⁰	2.32 ⁻³	3.60 ⁻⁴	1.03 ⁻⁷	2.82 ⁻⁴	1.55 ⁻⁴	1.81 ⁻³	7.25 ⁻⁴	4.35 ⁻⁴	3.06 ⁻⁴	2.27 ⁻⁴	1.74 ⁻⁴	1.36 ⁻⁴	1.08 ⁻⁴	8.72 ⁻⁵
26	1.65 ⁻²	1.03 ⁻²	7.75 ⁻⁹	2.52 ⁻⁴	2.85 ⁻³	1.34 ⁻⁶	2.04 ⁻³	6.47 ⁻⁴	1.55 ⁻²	6.42 ⁻³	3.82 ⁻³	2.70 ⁻³	2.01 ⁻³	1.40 ⁻³	1.10 ⁻³	8.74 ⁻⁴	7.06 ⁻⁴
27	1.83 ⁻³	2.69 ⁻³	5.75 ⁻⁹	3.73 ⁻⁸	6.92 ⁻⁴	9.90 ⁻⁸	1.46 ⁻³	4.33 ⁻⁴	2.26 ⁻³	4.40 ⁻⁴	2.77 ⁻⁴	2.29 ⁻⁴	1.76 ⁻⁴	1.39 ⁻⁴	1.11 ⁻⁴	8.97 ⁻⁵	7.34 ⁻⁵
43	8.82 ⁻¹⁰	3.29 ⁻⁸	2.11 ⁻¹¹	1.95 ⁻²	4.70 ⁻¹⁰	3.85 ⁻⁷	4.71 ⁻⁶	9.11 ⁻⁶	2.73 ⁻⁵	9.58 ⁻⁷	2.10 ⁻⁷	9.16 ⁻⁸	5.05 ⁻⁸	3.29 ⁻⁸	2.22 ⁻⁸	1.56 ⁻⁸	1.13 ⁻⁸
45	1.40 ⁻¹⁰	3.21 ⁻⁹	1.02 ⁻¹³	1.56 ⁻⁶	1.28 ⁻⁹	4.30 ⁻⁷	3.43 ⁻⁷	5.82 ⁻⁷	1.77 ⁻⁶	6.67 ⁻⁸	1.43 ⁻⁸	7.03 ⁻⁹	4.33 ⁻⁹	3.03 ⁻⁹	2.30 ⁻⁹	1.85 ⁻⁹	1.55 ⁻⁹
46	3.92 ⁻¹⁰	1.91 ⁻⁸	3.10 ⁻¹²	8.73 ⁻⁴	9.29 ⁻⁹	1.59 ⁻⁶	3.18 ⁻⁶	5.65 ⁻⁶	1.69 ⁻⁵	5.77 ⁻⁷	1.32 ⁻⁷	6.04 ⁻⁸	3.58 ⁻⁸	2.41 ⁻⁸	1.77 ⁻⁸	1.37 ⁻⁸	1.11 ⁻⁸
51	2.59 ⁻¹⁰	2.29 ⁻⁹	4.10 ⁻¹³	2.84 ⁻⁵	1.02 ⁻⁹	2.51 ⁻⁸	2.90 ⁻⁷	4.87 ⁻⁷	1.41 ⁻⁶	4.77 ⁻⁸	1.03 ⁻⁸	4.54 ⁻⁹	2.56 ⁻⁹	1.64 ⁻⁹	1.13 ⁻⁹	8.19 ⁻¹⁰	6.15 ⁻¹⁰
58	2.89 ⁻⁶	9.08 ⁻⁶	8.44 ⁻¹⁰	3.22 ⁻⁵	3.81 ⁻⁶	5.82 ⁻⁴	1.25 ⁻³	2.06 ⁻³	5.93 ⁻³	1.97 ⁻⁴	4.20 ⁻⁵	1.81 ⁻⁵	1.05 ⁻⁵	6.70 ⁻⁶	4.61 ⁻⁶	3.32 ⁻⁶	2.49 ⁻⁶
59	7.73 ⁻⁹	3.06 ⁻⁷	2.55 ⁻¹¹	1.70 ⁻⁴	1.65 ⁻⁷	3.98 ⁻⁴	4.12 ⁻⁵	6.90 ⁻⁵	1.98 ⁻⁴	6.91 ⁻⁶	1.45 ⁻⁶	6.29 ⁻⁷	3.54 ⁻⁷	2.39 ⁻⁷	1.64 ⁻⁷	1.19 ⁻⁷	8.89 ⁻⁸
60	1.58 ⁻¹¹	1.07 ⁻¹²	1.03 ⁻¹⁰	3.51 ⁻¹¹	9.86 ⁻¹²	5.14 ⁻⁵	2.41 ⁻¹⁰	3.99 ⁻¹⁰	8.16 ⁻¹⁰	1.11 ⁻¹⁰	6.77 ⁻¹³	5.32 ⁻¹³	4.18 ⁻¹³	3.31 ⁻¹³	3.03 ⁻¹³	2.46 ⁻¹³	2.00 ⁻¹³
61	6.45 ⁻⁶	1.47 ⁻⁵	5.74 ⁻⁹	2.85 ⁻⁵	7.05 ⁻⁶	2.76 ⁻⁴	2.50 ⁻³	4.03 ⁻³	1.17 ⁻²	4.03 ⁻⁴	8.49 ⁻⁵	3.67 ⁻⁵	2.07 ⁻⁵	1.31 ⁻⁵	8.95 ⁻⁶	6.41 ⁻⁶	4.77 ⁻⁶
62	6.54 ⁻⁷	1.93 ⁻⁶	8.56 ⁻¹⁰	1.53 ⁻³	1.60 ⁻⁶	4.23 ⁻⁵	3.67 ⁻⁴	5.87 ⁻⁴	1.70 ⁻³	6.05 ⁻⁵	1.31 ⁻⁵	5.72 ⁻⁶	3.24 ⁻⁶	2.07 ⁻⁶	1.42 ⁻⁶	1.02 ⁻⁶	7.67 ⁻⁷

Table E.5: Free-bound f -values for bound symmetry $J^\pi = 5/2^p$ obtained by integrating photoionization cross sections from \mathbf{R} -matrix calculations. The superscript denotes the power of 10 by which the number is to be multiplied.

In.	17	24	29	38	53	68	79	92	103	114	126	137
16	2.78 ⁻³	2.11 ⁻⁷	1.34 ⁻⁸	8.88 ⁻⁹	8.79 ⁻⁹	8.27 ⁻⁹	7.47 ⁻⁹	6.57 ⁻⁹	5.69 ⁻⁹	4.90 ⁻⁹	4.15 ⁻⁹	3.61 ⁻⁹
18	4.47 ⁻⁶	5.27 ⁻⁴	3.69 ⁻⁹	3.39 ⁻⁹	3.30 ⁻⁹	3.25 ⁻⁹	3.14 ⁻⁹	3.18 ⁻⁹	3.12 ⁻⁹	3.09 ⁻⁹	2.98 ⁻⁹	3.21 ⁻⁹
19	1.24 ⁻⁷	4.78 ⁻³	4.64 ⁻¹⁰	4.43 ⁻¹⁰	4.37 ⁻¹⁰	4.30 ⁻¹⁰	4.17 ⁻¹⁰	4.00 ⁻¹⁰	3.82 ⁻¹⁰	3.48 ⁻¹⁰	3.66 ⁻¹⁰	3.99 ⁻¹⁰
20	2.32 ⁻⁹	1.20 ⁻²	1.72 ⁻¹⁷	1.38 ⁻¹⁶	3.10 ⁻¹⁵	0	0	0	0	0	0	0
21	4.56 ⁻⁷	1.61 ⁻³	3.64 ⁻¹³	3.65 ⁻¹³	3.21 ⁻¹³	1.59 ⁻¹³	1.15 ⁻¹³	4.49 ⁻¹⁵	7.60 ⁻¹⁴	7.09 ⁻¹⁴	7.56 ⁻¹⁴	1.44 ⁻¹³
23	2.24 ⁻⁸	5.24 ⁻⁴	9.47 ⁻⁹	8.94 ⁻⁹	9.08 ⁻⁹	8.40 ⁻⁹	6.36 ⁻⁹	5.54 ⁻⁹	4.76 ⁻⁹	4.07 ⁻⁹	3.93 ⁻⁹	3.43 ⁻⁹
24	1.24 ⁻⁶	1.07 ⁻³	3.20 ⁻⁹	2.91 ⁻⁹	2.67 ⁻⁹	2.43 ⁻⁹	2.17 ⁻⁹	1.92 ⁻⁹	1.69 ⁻⁹	1.48 ⁻⁹	1.30 ⁻⁹	1.14 ⁻⁹
25	1.57 ⁻⁴	1.52 ⁻¹⁰	5.59 ⁻⁵	4.91 ⁻⁵	3.89 ⁻⁵	3.48 ⁻⁵	3.05 ⁻⁵	2.63 ⁻⁵	2.26 ⁻⁵	1.93 ⁻⁵	1.65 ⁻⁵	1.25 ⁻⁵
26	2.29 ⁻³	3.79 ⁻⁸	3.50 ⁻⁶	3.16 ⁻⁶	2.83 ⁻⁶	2.51 ⁻⁶	2.20 ⁻⁶	1.90 ⁻⁶	1.63 ⁻⁶	1.39 ⁻⁶	1.19 ⁻⁶	9.00 ⁻⁷
43	8.17 ⁻⁴	1.17 ⁻⁷	3.26 ⁻⁷	5.10 ⁻⁷	6.46 ⁻⁷	7.25 ⁻⁷	7.59 ⁻⁷	7.58 ⁻⁷	7.35 ⁻⁷	6.97 ⁻⁷	6.51 ⁻⁷	6.02 ⁻⁷
44	1.46 ⁻²	2.83 ⁻⁶	9.13 ⁻⁸	7.43 ⁻⁸	9.39 ⁻⁸	1.06 ⁻⁷	1.12 ⁻⁷	1.14 ⁻⁷	1.12 ⁻⁷	1.08 ⁻⁷	1.03 ⁻⁷	9.68 ⁻⁸
45	1.09 ⁻⁷	2.81 ⁻⁸	1.63 ⁻⁸	2.04 ⁻¹⁰	2.08 ⁻¹⁰	2.01 ⁻¹⁰	1.94 ⁻¹⁰	1.87 ⁻¹⁰	1.83 ⁻¹⁰	1.98 ⁻¹⁰	2.20 ⁻¹⁰	2.44 ⁻¹⁰
46	2.49 ⁻⁵	4.66 ⁻⁷	3.70 ⁻⁹	2.17 ⁻⁸	2.74 ⁻⁸	3.06 ⁻⁸	3.17 ⁻⁸	3.13 ⁻⁸	2.99 ⁻⁸	2.77 ⁻⁸	2.50 ⁻⁸	2.22 ⁻⁸
47	4.70 ⁻³	9.64 ⁻⁷	4.28 ⁻⁸	9.19 ⁻⁹	1.03 ⁻⁸	1.06 ⁻⁸	1.05 ⁻⁸	9.61 ⁻⁹	8.45 ⁻⁹	7.13 ⁻⁹	5.78 ⁻⁹	4.46 ⁻⁹
51	5.49 ⁻⁷	7.39 ⁻⁹	1.91 ⁻⁸	2.24 ⁻¹⁰	2.40 ⁻¹⁰	2.20 ⁻¹⁰	1.69 ⁻¹⁰	1.04 ⁻¹⁰	4.31 ⁻¹¹	4.57 ⁻¹²	1.03 ⁻¹¹	9.47 ⁻¹¹
52	3.19 ⁻⁷	1.35 ⁻⁷	2.87 ⁻⁷	7.10 ⁻⁷	9.12 ⁻⁷	1.04 ⁻⁶	1.11 ⁻⁶	1.13 ⁻⁶	1.12 ⁻⁶	1.09 ⁻⁶	1.04 ⁻⁶	9.99 ⁻⁷
55	5.58 ⁻⁵	6.96 ⁻⁸	3.70 ⁻⁶	5.17 ⁻⁶	6.57 ⁻⁶	7.40 ⁻⁶	7.76 ⁻⁶	7.76 ⁻⁶	7.51 ⁻⁶	7.11 ⁻⁶	6.62 ⁻⁶	6.08 ⁻⁶
57	1.23 ⁻⁵	9.69 ⁻⁴	1.91 ⁻⁹	3.11 ⁻¹⁰	4.07 ⁻¹⁰	4.68 ⁻¹⁰	5.02 ⁻¹⁰	5.15 ⁻¹⁰	5.15 ⁻¹⁰	5.06 ⁻¹⁰	4.92 ⁻¹⁰	4.75 ⁻¹⁰
58	6.08 ⁻⁴	1.62 ⁻⁴	1.33 ⁻⁸	5.77 ⁻⁹	5.26 ⁻⁹	4.56 ⁻⁹	3.83 ⁻⁹	3.16 ⁻⁹	2.57 ⁻⁹	2.10 ⁻⁹	1.70 ⁻⁹	1.41 ⁻⁹
59	1.27 ⁻⁵	2.48 ⁻⁵	8.56 ⁻⁹	2.70 ⁻⁸	2.53 ⁻⁸	2.30 ⁻⁸	2.04 ⁻⁸	1.77 ⁻⁸	1.52 ⁻⁸	1.31 ⁻⁸	1.11 ⁻⁸	9.56 ⁻⁹
61	1.26 ⁻³	8.08 ⁻⁵	1.74 ⁻⁹	4.53 ⁻⁹	3.89 ⁻⁹	3.29 ⁻⁹	2.76 ⁻⁹	2.31 ⁻⁹	1.95 ⁻⁹	1.65 ⁻⁹	1.41 ⁻⁹	1.24 ⁻⁹
62	1.12 ⁻⁴	2.75 ⁻⁶	2.04 ⁻⁷	2.38 ⁻⁷	2.25 ⁻⁷	2.03 ⁻⁷	1.81 ⁻⁷	1.57 ⁻⁷	1.36 ⁻⁷	1.17 ⁻⁷	9.93 ⁻⁸	8.59 ⁻⁸

Table E.6: Sample of the SS1 line list where several lines have been observed astronomically. The first column is for experimental/theoretical energy identification for the upper and lower states respectively where 1 refers to experimental while 0 refers to theoretical. The other columns are for the atomic designation of the upper and lower states respectively, followed by the air wavelength in angstrom and effective dielectronic recombination rate coefficients in $\text{cm}^3.\text{s}^{-1}$ for the given logarithmic temperatures. The superscript denotes the power of 10 by which the number is to be multiplied. The $1s^2$ core is suppressed from all configurations.

ET	Upper	Lower	λ_{air}	$\log_{10}(T)$					
				2.0	2.5	3.0	3.5	4.0	4.5
11	2s2p($^3P^\circ$)4f $^4D_{1/2}^e$	2s2p($^3P^\circ$)3d $^2P_{1/2}^\circ$	5116.73	5.53 ⁻¹⁹⁰	2.59 ⁻⁸¹	1.85 ⁻⁴⁷	2.89 ⁻³⁷	1.48 ⁻³⁴	3.27 ⁻³⁴
11	2s2p($^3P^\circ$)4f $^4D_{5/2}^e$	2s2p($^3P^\circ$)3d $^2P_{3/2}^\circ$	5119.46	5.14 ⁻¹⁶⁸	9.10 ⁻⁶²	1.11 ⁻²⁸	9.88 ⁻¹⁹	4.25 ⁻¹⁶	8.88 ⁻¹⁶
11	2s2p($^3P^\circ$)3p $^2P_{3/2}^e$	2s ² 4p $^2P_{1/2}^\circ$	5120.08	2.50 ⁻²⁶	1.64 ⁻¹⁹	7.84 ⁻¹⁸	3.26 ⁻¹⁷	3.79 ⁻¹⁷	1.76 ⁻¹⁷
11	2s2p($^3P^\circ$)4f $^4D_{3/2}^e$	2s2p($^3P^\circ$)3d $^2P_{1/2}^\circ$	5120.17	6.88 ⁻¹⁶⁹	1.51 ⁻⁶²	1.97 ⁻²⁹	1.80 ⁻¹⁹	7.78 ⁻¹⁷	1.63 ⁻¹⁶
11	2s2p($^3P^\circ$)3p $^2P_{3/2}^e$	2s ² 4p $^2P_{3/2}^\circ$	5121.83	1.20 ⁻²⁵	7.87 ⁻¹⁹	3.75 ⁻¹⁷	1.56 ⁻¹⁶	1.81 ⁻¹⁶	8.40 ⁻¹⁷
11	2s ² 7f $^2F_{5/2}^\circ$	2s ² 4d $^2D_{3/2}^e$	5122.09	6.05 ⁻²⁹	7.95 ⁻²²	2.03 ⁻¹⁸	9.32 ⁻¹⁸	6.66 ⁻¹⁸	3.55 ⁻¹⁸
11	2s ² 7f $^2F_{7/2}^\circ$	2s ² 4d $^2D_{5/2}^e$	5122.27	2.11 ⁻²⁸	1.95 ⁻²¹	3.05 ⁻¹⁸	1.44 ⁻¹⁷	1.03 ⁻¹⁷	5.43 ⁻¹⁸
11	2s ² 7f $^2F_{5/2}^\circ$	2s ² 4d $^2D_{5/2}^e$	5122.27	4.32 ⁻³⁰	5.68 ⁻²³	1.45 ⁻¹⁹	6.66 ⁻¹⁹	4.76 ⁻¹⁹	2.54 ⁻¹⁹
11	2s2p($^3P^\circ$)3p $^2P_{1/2}^e$	2s ² 4p $^2P_{1/2}^\circ$	5125.21	1.46 ⁻²⁶	8.64 ⁻²⁰	4.82 ⁻¹⁸	5.15 ⁻¹⁷	7.05 ⁻¹⁷	3.50 ⁻¹⁷
11	2s2p($^3P^\circ$)3p $^2P_{1/2}^e$	2s ² 4p $^2P_{3/2}^\circ$	5126.96	7.08 ⁻²⁷	4.20 ⁻²⁰	2.34 ⁻¹⁸	2.50 ⁻¹⁷	3.42 ⁻¹⁷	1.70 ⁻¹⁷
11	2s2p($^3P^\circ$)3p $^4P_{3/2}^e$	2s2p($^3P^\circ$)3s $^4P_{1/2}^\circ$	5132.95	4.96 ⁻²⁸	9.80 ⁻²⁰	1.65 ⁻¹⁷	2.49 ⁻¹⁶	2.26 ⁻¹⁵	1.48 ⁻¹⁵
11	2s2p($^3P^\circ$)3p $^4P_{5/2}^e$	2s2p($^3P^\circ$)3s $^4P_{3/2}^\circ$	5133.28	1.69 ⁻²⁷	1.09 ⁻¹⁹	1.71 ⁻¹⁷	1.66 ⁻¹⁶	1.50 ⁻¹⁵	1.08 ⁻¹⁵
11	2s2p($^3P^\circ$)3p $^4P_{1/2}^e$	2s2p($^3P^\circ$)3s $^4P_{1/2}^\circ$	5137.26	1.15 ⁻²⁸	5.07 ⁻²⁰	8.50 ⁻¹⁸	9.92 ⁻¹⁷	8.62 ⁻¹⁶	5.55 ⁻¹⁶
11	2s2p($^3P^\circ$)3p $^4P_{3/2}^e$	2s2p($^3P^\circ$)3s $^4P_{3/2}^\circ$	5139.17	1.57 ⁻²⁸	3.10 ⁻²⁰	5.23 ⁻¹⁸	7.89 ⁻¹⁷	7.15 ⁻¹⁶	4.68 ⁻¹⁶
01	2s ² 11p $^2P_{3/2}^\circ$	2s ² 5s $^2S_{1/2}^e$	5141.70	9.29 ⁻³³	1.36 ⁻²⁵	3.26 ⁻²¹	1.25 ⁻¹⁹	6.35 ⁻¹⁹	6.92 ⁻¹⁹
01	2s ² 11p $^2P_{1/2}^\circ$	2s ² 5s $^2S_{1/2}^e$	5141.76	2.10 ⁻³³	4.79 ⁻²⁶	1.60 ⁻²¹	6.26 ⁻²⁰	3.16 ⁻¹⁹	3.48 ⁻¹⁹
11	2s2p($^3P^\circ$)3p $^4P_{1/2}^e$	2s2p($^3P^\circ$)3s $^4P_{3/2}^\circ$	5143.49	5.77 ⁻²⁸	2.55 ⁻¹⁹	4.27 ⁻¹⁷	4.99 ⁻¹⁶	4.34 ⁻¹⁵	2.79 ⁻¹⁵
11	2s2p($^3P^\circ$)3p $^4P_{5/2}^e$	2s2p($^3P^\circ$)3s $^4P_{5/2}^\circ$	5145.16	3.97 ⁻²⁷	2.56 ⁻¹⁹	4.01 ⁻¹⁷	3.90 ⁻¹⁶	3.54 ⁻¹⁵	2.53 ⁻¹⁵
11	2s2p($^3P^\circ$)3p $^4P_{3/2}^e$	2s2p($^3P^\circ$)3s $^4P_{5/2}^\circ$	5151.08	5.59 ⁻²⁸	1.11 ⁻¹⁹	1.86 ⁻¹⁷	2.81 ⁻¹⁶	2.55 ⁻¹⁵	1.67 ⁻¹⁵
11	2s2p($^3P^\circ$)4f $^4G_{5/2}^e$	2s2p($^3P^\circ$)3d $^2P_{3/2}^\circ$	5162.53	1.92 ⁻¹⁷¹	6.83 ⁻⁶⁶	5.01 ⁻³³	3.80 ⁻²³	1.56 ⁻²⁰	3.20 ⁻²⁰
11	2s2p($^3P^\circ$)3d $^2D_{5/2}^\circ$	2s ² 5g $^2G_{7/2}^e$	5162.98	7.68 ⁻³³	5.07 ⁻²⁶	2.23 ⁻²⁴	2.27 ⁻²⁴	7.55 ⁻²⁵	2.38 ⁻²⁵
00	2s2p($^3P^\circ$)4s $^2P_{3/2}^\circ$	2s ² 11s $^2S_{1/2}^e$	5172.37	8.25 ⁻¹⁰⁸	1.12 ⁻⁴³	6.57 ⁻²⁴	3.60 ⁻¹⁸	7.20 ⁻¹⁷	5.71 ⁻¹⁷
00	2s2p($^3P^\circ$)4s $^2P_{1/2}^\circ$	2s ² 11s $^2S_{1/2}^e$	5187.14	9.10 ⁻¹⁰⁸	7.19 ⁻⁴⁴	3.55 ⁻²⁴	1.84 ⁻¹⁸	3.63 ⁻¹⁷	2.86 ⁻¹⁷
10	2s2p($^3P^\circ$)4s $^4P_{3/2}^\circ$	2s ² 9s $^2S_{1/2}^e$	5196.92	7.54 ⁻⁹⁸	1.97 ⁻⁴³	9.74 ⁻²⁷	5.69 ⁻²²	5.63 ⁻²¹	3.57 ⁻²¹
10	2s2p($^3P^\circ$)4s $^4P_{1/2}^\circ$	2s ² 9s $^2S_{1/2}^e$	5203.44	1.74 ⁻⁹⁸	3.58 ⁻⁴⁴	1.65 ⁻²⁷	9.41 ⁻²³	9.23 ⁻²²	5.84 ⁻²²
11	2s2p($^3P^\circ$)3p $^4D_{5/2}^e$	2s ² 4p $^2P_{3/2}^\circ$	5203.77	7.63 ⁻³³	2.44 ⁻²⁴	4.07 ⁻²²	7.12 ⁻²¹	1.35 ⁻¹⁹	1.71 ⁻¹⁹
11	2s2p($^3P^\circ$)4p $^4S_{3/2}^e$	2s2p($^3P^\circ$)3d $^4D_{1/2}^\circ$	5204.20	2.74 ⁻¹³⁷	2.03 ⁻⁵⁶	2.33 ⁻³¹	6.55 ⁻²⁴	5.86 ⁻²²	8.17 ⁻²²
11	2s2p($^3P^\circ$)4p $^4S_{3/2}^e$	2s2p($^3P^\circ$)3d $^4D_{3/2}^\circ$	5205.70	1.73 ⁻¹³⁶	1.28 ⁻⁵⁵	1.48 ⁻³⁰	4.15 ⁻²³	3.71 ⁻²¹	5.18 ⁻²¹
11	2s2p($^3P^\circ$)4p $^4S_{3/2}^e$	2s2p($^3P^\circ$)3d $^4D_{5/2}^\circ$	5207.98	3.34 ⁻¹³⁶	2.47 ⁻⁵⁵	2.84 ⁻³⁰	8.00 ⁻²³	7.15 ⁻²¹	9.98 ⁻²¹
11	2s2p($^3P^\circ$)3p $^4D_{3/2}^e$	2s ² 4p $^2P_{1/2}^\circ$	5208.74	1.87 ⁻³¹	3.80 ⁻²⁴	4.99 ⁻²²	1.05 ⁻²⁰	1.62 ⁻¹⁹	1.83 ⁻¹⁹
11	2s2p($^3P^\circ$)3p $^4D_{3/2}^e$	2s ² 4p $^2P_{3/2}^\circ$	5210.56	2.50 ⁻³⁰	5.10 ⁻²³	6.70 ⁻²¹	1.41 ⁻¹⁹	2.17 ⁻¹⁸	2.46 ⁻¹⁸
11	2s2p($^3P^\circ$)3p $^4D_{1/2}^e$	2s ² 4p $^2P_{1/2}^\circ$	5212.65	1.15 ⁻³⁰	2.43 ⁻²³	3.42 ⁻²¹	1.01 ⁻¹⁹	1.06 ⁻¹⁸	8.41 ⁻¹⁹
11	2s2p($^3P^\circ$)3p $^4D_{1/2}^e$	2s ² 4p $^2P_{3/2}^\circ$	5214.46	5.52 ⁻³¹	1.17 ⁻²³	1.64 ⁻²¹	4.85 ⁻²⁰	5.09 ⁻¹⁹	4.03 ⁻¹⁹
11	2s2p($^3P^\circ$)4p $^4D_{7/2}^e$	2s2p($^3P^\circ$)3d $^4F_{5/2}^\circ$	5244.05	1.17 ⁻¹⁵⁸	1.89 ⁻⁶¹	3.48 ⁻³¹	4.16 ⁻²²	9.58 ⁻²⁰	1.65 ⁻¹⁹
11	2s2p($^3P^\circ$)4p $^4D_{7/2}^e$	2s2p($^3P^\circ$)3d $^4F_{7/2}^\circ$	5249.53	2.53 ⁻¹⁵⁷	4.08 ⁻⁶⁰	7.50 ⁻³⁰	8.98 ⁻²¹	2.07 ⁻¹⁸	3.55 ⁻¹⁸
11	2s2p($^3P^\circ$)4p $^4D_{5/2}^e$	2s2p($^3P^\circ$)3d $^4F_{3/2}^\circ$	5249.90	1.29 ⁻¹²⁶	6.68 ⁻⁵⁰	3.73 ⁻²⁶	3.70 ⁻¹⁹	1.86 ⁻¹⁷	1.97 ⁻¹⁷
11	2s2p($^3P^\circ$)4p $^4D_{5/2}^e$	2s2p($^3P^\circ$)3d $^4F_{5/2}^\circ$	5253.56	2.49 ⁻¹²⁵	1.29 ⁻⁴⁸	7.20 ⁻²⁵	7.15 ⁻¹⁸	3.59 ⁻¹⁶	3.80 ⁻¹⁶
11	2s2p($^3P^\circ$)4p $^4D_{3/2}^e$	2s2p($^3P^\circ$)3d $^4F_{3/2}^\circ$	5256.09	2.63 ⁻¹²⁵	1.09 ⁻⁴⁸	5.69 ⁻²⁵	5.52 ⁻¹⁸	2.75 ⁻¹⁶	2.91 ⁻¹⁶
11	2s2p($^3P^\circ$)4p $^4D_{7/2}^e$	2s2p($^3P^\circ$)3d $^4F_{9/2}^\circ$	5257.24	2.45 ⁻¹⁵⁶	3.96 ⁻⁵⁹	7.27 ⁻²⁹	8.71 ⁻²⁰	2.01 ⁻¹⁷	3.44 ⁻¹⁷
11	2s2p($^3P^\circ$)4p $^4D_{5/2}^e$	2s2p($^3P^\circ$)3d $^4F_{7/2}^\circ$	5259.06	1.26 ⁻¹²⁴	6.53 ⁻⁴⁸	3.64 ⁻²⁴	3.61 ⁻¹⁷	1.81 ⁻¹⁵	1.92 ⁻¹⁵
11	2s2p($^3P^\circ$)4p $^4D_{1/2}^e$	2s2p($^3P^\circ$)3d $^4F_{3/2}^\circ$	5259.66	1.46 ⁻¹²⁶	5.35 ⁻⁵⁰	2.67 ⁻²⁶	2.65 ⁻¹⁹	1.51 ⁻¹⁷	1.78 ⁻¹⁷

Appendix F

Input Data for DVR3D Code

In this appendix we present a sample of the DVR3D input data files that have been used to generate the H_2D^+ line list. This is for the purpose of thoroughness and to enable the interested researcher to reproduce and check our results. The contents of the missing files can be easily deduced by comparing the given files. It should be remarked that the structure of the DVR3D data files is fully explained in the write-up of this code as given by Tennyson *et al* [244].

F.1 Input Files for Stage DVR3DRJZ

For $J = 0$ even

```
&PRT ZR2R1=.FALSE.,
      zembed=.false.,zmors2=.false.,ztran=.true., /
3
44 0 2000 36 1000 2000 2 1 20 0
H2D+: J=0

2.013814000      1.007537200      1.007537200
2.013553200      1.007276470      1.007276470
66000.000      45000.000000
1.7100      0.10000      0.01080
0.0000      0.00000      0.00750
4073.99136362
```

For $J = 0$ odd

```
&PRT ZR2R1=.FALSE.,
      zembed=.false.,zmors2=.false.,ztran=.true., /
3
44 0 2000 36 1000 2000 2 1 20 1
H2D+: J=0

2.013814000      1.007537200      1.007537200
2.013553200      1.007276470      1.007276470
66000.000      45000.000000
1.7100      0.10000      0.01080
0.0000      0.00000      0.00750
4073.99136362
```

For $J = 10$ even

```

&PRT ZR2R1=.FALSE.,
      zembed=.false.,zmors2=.false.,ztran=.true., /
3
44 10 2000 36 1000 2000 2 1 20 0
H2D+: J=10

2.013814000      1.007537200      1.007537200
2.013553200      1.007276470      1.007276470
66000.000      45000.000000
1.7100      0.10000      0.01080
0.0000      0.00000      0.00750
4073.99136362

```

For $J = 10$ odd

```

&PRT ZR2R1=.FALSE.,
      zembed=.false.,zmors2=.false.,ztran=.true., /
3
44 10 2000 36 1000 2000 2 1 20 1
H2D+: J=10

2.013814000      1.007537200      1.007537200
2.013553200      1.007276470      1.007276470
66000.000      45000.000000
1.7100      0.10000      0.01080
0.0000      0.00000      0.00750
4073.99136362

```

For $J = 20$ even

```

&PRT ZR2R1=.FALSE.,
      zembed=.false.,zmors2=.false.,ztran=.true., /
3
44 20 2000 36 1000 2000 2 1 20 0
H2D+: J=20

2.013814000      1.007537200      1.007537200
2.013553200      1.007276470      1.007276470
66000.000      45000.000000
1.7100      0.10000      0.01080
0.0000      0.00000      0.00750
4073.99136362

```

For $J = 20$ odd

```

&PRT ZR2R1=.FALSE.,
      zembed=.false.,zmors2=.false.,ztran=.true., /
3
44 20 2000 36 1000 2000 2 1 20 1
H2D+: J=20

2.013814000      1.007537200      1.007537200
2.013553200      1.007276470      1.007276470
66000.000      45000.000000
1.7100      0.10000      0.01080
0.0000      0.00000      0.00750
4073.99136362

```

F.2 Input Files for Stage ROTLEV3

For $J = 9$

```

&PRT toler = 1.0d-4, ztran=.true.,zdcare=.true.,zpfun=.true. /
2000 585 2 18000
Rotation for H2D+ J=9
4073.99136362

```

For $J = 13$

```

&PRT toler = 1.0d-4, ztran=.true.,zdcare=.true.,zpfun=.true. /
2000 550 2 25200
Rotation for H2D+ J=13
4073.99136362

```

For $J = 17$

```
&PRT toler = 1.0d-4, ztran=.true., zdcare=.true., zpfun=.true. /
2000 407 2 32400
Rotation for H2D+ J=17
4073.99136362
```

F.3 Input Files for Stage DIPOLE

```
&PRT zprint=.true., zstart=.true., /
Dipole Transitions for H2D+
50
4073.99136362
```

F.4 Input Files for Stage SPECTRA

For $T = 300$ K

```
&PRT zsort=.true., zpfun=.false., GZ=4073.99136362 /
Spectra for dipole moment of h2d+, T=300k
1.0 3.0
300.0 0.00001 1.0 18000.0 1.0 76.485
&SPE zemit=.false., zplot=.true., zfreq=.true., zene=.true., zprof=.false., prthr=0.0d0, /
```

F.5 Input Files for Spectra-BT2

These files are used to generate temperature-dependent synthetic spectra data used in plotting Figure 5.4.

For $T = 100$ K

```
&PRT zsort=.true., zout=.false., zpfun=.false., GZ=0.0, smin=1.0d-28, emin=-1.0d10, emax=1.0d5,
wsmx=10000.0d0, wsmin=1000.0d0, zband=.false., / Spectra_H2D+_at_100K
1.0 3.0
100.0 1.0d-4 1000.0 10000.0 0.500 15.119
&SPE zplot=.true., zlist=.true., z90=.false., zassign=.true., zemit=.false., emax1=1.0d6, emax2=1.0d6,
zprof=.true., zdop=.false., npoints=90000, zfreq=.true., jmax=20 /
```

For $T = 500$ K

```
&PRT zsort=.true., zout=.false., zpfun=.false., GZ=0.0, smin=1.0d-28, emin=-1.0d10, emax=1.0d5,
wsmx=10000.0d0, wsmin=1000.0d0, zband=.false., / Spectra_H2D+_at_500K
1.0 3.0
500.0 1.0d-4 1000.0 10000.0 0.500 164.53
&SPE zplot=.true., zlist=.true., z90=.false., zassign=.true., zemit=.false., emax1=1.0d6, emax2=1.0d6,
zprof=.true., zdop=.false., npoints=90000, zfreq=.true., jmax=20 /
```

For $T = 1000$ K

```
&PRT zsort=.true., zout=.false., zpfun=.false., GZ=0.0, smin=1.0d-28, emin=-1.0d10, emax=1.0d5,
wsmx=10000.0d0, wsmin=1000.0d0, zband=.false., / Spectra_H2D+_at_1000K
1.0 3.0
1000.0 1.0d-4 1000.0 10000.0 0.500 516.31
&SPE zplot=.true., zlist=.true., z90=.false., zassign=.true., zemit=.false., emax1=1.0d6, emax2=1.0d6,
zprof=.true., zdop=.false., npoints=90000, zfreq=.true., jmax=20 /
```

For $T = 2000$ K

```
&PRT zsort=.true., zout=.false., zpfun=.false., GZ=0.0, smin=1.0d-28, emin=-1.0d10, emax=1.0d5,
wsmx=10000.0d0, wsmin=1000.0d0, zband=.false., / Spectra_H2D+_at_2000K
1.0 3.0
2000.0 1.0d-4 1000.0 10000.0 0.500 2487.98
&SPE zplot=.true., zlist=.true., z90=.false., zassign=.true., zemit=.false., emax1=1.0d6, emax2=1.0d6,
zprof=.true., zdop=.false., npoints=90000, zfreq=.true., jmax=20 /
```